Warren, Rebecca Louisa (2012) *Microrheology to explore protein and cell dynamics.* PhD thesis.

http://theses.gla.ac.uk/3344/

Copyright and moral rights for this thesis are retained by the author

A copy can be downloaded for personal non-commercial research or study, without prior permission or charge

This thesis cannot be reproduced or quoted extensively from without first obtaining permission in writing from the Author

The content must not be changed in any way or sold commercially in any format or medium without the formal permission of the Author

When referring to this work, full bibliographic details including the author, title, awarding institution and date of the thesis must be given

Glasgow Theses Service
http://theses.gla.ac.uk/
theses@gla.ac.uk

Microrheology to explore protein and cell dynamics

Rebecca Louisa Warren

B.Sc(hons), M.Sc, M.Res

Submitted in fulfilment of the requirements for the Degree of Doctor of Philosophy

Division of Biomedical Engineering

School of Engineering

University of Glasgow

April 2012

Abstract

In this thesis, I explore the applications of optical tweezers and passive video particle tracking microrheology for bioanalytical applications.

Microrheology is a branch of rheology that has the same principles as conventional bulk rheology, but which works *on micron length scales*. Microrheological techniques relate the free or the driven motion of micron-sized tracer particles suspended in the fluid under investigation to the 'elastic' and 'viscous' components of the material. These components can be related to the dynamics of the molecules that make up the fluid, and thus microrheology has the potential to reveal new information about the microscopic properties of complex materials.

Optical tweezers are sensitive instruments that have been used to apply forces on the order of *pN* and to measure the displacements down to *nm* of objects ranging in size from 10 nm to over 100μm, making them an essential tool for microrheology. Here, we have developed a new set of analytical methods for microrheological measurements of biological and bio-analytical systems. In particular, we have developed two new self-consistent procedures for measuring the linear viscoelastic properties of materials across the widest frequency range achievable with optical tweezers (*Phys.Review E.* (2010) 81:2, and *J. Optics* (2011) 13:4). Furthermore, we present a straightforward procedure for measuring the *in vivo* linear viscoelastic properties of single cells *via* passive video particle tracking microrheology of single beads attached to the cells' exterior. Notably, the procedure presented here represents an alternative methodology that can be extended to many experimental formats and provides a simple addition to existing cellular physiology studies.

In addition, we introduce new methodologies for deriving the concentration scaling laws of polymer and biopolymer solutions from microrheological measurements carried out with optical tweezers. These methods have been adopted to investigate the concentration scaling laws of *in vitro* reconstituted actin solutions and actin/myosin solutions.

Contents

List of Figures

the cycle begins anew. Image created by author, but based upon an image from Ref. [89].

[p26] **Figure 2.1:** (Image created by author, but based on an image from Ref. [120]). The motion of the black polymer chain is constrained by the surrounding blue chains, which cannot be crossed, as if the black chain were confined to a tube (pink dashed lines) of diameter D_e

[p28] **Figure 2.2:** (Taken from Ref. [87]) Schematic representation of a semiflexible chain within an entangled isotropic solution (with other chains represented by points) within (a) the loosely-entangled coil regime, in which $L_c >> L_p$ but $L_p << D_e$ where D_e is the tube diameter, (b) the tightly-entangled coil regime, where $L_c >> L_p$ and $L_p >> D_e$, (c) the loosely-entangled rod regime, where $L_c << L_p$ and where rotation of the rod is impeded by entanglements but fluctuations of the bending modes are not, and (d) the tightly-entangled rod regime, in which $L_c << L_p$ and in which both rotations and shape fluctuations are impeded by entanglements and relax only via reptation. Tightly-entangled solutions of coil-like and rod-like polymers have a similar local geometry.

[p30] **Figure 2.3:** (Image created by author, but based on an image from Ref. [117]. Schematic representation of the stress tensor contributions in Equation 2.3.

[p34] **Figure 2.4:** (Taken from Ref. [87]) Schematic of $G'(\omega)$ (solid line) and $G''(\omega)$ (dotted line) for a tightly-entangled solution of coil-like chains with $L_c >> L_p$. Slopes indicate regimes with a nontrivial power law dependence on frequency, (curvature) and (tension) indicate frequency regimes in which $G^*(\omega)$ is dominated by the curvature or tension contributions. Time scales are defined in the text.

[p36] **Figure 2.5:** (Taken from Ref. [87]) Schematic diagram that shows the evolution of $G'(\omega)/\rho$ with ρ for solutions of coil-like chains. The three lines are sketches of the behaviour predicted for dilute or unentangled solutions (D), loosely-entangled solutions (L), and tightly-entangled solutions (T), all of which exhibit a common asymptote for $G'(\omega)/\rho$ at high frequencies. Slopes represent regimes with a nontrivial power law dependence on frequency, and powers of ρ indicate the predicted dependence of the plateau moduli on concentration. Time scales shown are those relevant to the dilute and loosely-entangled regime, so τ_{rep} is the reptation time of the loosely-entangled solution.

[p39] **Figure 2.6:** (Taken from Ref. [87]) Schematic of the predicted evolution of $G'(\omega)/\rho$ (solid lines) and $G''(\omega)/\rho$ (dotted lines) with concentration for a solution of rod-like polymers. Of the three concentrations shown, one is in the dilute regime (D) and two are in the tightly-entangled regime (T), one for $L_c > L_p^{2/3} L_e^{1/3}$ (which exhibits a high-frequency tension-dominated plateau but no low-frequency orientation-dominated plateau) and one for $L_c < (L_p L_e)^{1/2}$ (which exhibits no tension-dominated plateau but exhibits a narrow orientation-dominated plateau and a low-shear viscosity with a significant orientational contribution.) The time τ_{rod}^{-1} refers to the orientational relaxation time of the tightly-entangled solution. The

corresponding relaxation time for the dilute solution is of order τ_{rep} as described in the text. A loosely-entangled solution (not shown) would look similar to the dilute solution except for the appearance of a value of τ_{rod}^{-1} intermediate between those of dilute and tightly-entangled solutions. The overlapping lines for $G''(\omega)/\rho$ at intermediate frequencies, between τ_{rep}^{-1} and $\tau_{\|}^{-1}$, where $G''(\omega) \propto \omega$, all correspond to the behaviour obtained for the viscous (*i.e.* tension) contribution to the polymer stress of a solution of rigid rods.

[p40] **Figure 2.7:** (Taken from Ref. [87]) Calculated moduli $G'(\omega)$ (solid line) and $G''(\omega)$ (dotted line) for monodisperse solutions with (a) $L_c = L_p/4$, (b) $L_c = L_p$ and (c) $L_c = 10L_p$. The remaining parameters are given values: L_p = 17 μm, ρ = 39 μm $^{-2}$, D_e = 0.2 μm, L_e=2.2 μm, η_s = 0.01 Poise, and d = 0.007 μm, which are believed to be representative of a 1 mg/mL solution of actin. The straight solid line in each figure has a slope of 3/4 and is the predicted high-frequency asymptote of $G''(\omega)$.

[p41] **Figure 2.8:** (Taken from Ref. [87]) Calculated moduli $G'(\omega)$ (solid line) and $G''(\omega)$ (dotted line) for a polydisperse actin solution with $\overline{L_c} = 17\mu m$ and an exponential distribution of chain lengths for the same values of L_p, D_e etc. as in Figure 2.7.

[p41] **Figure 2.9:** (Taken from Ref. [87]) Values of $G'(\omega)$ (solid line) and $G''(\omega)$ (dotted line) for a system approximating a lightly cross-linked gel.

[p46] **Figure 3.1:** Cycle of ATP production from creatine phosphate and ADP.

[p48] **Figure 3.2:** Optical tweezers configuration. From left to right; (LZ) Ti:sapphire laser system, (L1 and L2) beam telescope, (M1 and M2) folding mirrors, (SLM) boulder fast SLM, (L3), (PBS) polarising beam splitter cube, (M3) mirror, (CAM) Prosilica fast camera, (O) objective lens, (CL) condensing optics, (B) 250W halogen bulb. Image taken from [155].

[p49] **Figure 3.3:** Spatial light modulator (SLM) holograms designed to create a single trap (left), two traps (centre) and three traps (right). Red circles indicate the approximate positions of where the first order traps would lie.

[p52] **Figure 4.1:** Bead trapped in a stationary ('static') optical trap.

[p56] **Figure 4.2:** Diagram of experimental procedure: Step I measures the bead trajectory in a static optical trap. Step II measures the displacement of the bead in response to a uniform fluid flow.

[p59] **Figure 4.3:** The MSD vs. lag time of a 5μm diameter bead in water (with κ = 0.8 μN/m) and in two water-based solutions of PAM at concentrations of 0.5% and 1% w/w (both with κ = 1.7 μN/m). The line is the Einstein prediction of the MSD for 5μm diameter bead in water at 25 °C.

[p59] **Figure 4.4:** The normalised MSD vs. lag time of a 5μm-diameter bead in water (with κ = 0.8 μN/m) and in two water-based solutions of PAM at concentrations of 0.5% and 1% w/w (both with κ = 1.7 μN/m).

[p60] **Figure 4.5:** (A) The coordinates of a 5μm diameter bead vs time for two different solutions and for two uniform fluid flow fields of different magnitudes $\left|\vec{V}_s\right|$ at 25 °C. In both cases the data was averaged over three measurements and the x coordinate has been normalised by the steady-state displacement Δx. In water κ = 1.7 μN/m, $\left|\vec{V}_s\right|$ = 20 μm/s, and Δx = 0.523 μm. In 1% w/w of PAM κ = 8.6 μN/m, $\left|\vec{V}_s\right|$ = 3 μm/s, and Δx = 1.115 μm. (B) The graph highlights the start-up behaviour of both the above systems.

[p61] **Figure 4.6:** Storage (circles) and loss (squares) moduli vs. frequency of a solution of 1% w/w of PAM in water measured by means of both Equation 4.6 (solid symbols at high frequencies) and Equation 4.11 (open symbols at low frequencies) applied directly to the experimental data presented in Figures. 4.4 and 4.5 respectively. The dotted lines are guides to the gradients.

.

[p62] **Figure 4.7:** Storage (circles) and loss (squares) moduli vs. frequency of a solution of 1% w/w of PAM in water measured by means of both Equation 4.4 (solid symbols at high frequencies) and Equation 4.9 (open symbols at low frequencies) applied directly to the experimental data presented in Figs. 4.4 and 4.5 but smoothed. The dotted lines are guides to the gradients.

[p64] **Figure 4.8:** Diagram of experimental procedure: Step I measures the bead trajectory in a static optical trap. Step II measures transient displacement of a bead flipping between two optical traps (spaced at fixed distance D_0) that alternately switch on/off.

[p68] **Figure 4.9:** The normalised position autocorrelation function vs. lag-time of a 5μm diameter bead (squares) in water (with $\kappa = 2.7\mu N/m$) and (circles) in a water-based solution of PAM at concentrations of 1 % w/w (with $\kappa = 2.2\mu N/m$). The continuous and dotted lines represent Equation 4.16 for a 5μm diameter bead in water at T = 25ºC with $\kappa = 2.7\mu N/m$ and $\kappa = 2.2\mu N/m$, respectively.

[p69] **Figure 4.10:** The trajectory of a 5μm diameter bead flipping between two optical traps κ_1 (bottom) and κ_2 (top) repeatedly switching after a duration P = 20 s. The bead is suspended in (squares) water (with $\kappa_1 = 2.7\mu N/m$ and $\kappa_2 = 2.5\mu N/m$) and (circles) a water-based solution of PAM at concentrations of 1 % w/w (with $\kappa_1 = 2.1\mu N/m$ and $\kappa_2 = 2.2\mu N/m$).

[p70] **Figure 4.11:** The normalised mean position of all step-down data shown in Figure 4.10, *i.e.* when simultaneously trap 2 (top) switches off and trap 1 (bottom) switches on.

[p71] **Figure 4.12:** Storage (G') and loss (G'') moduli of water vs. frequency, analysed using both Equation 4.18 (high frequencies) and Equation 4.22 (low frequencies) applied directly to the experimental data presented in Figure 4.9 and Figure 4.11, respectively. The lines represent the expected limiting behaviour of the moduli when the material reaches the terminal region: $G'' \propto \omega$ for a Newtonian fluid, and $G' \propto \omega^2$ and $G'' \propto \omega$ for a viscoelastic fluid.

[p71] **Figure 4.13:** Storage (G') and loss (G'') moduli vs. frequency of a solution of 1% w/w of PAM in water measured by means of both Equation 4.18 (high frequencies) and Equation 4.22 (low frequencies) applied directly to the

dotted lines are a guide for the gradients.

[p130] **Figure 7.10:** The normalised loss modulus $G''(\omega)/G''_{Actin}(\omega)$ vs. ratio of myosin:actin (for data extracted from the complex moduli of Figure 7.9) for actin/S1 samples at a frequency of 80 and 400 rad/s, and at S1:actin ratios of 1:1→16:1 .(A) Linear graph: The lines have been added to demonstrate the general trends of the concentration dependence. (B) Log-log graph: The dotted lines are a guide for the gradient.

[p131] **Figure 7.11 [A]:** The normalised storage modulus $G''(\omega)/G''_{Actin}(\omega)$ vs. ratio of myosin:actin (for data extracted from the complex moduli of Figure 7.19) for actin/S1 samples at a frequency of 50 rad/s, and at S1:actin ratios of 1:1→16:1. The data is shown on a linear plot where the lines are added simply to illustrate the shape of the concentration dependence.

[p132] **Figure 7.11 [B]:** The normalised storage modulus $G''(\omega)/G''_{Actin}(\omega)$ vs. ratio of myosin:actin (for data extracted from the complex moduli of Figure 7.9) for actin/S1 samples at a frequency of 50 rad/s, and at S1:actin ratios of 1:1→16:1. The data is shown on a log-log plot where the dotted lines are a guide for the gradient.

[p139] **Figure 8.1:** (Taken from Ref. [218]). Distribution of actin in astrocyte cells under different osmotic conditions. Cells were incubated in Krebs-HEPES medium of different osmolarities and then fixed and stained with rhodamine-phalloidin. Actin was visualised by fluorescence microscopy. (A): cells in iso-osmotic medium; (B): cells maintained in 50% hypo-osmotic medium for 2 min; (C): cells maintained in 50% hypo-osmotic medium for 15 min; (D): cells maintained in 50% hypo-osmotic medium for 2 hours.

[p136] **Figure 8.2:** Normalised MSDs of optically trapped beads in water (blue) and actin (red) (left) and of a bead stuck to a cell (right).

[p138] **Figure 8.3:** (Left) Top view of a 5μm diameter silica bead chemically bound to the surface of a Jurkat cell and (Right) Side view of left image.

[p139] **Figure 8.4:** (Top) Change in volume measured for a single Jurkat cell, with left image showing the cell in the isotonic solution, and the right image showing the cell 7 minutes after the solution was made hypotonic. (Middle left) Volume change of a Jurkat cell plotted as a function of time in our experiment and in (Middle right) Ref. [227] for a human melanoma cell.(Bottom) The volume change plotted as a function of the radius.

[p141] **Figure 8.5: [A-F]:** The $\Pi(\tau)$ vs. lag-time of a 5μm diameter silica bead chemically bound to a Jurkat cell in iso-osmotic (PBS) solution (squares) and in hypo-osmotic solution (circles) after addition of 10% v/v distilled water to the PBS buffer, and measured at time intervals (Δt) of (A) 2 min, (B) 7 min, (C) 12 min, (D) 18 min, (E) 23 min and (F) 28 min respectively.

[p145] **Figure 8.6:** The absolute value of $\beta_n G'_{cn}(0)$ measured in PBS and in 10% hypotonic solution (squares) or in isotonic PBS solution (circles). The arrow indicates the time at which the PBS solution is made hypotonic by the addition of water. The single PBS measurement at 4.5 minutes was an average of three PBS measurements, and the standard deviation was used as the error in all readings. The dotted line is to compare later hypotonic measurements with the initial measurement in PBS.

[p147] **Figure 8.7:** The real (storage, $G'_c(\omega)$) and the imaginary (loss, $G''_c(\omega)$) parts of the complex modulus ($G^*_c(\omega)$) scaled by G'_0 vs. frequency, of a Jurkat cell in iso-osmotic (PBS) solution (A) and in hypo-osmotic solution (B-G) after the addition of 10% v/v distilled water to the PBS buffer and measured at time intervals (Δt) of (A) 2 min, (B) 7 min, (C) 12 min, (D) 18 min, (E) 23 min and (F) 28 min, respectively. The moduli have been evaluated by using Equation 8.3 on the normalised MSD data shown in Figure 8.6. The lines are guides for the gradients.

.

List of Tables

Acknowledgements

I would firstly like to thank Professor Jon Cooper for giving me the opportunity to carry out this research within his group, and for his guidance and support throughout this PhD.

Grazie mille to Manlio Tassieri – without whom this PhD would not have been possible – for being a tireless teacher whose enthusiasm for all things microrheological is infectious.

I would like to thank everyone within the Division of Biomedical Engineering, for their camaraderie, their scientific know-how, and their coffee time chats. Specific thanks must go to Andrew Glide for general all-round helpfulness, and to Shelley Li, for help with experiments.

I appreciate very much the help, advice and laser know-how from the Optics crew in the Physics Department at Glasgow University, especially Graham Gibson, Darryl Preece, Richard Bowman and Miles Padgett.

Thanks must be given to Justin Molloy who spent a cheerful week instructing me in the 'proper' biology needed to extract actin and myosin directly from the source (see below!).

I would like to thank Matt Lang & lab at Massachusetts Institute of Technology for putting up with me for months at a time. I met some friends for life in Boston, and will treasure my time there.

Special, special thanks go to all my friends, who have tirelessly supported me throughout this experience. To my fellow (future and present) PhDs: Anne-Marie (flatmate extraordinaire) Kat, Kit, Heather, Jenna, Alasdair, Alexia, Gordon, Becky, Dayana, Louise, Jeremy, Abeer, Dave, Ellie and Liliana; I salute you! To my non-scientific friends who have suffered through all my science moods, thank-you: Adele, Leanne, Gillian, Kat, Katie and Linzy.

Huge thanks to my family for putting up with me: my mum, dad, sister Lucy and brother Andrew. Mum, you finally have a Doctor in the family (just not the kind you were expecting!).

Most of all I would like to thank the bunny from which I obtained the actin and myosin proteins for this thesis. I hope I made sure your sacrifice was worthwhile!

Author's Declaration

I declare that the work described in this thesis has been carried out by me unless otherwise cited or acknowledged. It is entirely of my own composition and has not, in whole or in part, been submitted for any other degree.

Rebecca Louisa Warren
September 2011

Glossary

MSD	Mean-square displacement
VPT	Video particle tracking
PPTM	Passive particle tracking microrheology
DWS	Diffusing wave spectroscopy
DLS	Dynamic light scattering
AFM	Atomic force microscopy
WLC	Worm-like chain
ATP	Adenosine triphosphate
ADP	Adenosine diphosphate
ABP	Actin-binding protein
$G^*(\omega)$	Complex shear modulus
$G'(\omega)$	Storage (elastic) modulus
$G''(\omega)$	Loss (viscous) modulus
$\left\langle \Delta r^2(t) \right\rangle$	Mean-square displacement
$\Pi(\tau)$	Normalised mean-square displacement
nMSD	Normalised mean-square displacement
nPAF	Normalised position autocorrelation function
VAF	Velocity autocorrelation function
PAM	Polyacrylamide
FDT	Fluctuation-dissipation theorem

Chapter 1

INTRODUCTION

Over the past decade an emerging trend in the field of biology has been the increasing application of more quantitative disciplines, such as physics and engineering, in solving problems associated with bio-materials and bio-mechanics. The convergence of these subjects arises from the fact that many biological systems pose questions best addressed, or indeed, exclusively answered, by mechanical or physical means. The field of rheology has wide ranging applications, but has developed into an extremely useful tool for probing the mechanics of cells and proteins.

At heart, rheology is the study of how matter 'flows'. It is predominantly concerned with the mechanical properties of complex (viscoelastic) fluids, which are substances other than elastic solids or Newtonian fluids (*e.g* water). Most materials, especially ones of interest to biology, can act both "solid-like" and "liquid-like", depending upon the frequency at which they are studied. We define these behaviours as being either *viscous* (like water) or *elastic* (like a solid), the relative proportions of which are reliant upon the time scale upon which they are probed. Traditionally these *viscoelastic* properties were measured on a bulk scale, using a rheometer. With the advent of new techniques designed to probe matter at the intermediate level between bulk and molecular scale, *microrheology* has become increasingly popular as a means of providing mechanical information about biological systems.

In general, microrheology tracks the Brownian trajectory of micron-sized probes with high temporal and spatial resolution in order to derive the mechanical properties of the material in question. Although microrheology is considered to be a modern invention, it can trace its origins back to the biologist Robert Brown, who, in 1827, became intrigued by the random motion of pollen grains suspended in water [1]. His subsequent studies gave rise to the name 'Brownian

motion' to describe this movement; thus, right from its first observation, microrheology and biology were intertwined. Einstein and Smoluchowshi later (independently) explained Brownian behaviour in terms of a statistical analysis of the collisions of pollen with the surrounding solvent molecules, laying in place the theory for modern-day microrheology [2, 3].

The technological developments obtained over the last decades and the commercialisation of "high-tech" equipment at low prices has encouraged scientists to develop new micro and nano-scale investigative procedures. Microrheological techniques are powerful methods to characterise the mechanics and structure of novel and complex materials on length and time scales much shorter than those measured with bulk techniques. Indeed, microrheology corresponds well with the range of sensitivity required to study a wide range of biological processes by possessing the ability to probe mechanical systems on the *nm* length scale, μs time scale and with *pN* forces. Another advantage is the necessary sample volume. A conventional rheometer requires a sample size of >1ml, which, whilst practical for the characterisation of food stuffs and industrial products, is not viable for the study of biological samples such as proteins and cells that exist mainly in small quantities. The size of sample required for microrheological techniques is on the order of $\sim\mu l$, making these methods perfect for biological materials. *Developing microrheological techniques further will allow the study of both new systems and different material properties than conventional methods, and bring about new possibilities for understanding the microscopic properties of complex materials.*

The elegance of microrheology becomes apparent when we consider that in order to obtain the viscoelastic properties of a substance, one need only measure the position of a tracer particle placed in the fluid of interest. In their pioneering paper, Mason & Weitz [4] proved that in an incompressible, homogeneous material the response of an individual micron-sized probe due to external forcing or thermal fluctuations is a reflection of the bulk viscoelastic properties of the surrounding medium. They demonstrated that the mean-square displacement (MSD) of a micron sized tracer particle can be directly related to the viscoelastic properties *via* a property known as the complex shear modulus (which encodes the elastic and viscous components).

Microrheology has many applications within the field of biology. Its main purpose thus far has been to study the *in vitro* properties of the proteins that form the cytoskeleton of cells. The cytoskeleton is a hugely important structure that acts like a "scaffold" to the cell, providing structural stability and shape; but rather than being a static structure, it undergoes constant remodelling in order to adapt to different internal and external conditions. The filamentous proteins that comprise the cytoskeleton have interesting physical properties that determine their viscoelastic behaviour. Developing rigorous models of this behaviour *in vitro* will lead to a better understanding of how the cytoskeleton acts within the cell. This 'bottom-up' approach to cellular

mechanics is now a well-accepted form of experimental bio-analytical science, where models are built from a limited number of components [5]. Increasing numbers of ingredients are added until more cell-like structures are formed; for example, adding cross-linking proteins to networks of the cytoskeletal protein actin drastically increases the magnitude of the rheological response to that approximating the response of a cell.

This thesis aims to explore various aspects of microrheology with optical tweezers and video particle tracking and to apply these methods towards biological samples, namely filamentous protein solutions and single cells. Firstly we develop two new methods of using an optical tweezer setup to measure viscoelastic properties over the widest frequency range accessible with optical tweezers. Secondly, we develop a method of measuring the scaling laws that govern the concentration dependence of material linear viscoelastic properties. These scaling laws are applied to examples of Newtonian fluids, viscoelastic materials and biological samples. Optical tweezer measurements are used to analyse the viscoelastic moduli of protein solutions, specifically networks of actin and networks of actin and the motor protein myosin. Finally, a new video particle tracking technique for measuring the viscoelastic properties of single cells is presented.

1.1 Microrheology

Microrheology describes a collection of techniques designed to probe the viscoelastic properties of very small samples or objects such as cells. There are two ways in which microrheology can probe the viscoelastic properties of materials: (i) the *active* manipulation of probe particles by the local application of stress; and (ii) the *passive* measurement of probe diffusion due to thermal energy. Both methods require a means of accurately detecting the particle trajectory, the most common example of which is video-tracking, whereby the particle position is measured and then analysed so as to calculate the material's viscoelastic properties. Figure 1.1 shows how video particle tracking (VPT) can be either used passively, or be actively when combined with either optical or magnetic tweezers.

Passive microrheology deals with small thermal fluctuations, thus it uncovers the linear viscoelastic properties of a fluid. It reveals the viscoelasticity of the material at thermal equilibrium. Compared to active techniques, passive methods are more straightforward to perform and do not need calibration. All that is needed is a way of measuring the position of a tracer probe in the material of interest. In contrast, active microrheology, which needs to be calibrated, can be used to exert larger forces and deformations on the system, which can push the viscoelastic response into the non-linear regime where deformations in the system may be irreversible. The larger forces created with active methods are more comparable to the forces that would be experienced under physiological conditions *i.e.* blood cells are subjected to high shear stresses as they circulate the body.

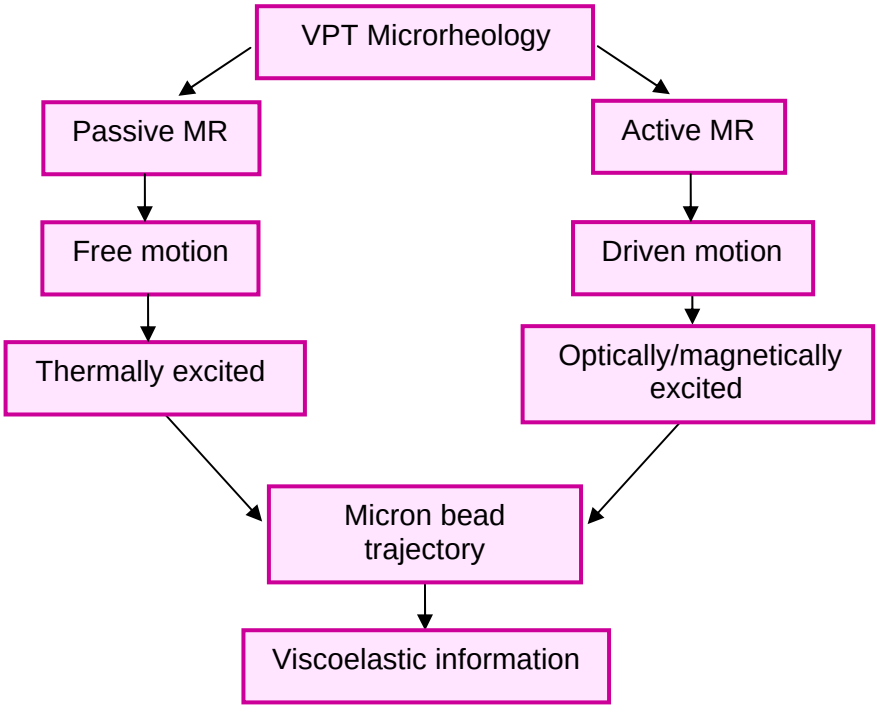

Figure 1.1: *Flow diagram showing the ways in which video particle tracking can be used to obtain viscoelastic information by either passive or active means.*

Microrheology can be approached with a toolkit of several diverse techniques. The decision of which one to use should depend upon a number of factors *e.g.* the required frequency range of interest, the magnitude of moduli to be measured, or whether an homogenous bulk measurement or a local measure of heterogeneity is the desired result. Table 1.1 provides a succinct diagram describing the typically accessible frequencies, moduli, forces and spatial resolution measurable with each microrheological technique. *Note that in this thesis, two methods have been developed to remove the lower limitation of the frequency range accessible with optical tweezers.*

	Passive Video Particle Tracking	Diffusing Wave Spectroscopy	Atomic Force Microscopy	Magnetic Tweezers	Optical Tweezers
Frequency [Hz]	$0.01 \leftrightarrow 1x10^4$	$10 \leftrightarrow 1x10^6$	$0.1 \leftrightarrow 10{,}000$	$0.01 \leftrightarrow 1000$	$0.01 \leftrightarrow 10^6$
Moduli [Pa]	$1x10^{-5} \leftrightarrow 1$	$0.001 \leftrightarrow 1000$	$0.1 \leftrightarrow 1x10^4$	$0.001 \leftrightarrow 1x10^4$	$0.001 \leftrightarrow 100$
Forces	fN	fN	10 pN-1nN	10fN-10nN	1-100pN
Sample Volume	~ µl	$\sim 10^2$ µl	~ 10^2 µl	~ µl	~ µl

Table 1.1: *Comparison of different microrheological techniques, showing accessible frequencies, moduli, forces and sample volume, based upon the use of a micron size tracer (where applicable) [6-8].*

1.1.1 Passive particle tracking microscopy

The simplest of the microrheology methods involves measuring the thermal fluctuations of probe particles that are free to diffuse in a viscoelastic material. Typically this is done using high speed digital video-microscopy which allows the position of multiple tracers to be recorded at once [9]. The use of multiple probes enables a better statistical analysis of the rheological moduli, in addition to providing a detailed analysis of the sample heterogeneity [10]. The accessible frequency range of passive particle tracking microrheology (PPTM) is limited at the upper end by the acquisition rate of the recording device, and at the lower end by the time that the beads take to fall out of the plane of focus. This sedimentation rate of particles can be improved by more buoyant probes. The use of fluorescently labelled particles improves the resolution of the technique (*i.e.* so that tracer particles of size ~nm can be tracked) but introduces new challenges in the form of photobleaching, which can limit the lifetime of an experiment. Examples of systems measured using PPTM cover a wide range from complex fluids [11] to gel-forming amyloid fibril networks [12], actin networks [13] and whole single cells [14].

1.1.2 Diffusing wave spectroscopy

Diffusing wave spectroscopy (DWS) is an extension of the dynamic light scattering (DLS) technique, which itself measures the light scattering from small particles and uses the autocorrelation of the intensity fluctuations to provide information about the particle size. DWS is designed to consider the multiple scattering from numerous colloidal tracers dispersed throughout a transparent viscoelastic substance [4, 15, 16]. The frequency range accessible with DWS is the highest of all the microrheological techniques, up to 10^6 Hz. However, the overriding disadvantage is that the low-frequency response (i.e. ~10Hz) is limited by the size of the sample cuvette. This can be improved upon by using a back scattering geometry to obtain the frequency response down to 0.1Hz. DWS has been used in the rheology of many substances, including many of interest in biology such as the ubiquitous actin networks [15]. Additionally, by using a technique that monitors the scattering from red blood cell particles, the dynamics of blood [17] and tissue [18] have been studied.

1.1.3 Atomic force microscopy

Atomic force microscopy (AFM) was not designed with microrheology in mind; instead, its main applications lie in imaging and sensing. Indeed, it functions by either examining a surface with a cantilever, or by attaching a molecule of interest between the cantilever and surface. Usually a colloidal bead is attached to the cantilever in order to simplify the probe geometry and measure the mechanical interaction between the bead and the surface. Because the mechanical properties (*i.e.* the Young's modulus, a measure of elastic stiffness) can be obtained this way, AFM can be considered to be part of the family of microrheological techniques. If a Hertzian approximation (*i.e.*

small strains between continuous frictionless surfaces) is applied then the viscoelasticity can be calculated with regard to the Young's modulus. Although the moduli can be modelled with standard rheological theory, problems still exist in separating the viscoelasticity of the surface from the electrostatic interaction of the cantilever with the surface [6]. An advantage of AFM is the high moduli that can be measured (Table 1.1), and this has been utilised to study many biological systems such as cells [19, 20], viruses [21], biofilms [22] and single proteins [23].

1.1.4 Magnetic tweezers

One of the principal methods by which active microrheology is performed is with magnetic tweezers. Much larger forces are obtainable than with other techniques, up to around 10nN, which extends the accessible moduli values to far above those achievable with other methods. Magnetic microrheology combines strong electromagnets with video tracking in order to monitor the response of either superparamagnetic or ferromagnetic particles to driving forces (either translational or rotational). Strong magnetic fields are required to induce a magnetic dipole in the beads, and magnetic field gradients are applied in order to produce the force. The force $\vec{F}(t)$ on a particle is given by:

$$\vec{F}(t) = \nabla(\vec{m}(t).\vec{B}(t)) \tag{1.1}$$

where $\vec{m}(t)$ is the induced magnetic moment of the particle and $\vec{B}(t)$ is the imposed magnetic field [24, 25].

In the past, a disadvantage of the magnetic manipulation technique was the lack of manoeuvrability of the tracer particles, but the more complex magnetic systems in use today have improved upon this issue. Magnetic tweezers are commonly employed in whole cell studies [26-28] where the high forces mean physiological conditions can be recreated more readily.

1.1.5 Optical tweezers

As the primary tool in this thesis, optical tweezers will be described in more detail than the other microrheological techniques.

Optical tweezers are based on the pioneering work of Ashkin [29-31] who demonstrated that the forces exerted by a strongly focused beam of light could be used to trap and move a micron-sized object. Since then, they have been extensively developed and have proved to be an invaluable tool throughout the biological and physical sciences. Indeed, many of the early uses of optical tweezers were in biological systems, capturing and manipulating biological samples such as bacteria [32]. These versatile instruments have been used to apply forces on the order of *pN* and to measure

displacements, in the *nm* range, of objects ranging in size from 10 nm to over 100 μm [33, 34]. The fact that the mechanical stiffness of optical tweezers can be adjusted over a force range that covers those relevant to biological molecules makes them particularly suitable to perform studies that currently challenge other techniques, such as atomic force microscopy.

Optical tweezers have found particular use in cell biology [35, 36] and have been successfully used as sensitive tools (*i.e.* as force transducers) for purposes such as measuring the compliance of bacterial tails [37], the forces exerted by single motor proteins [38], the stretching of single deoxyribonucleic acid (DNA) molecules [39], the mechanical properties of human red blood cells [40], and the ability to make high resolution mechanical measurements on individual biological molecules [32, 41-43].

Beyond trapping a single particle, multiple optical traps can now be generated using holographic elements [44-48]. In conjunction with recent advances in camera technology [49, 50] this has meant that many particles can now be trapped simultaneously and their positions tracked at frame rates of *kHz* for indefinite periods of time [51]. This ability to trap, position and track many particles has found particular use in colloidal science [52-55] where the hydrodynamic interactions between particles are of great importance in understanding common colloid phenomena such as sedimentation and aggregation. Another advantage of high-speed cameras is the ability to study hydrodynamic interactions between particles trapped in much less viscous media, such as air [56, 57] allowing investigation into aerosols. It also allows the observation of a parametrically excited resonance within a Brownian oscillator [56], and under-damped modes in periodic arrays of trapped particles [57].

The inherent size scale of optical tweezers makes them readily applicable to microfluidic systems. These systems offer many advantages over conventional methods for biological and chemical measurements. The miniaturisation of micro-analytical devices results not only in a low fabrication cost and a reduction in the volume of potentially expensive reagents used, but also in an increased speed of analysis and the ability to run multiple analytical processes in parallel. In recent years there have been a number of applications using optical tweezers with microfluidics; for example to sort cells [58-60], or to manipulate and measure fluids within micro-devices [61-63]. One of the most prominent applications in microfluidics has been the work by Guck *et al*. with their ‘optical stretcher’ [64-66]. An object placed in a dual beam trap becomes stretched: while the total force acting on the object is zero there is a momentum transfer from the light to the surface as the light passes through the interface acting away from the beam propagation direction. Hence, a suitably elastic object will become stretched in a dual beam trap. The technique allows one to probe the viscoelastic properties of the trapped particles which is particularly useful for cellular material where the deformability provides information about the cytoskeleton. This has been shown to be

useful as a cell marker for detecting cancerous cells [67]. By integrating the device into a microfluidic system cells can be analysed in a high throughput manner [68, 69].

The physics describing the ability of a tightly focused beam of light to confine a microscopic particle in three dimensions can be simply explained by the difference in refractive index between the suspending medium and the probe particle, and by the principle of conservation of momentum. At the heart of trapping physics is the momentum change experienced by a photon of momentum:

$$\left|\vec{p}\right| = h/\lambda \tag{1.2}$$

(where h is Planck's constant, and λ is the wavelength of light), when light is refracted by a transparent dielectric object; this results in an equal and opposite momentum change (and hence force) on the object.

The force experienced by a dielectric particle in a laser beam can be separated into two components; the scattering force and the gradient force (see Figure. 1.2). The scattering force acts in the direction of light propagation and is due to the incident light being absorbed by the particle. This means that the net momentum transfer is in the forward direction because, for an isotropic scatter, all the other forces cancel each other out. The scattering force is dominant until the laser is tightly focused which produces a steep intensity gradient. A dipole in an inhomogeneous electric field will experience a force in the direction of the field gradient; thus when the focused laser induces dipoles in a dielectric particle, they will interact with the inhomogeneous field near the focus point and produce the gradient force. It is dependent upon the both the polarisability of the particle and the intensity gradient at the focus.

For stable trapping to occur the axial component of the gradient force needs to be greater then the scattering force that pushes the particle forward. This is achieved by using a high numerical aperture lens to focus the beam to a diffraction limited spot, where the equilibrium position of the trapped particle is slightly beyond the focal point.

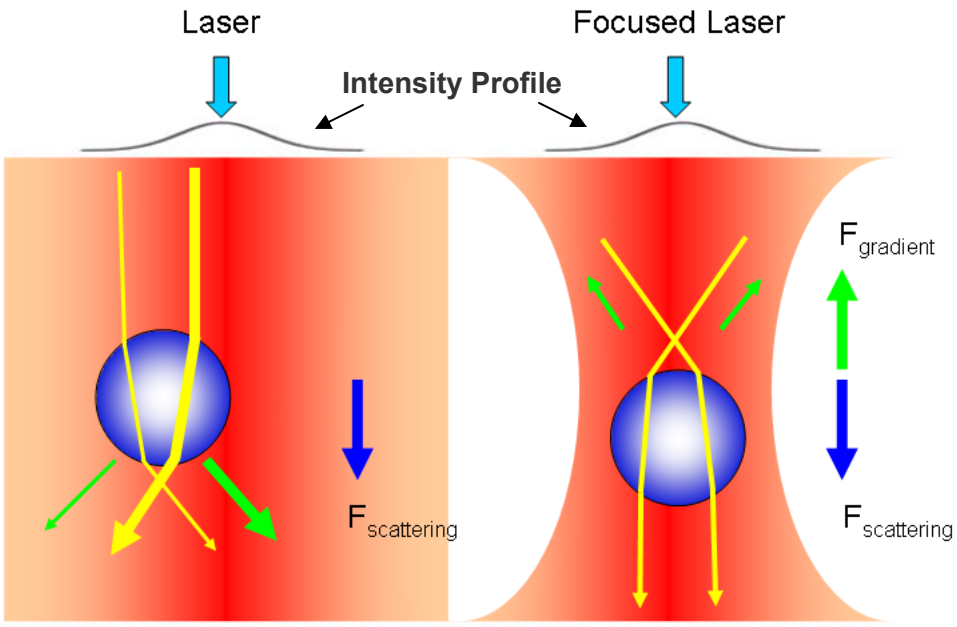

Figure 1.2: *Forces acting on a particle in an unfocused (left) and focused (right) laser beam (of Gaussian intensity profile). Laser paths are denoted by yellow lines; the stronger the beam, the thicker the line. In the unfocused beam the gradient force acts in the approximate same direction as the scattering force, pushing the beam forwards and towards the beam centre. In the focused trap, the gradient force acts towards the focal point of the laser beam, balancing out the scattering force and creating a stable trap. Image created by author.*

The optical trap forms a potential well which in good approximation can be described as a harmonic potential with energy $1/2kx^2$ in one dimension (as in Figure 1.3). For small displacements the restoring force is proportional to the offset from equilibrium position:

$$F = -kx \tag{1.3}$$

(where k is the trap strength and x is the displacement from equilibrium); so effectively the system acts as a Hookean spring where the characteristic trap stiffness is proportional to the intensity of light.

Optical tweezers have the potential to measure the high frequency dynamic properties of a material to a high accuracy *via* the statistical mechanical analysis of the bead trajectory, as shown in this thesis. However, the low frequency viscoelasticity of a material is typically inaccessible with optical tweezers, hence tweezers are usually combined with other techniques such as rotational bulk rheometry [71] or passive video particle tracking [72].

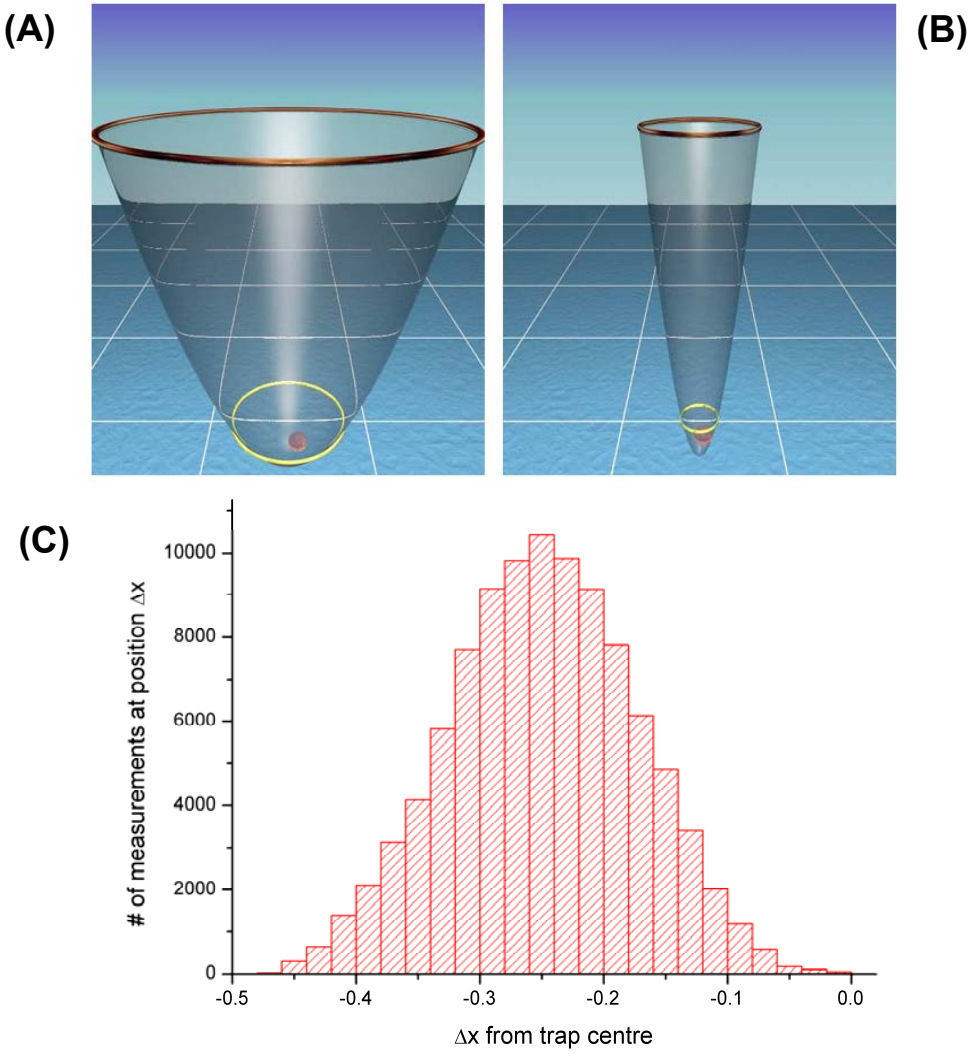

Figure 1.3: *(A and B, taken from Ref. [70]) Animation showing a bead in two optical trap potential wells with (A) weak trap strength and (B) strong trap strength.. The vertical axis represents the potential energy and the horizontal axis represents the distance from the centre of the trap. The yellow rings represent the thermal energy* $k_B T$. *With a lack of external forces the particle will be located below the thermal energy line. An example of a typical distribution of bead positions is shown in (C) (created from measurements from this thesis).*

The high degree of sensitivity shown by optical tweezers has encouraged many scientists to make use of them in the exploration of various biophysical systems, such as the dynamics of biopolymer solutions at different concentration regimes *i.e.* from highly concentrated biopolymer solutions, where the dynamics of the whole polymer-network are explored, down to the single molecule dynamics [73-76].

1.2 Theory of microrheology

Microrheology, like rheology, is concerned with the relationship between the stress (applied force) and the strain (deformation) in a material. To understand this, let us introduce two behaviours that

identify how a material can store energy; the first of which is classed as purely *elastic* (solid-like) behaviour and second as purely *viscous* behaviour (*e.g.* the behaviour of water).

Elasticity is the capacity to store energy, and manifests itself as the ability of a material to return to its original shape after being deformed by an external applied stress, σ. A purely elastic material can only deform under stress, it cannot flow, and the amount of deformation of the system is termed strain, γ. At small stress, simple elastic materials are characterised by a linear stress-strain relationship, written as:

$$\sigma = k\gamma \tag{1.4}$$

where σ is the applied stress, γ is the strain and k is the elastic (or Young's) modulus.

At the other extreme, a purely viscous (Newtonian) fluid is characterised only by its viscosity and has no component of elasticity. Real materials, and especially soft materials (as in biology), are neither ideal solids nor ideal Newtonian fluids. Real soft materials exhibit both elastic and viscous responses, and are termed viscoelastic (*e.g.* custard, blood and single cells, Figure 1.4).

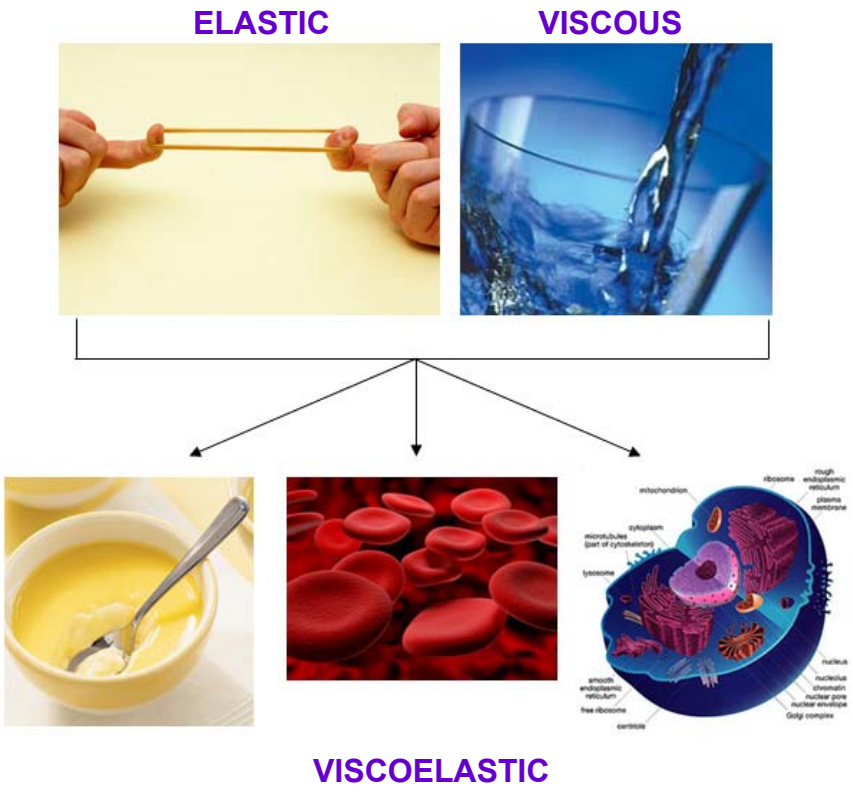

Figure 1.4: *Examples of a purely elastic material (rubber band), a purely viscous material (water), and viscoelastic materials (corn-flour custard, blood, and single cells). Images from [77,78]*

For a Newtonian fluid the stress is proportional to the strain rate *via:*

$$\sigma = \eta\dot{\gamma} \tag{1.5}$$

where η is the *viscosity* (Newton's law for a viscous fluid). For a viscoelastic material, the stress-strain relationship is more complicated, and is a function of time, direction, and the extent of deformation. It can be expressed in terms of the shear relaxation modulus, $G(t)$, which for a viscoelastic material is a time dependent parameter. $G(t)$ is related to the stress and the strain by the convolution integral [79]:

$$\sigma = \int_{-\infty}^{t} G(t-\tau)\left(\frac{d\gamma}{d\tau}\right)d\tau \tag{1.6}$$

The physical meaning of $G(t)$ becomes apparent if we consider that, for a perfectly elastic solid, $G(t)$ simplifies to a constant value proportional to σ/γ (specifically 1/3 E, where E is the Young's modulus of the elastic solid). An alternative way to express the time dependency of the shear modulus is *via* the frequency-dependent *complex* shear modulus, $G^*(\omega)$, which is the Fourier transform of the time derivative of the time-dependent shear relaxation modulus, $G(t)$:

$$G^*(\omega) = F\left[\frac{dG(t)}{dt}\right] \tag{1.7}$$

The conventional method of measuring the complex shear modulus in a bulk rheometer is based on the imposition of an oscillatory stress, $\sigma(\omega,t)$ and the measurement of the resulting strain, $\gamma(\omega,t)$, or *vice versa.* If the strain can be expressed as $\gamma = \gamma_0 \sin(\omega t)$ (where γ_0 is the amplitude of the strain, and ω is the frequency of oscillation), then the resulting strain rate will be $\dot{\gamma} = \omega\gamma_0 \cos(\omega t)$. Substituting these values into Equation 1.6 and denoting $(t-\tau)$ as s gives:

$$\begin{aligned}\sigma &= \int G(s)\omega\gamma_0 \cos[\omega(t-s)]ds \\ &= \gamma_0\left[\omega\int_0^{\infty} G(s)\sin\omega s\, ds\right]\sin\omega t + \gamma_0\left[\omega\int_0^{\infty} G(s)\cos\omega s\, ds\right]\cos\omega t\end{aligned} \tag{1.8}$$

It is clear that the term that includes $\sin(\omega t)$ is in phase with the strain, whereas the term that includes $\cos(\omega t)$ is 90º out of phase. The quantities in brackets are functions of frequency, but not of elapsed time, so Equation 1.8 can be conveniently written:

$$\sigma = \gamma_0\left(G'\sin\omega t + G''\cos\omega t\right) \tag{1.9}$$

which defines two frequency-dependent functions; the shear storage (elastic) modulus, $G'(\omega)$, and the shear loss (viscous) modulus, $G''(\omega)$.

An alternative way to express the stress is to display the amplitude, $\sigma_0(\omega)$, of the stress and the phase angle $\delta(\omega)$ between the stress and the strain [77]:

$$\sigma = \sigma_0 \sin(\omega t + \delta) = \sigma_0 \cos\delta \sin\omega t + \sigma_0 \sin\delta \cos\omega t \tag{1.10}$$

Comparing Equations 1.9 and 1.10 shows that:

$$\begin{aligned} G' &= (\sigma_0/\gamma_0)\cos\delta \\ G'' &= (\sigma_0/\gamma_0)\sin\delta \\ G''/G' &= \tan\delta \end{aligned} \tag{1.11}$$

It is usually convenient to express the sinusoidally varying stress as a complex quantity; hence the resulting modulus is also complex and can be written as:

$$\frac{\hat{\sigma}(\omega)}{\hat{\gamma}(\omega)} = G^*(\omega) = G'(\omega) + iG''(\omega) \tag{1.12}$$

where $\hat{\sigma}(\omega)$ is the Fourier transform of the stress and $\hat{\gamma}(\omega)$ is the Fourier transform of the strain.

Whilst bulk rheology analyses the response of material to an imposed stress (or strain), microrheology obtains the material's linear viscoelastic properties (*i.e.* $G^*(\omega)$) *via* the analysis of the trajectory of tracer particles embedded in the material. Passive microrheology deals with thermally fluctuating particles, as originally demonstrated by Mason and Weitz in their pioneering paper [4].

The analysis of the thermal fluctuations of a tracer particle is carried out by using the mean-square displacement (MSD) of that particle. This can be defined as:

$$\left\langle \Delta r^2(\tau) \right\rangle \equiv \left\langle [\vec{r}(t+\tau) - \vec{r}(t)]^2 \right\rangle_t \tag{1.13}$$

where t is the absolute time and τ is the lag time (*i.e.* the time interval). The average is taken over all initial times t.

In a purely viscous fluid, the MSD, $\left\langle \Delta r^2(\tau) \right\rangle$, of a particle as it diffuses in *d*-dimensions grows linearly with the time interval, Δt, as described in Eq. 1.14 (the Einstein Equation for the MSD, shown as the line with unity slope in Fig 1.5):

$$\left\langle \Delta r^2(\tau) \right\rangle = 2dD\Delta t \tag{1.14}$$

The growth rate is given by the diffusion coefficient D, which obeys the Stokes-Einstein Relation:

$$D = \frac{k_B T}{6\pi a \eta} \tag{1.15}$$

where k_B is the Boltzmann constant, T is the absolute temperature, a is the particle radius, and η is the viscosity of the fluid. The denominator $6\pi a \eta$ arises from Stokes' Law for the drag force exerted on spherical objects in a continuous viscous fluid.

For elastic solids an embedded particle will not diffuse and the MSD will be constant with time (dashed line with slope 0 on Figure 1.5). For viscoelastic materials therefore, the evolution of the MSD over time lies somewhere between the above limits for elastic and viscous cases (red dotted line, Figure 1.5)

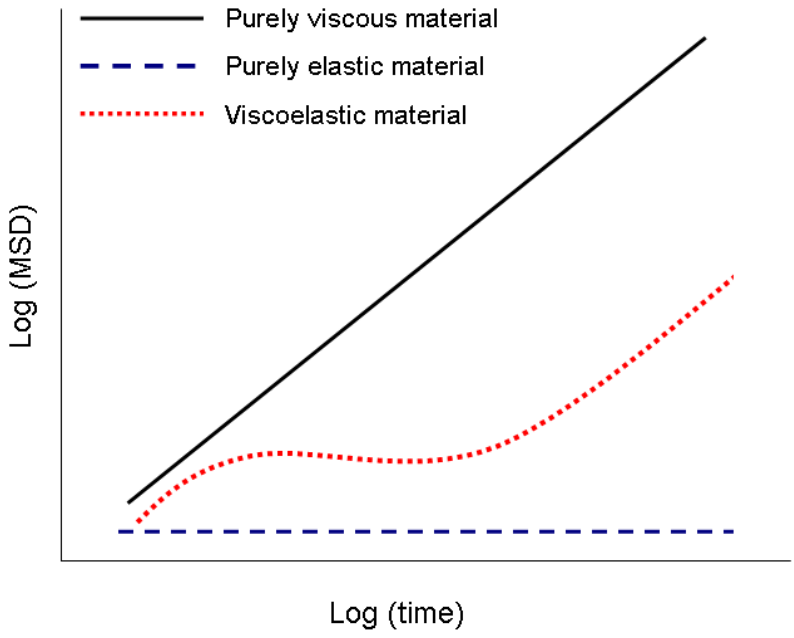

Figure 1.5: *Example of the evolution of the MSD of a viscoelastic material over time. Image adapted from [120]*

Once the MSD of a probe particle is measured it can be related to the complex shear modulus by means of a generalised Langevin equation, as shown by Mason and Weitz [4]:

$$m\dot{\vec{v}}(t) = \vec{f}_R(t) - \int_0^t \zeta(t-\tau)\vec{v}(\tau)d\tau \tag{1.16}$$

where m is the particle mass, $\vec{v}(t)$ is the particle velocity, and $\vec{f}_R(t)$ is the Gaussian white noise term, modelling stochastic thermal forces acting on the particle. The integral term represents the viscous damping force of the fluid, which incorporates a generalised time-dependent memory function $\zeta(t)$.

By performing the Laplace transform of Equation 1.16, the viscoelastic memory function can be expressed as a function of the velocity autocorrelation function (VAF) in Laplace space, defined as $\langle v(0)\tilde{v}(s)\rangle$, as shown in the next steps; Firstly, the unilateral Laplace transform of Equation 1.16 results in:

$$m\left[s\,\tilde{v}(s)-v(0)\right]=\tilde{f}_R(s)-\tilde{\zeta}(s)\tilde{v}(s) \tag{1.17}$$

where s is the Laplace frequency. Expressed in terms of the VAF Equation 1.17 becomes:

$$\tilde{v}(s)=\frac{\left[\tilde{f}_R(t)+m\,v(0)\right]}{ms+\tilde{\zeta}(s)} \tag{1.18}$$

Based on the same statistical mechanics assumptions adopted by Mason and Weitz [4], at thermal equilibrium where $\langle v(0)f_R(t)\rangle=0$ and $m\langle v(t)v(t)\rangle=3k_BT$ at any time, Equation 1.18 can be reorganised as:

$$\langle v(0)\tilde{v}(s)\rangle=\frac{6k_BT}{ms+\tilde{\zeta}(s)}\equiv s^2\langle\Delta\tilde{r}^2(s)\rangle \tag{1.19}$$

where the identity of $\frac{s^2}{2}\langle\Delta\tilde{r}^2(s)\rangle$ links the VAF to the MSD [80, 81]. Moreover, by following Mason & Weitz [4] and assuming the validity of the assumption that the microscopic memory function is proportional to the bulk frequency-dependent viscosity of the fluid $\tilde{\zeta}(s)=6\pi a\tilde{\eta}(s)$, Equation 1.19 can be written as:

$$\tilde{G}(s)=s\tilde{\eta}(s)=\frac{s}{6\pi a}\left[\frac{6k_BT}{s^2\langle\Delta\tilde{r}^2(s)\rangle}-ms\right] \tag{1.20}$$

where $\tilde{G}(s)$ is the complex modulus, $G^*(\omega)$, expressed in the Laplace domain.

Note that the second term in the brackets is due to the inertia of the particle and it is easy to demonstrate that, for a micron-sized bead of density of order of 1g/cm^3 (thus mass $\sim10^{-15}kg$) suspended in water, the product ms is negligible compared with the first term for the majority of the experimentally accessible frequencies (*i.e.* $s<10^6\,Hz$).

1.3 Definition of a semiflexible polymer

To a first approximation a polymer that has an aspect ratio $p >> 1$ (where p is defined as the ratio between the polymer contour length, L_c, and its diameter, d) can be described as a homogeneous elastic filament with a constant circular cross-section and it can be characterised by its Young's modulus, E. Once the Young's modulus is known the deformation of that polymer (stretching, bending, and twisting) can be predicted. For sufficiently small amplitudes of excitation some simplifying assumptions can be applied: (i) it can be assumed that the cross section is constant during bending; (ii) the different types of deformations can be considered independent of each other; and (iii) the filament is inextensible. These collective assumptions form the basis of the worm-like chain (WLC) model [82]. In particular, since the energy per unit length required to change the length of such a filament by a specified fractional strain is proportional to Ed^2 and the energy per length required to bend it into an arc of radius R is of the order Ed^4/R^2, then the ratio between the arc bending energy and the strain energy is relative to $(d/R)^2$; thus, the WLC chain model is justified as long as $d/R << 1$.

The smallest excitations to which a polymer chain is subject are caused by thermal energy. These represent an important feature of the microscopic structures of semiflexible polymers solutions. The conventional measure for the degree of thermal flexing of a polymer is the persistence length, L_p. The persistence length is defined, by the correlation function of Equation 1.21, as the characteristic distance along the polymer chain over which the directions of unit vectors, $\vec{u}(s)$, drawn tangent to the polymer contour, become uncorrelated (Figure 1.6):

$$\left\langle \vec{u}(s) \bullet \vec{u}(s') \right\rangle = e^{-|s-s'|/L_p} \tag{1.21}$$

where the brackets denote the average over thermal fluctuations, and s is the distance along the chain contour, measured from an arbitrary point s'.

The persistence length increases with increasing filament ridigity and decreases with increasing temperature:

$$L_p = \frac{EI}{k_B T};\ I = \frac{\pi}{64} d^4 \tag{1.22}$$

where I is the moment of inertia of the filament cross section of diameter d, k_B is Boltzman's constant and T is the temperature. The product EI is also defined as the 'flexural rigidity' or 'bending modulus' (κ).

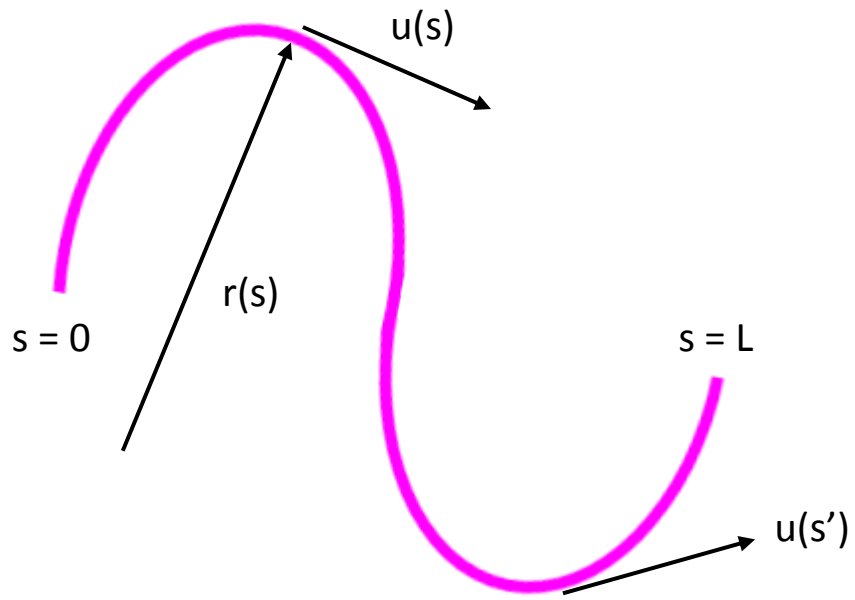

Figure 1.6: *Geometrical representation of a linear semiflexible polymer. Image adapted from [120].*

Polymers for which the persistence length and contour length are comparable ($L_c / L_p \sim 1$) are classified as *semiflexible polymers* .Examples include the cell cytoskeletal components actin [83] and microtubules [84], as well as DNA [85]. These long chain molecules possess mechanical properties that lie between those of flexible chains ($L_p \to 0$) and rigid rods ($L_p \to \infty$). Their viscoelastic properties are not fully understood and current models describing their behaviour draw from models of both flexible and rigid polymers. The model developed by Morse [86-88] (see Chapter 2) provides one of the most comprehensive descriptions of the viscoelastic behaviour of semiflexible polymer solutions. For this reason, it is referred to throughout this thesis.

1.4 Actin and its role in the cell

In order for cells to organise themselves in space and to interact mechanically with their environment, they have to be able to adapt their shape and internal structure [89]. The ability to rearrange their internal components to fit their circumstances enables them to grow, divide and migrate. The structure primarily responsible for regulating these mechanical properties is known as the cytoskeleton, a complex system of filaments. The building block of the most abundant of these filaments is the protein actin. At low salt concentrations actin exists as a globular ~43kDa protein (G-actin) with a diameter of approximately 5nm. As the ionic (K^+ or Mg^{2+}) strength increases to physiological levels G-actin self-assembles into filaments (F-actin), a double helical polymer with

diameter ~7nm and a contour length of up to 20μm [87, 90]. This is the form which actin predominantly takes *in vivo*; thus, studying the dynamics of reconstituted actin *in vitro* has the potential to provide predictive models for the behaviour of cells. Note that throughout this thesis the term 'actin' refers to F-actin.

Actin is one of the most abundant and conserved proteins in eukaryotes, comprising ~10% by weight of the total protein found in mammalian cells [91]. It was originally identified as a component of the protein complex acto-myosin that was found to be responsible for producing contractile forces in skeletal muscle [92] (Figure 1.7). There are numerous aspects of cell physiology that rely on actin in some way. Functions of actin include: forming the dynamic component of the cell cytoskeleton – 'microfilaments' – alongside intermediate filaments and microtubules; acting as a track for transporting non-conventional in non muscle cells; and cell motility.

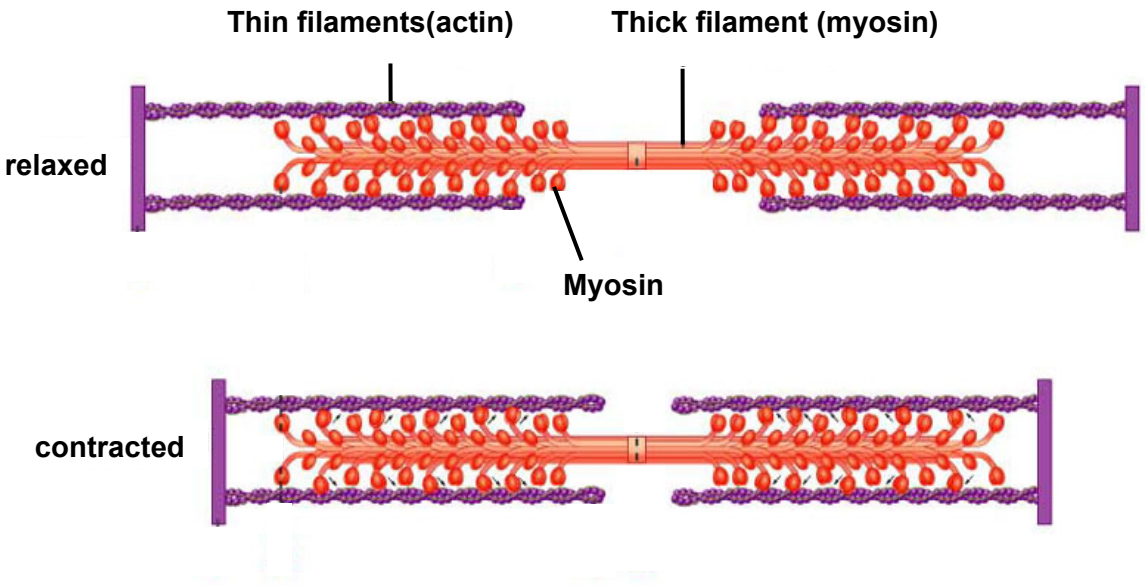

Figure 1.7: *Process of muscle contraction in a sarcomere. The 'thin' actin filaments are pulled along the 'thick' myosin filaments to produce the contraction [93].*

The cell's structural stability is determined by the network structures that actin forms in the cell cytoplasm, with the highest concentration of actin being found in the cortex, just beneath the plasma membrane. The shape of the cell is also influenced by these, which in term dictates how the cell interacts with its environment. Commonly this interaction may occur *via* long finger-like structures called microvilli formed from membrane tethered actin bundles. The relationship between cytoskeletal actin and the cell plasma membrane is an important one. Biochemical signals between actin and the membrane are sent either through proteins that bridge the membrane or by way of peripheral membrane proteins that act as adapter proteins. Cell migration is also a result of actin dynamics; lamellipodia and filopodia are both actin projections, formed during cell migration,

that allow directed movement of the cell. Additionally, actin and myosin-II are assembled into a contractile ring during cytokinesis, the process by which cells divide. Actin filaments are accumulated at the cell cortex and contraction forces generated by the myosin cause daughter cells to separate in order to complete the cell division [89].

Actin is highly conserved, with the amino acid sequences from different species being around 90% identical [89]. Extracellular actin has been implicated in various human and animal diseases; for instance, it is thought to play a role in the development of *e.coli* infections [94], as well as contributing to fibrin clotting [95] and cystic fibrosis [96]. For such a ubiquitous protein, it is essential that we have an in-depth understanding of actin's mechanical behaviour.

In skeletal-muscle cells actin assembles into so called *thin* filaments, which, in tandem with the *thick* filaments of myosin, form the basis of the sarcomere. The sarcomere is the basic unit of myofibrils, which are the principle component of skeletal-muscle cells. It is the movement of myosin along the actin filaments that produce muscular contraction (Figure 1.7) *via* the intermittent movement of individual myosin heads. Cross-bridges between actin and myosin are formed by a specific part of the myosin molecules that protrudes from the myosin thick filament in order to interact with the actin filament. The fuel for this reaction is the hydrolysis of an adenosine triphosphate (ATP) molecule.

Additionally, actin relies on a large number of other proteins to be able to carry out the actions described above. Over time genetic, immuno-chemical and biochemical studies have all identified numerous (>100) actin binding proteins (ABP) that interact with actin in order to form required structures. This means that the complex and dynamic mechanical properties of the actin cytoskeleton are regulated at multiple levels by a variety of ABPs. The function of some ABPs is to cross-link actin filaments or to promote the interaction of filaments with other elements of the cytoskeleton. Myosin is one of these proteins. As already mentioned myosin-II interacts with actin in skeletal-muscle cells, but other types of myosin are commonly found in virtually all eukaryotic cells.

1.5 Myosin-II

It is the interaction of actin with the motor protein myosin II, in the presence of ATP, that produces the forces required to contract striated muscle fibres. Myosins are a large family of proteins with at least 24 different classes identified [97]; all are responsible for actin based motility. One specific class of myosin-II is abundantly expressed in skeletal muscle cells, and has become one of the most commonly studied myosins.

Skeletal muscle myosin-II is a 500kDa protein formed of two heavy chains and two pairs of light chains (Figure 1.8) – the regulatory light chain (RLC) and the essential light chain (ELC). A myosin-II molecule is a homodimer comprised of two heavy chains wrapped around each other for around 80% of their length, forming a helix. The amino terminal of each heavy chain is referred to as the 'head' and is the section of the protein which encompasses the motor domain, the portion that interacts with actin.

The heavy chain tails self associate to form filaments both *in vivo* and *in vitro* at low ionic strengths. In practice, these thick myosin filaments are problematic to work with experimentally. A common alternative is proteolytically produced fragments of myosin-II that are soluble and enzymatically active (Figure 1.8 and Figure 1.9). The S1 fragment is comprised of a single head domain attached to a part of the heavy chain. It retains its ability to bind to actin; indeed, if ATP is present the head domain alone can generate movement [98, 99]. Heavy meromyosin (HMM) is also soluble at low ionic strengths and contains two head domains, the two light chain pairs, and a portion of the heavy chain. S1 and HMM are commonly used to study the kinetic and biophysical characteristics of myosin-II.

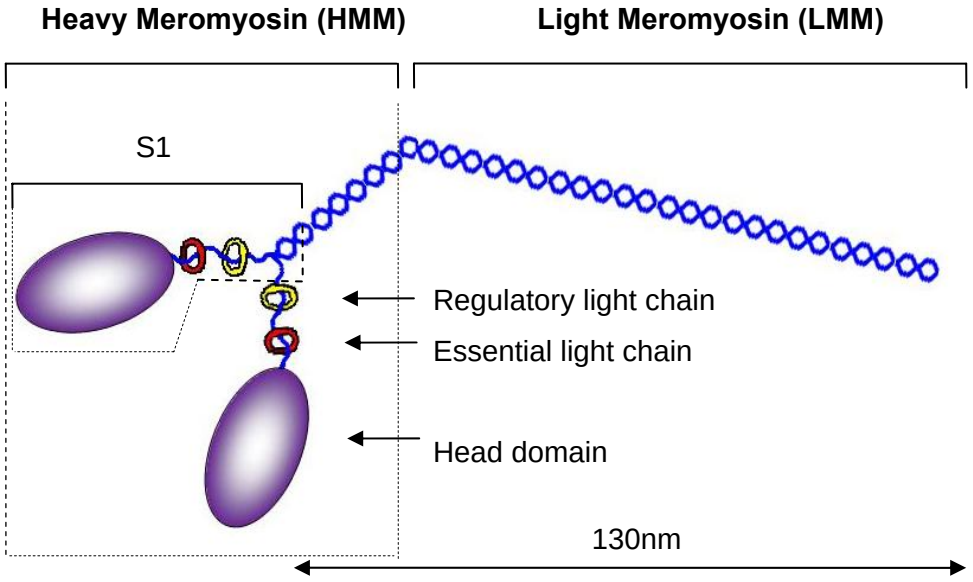

Figure 1.8: *Structure of a myosin-II molecule. The myosin fragments are composed of two head domains, two pairs of light chains, and a section of tail, (HMM) and a single head domain and one pair of light chains (S1).Image created by author.*

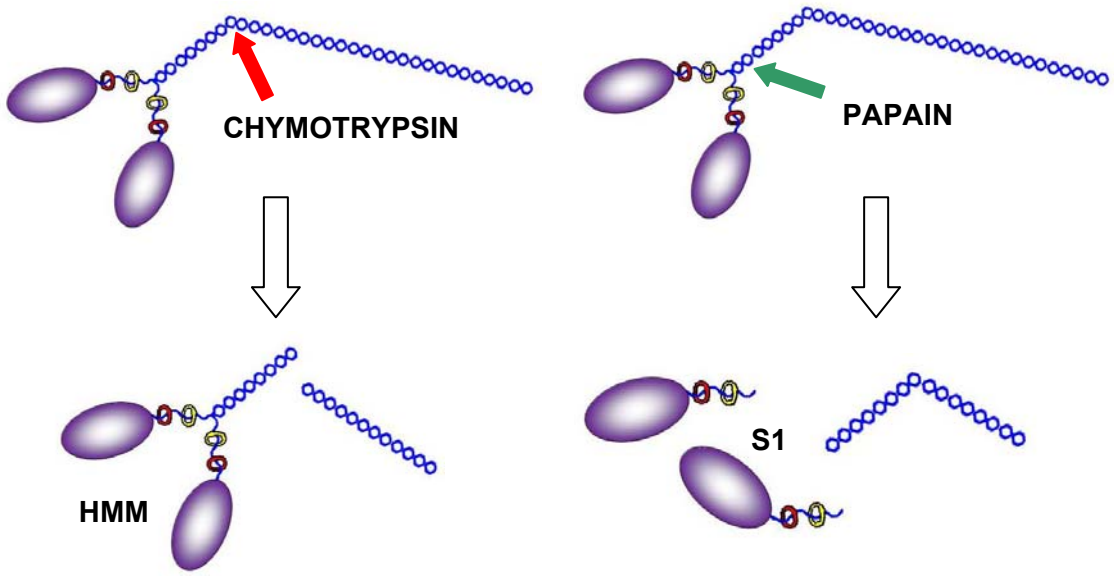

Figure 1.9*: Proteolytic digestion of myosin-II results in myosin-II fragments HMM and S1. The fragments are formed by digesting the myosin-II molecule with chymotrypsin (HMM) or papain (S1). Image created by author.*

The cycle of structural changes that myosin undergoes to walk along an actin filament begins with the myosin head being locked tightly onto actin in a *rigor* (fixed) configuration (Figure 1.10). In the presence of ATP this configuration is very short-lived, as the ATP molecule binds to a cleft on the myosin head thus slightly changing the conformation of the actin binding site. This causes the myosin to be released from the actin and leaves it free to move along the filament. The myosin cleft then closes around the ATP molecule, causing the head to be displaced along the filament by a distance of around 5nm [89]. The ATP is hydrolysed into adenosine diphosphate (ADP) and a phosphate, which both remain bound to the myosin. As the myosin head reaches a new actin binding site, it begins to weakly bind to the actin, causing the loss of the phosphate molecule, which in turn prompts the tight actin binding. This phosphate release produces the force generating power stroke, whereby the myosin head changes shape to regain the original *rigor* conformation, losing the bound ADP molecule in the process.

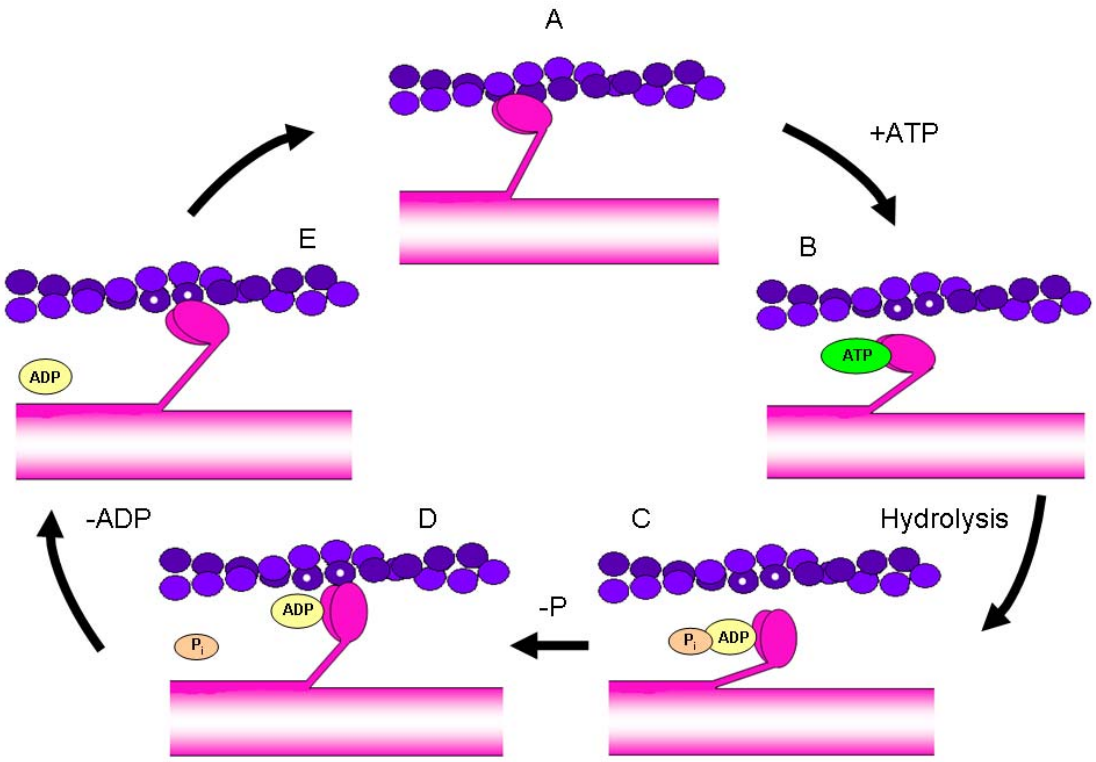

Figure 1.10: *ATP hydrolysis cycle of myosin and actin: (A) The myosin head is attached to the actin filament in a short lived rigour configuration. (B) A molecule of ATP binds to the myosin head, at a cleft on the side furthest from the actin filament, causing a slight conformational change, which weakens the affinity of the myosin for the actin, allowing it the freedom to move along the filament. (C) The myosin cleft closes around the ATP molecule, displacing it along the filament by around 5nm, whilst hydrolysing the ATP into ADP and inorganic phosphate (P_i). (D) The weak binding of myosin to the new site on the actin filament releases the phosphate molecule and triggers the power stroke that generates the shape change through which the head regains its original conformation. (E) The ADP molecule is lost and the cycle begins anew. Image created by author, but based upon an image from Ref. [89].*

The time scale at which the myosin head interacts with the actin filament is necessarily dependent up on the ATP concentration, and has been shown to be dependent upon load [100]. However, the release of the hydrolysis products (ADP and phosphate) is expected to occur within approximately 30ms of myosin binding to actin. In physiological ATP conditions, it has been measured that the S1 myosin fragment stays bound to the actin for a time scale on the order of tens of milliseconds [101].

1.6 Single cell microrheology

Eukaryotic cells have a highly complex mechanical structure that is stabilised by a contractile filamentous soft cytoskeleton spanning the entire cell body. This structure is in a constant state of flux in order to adapt the cell to both its internal and external environment. This ability to remodel

relies on the precise interplay between the main components of the cytoskeleton and the numerous proteins that bind them, which gives cells the ability to modulate their mechanical state over a surprisingly wide range from almost fluid to almost solid. When probed, the rheological behaviour of cells shares many features with those of semiflexible polymer networks, and this behaviour has been studied with various forms of microrheology, either passively [14, 102, 103], or in response to either an applied force [26, 102, 104-108] or an internally generated force, as in the case of acto-myosin contractility [109].

Typically cells are studied in one of two ways; either tracer probes (beads that have been ingested into the cell or biological vesicles that are components of the cell) are monitored passively, or beads stuck to the surface of the cell are manipulated actively, usually by magnetic tweezers [26, 102, 105]. The passive method has the advantage of not perturbing the cell too greatly, and obtains the high frequency linear viscoelastic properties of the cell to high accuracy. Actively perturbing the cell *via* magnetically manipulated beads on the cell surface suffers from the same disadvantage of all active microrheological techniques; only a single frequency at a time can be analysed, thus measurements can take a long time. Any transient changes in cell physiology may be difficult to detect. With active microrheology care must be taken not to fall within the cells' non-linear viscoelastic regime.

1.9 Aims of this thesis

This thesis aims to explore various aspects of using optical tweezers and video particle tracking microrheology for bioanalytical applications. Firstly we summarise the model developed by Morse [86-88, 110] in order to deal with the viscoelastic properties of semiflexible polymers. This is a comprehensive model that interpolates smoothly between flexible and rod-like polymers, and we use it as the basis for explaining the rheological behaviour of the biopolymers and cells studied throughout this thesis. The aims are therefore:

(I) We describe an analytical method for analysing the mean-square displacements of micron-sized optically-trapped tracer probes embedded in a material of interest. This method relies on a static optical trap, and builds upon the method introduced by Mason and Weitz [4] by using a generalised Stokes-Einstein relation to relate the mean-square displacement of a particle to the complex shear modulus *via* the velocity autocorrelation function (VAF). Following this, two new *wideband* frequency methods (termed 'flow-field' and 'two-trap') are introduced; both of these techniques are a mixture of passive and active microrheology and extend the lower limit of the frequency range accessible with non-oscillating optical tweezers. These analytical methods are applied to a Newtonian system (water) and a viscoelastic system (polyacrylamide).

(II) We investigate the concentration scaling laws of polymer solutions. This is done in order to demonstrate that it may not be strictly necessary to derive these scaling laws from the frequency-domain, thus bypassing the need to carry out a Fourier transform of experimental data. Instead, we derive concentration dependences from the time-dependent data (*i.e.* thermal fluctuations of tracer particles), in three steps: (i) we calculate the contribution to the time-dependent data from the system (*i.e.* the ensemble of laser, bead radius, and solvent viscosity), (ii) we relate the time-dependent thermal fluctuations to the viscosity of the solution, then (iii) we show how the thermal fluctuations and solution viscosity are related to the concentration of the solution.

(III) The concentration scaling laws and viscoelastic properties of a range of protein solutions are then explored. Initially we study pure actin solutions before moving onto the effect of myosin fragments (S1 and HMM) upon actin networks.

(IV) We present a straightforward procedure for measuring the *in vivo* mechanics and linear viscoelastic properties of single cells *via* passive video particle tracking microrheology of single beads attached to the cells' exterior. In particular, the procedure consists of measuring the thermal fluctuations of a bead chemically bound to the cell (Figure 1), for a sufficiently long time. Notably, the procedure presented here represents an alternative methodology that can be extended to many experimental formats and provides a simple addition to existing cellular physiology studies (e.g. those monitoring cell pharmacological response). Indeed, when compared to single cell viscoelasticity assays such as magnetic tweezers, atomic force microscopy and optical stretcher, our method has the advantage of revealing the changes of the cell's viscoelastic properties over a wide range of frequencies (here from ~0.6 Hz up to ~600 Hz), to a high level of accuracy, whilst it experiences an induced physiological process.

Chapter 2

THEORY OF SEMIFLEXIBLE POLYMERS

2.1 Morse's model of semiflexible polymer viscoelasticity

The viscoelastic properties of semiflexible polymer solutions are still a matter of much debate, and an analytical model describing their behaviour has yet to be unanimously agreed upon. Edwards [111] first developed the 'tube' model as a mean field description of the topological confinement exerted on a given chain by the surrounding chain (Figure 2.1). De Gennes coined the phrase 'reptation' to describe the diffusion of a chain along its own length [112]. Doi and Edwards [113-118] combined these two theories to create models of entangled polymer states for two extremes; 1) flexible (coil-like) and 2) rigid-rod. All current semiflexible polymer solution models are extrapolated from Doi and Edwards, including the model introduced by Morse [86-88, 110], which interpolates smoothly between flexible polymers (with a contour length much greater than the persistence length $L_c >> L_p$) and rod-like polymers ($L_c << L_p$). This chapter will briefly summarise the main ideas introduced by Morse to deal with semiflexible polymer viscoelasticity.

The majority of semiflexible polymers, in which the degree of backbone rigidity is intermediate between the flexible and rod-like extremes, possess a persistence length around $10-10^3$ times greater than the steric diameter, d, of the polymer. The degree to which the partial rigidity of a molecule will affect the viscoelastic behaviour of a solution depends upon the ratio L_c / L_p, the solution concentration, and the length and time scales probed by the experiment. In a *dilute* solution, Morse states that the fluctuation modes of the polymer with a wavelength $\lambda >> L_p$ (where λ is measured along the polymer backbone) are describable as Zimm modes [119] of a Gaussian

chain (but one with enormous statistical segment length), whilst modes with $\lambda << L_p$ are better described as bending modes of a nearby rigid chain. The low-frequency viscoelastic behaviour of an *entangled* solution of long semiflexible chains, for which $L_c >> L_p >> d$, is expected to differ quantitatively from that of an entangled solution of flexible chains only if L_p exceeds the entanglement length of the solution, so that the relaxation of bending modes with wavelength $\lambda \leq L_p$ is impeded by entanglement with neighbouring chains. The low-frequency behaviour of more rod-like chains, with $L_p \geq L_c >> d$, is expected to differ quantitatively from that of an entangled solution of completely rigid rods only when the root mean-square magnitude of the thermally excited transverse fluctuations of the chain (*i.e* transverse to its end-to-end vector) become larger than the radius of the tube formed by neighbouring chains, thus, again, impeding the relaxation of the bending modes.

These regimes in which relaxation of the polymers bending modes is strongly impeded by the presence of other chains is reasonably described by a reptation model, in which the polymer is confined to a tube with a diameter D_e, much less than its persistence length, and in which the conformation of the tube is itself described by a WLC model. Systems that fit this description are described as *tightly-entangled* as opposed to the *loosely-entangled* regimes described by the Doi-Edwards models. The geometry of the tubes in all of these regimes can be characterised by either the tube diameter, D_e, or an entanglement length, L_e, which defined as the contour distance between collisions of the polymer with walls of the tube.

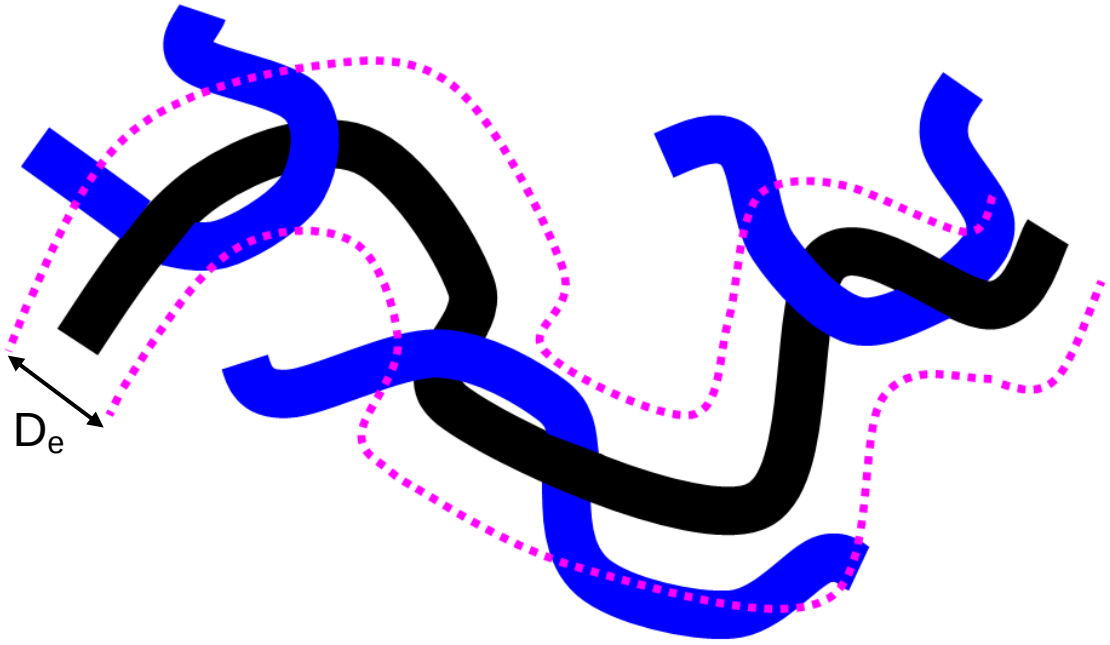

Figure 2.1: *(Image created by author, but based on an image from Ref. [120]). The motion of the black polymer chain is constrained by the surrounding blue chains, which cannot be crossed, as if the black chain were confined to a tube (pink dashed lines) of diameter* D_e.

By considering the WLC model Morse identifies all possible regimes of polymer concentration and chain length expected for solutions of semiflexible polymers, then characterises the regimes of dynamic behaviour of entangled solutions in terms of four different length scales: the contour length L_c, the persistence length L_p, the entanglement length L_e (dependent upon both L_P and the mesh size L_m) and the chain diameter d.

The sections of Morse's model relevant to the work carried out in this thesis will be described succinctly in this chapter. This can be summarised as follows; (I) the concentrations regimes and the chain length for semiflexible polymer solutions are introduced, (II) a general expression for the stress tensor is presented, (III) the time scales involved in stress relaxation are discussed and finally, (IV) a qualitative description of the viscoelastic response of the various concentration regimes is provided.

2.1.1 Concentration regimes

In the limit of *coil-like polymer* solutions ($L_c >> L_p$), by beginning from a dilute solution and increasing the polymer concentration ρ (the contour length per unit volume) above the overlap concentration of $\rho^*_{coil} = L / R_g^3$ (where R_g is the radius of gyration), there should be two distinct isotropic entangled regimes leading to a nematic liquid-crystalline phase at higher concentrations.

Loosely-entangled regime: At relatively low concentrations (below the crossover concentration to the tightly-entangled regime, which is discussed below), where $L_e >> L_p$, the resulting confinement of the polymer chain within the tube is very loose. A polymer within an entangled solution may therefore execute a random walk between entanglements or collisions with the walls of surrounding tubes (Figure 2.2a).

Tightly-entangled regime: The condition $L_p >> L_e$ is only satisfied at concentrations above the crossover concentration of the polymer $\rho^{**}_{coil} = 1/L_p^2$ (for which $L_p \sim L_e \sim L_m$), at which concentration the solution becomes tightly entangled. This results in the polymer being confined to a weakly curved tube of diameter $D_e << L_p$. The polymer tangent $\vec{u}(s)$ can, therefore, only meander slightly between entanglements (Figure 2.2b).

Liquid-crystalline phase: This phase is induced by increasing the concentration further. Khoklov & Semonov [121, 122] predict that it will begin at $\rho_{nem} \cong 6.7/(L_p d)$ where d is the effective steric chain diameter.

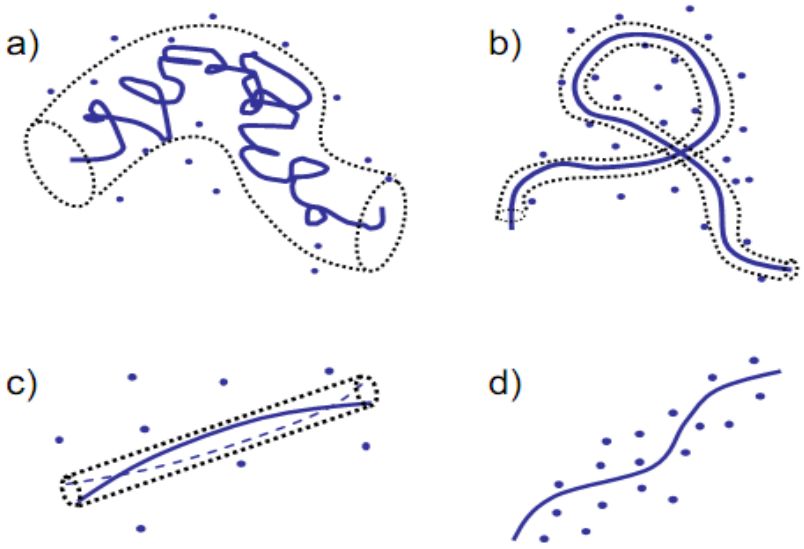

Figure 2.2: *(Taken from Ref. [87]) Schematic representation of a semiflexible chain within an entangled isotropic solution (with other chains represented by points) within (a) the loosely-entangled coil regime, in which* $L_c >> L_p$ *but* $L_p << D_e$ *where* D_e *is the tube diameter, (b) the tightly-entangled coil regime, where* $L_c >> L_p$ *and* $L_p >> D_e$*, (c) the loosely-entangled rod regime, where* $L_c << L_p$ *and where rotation of the rod is impeded by entanglements but fluctuations of the bending modes are not, and (d) the tightly-entangled rod regime, in which* $L_c << L_p$ *and in which both rotations and shape fluctuations are impeded by entanglements and relax only via reptation. Tightly-entangled solutions of coil-like and rod-like polymers have a similar local geometry.*

In the limit of *rod-like polymer* solutions ($L_c << L_p$), similar concentration regimes are indentified. Below the overlap concentration of $\rho^*_{rod} \approx 1/L_c^2$ the solution is dilute, since rods can diffuse freely without colliding with other chains. As with the coil-like regime, there should exist at higher concentrations two possible isotropic concentration regimes leading to a nematic liquid-crystalline phase.

Loosely-entangled regime: At concentrations greater than ρ^*_{rod} but less than a cross-over concentration of $\rho^{**}_{rod} \approx \left(L_p / L_c\right)^{1/2} \rho^*_{rod}$ the rotation of each chain is hindered by the presence of other chains but the fluctuation of the polymers' bending modes is unaffected (Figure 2.2c).

Tightly-entangled regime: At concentrations above ρ^{**}_{rod} the overall orientation and shape of each chain is constrained by the presence of other chains (Figure 2.2d). Distortions of the polymers' shapes can relax only via disengagement of the polymer by reptation.

Liquid-crystalline phase: This phase is expected to occur at a concentration $\rho_{nem} \approx 4.3/(L_c d)$ as predicted by Onsager [123].

2.1.2 Stress tensor

Morse calculates a general expression for the stress tensor of a solution of worm-like chains that can be applied to any concentration regime. In particular, the stress tensor of a solution subjected to a macroscopic fluid velocity **v** with a spatially homogeneous rate-of-deformation tensor $\kappa(t) \equiv (\nabla \mathrm{v})^T$ is given in the Kramers-Kirkwood theory [124, 125] by a sum:

$$\sigma = \eta_s (\kappa + \kappa^T) + \sigma_p \tag{2.1}$$

where σ_p is the polymer stress and η_s is the solvent viscosity.

The polymer stress tensor can be divided into the intermolecular and intramolecular contributions. These arise from forces associated with Van der Waals or steric interactions respectively:

$$\sigma_p = \sigma_{\text{inter}} + \sigma_{\text{intra}} \tag{2.2}$$

The *intermolecular stress contribution* is negligible over all the frequency ranges for concentrations up to ρ_{nem} for both the limit cases of coil-like and rod-like polymers.

The *intramolecular stress contribution* is expected to play a much bigger role in determining the viscoelastic properties of systems of long semiflexible chains. It can be expressed as a sum:

$$\sigma_{intra} = \sigma_{curve} + \sigma_{orient} + \sigma_{tens} - ck_BT\delta \tag{2.3}$$

The physical basis of these contributions is described as follows (Figure 2.3);

i) σ_{curve} is the curvature contribution arising from forces that oppose the transverse deformation or the rotation of chain segments.

ii) σ_{orient} is the orientational contribution that reduces in the appropriate limit to the Brownian stress of a rigid-rod solution.

iii) σ_{tens} is the tension contribution that arises from the tangential forces that resist the stretching or the compression of the chain.

iv) $ck_BT\delta$ is the ideal solution osmotic pressure arising from the translational entropy of the molecule as a whole.

To calculate the linear viscoelastic properties of a fluid Morse derived the relaxation of the intramolecular stress in a system that is subjected to an infinitesimal step strain $\delta\varepsilon$ at time t=0. The relaxation modulus $G(t)$ is defined by expressing the resulting stress, $\sigma(t)$, as a product $\sigma(t) = G(t)(\delta\varepsilon + \delta\varepsilon^T)$.

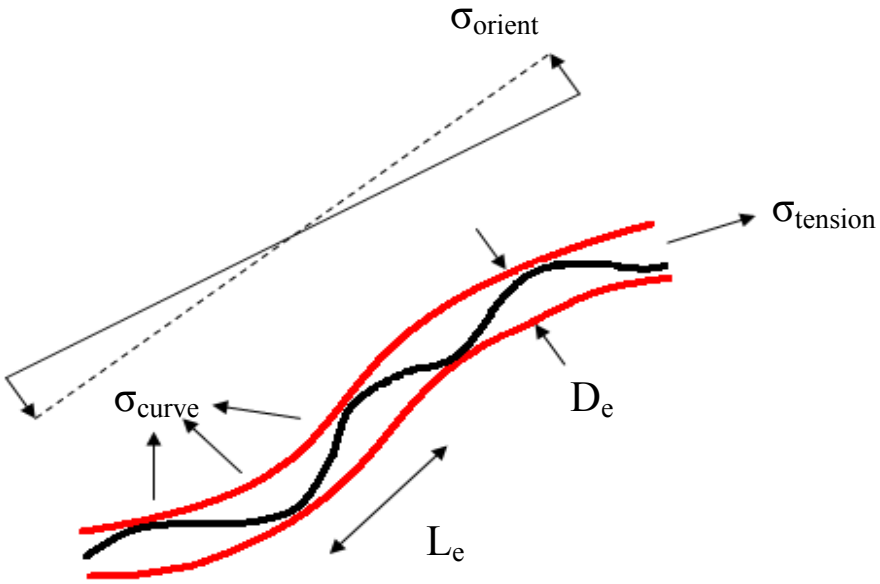

Figure 2.3: *(Image created by author, but based on an image from Ref. [117]. Schematic representation of the stress tensor contributions in Equation 2.3.*

The complex shear modulus is thereby expressed as the Fourier transform of the dynamic modulus:

$$G^*(\omega) \equiv G'(\omega) + iG''(\omega) \equiv i\omega \int_0^\infty G(t) e^{-i\omega t} dt \tag{2.4}$$

where $G'(\omega)$ is the storage modulus and $G''(\omega)$ is the loss modulus. The zero-frequency viscosity η_0 is given by the integral $\int_0^\infty G(t)dt$. It is possible to express the $G(t)$, $G^*(\omega)$ and η_0 in terms of the sums of the different stress contributions, such as:

$$G^*(\omega) \equiv G_{curve}(\omega) + G_{orient}(\omega) + G_{tension}(\omega) \tag{2.5}$$

2.1.3 Time scales

Morse identifies a set of time scales relevant to the viscoelastic behaviour, by considering the characteristic time scales for the decay of $G_{curve}(t)$, $G_{orient}(t)$, and $G_{tens}(\omega)$. These relaxation times have been identified by simple physical arguments similar in kind to those used previously by Isambert and Maggs [126, 127]. Here, we will summarise the definition of each of Morse's time scales.

I) Reptation

Morse states that the curvature and orientational stress both relax as a result of reptation. This

curvilinear diffusion is characterised by a diffusivity given by the Einstein relation:

$$D_{rep} = k_B T / \zeta L_c \tag{2.6}$$

where ζ is the friction coefficient for motion of the chain parallel to its own contour and it is independent of L_c. The contribution of a chain segment to the *curvature stress* relaxes immediately when the segment is carried by diffusion to the end of the tube and it is replaced by a segment whose curvature (but not orientation) is chosen randomly from an equilibrium probability distribution. Consequently the longest relaxation time for the curvature stress is given by the disengagement time (or reptation time):

$$\tau_{rep} \equiv L_c^2 / (\pi^2 D_{rep}) \propto L_c^3 \tag{2.7}$$

which is on the order of the time needed for the polymer to diffuse its own contour length.

The *orientational stress* relaxes with a relaxation time determined by the time required to randomise the orientation of the ends of the chain. In the limit of *coil-like chains*, with $L_c >> L_p$, the polymer must diffuse only a distance L_p in order to randomize the orientation of the end, giving a relaxation time:

$$\tau_{end} \equiv L_p^2 / D_{rep} \propto L_c L_p^2 \tag{2.8}$$

which in this limit is much less than τ_{rep}. In the limit of *rod-like polymers*, with $L_c << L_p$ the relaxation of the orientation of the polymer (which in this limit rotates as an almost rigid body) has been found by Morse (in agreement with Refs.[128, 129]) to occur with a relaxation time:

$$\tau_{rod} \equiv L L_p / 6 D_{rep} \propto L_c^2 L_p \tag{2.9}$$

This time is much longer than τ_{rep}, which stems from the fact that in this regime the chain must diffuse many times its own length before its overall orientation is randomised.

II) Contour density fluctuations

A non-zero value of the *tension stress*, σ_{tens}, is produced when segments of the chain are stretched or compressed tangentially (Figure 2.3). In order to describe how σ_{tens} relaxes, Morse introduces (similarly to Refs. [126, 127]) a dimensionless contour length density $\phi(s,t)$ which is defined as the length of polymer contour length per unit length of the tube, averaged over a segment of tube of length L_e. The density $\phi(s,t)$ is always slightly greater than 1 as a result of the wrinkling of the polymer within the tube. By solving a differential equation describing the temporal evolution of

$\phi(s,t)$ on a specified polymer, Morse defines a diffusive coefficient for the contour length density as follows:

$$D_\phi \propto \frac{k_B T}{\zeta}\frac{L_p^2}{L_e^3} \tag{2.10}$$

The time needed for tension to relax to a small fraction of its initial value is thus given in the limit $L_c >> L_p$ of *coil-like chains* by:

$$\tau_{\phi p} \equiv L_p^2 / 9D_\phi \propto L_e^3 \tag{2.11}$$

This is the time needed for the excess length to diffuse a distance equal to L_p. In the *rod-like limit,* $L_c << L_p$, this time needed for the excess length to diffuse the full chain length is given by:

$$\tau_{\phi L} \equiv L_c^2 / \pi D_\phi \propto L_e^3 L^2 / L_p^2 \tag{2.12}$$

These relaxation times are expected to vary with ρ, L_c and L_p as:

$$\tau_{\phi p} \propto \rho^{-6/5} L_p^{3/5} \tag{2.13}$$

$$\tau_{\phi L} \propto \rho^{-6/5} L_p^{-7/5} L_c^2 \tag{2.14}$$

These results are significantly different from those obtained by the authors of Refs. [126, 127] who obtained a scaling expression of the diffusive coefficient for the contour length density as $D_\phi \propto \frac{k_B T}{\zeta}\frac{L_p}{L_e^2}$ by requiring that the frequency $\omega(q) \approx D_\phi q^2$ of long wavelength tangential diffusion modes matches the frequency $\omega(q) \approx k_B T L_p q^4 / \zeta$ of short wavelength transverse undulations at a crossover frequency of $q \approx 1/L_e$. The authors of Refs. [126, 127] thus provided the time needed to relax fluctuations of a section of filament of length L_p:

$$\tau_p \propto \rho^{-4/5} L_p^{7/5} \tag{2.15}$$

and the time needed to relax the density fluctuations in the whole tube:

$$\tau_{relax} \propto \rho^{-4/5} L_p^{-3/5} L_c^2 \tag{2.16}$$

All the characteristic times introduced above are valid only to describe behaviour at time scales longer than an entanglement time:

$$\tau_e \sim \zeta_\perp L_e^4 / k_B T L_p \tag{2.17}$$

which is the relaxation time of an undulation mode of wavelength L_e, and $\zeta_\perp$ is the friction coefficient of transverse undulations of the polymer within the tube.

In the case of *rods* with length $L_c \leq (L_p L_e)^{1/2}$, the tension can relax via tangential motion even before entanglement begins to hinder the relaxation of undulation modes with wavelength $q^{-1} > L_e$. The relaxation time for tension in this case is given roughly by the time:

$$\tau_\parallel \propto L_c^2 / D_\phi(\tau_\parallel) \tag{2.18}$$

which is the time required for tension to diffuse the length of the chain.

III) Unentangled chains

Finally, in order to describe *unentangled and loosely-entangled chains*, Morse introduces the following time scales:

$$\tau_p \sim \zeta_\perp L_p^3 / k_B T \tag{2.19}$$

$$\tau_L \sim \zeta_\perp L_c^4 / k_B T L_p \tag{2.20}$$

that give, respectively, the relaxation time for a bending mode of contour wavelength approaching L_p on a coil-like chain, of length $L_c >> L_p$, and the relaxation time for the longest wavelength bending mode of a rod-like chain, of length $L_c << L_p$. In the case of unentangled coil-like chains, modes of contour wavelength $>> L_p$ are best described as modes of a coarse-grained Rouse or Zimm model of a flexible chain with a terminal relaxation time $\tau_c \sim \tau_p (L / L_p)^\alpha$ given by the relaxation time for a mode with $q \sim 1/L$.

2.1.4 Viscoelastic response

Based upon the above arguments, Morse provides a qualitative description of the frequency dependence of $G^*(\omega)$ in the various regimes of concentration and chain length. Here the model predictions for the two limits of coil-like and rod-like chains are presented separately. In each case the behaviour predicted in the tightly-entangled regime is introduced first and then the comparisons to the behaviour expected for loosely-entangled and unentangled solutions are discussed.

In the limit of *coil-like polymer* solutions ($L_c >> L_p$), the decay times for the three stress contributions form a hierarchy:

$$\tau_{rep} >> \tau_{end} >> \tau_{\phi p} \tag{2.21}$$

Because $G_{orient}(t)$ is seen to decay with a time τ_{end}, which is much smaller than the decay time τ_{rep} for $G_{curve}(t)$, whilst also having an initial value $G_{orient}(0) << G_{curve}(0)$, the orientational contribution is expected to make a negligible contribution to $G(t)$ at all times, and as such may be ignored in this limit. The total modulus $G(t)$ may thus be approximated as the sum of a large but rapidly decaying tension contribution $G_{tens}(t)$ and a much smaller but more slowly decaying curvature contribution, $G_{curve}(t)$, as pointed out by Maggs [124]. If the time scales τ_{rep}, $\tau_{\phi p}$, and τ_e become sufficiently widely separated, this will lead to a complex modulus $G^*(\omega)$ of the form shown in Figure 2.4, which can in theory exhibit two distinct plateaus: a low-frequency, curvature-dominated plateau within which $G'(\omega) \cong G_{curve}(0)$, and a higher frequency tension-dominated plateau within which $G'(\omega) \cong G_{tens}(0)$.

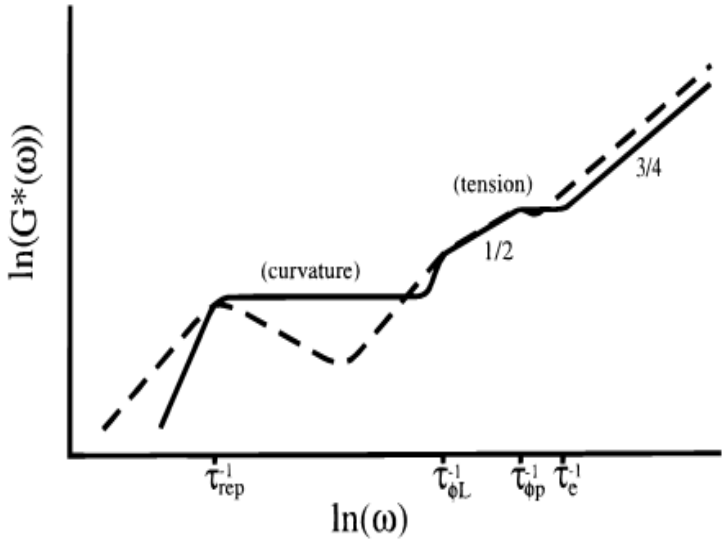

Figure 2.4: *(Taken from Ref. [87]) Schematic of $G'(\omega)$ (solid line) and $G''(\omega)$ (dotted line) for a tightly-entangled solution of coil-like chains with $L_c >> L_p$. Slopes indicate regimes with a nontrivial power law dependence on frequency, (curvature) and (tension) indicate frequency regimes in which $G^*(\omega)$ is dominated by the curvature or tension contributions. Time scales are defined in the text.*

The curvature stress, which dominates the low-frequency plateau, has a free energy scale of order k_BT per entanglement and is predicted to vary with ρ, L_c, and L_p as:

$$G_{curve}(0) \propto \rho k_B T / L_e \propto \rho^{7/5} L_p^{-1/5} \tag{2.22}$$

where $L_e \approx L_p(\rho L_p^2)^{-2/5}$.

The tension stress, which dominates the high-frequency behaviour of $G^*(\omega)$, exhibits a more complex frequency dependence. For frequencies $\tau_{\phi p}^{-1} \le \omega \le \tau_e^{-1}$, Morse's model is found to lead to a plateau in $G'(\omega)$ with a predicted plateau value of:

$$G_{tens}(0) \propto k_B T \rho^{11/5} L_p^{7/5} \tag{2.23}$$

This plateau modulus, larger than $G_{curve}(0)$ by a factor of order $(L_p / L_e)^2$, is the same one predicted by MacKintosh *et al.* [130], who focused exclusively on this contribution to the stress, but did not allow for any relaxation of the tension; an assumption that is more applicable to cross-linked gels. In addition, Morse found that $G^*_{tens}(\omega)$ varies with frequency as $G^*_{tens}(\omega) \propto (i\omega)^{1/2}$ for frequencies $\tau_{\phi L}^{-1} \le \omega \le \tau_{\phi p}^{-1}$ and exhibits fluid-like terminal behaviour with $G^*(\omega) \propto (i\omega)$ at frequencies $\omega \le \tau_{\phi L}^{-1}$.

At frequencies $\omega \ge \tau_e^{-1}$ Morse calculates a universal high-frequency limiting form for the complex modulus as:

$$\lim_{\omega \ge \tau_e^{-1}} G^*_{tens}(\omega) \cong \frac{2^{3/4}}{15} \frac{\rho k_B T}{L_p} \left(i\omega \frac{\zeta_\perp L_p^3}{k_B T} \right)^{3/4} \tag{2.24}$$

which contains a precise numerical prefactor. In Figure 2.5, a schematic diagram is shown of the expected frequency dependence of the ratio $G'(\omega)/\rho$ (because this ratio approaches a concentration-independent limiting form at high frequencies) in each concentration regime.

Dilute solutions of coils, with concentrations below the overlap concentration ρ^*, are expected to exhibit three frequency regimes. For all $\omega >> \tau_p^{-1}$, $G'(\omega)$ is expected to exhibit the high-frequency limiting behaviour of Equation 2.24. For all $\omega << \tau_p^{-1}$ the frequency dependence of $G^*(\omega)$ can be described by a Rouse or Zimm model [119, 131], which yield complex moduli of the form:

$$G^*(\omega) \sim \frac{\rho k_B T}{L_p} (i\omega\tau_p)^{1/\alpha} \tag{2.25}$$

with $1/2 \le \alpha^{-1} \le 2/3$, over the frequency range $\tau_c^{-1} \le \omega \le \tau_p^{-1}$, (where τ_c is the terminal relaxation time) in which $G^*(\omega)$ is dominated by modes of wavelengths between L_p and L_c, and yields fluid-like terminal behaviour, with $G^*(\omega) \propto i\omega$, for $\omega << \tau_c^{-1}$.

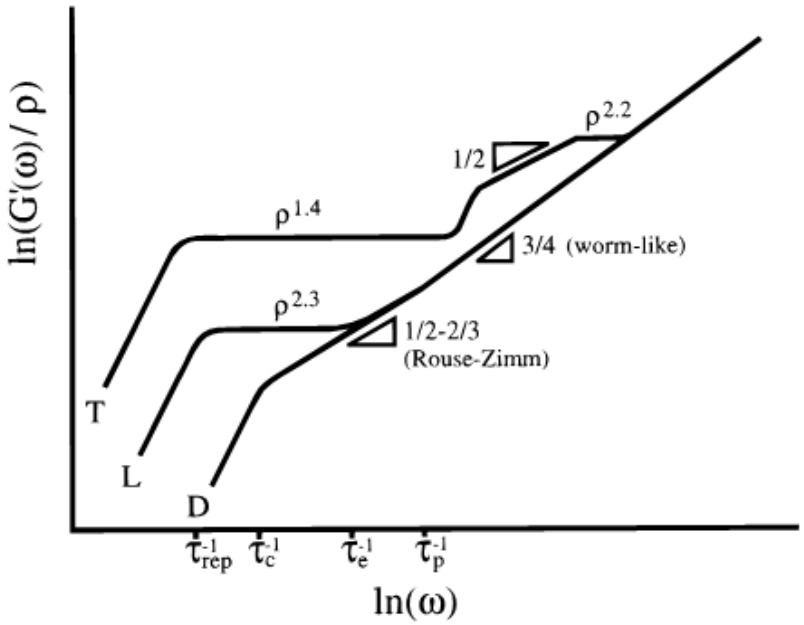

Figure 2.5: *(Taken from Ref. [87]) Schematic diagram that shows the evolution of* $G'(\omega)/\rho$ *with* ρ *for solutions of coil-like chains. The three lines are sketches of the behaviour predicted for dilute or unentangled solutions (D), loosely-entangled solutions (L), and tightly-entangled solutions (T), all of which exhibit a common asymptote for* $G'(\omega)/\rho$ *at high frequencies. Slopes represent regimes with a nontrivial power law dependence on frequency, and powers of* ρ *indicate the predicted dependence of the plateau moduli on concentration. Time scales shown are those relevant to the dilute and loosely-entangled regime, so* τ_{rep} *is the reptation time of the loosely-entangled solution.*

Loosely-entangled solutions of semiflexible coils, with concentrations $\rho^* << \rho << \rho^{**}$, are (by definition) characterised by an entanglement length $L_e >> L_p$, and exhibit viscoelastic behaviour identical to that of entangled solutions of flexible chains for all $\omega << \tau_p^{-1}$. In this regime $G^*(\omega)$ develops an elastic plateau with a plateau modulus $G'(\omega) \approx \rho k_B T / L_e$ that extends over a frequency range $\tau_{rep}^{-1} << \omega << \tau_e^{-1}$. In this case τ_{rep} refers to the disengagement time of a loosely-entangled chain and τ_e refers to the Rouse-Zimm relaxation time of a flexible sub-chain of contour length L_e, with $L_e >> L_p$. In studies of entangled solution of semiflexible polymers, the plateau modulus has been found experimentally to vary with polymer concentration (ρ) roughly as $G' \propto \rho^{2.3}$, both in good solvents [132, 133] and in ϑ-solvents [134-136]. The disengagement time, τ_{rep}, is also found to increase with increasing polymer concentration in this regime. At frequencies $\omega >> \tau_e^{-1}$ the behaviour of $G'(\omega)/\rho$ is expected to become identical to that of a dilute solution, giving $G^*(\omega) \propto (i\omega)^{1/\alpha}$ (where $1/\alpha \cong 2/3$) for frequencies $\tau_e^{-1} << \omega << \tau_p^{-1}$ and $G^*(\omega) \propto (i\omega)^{3/4}$ for frequencies $\omega >> \tau_p^{-1}$.

Upon entering the *tightly-entangled regime*, one thus expects to see the following: (i) the disappearance of the remaining Rouse-Zimm regime in which $G^*(\omega) \propto (i\omega)^{1/\alpha}$, (ii) a change in the concentration-dependence of the plateau modulus from $G' \propto \rho^{2.3}$ for $\rho << \rho^{**}$ to $G' \propto \rho^{1.4}$ for $\rho >> \rho^{**}$,(iii) a saturation in the value of τ_{rep} with increasing polymer concentration, and (iv) the development at sufficiently high polymer concentrations of a second, tension-dominated plateau at frequencies $\omega \geq \tau_{\phi p}^{-1}$. The predicted width of the tension-dominated plateau vanishes for $\rho \approx \rho^{**}$, so this feature is found in numerical calculations to first appear as a slight shoulder in $G'(\omega)$ and to then widen only slowly with increasing concentration.

In the limit of *rod-like polymer* solutions, $L_c << L_p$ the orientational contribution $G_{orient}(t)$ cannot be neglected as in the case of coil-like polymers. It can make a significant contribution to the low-frequency behaviour of $G^*(\omega)$ because, as explained before, for such types of polymers the time τ_{rod} is longer than the time τ_{rep} for the relaxation of $G_{curve}(t)$. The time dependence of $G_{orient}(t)$ has been found by Morse to be, over all the concentration regimes, exponential, with a form:

$$G_{orient}(t) = \frac{3}{5}\frac{\rho k_B T}{L} e^{-t/\tau_{rod}} \tag{2.26}$$

where τ_{rod} is the time needed to re-randomise the rod orientations.

In the *dilute regime,* τ_{rod} is independent of concentration and varies with L_c roughly as $\tau_{rod} \cong \zeta L^3 / k_B T$ .In the loosely-entangled regime, τ_{rod} has been predicted to increase with increasing concentration as $\tau_{rod} \cong (\zeta L^3 / k_B T)(\rho L^2)^{\gamma}$, where $\gamma = 2$ in the Doi and Edwards cage model of semidilute rigid rods [117, 118] and $\gamma = 1$ in a competing model introduced by Fixman [134, 135]. In the tightly-entangled regime, τ_{rod} is given by Equation 2.9, which yields a value that is independent of polymer concentration, ρ, but that depends upon the persistence length, L_p.

The curvature modulus $G_{curve}(\omega)$ in *unentangled or loosely-entangled solutions* is predicted by Morse to exhibit a power law behaviour:

$$G_{curve}(\omega) \propto \frac{\rho k_B T}{L_p}\left(i\omega \frac{\zeta_\perp L_p^3}{k_B T}\right)^{1/4} \tag{2.27}$$

for all $\omega \geq \tau_L^{-1}$, and is expected to exhibit fluid-like behaviour for $\omega \leq \tau_L^{-1}$. This contribution

becomes greater than $G_{orient}(\omega)$ for all $\omega \geq \tau_L^{-1}$, leading to a curvature-dominated power law regime in which $G^*(\omega) \propto (i\omega)^{1/4}$ as shown in Figure 2.6.

The tension contribution to $G^*(\omega)$ in an unentangled or loosely-entangled solution of rods is expected to exhibit the limiting behaviour of Equation 2.24 for all $\omega >> \tau_{\|}^{-1}$ and to exhibit fluid-like behaviour for $\omega << \tau_{\|}^{-1}$.

Upon entering the *tightly-entangled regime*, by increasing either the polymer concentration or chain length of a solution of semiflexible rods, one thus expects to see the following: (i) the orientational relaxation time τ_{rod} becomes almost concentration independent; (ii) the curvature-dominated power law regime predicted for loosely-entangled chains, in which $G^*(\omega) \propto (i\omega)^{1/4}$, evolves into a curvature-dominated plateau, with a plateau modulus $G' \propto \rho^{1/4}$; (iii) at higher polymer concentrations or chain lengths, for which $L_c \geq (L_p L_e)^{1/2}$, the curvature stress begins to dominate η_0 and a high-frequency tension-dominated plateau begins to form at frequencies $\tau_{\phi L}^{-1} \leq \omega \leq \tau_e^{-1}$; (iv) for $L_c \geq L_p^{2/3} L_e^{2/3}$, the disappearance of any orientation-dominated plateau in $G'(\omega)$, as a result of the growth of $G'_{curve}(\omega)$.

For the largest concentrations and/or chain lengths discussed above, the frequency dependence thus becomes rather similar to that predicted for coil-like chains, the only qualitative difference being the absence, in solutions of rod-like chains, of a power-law regime in which $G^*_{tens}(\omega) \propto (i\omega)^{1/2}$, which is predicted to appear only for $L_c >> L_p$.

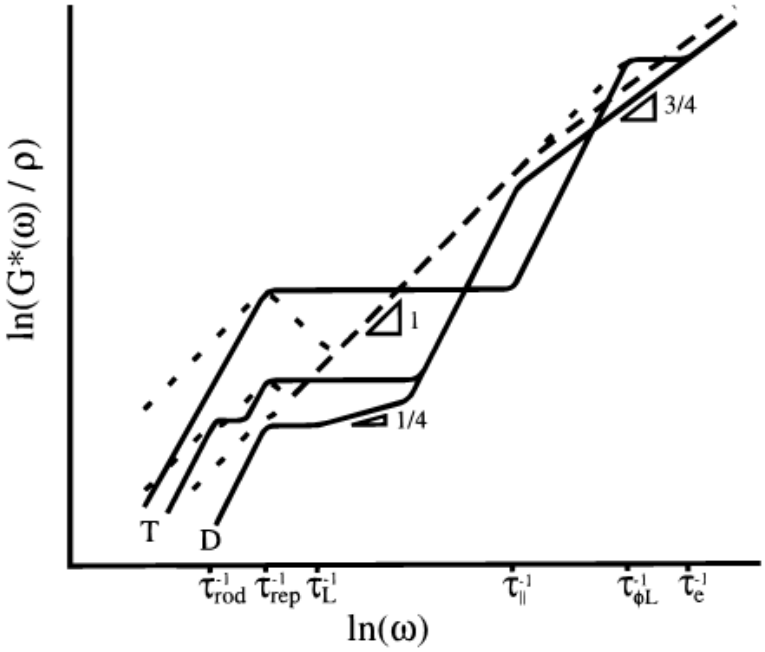

Figure 2.6: *(Taken from Ref. [87]) Schematic of the predicted evolution of* $G'(\omega)/\rho$ *(solid lines) and* $G''(\omega)/\rho$ *(dotted lines) with concentration for a solution of rod-like polymers. Of the three concentrations shown, one is in the dilute regime (D) and two are in the tightly-entangled regime (T), one for* $L_c > L_p^{2/3} L_e^{1/3}$ *(which exhibits a high-frequency tension-dominated plateau but no low-frequency orientation-dominated plateau) and one for* $L_c < (L_p L_e)^{1/2}$ *(which exhibits no tension-dominated* plateau but *exhibits a narrow orientation-dominated plateau and a low-shear viscosity with a significant orientational contribution.) The time* τ_{rod}^{-1} *refers to the orientational relaxation time of the tightly-entangled solution. The corresponding relaxation time for the dilute solution is of order* τ_{rep} *as described in the text. A loosely-entangled solution (not shown) would look similar to the dilute solution except for the appearance of a value of* τ_{rod}^{-1} *intermediate between those of dilute and tightly-entangled solutions. The overlapping lines for* $G''(\omega)/\rho$ *at intermediate frequencies, between* τ_{rep}^{-1} *and* $\tau_{\|}^{-1}$*, where* $G''(\omega) \propto \omega$*, all correspond to the behaviour obtained for the viscous (i.e. tension) contribution to the polymer stress of a solution of rigid rods.*

Finally, it is interesting to observe (see Figure 2.7) how Morse's model, described so far, predicts the behaviour of $G^*(\omega)$ as a function of the contour length L for a series of monodisperse tightly-entangled solutions with equal characteristic parameters (e.g. ρ, L_p, d) that are believed to be representative of a 1 mg/mL solution of actin. A sample of actin with polydisperse filament lengths, $\overline{L_c} = 17\mu m$, would be expected to exhibit the moduli shape of Figure 2.8.

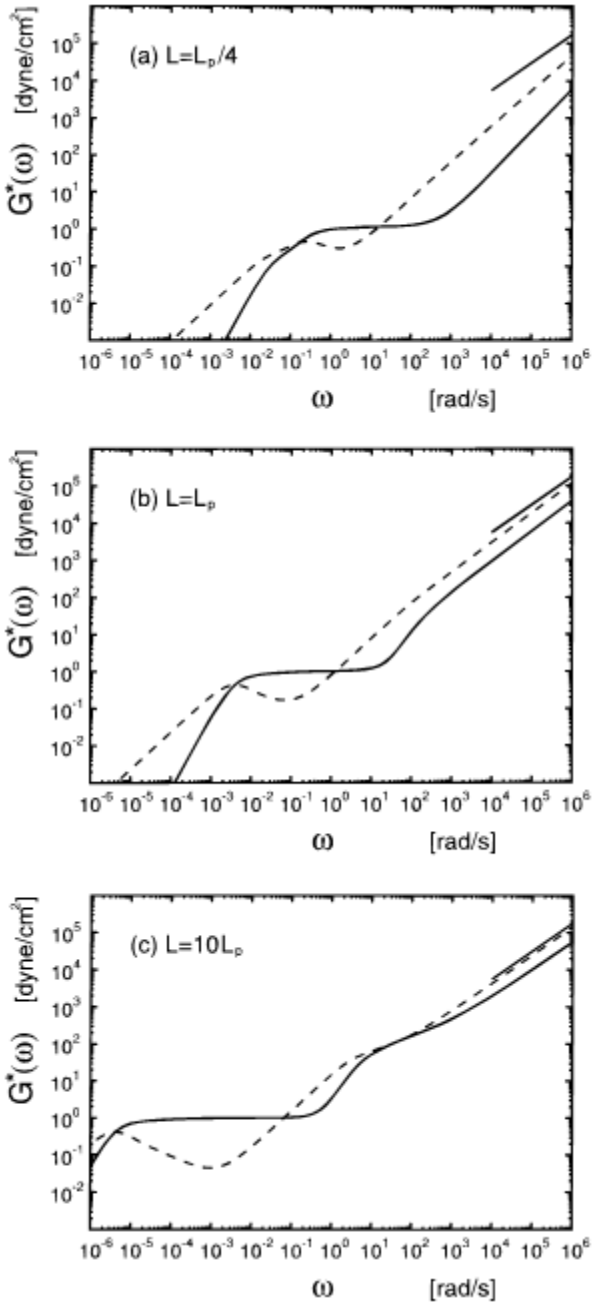

Figure 2.7: *(Taken from Ref. [87]) Calculated moduli* $G'(\omega)$ *(solid line) and* $G''(\omega)$ *(dotted line) for monodisperse solutions with (a)* $L_c = L_p/4$*, (b)* $L_c = L_p$ *and (c)* $L_c = 10L_p$*. The remaining parameters are given values:* L_p *= 17 µm,* ρ *= 39 µm* $^{-2}$*,* D_e *= 0.2 µm,* L_e *=2.2 µm,* η_s *= 0.01 Poise, and* d *= 0.007 µm, which are believed to be representative of a 1 mg/mL solution of actin. The straight solid line in each figure has a slope of 3/4 and is the predicted high-frequency asymptote of* $G''(\omega)$*.*

Morse briefly describes the behaviour that would be expected to occur in a chemically or physically cross-linked gel. The presence of cross-links between two chains would be expected to prevent the tangential motion of each chain along its own tube. Since this tangential motion is vital for the redistribution of excess length, by suppressing it the otherwise rapid relaxation of tension following a step deformation is also suppressed. This has the result that even a relatively low

density of cross-links can significantly affect the low-frequency behaviour of $G^*(\omega)$ by producing a broad elastic plateau in $G'_{tens}(\omega)$ with a plateau modulus that can be orders of magnitude higher than that predicted for mobile chains (Figure 2.9).

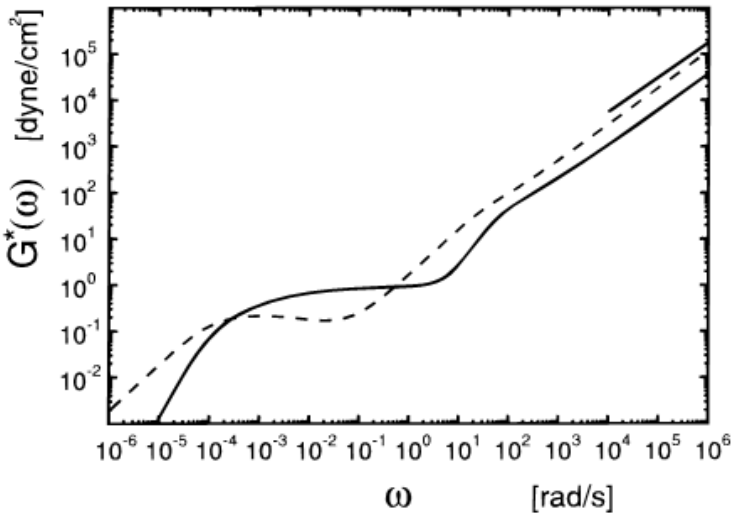

Figure 2.8: *(Taken from Ref. [87]) Calculated moduli $G'(\omega)$ (solid line) and $G''(\omega)$ (dotted line) for a polydisperse actin solution with $\overline{L}_c = 17\,\mu m$ and an exponential distribution of chain lengths for the same values of L_p, D_e etc. as in Figure 2.7.*

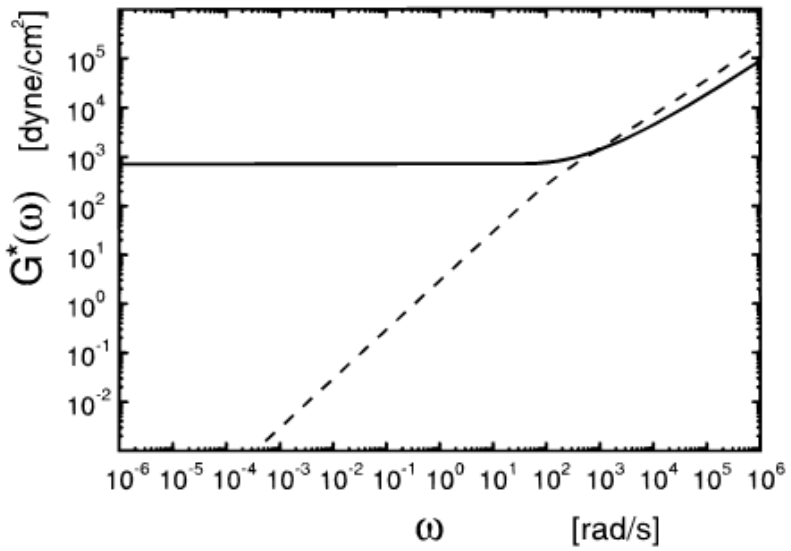

Figure 2.9: *(Taken from Ref. [87]) Values of $G'(\omega)$ (solid line) and $G''(\omega)$ (dotted line) for a system approximating a lightly cross-linked gel.*

2.2 Tube diameter in the tightly-entangled regime

In a later paper [110] Morse provides a quantitative description of the forces confining each polymer to a tube in tightly-entangled solutions, thereby predicting values for the tube diameter and plateau modulus in such regimes. In the tightly-entangled concentration regime the geometrical mesh size, $L_m \equiv \rho^{-1/2}$, is much less than L_p and the tube diameter, D_e, and entanglement length, L_e, are expected to be much less than L_p. It is reasonable to assume that each chain in a tightly-entangled solution is effectively confined to a tube like region over time scales much less than the reptation time, τ_{rep}. In the limit of very long chains, and correspondingly long reptation times, the topological structure of a network of uncrossable chains may be treated as if it were permanent for the purposes of describing averages of confirmations over shorter times.

Morse developed two analytical approximations describing the confinement forces acting on a randomly chosen test chain embedded in a ‘‘thicket’’ of uncrossable chains: the binary collision approximation (BCA) and effective-medium approximation (EMA). The scaling relation resulting from the BCA had previously been obtained by several others authors [4, 126, 128], but Morse also estimated the prefactors. So, prior to the introduction of the EMA, there was broad agreement regarding the scaling law. The approximations are summarised as follows.

The binary collision approximation gives a rather detailed description of the interaction of a test chain with individual nearby medium chains, but neglects any effects arising from the collective elastic relaxation of the network. It yields the following expression for the elastic modulus:

$$G \approx 0.40 k_B T \rho^{7/5} L_p^{-1/5} \tag{2.28}$$

The effective-medium approximation starts from a very different point of view, by treating the network surrounding the test chain as an elastic continuum with a shear modulus equal to the self-consistently determined plateau modulus of the solution, and the test chain as a thread embedded in this medium. The expression thus obtained is:

$$G \approx 0.82 k_B T \rho^{4/3} L_p^{-1/3} \tag{2.29}$$

Experimental studies of actin by Tassieri *et al*. [139] focused on measuring the persistence length of actin in various buffers in order to show that the correct approximation is, in fact, the EMA prediction.

Chapter 3

MATERIALS AND METHODS

3.1 Actin extraction

Actin and myosin were obtained directly from fresh rabbit muscle and prepared using standard preparatory techniques following the methods described by Pardee & Spudich [140]. Back and leg muscle was removed from a rabbit and placed on ice, before being minced in a Waring blender. 300ml of Guba-Straub buffer [see Appendix] was added per 100g muscle. The solution was stirred for precisely 15 mins, in order to dissolve the myosin, then it was centrifuged at 9000 rpm for 30 mins in a Sorvall GS3 rotor. The myosin supernatant and actin precipitate were then separated.

The actin precipitate was mixed with 2L of actin extraction buffer [see Appendix] for 10 mins at 4ºC then filtered through 4-ply cheesecloth. The residue remaining on the cheesecloth was scraped off into a beaker and extracted further with 1L of 1mM EDTA (pH 7.0) for 10 mins at 4ºC, before once more being filtered. This extraction procedure was repeated twice more using 2L of deionised water for 5 mins at 4ºC, followed by one more filtration through cheesecloth. 2X volume of cold acetone was added and the mixture stirred for 30 mins before another cheesecloth filtration. The acetone step was repeated 4 times using 1X volume cold (4 ºC) acetone which was stirred for 15 mins. Finally the acetone was allowed to evaporate overnight in an evacuated jar and the actin stored at -20ºC.

3.2 G-actin preparation

It was necessary to polymerise the actin so that it could be purified *via* the removal of tropomyosin. 6g of acetone dried actin powder was stirred into 120ml ACEX [see Appendix] for 30 mins on ice in a cold room. The mixture was filtered through 4-ply cheesecloth and the exudate was collected in a beaker. The pellet was stirred in 80ml ACEX, for 10 mins, then once again squeezed through the cheesecloth and the exudate collected. A small sample was taken for optical density measurements. The total exudate was centrifuged at 20,000rpm for 15 mins in a Sorvall SS34 rotor. The resultant pellet was loose so the supernatant was pipetted out. The volume of supernatant was measured.

In order to polymerise and purify the actin the supernatant was stirred and various stock solutions were added to bring it to concentrations of 5mM Tris-Cl, 50mM KCl, 2mM $MgCl_2$ and 1mM ATP. The solution was left for 2 h at 4ºC.

KCl was used to remove the tropomyosin. The actin solution was brought to a concentration of 800mM KCl and a pH of 8.3-8.5. It was ultracentrifuged in a Beckman Ti35 rotor at 32,000rpm for 3 h at 4ºC. The pellets were washed with ACEX buffer, and then left in a small volume of buffer to soften. They were transferred to a homogeniser tube on ice, and ACEX buffer was added in order to give a final actin concentration of 5mg/ml. The sample was homogenised gently for 30 mins.

The actin was depolymerised by dialysing in ACEX overnight, with three 660ml changes. The next day the actin was centrifuged at 13,000rpm for 15 mins in a Sorvall SM24 rotor to remove any precipitate. The volume of supernatant was measured, and a small sample taken for optical density measurements (see Appendix). The G-actin was aliquoted and frozen in liquid nitrogen. The final stock concentration was ~ 5mg/ml.

3.3 Myosin extraction

The myosin supernatant was initially extracted along with the actin as described in Section 3.1.2. Two sheets of Whatman #1 filter paper were mashed together with a small volume of buffer in order to form a 0.5” pad in a Buchner funnel, through which the myosin supernatant was filtered. 10X volume of cold swirling water was then added to the supernatant in a large tub to induce precipitation and left overnight for the precipitated myosin to settle. The supernatant was removed and the slurry was centrifuged at 9000rpm for 15 mins. 20ml of 3M KCl was added per 100ml, followed by another centrifugation. The mixture was stirred until the myosin was in solution. 10X volume of cold water was added, before centrifugation at 5,000g for 16 mins in a Sorvall GS3

rotor. The resulting pellet had myosin prep solution [see Appendix] added to it in the volume calculated by:

$$\frac{[required]}{[stock]-[required]} * Volume\ of\ myosin \quad = \quad Volume\ of\ myosin\ prep\ solution \tag{3.1}$$

A small volume was removed for optical density analysis. After a clarifying spin an equal amount of cold glycerol (analytical reagent grade) was added to the myosin and well mixed to prevent the myosin from freezing solid. Air bubbles were removed via centrifugation and then the mixture was stored at -20ºC.

3.4 Myosin fragment preparation: S1 and HMM

The S1 subfragment of myosin-II was prepared via a papain digestion. 3ml of the myosin II-glycerol mixture was added to 2.7ml of cold deionised water in order to precipitate the myosin. The mixture was centrifuged at 17,000rpm in the Sorvall SS34 for 15 mins, giving approximately 75mg myosin in the precipitant. The myosin pellet was redissolved into an equal volume of low salt buffer [see Appendix]. Activated papain stock solution [Sigma-Aldritch] was added to the myosin to a final concentration of 0.03 mg/ml and digestion was allowed to proceed for 10 mins at 23ºC, with thorough mixing throughout. The digestion was stopped by adding 2-fold molar excess of E64 inhibitor [Sigma-Aldritch]. The digestion products were then dialysed against low salt buffer with 2mM DTT added. The insoluble products were removed by centrifugation at 20,000rpm for 30 mins in the SS34. The soluble S1 fragment was purified by using an anion exchange column, where the S1 elution on a linear salt gradient (0-1M NCl) produced a single peak. The S1 fractions were collected by ultrafiltration on an Amicon spin column. A sample was taken for optical density measurements before the S1 was aliquoted and frozen in liquid nitrogen. It was stored at -80ºC in the presence of 30% (w/v) sucrose. Optical density measurements gave the final stock concentration as ~5.2mg/ml.

The HMM fragment was prepared using a chymotrypsin [Sigma-Aldritch] digestion. After the myosin II was precipitated and centrifuged as with the papain digestion above, the myosin pellets were redissolved in 2X high salt buffer [see Appendix]. Digestion took place for 10 mins at 23ºC, by adding 0.05mg/ml TLCK-treated chymotrypsin [Sigma-Aldritch]. The digestion process was stopped by adding PMSF [Sigma T9777] to a final concentration of approximately 0.25mM. The digestion products were then dialysed against low salt buffer for 12 h at 4ºC in a cold room. The light meromyosin (LMM) and undigested material was pelleted by centrifugation 1t 75,000rpm for 10 mins in the Beckman TL100.3. A sample was taken for SDS-PAGE and for optical density measurements. The HMM was aliquoted and frozen in liquid nitrogen then stored at -80ºC. Optical density measurements gave the final stock concentration as ~ 1.25mg/ml.

3.5 Actin polymerisation

One twentieth volume of 20x$AB^{+}_{/CP}$ [see Appendix] buffer (without creatine phosphokinase, see below) was added to G-actin to give a final polymerisation buffer concentration of 1x$AB^{+}_{/CP}$. The actin was left for 2 h at room temperature to polymerise [141].

3.6 Actin and S1/HMM networks

To prepare active actin/myosin networks, actin was first polymerised as described above. Approximately 30 seconds before S1 or HMM were mixed with the actin, creatine phosphokinase (CPK) [Sigma-Aldritch] was added to the buffer. CPK enables creatine phosphate (CP) to react with ADP to produce ATP, creating a cycle of ATP production to sustain the dynamic interaction of the myosin fragments with actin; thus preventing a fixed or *rigor* configuration (Figure 3.1). HMM and S1 were diluted accordingly before being added to the F-actin.

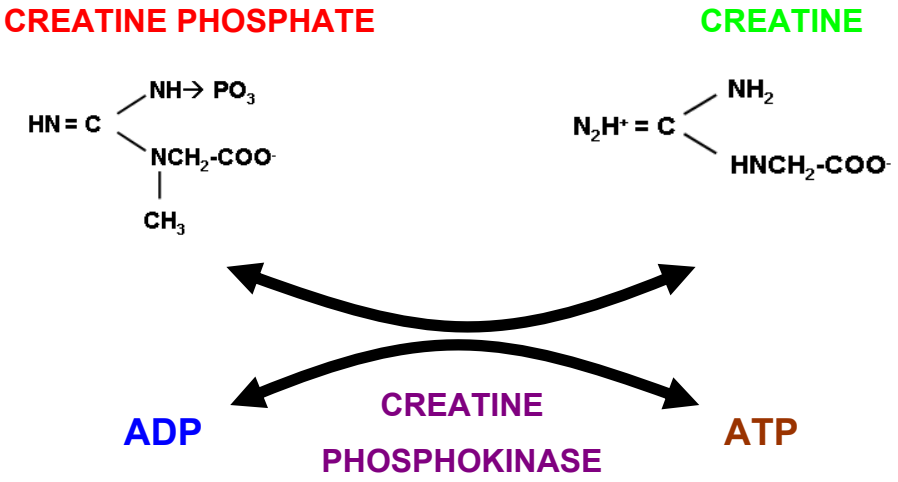

Figure 3.1: *Cycle of ATP production from creatine phosphate and ADP.*

3.7 Jurkat cell culture

T-cells play an important role in the regulation of immune responses in the human body. The disregulation of T-cell triggering has been linked to the development of a number of autoimmune diseases [142-144]. The actin cytoskeleton controls multiple aspects of T-cell function, such as maintenance of cell shape, signalling, differentiation, and T-cell migration within tissues. Quiescent T-cells exhibit 'ball' morphology, with cortical actin filaments distributed underneath the cell membrane. Jurkat cells are a line of T-lymphocytes that express the protein CD4 on their surface, which is the protein targeted by the HIV virus. For this reason, CD4+ expressing T-lymphoma cells are often used to study T-cell signalling [145] and HIV-1 dissemination in viral pathogenesis [146] .

Jurkat cells were obtained from ATCC (clone E6-1, TIB-152) and maintained in RPMI 1640 (1x) media containing L-Glutamine and 25mM HEPES [Gibco, Invitrogen]. Prior to experiments they were suspended in PBS [Gibco, Invitrogen], mixed with functionalised beads and allowed to equilibrate for ~ 10min.

3.8 Functionalised beads

Anti-CD4+ [Invitrogen] was attached to 5µm carboxylate functionalised silica beads [Bangs Laboratories Inc] using a method based on a previously protocol [147]. The adaptation of the method involved first binding a short heterobifunctional polyethylene glycol chain to the beads to provide a flexible linker to which the anti-CD4+ was subsequently bound. The microspheres were washed (3x) with 0.1 M Na2CO3 buffer (pH 9.6) using centrifugation between washes to remove the supernatant liquid. This ensured that all the carboxylate groups were deprotonated. Following the final wash, the beads were resuspended in RO water and centrifuged again. After removal of the water, the remaining pellet was resuspended in freshly prepared 0.02 M sodium phosphate buffer (pH 6) containing 2 mM 1-ethyl-3-(3-155dimethylaminopropyl)-carbodiimide [EDC, Sigma] and 5 mM sulfo-N-hydroxysuccinimide [sulfo-NHS, Thermo-Fisher]. The microsphere solution was then agitated for 15 minutes to allow the sulfo-NHS to activate the carboxylate groups on the surface of the microspheres. The solution was centrifuged, then the supernatant removed and replaced by a 10 mM solution of the flexible linker, O-(2-Aminoethyl)-O′-160(2-carboxyethyl)polyethylene glycol 3,000 hydrochloride [Aldrich] in pH 7.4 phosphate buffer. The activated microspheres were then agitated in the flexible linker solution for 2 h at 4ºC, before further centrifugation and washing with pH 7.4 buffer. The anti-CD4+ was then bound to the carboxylate terminals of the PEG linker from a 1 mg/ml solution of anti-CD4+, using the same EDC/sulfo-NHS activation procedure outlined above.

3.9 Polyacrylamide

Polyacrylamide (PAM) [Polysciences, Inc] was prepared a molecular weight of 5-6 million Da.

3.10 Optical tweezers instrumentation

Two different optical tweezer systems were employed throughout this thesis, which will be described here. On the first system, trapping was achieved using a continuous wave Ti:sapphire laser system (M Squared, SolsTiS) which provided up to 1W at 830nm (Figure 3.2). Holographic optical traps were created using a spatial light modulator (Boulder XY series). The tweezers were based around an inverted microscope with a 100 x 1.3 NA objective lens (Zeiss, Plan-Neoflur) used to both focus the trapping beam and to image the particle motion. Samples were mounted in a motorised microscope stage (ASI, MS-2000). Two complementary metal-oxide semiconductor cameras are used to view the sample, with bright-field illumination: one provides a wide field of view (Prosilica EC1280M), while the other takes high-speed images of a reduced field of view (Prosilica GV640M). These images are processed in real time at 1 kHz using our own LABVIEW (National Instruments) particle tracking software running on a standard desktop PC [49].

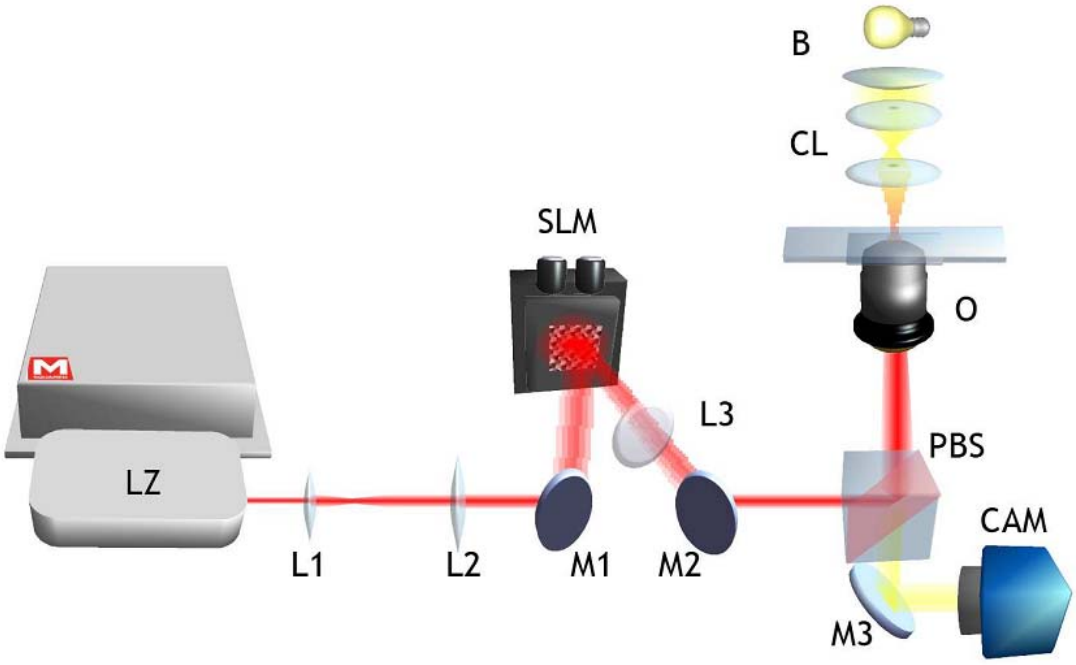

Figure 3.2: *Optical tweezers configuration. From left to right; (LZ) Ti:sapphire laser system, (L1 and L2) beam telescope, (M1 and M2) folding mirrors, (SLM) boulder fast SLM, (L3), (PBS) polarising beam splitter cube, (M3) mirror, (CAM) Prosilica fast camera, (O) objective lens, (CL) condensing optics, (B) 250W halogen bulb. Image taken from [155].*

An alternative optical tweezer setup was also employed, consisting of a continous wave Ti:sapphire laser (Coherent, Model 890) pumped by a solid state single frequency laser (Coherent model Verdi V5, λ=532nm). The Ti:sapphire was tunable from 690-1100nm. The samples were loaded on a motorised stage (Prior Pro-Scan II), and optical traps were again created using a spatial light modulator (Hamamatsu). A Prosilica PCI-6713 camera was used to view the particles, and as above, custom Labview software was used for position analysis.

The bead position was measured by detecting the bead centre of mass over a specific number of data points (usually 100,000 to 500,000), then the output time and position data were analysed by a code written in Labview. No correction was applied for Faxen's law as the beads were measured in solution in a chambered microscope slide, far from the cover slip and far from the walls of the chamber. The power output of the trap was varied between measurements as the beads became increasingly difficult to trap with increased polymer concentration. This had no bearing on the analysis as the data was normalised to take into account the optical trap strength, as discussed in the next section.

Spatial light modulators are based upon holographic technology and allow multiple particles to be trapped at once [148] (Figure 3.3). During the development of optical tweezers, an obvious desire arose to trap multiple particles in independently steerable traps. Two traps are readily produced using separate steering mirrors and a pair of beam splitters [149]. For more traps it is possible to time share a single beam to create multiple traps, either by using a rapid scanning galvo-mirror [150] or, for higher speed, acousto-optic beam deflectors [151]. The latter technology makes it possible to trap hundreds of particles in complicated patterns. However, neither of these scanning approaches allows simultaneous and easy control of the axial position of the traps, for which one needs holographic tweezers. The term holographic optical tweezers was coined by Curtis *et al*. in 2002 in their seminal paper on the use of a commercially obtained spatial light modulator acting as a programmable diffractive optical element to split a single laser beam into many optical traps that could be independently positioned in 3D and for which the point spread function for each of the traps could be independently controlled [48].

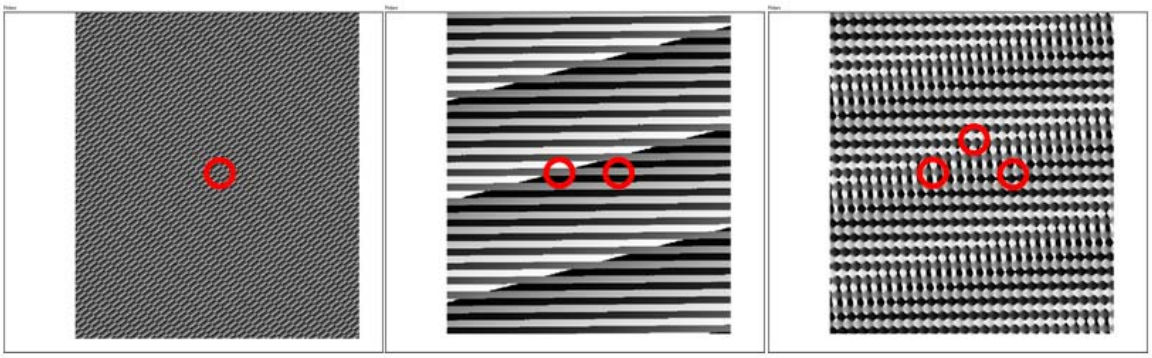

Figure 3.3: *Spatial light modulator (SLM) holograms designed to create a single trap (left), two traps (centre) and three traps (right). Red circles indicate the approximate positions of where the first order traps would lie. Image created by author.*

The use of a spatial light modulator in this thesis presents to us the opportunity to perform transient measurements with the optical tweezers, as will be discussed in detail in Chapter 4.

3.11 Optical tweezers calibration

The optical tweezers can be calibrated and the trap stiffness calculated by using the principle of Equipartition of Energy:

$$\frac{3}{2}k_B T = \frac{1}{2}\kappa\left\langle r^2 \right\rangle \tag{3.1}$$

where k_B is the Boltzmann constant, T is the absolute temperature, and $\left\langle r^2 \right\rangle$ is the time-independent variance of the particle displacement from the trap centre, the origin of $\vec{r}$. Despite all the possible methods for determining the optical trap stiffness (*e.g.* using the power spectrum or the drag force [34, 152, 153]), the equipartition method is the only method independent of the viscoelastic properties of the material under investigation and is thus essential from a rheological point of view.

3.12 Experimental protocol

For optical tweezer measurements using one or more traps, silica beads [5μm, Bangs Laboratories Inc] were added to the required sample, before the sample was placed in a chambered microscope slide. A glass cover-slip was used to seal the chamber, and nail varnish was used around the edges of the cover-slip to keep the chamber air-tight in order to prevent evaporation. The beads were then optically trapped and their position measured for a length of time. When the beads were required to be subjected to a flowfield, this was achieved by suddenly moving the motorised microscope stage at a predetermined speed and direction

For experiments involving the viscoelastic properties of Jurkat cells, the beads were optically trapped and then moved to the equatorial plane of the cell. They were held for a sufficient time (~2 min) until the binding process to the cell was completed. The optical trap was then switched off and the bead position monitored (see Chapter 8).

Chapter 4

MICRORHEOLOGY WITH OPTICAL TWEEZERS

The aim in this Chapter is to present two new self-consistent procedures for measuring the linear viscoelastic properties of materials, from non-oscillatory measurements, across the widest frequency range achievable with optical tweezers [154, 155]. The Chapter consists of a description of how basic static measurements of the linear material viscoelasticity can be carried out using optical tweezers, followed by the presentation of two new wideband techniques developed as part of this thesis. These are referred to as the 'Flow-field' method and the 'Two trap' method, respectively.

Optical tweezers have been successfully used with Newtonian fluids for rheological purposes such as determining the fluid viscosity with a high accuracy, measuring the hydrodynamic interactions between particles, or estimating the wall effect on the Stokes drag coefficient (*i.e.* Faxén's correction), as reviewed in Ref. [76]. Conversely, when optical tweezers are adopted for measuring the viscoelastic properties of complex fluids the results are either (I) limited to the material's high-frequency response [156-158] (discarding the essential information related to long time scales *i.e.* low-frequency material behaviour), or (II) supported by low-frequency measurements performed by different techniques (*e.g.* rotational rheometry [71] or PPTM [72]) but either without showing a clear overlapping region between the results [71] or leaving a macroscopic gap of information in the range of frequencies explored [72]. Some oscillatory measurements have been obtained at relatively low frequencies on non-Newtonian fluids using optical tweezers [159, 160] by performing lengthy experiments. These are, however, accompanied by an incomplete analysis of the frequency-dependent viscosity data.

The two wideband microrheological methods presented here aim to remove the lower frequency limitation of non-oscillatory optical tweezer measurements. They both consist of two steps. The first step (common to both of the methods) consists of measuring the thermal fluctuations of a trapped bead for a sufficiently long time, in what we refer to as a static measurement. It is designed to provide the high frequency viscoelastic response of the material, and because it is relevant to both techniques, it will be discussed first. The second step of both methods involves imposing a transient between two steady states, and is designed to extract the material's low frequency viscoelastic response. In the second technique - 'Two trap' - we also present an equivalent way of taking static measurements in the first step.

4.1 Static measurements with optical tweezers

In the case of static measurements, the optical tweezers are fixed in space, and only the thermal fluctuations of the trapped bead are of interest (Figure 4.1). The experimental procedure is analytically described through the analysis of the motion of a bead trapped in a stationary harmonic potential of force constant, κ. The equation describing the bead position $\vec{r}(t)\forall t$ r can be derived by means of a generalised Langevin equation, which in three dimensions is:

$$m\vec{a}(t) = \vec{f}_R(t) - \int_{t_0}^{t} \zeta(t-\tau)\vec{v}(\tau)d\tau - \kappa\vec{r}(t) \tag{4.1}$$

where m is the mass of the particle, $\vec{a}(t)$ is its acceleration, $\vec{v}(t)$ is the bead velocity, and $\vec{f}_R(t)$ is the usual Gaussian white noise term, modelling stochastic thermal forces acting on the particle. The integral term represents the viscous damping of the fluid, which incorporates a generalised time-dependent memory function, $\zeta(t)$. In all measurements carried out with optical tweezers, the tweezers can be calibrated and the trap stiffness calculated by using the principle of Equipartition of Energy (Equation 3.1).

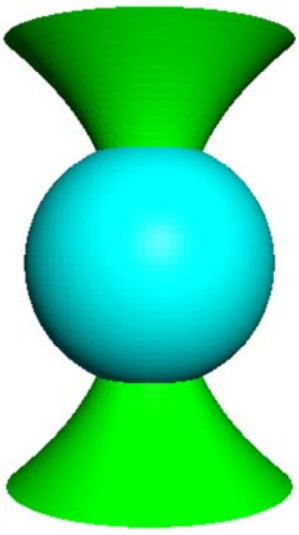

Figure 4.1: *Bead trapped in a stationary ('static') optical trap.*

The thermal fluctuations of the trapped bead can also be investigated to determine the high-frequency viscoelastic properties of the material through the analysis of the time dependence of the mean-square displacement $\left\langle \Delta r^2(\tau) \right\rangle \equiv \left\langle \left[\vec{r}(t+\tau) - \vec{r}(t) \right]^2 \right\rangle_t$. The average is taken over all initial times t and the number of particles considered in the experiment, if more than 1. By performing the Laplace transform of Equation 4.1, the viscoelastic memory function can be expressed as a function of the velocity autocorrelation function (VAF) in Laplace space, defined as $\left\langle \nu(0)\tilde{\nu}(s) \right\rangle$. Taking the unilateral Laplace transform of Equation 4.1 results in:

$$m\left[s\,\tilde{\nu}(s) - \nu(0) \right] = \tilde{f}_R(s) - \tilde{\zeta}(s)\tilde{\nu}(s) - \kappa\tilde{r}(s) \tag{4.2}$$

where s represents the frequency in the Laplace domain.

In terms of the VAF Equation 4.2 becomes:

$$\tilde{\nu}(s) = \frac{\left[\tilde{f}_R(s) + m\,\nu(0) \right]}{ms + \tilde{\zeta}(s) + \dfrac{\kappa}{s}} \tag{4.3}$$

Based on the same statistical mechanics assumptions adopted by Mason and Weitz in the study of thermally excited free particles [4] at thermal equilibrium, where $\left\langle \nu(0) f_R(t) \right\rangle = 0$ and $m\left\langle \vec{\nu}(t)\vec{\nu}(t) \right\rangle = 3k_B T \;\; \forall t$, Equation 4.3 can be reorganised as:

$$\left\langle \nu(0)\tilde{\nu}(s) \right\rangle = \frac{6k_B T}{\left[ms + \tilde{\zeta}(s) + \dfrac{\kappa}{s} \right]} \equiv s^2 \left\langle \Delta\tilde{r}^2(s) \right\rangle \tag{4.4}$$

where s is the Laplace frequency. Following Mason and Weitz [4] in assuming that the bulk Laplace frequency-dependent viscosity of the fluid, $\tilde{\eta}(s)$, is proportional to the microscopic memory function $\tilde{\zeta}(s) = 6\pi a\tilde{\eta}(s)$, where a is the bead radius, Equation 4.4 can be written as:

$$\tilde{\eta}(s) = \frac{1}{6\pi a}\left[\frac{6k_B T}{s^2 \left\langle \Delta\hat{r}(s) \right\rangle} - ms - \frac{\kappa}{s} \right] \tag{4.5}$$

where the first term in the brackets reflects the viscoelasticity of the medium, the second term is related to the inertia of the bead, and the third term takes into account the optical trap strength. It is easy to demonstrate that, for a micro-bead of density on order of 1 g/cm^3 suspended in water, the product ms is negligible compared with the first term for the majority of the experimentally accessible frequencies *i.e.* $s \le 10^6\ s^{-1}$. With regard to the optical trap strength, two limiting cases can be distinguished: (i) in the limit $\kappa / s \to 0$, which can be obtained either for vanishing trap strength or for measurements performed at high frequencies, but lower than $10^6\ s^{-1}$, Equation 4.5

recovers the generalised Stokes-Einstein relationship derived by Mason and Weitz [4]; and (ii) in the limit $\kappa / s \to \infty$, which can be obtained either for a strong optical trap or for measurements performed at very low frequencies, Equation 4.5 gives the same result as if the bead were embedded in a purely elastic continuum with elastic constant of $\kappa / 6\pi a$. For all intermediate cases, where $0 < \kappa / s < \infty$, it is possible to show that from Eq. 4.5, the complex modulus can be expressed directly in terms of the time-dependent MSD:

$$G^*(\omega) = s\hat{\eta}(s)\big|_{s=i\omega} = \frac{\kappa}{6\pi a}\left[\frac{2\langle r^2\rangle}{i\omega\langle \Delta\hat{r}^2(\omega)\rangle} - 1\right] \tag{4.6}$$

where $\langle \Delta\hat{r}^2(\omega)\rangle$ is the Fourier transform of $\langle \Delta r^2(\tau)\rangle$.

In principle, Equation 4.6 is a simple expression relating the material complex modulus $G^*(\omega)$ to the observed time-dependent bead trajectory, $\vec{r}(t)$, *via* the Fourier transform of the MSD. In practice, the evaluation of this Fourier transform, given only a finite set of data points over a finite time domain, is nontrivial since interpolation and extrapolation from that data can yield serious artefacts if handled carelessly. In order to express the Fourier transform in Equation 4.6 in terms of the N experimental data points $\left(t_k, \langle \Delta r^2(\tau)\rangle_k\right)$ (where $k = 1.....N$) which extend over a finite range, exist only for positive t, and *need not* be equally spaced, we adopt the analytical method introduced in Ref. [161]. In particular, we refer to Equation 10 of Ref. [161] which is equally applicable to finding the Fourier transform $\hat{g}(\omega)$ of any time-dependent quantity $g(t)$ sampled at a finite set of data points (t_k, g_k), giving :

$$-\omega^2\hat{g}(\omega) = i\omega g(0) + \left(1 - e^{-i\omega t_1}\right)\frac{(g_1 - g(0))}{t_1} + \dot{g}_\infty e^{-i\omega t_N} + \sum_{k=2}^{N}\left(\frac{g_k - g_{k-1}}{t_k - t_{k-1}}\right)\left(e^{-i\omega t_{k-1}} - e^{-i\omega t_k}\right) \tag{4.7}$$

where $\dot{g}_\infty$ is the gradient of $g(t)$ extrapolated to infinite time. Also $g(0)$ is the value of $g(t)$ extrapolated to $t = 0^+$. An identical formula can be written for $\langle \Delta\hat{r}^2(\omega)\rangle$, with g being replaced with $\langle \Delta r^2\rangle$. This analytical procedure has the advantage of removing the need for Laplace and inverse-Laplace transformations of experimental data [11].

4.1.2 The normalised mean-square displacement

Here, we introduce the normalised mean-square displacement, $\left\langle \Delta r^2(\tau) \right\rangle / 2\left\langle r^2 \right\rangle$, (*i.e.* the MSD divided by twice the variance, as seen in Equation 4.6) which is a parameter that we make use of throughout this thesis, and which we term $\Pi(\tau)$. In Chapter 4.3 we show how $\Pi(\tau)$ is related to the normalised position autocorrelation function.

To understand the physical basis of the normalised mean-square displacement, we need to consider the MSD of a bead in an optical trap. At short time intervals (high frequencies) the optical trap only exerts negligible forces upon the trapped bead (as the displacements from the trap centre are small), thus the thermal forces dominate; however, at long time intervals (low frequencies) the bead is constrained by the optical trap, and the bead's MSD reaches a constant value. Experimentally we find that the MSD tends to a value of twice the variance, $2\left\langle \vec{r}^2 \right\rangle$, at long time intervals. The reason for this can be explained by considering a series of numbers flipping randomly between 1 and -1 for a sufficiently long period of time. The *mean* value of this series would be zero, and the variance $\left\langle \vec{r}^2 \right\rangle$ would be equal to $\left\langle (\pm 1 - 0)^2 \right\rangle = 1$. The MSD for each point would be either 4 or 0, depending upon the specific event (1→-1, -1→1 or 1→1, -1→-1 respectively). Averaging over a sufficiently long measurement would give a value of 2, which is twice the variance. Thus for long time intervals, and for a bead that is subject to a restraining optical force, the following holds true:

$$\frac{\left\langle \Delta\vec{r}(\tau)^2 \right\rangle}{2\left\langle \vec{r}^2 \right\rangle} = 1 = \Pi(\tau) \tag{4.8}$$

This ratio is a dimensionless parameter that is neither dependent upon optical trap strength nor bead radius, thus it provides a direct comparison between different fluids and viscosities, as discussed in greater detail in Chapter 5. In addition, it determines the so called 'cut-off" frequency of static optical tweezer measurements, below which the elastic nature of the optical trap masks the elastic response of the material.

Note that, this is the first time in more than 40 years of optical tweezers study that it has been explicitly stated that for a constrained bead, $\lim_{\tau \to \infty} \Pi(\tau) = 1$.

As mentioned above, the optical tweezers exert a non-negligible force on a trapped bead only at low frequencies. As a result of this, the low frequency viscoelastic response of a material has never before been obtained with non-oscillating optical tweezers. We present two methods that measure this low frequency response over the greatest range possible with non-oscillating tweezers.

4.2 Wideband microrheology with optical tweezers: 'Flow-field' method

4.2.1 Analytical method

In this section a new broadband microrheological technique is described that has been designed to obtain the widest possible frequency range using non-oscillating optical tweezers. In particular, the experimental procedure consists of two steps: (I) measuring the thermal fluctuations of a trapped bead for a sufficiently long time, as introduced above, and (II) measuring the transient bead displacement, from the optical trap centre, in response to a uniform fluid flow field entraining the bead (Figure 4.2). The flow is switched on at time zero by translating the whole fluid sample while the trap is held fixed. The imposed constant velocity motion continues until a steady displacement of the bead is reached.

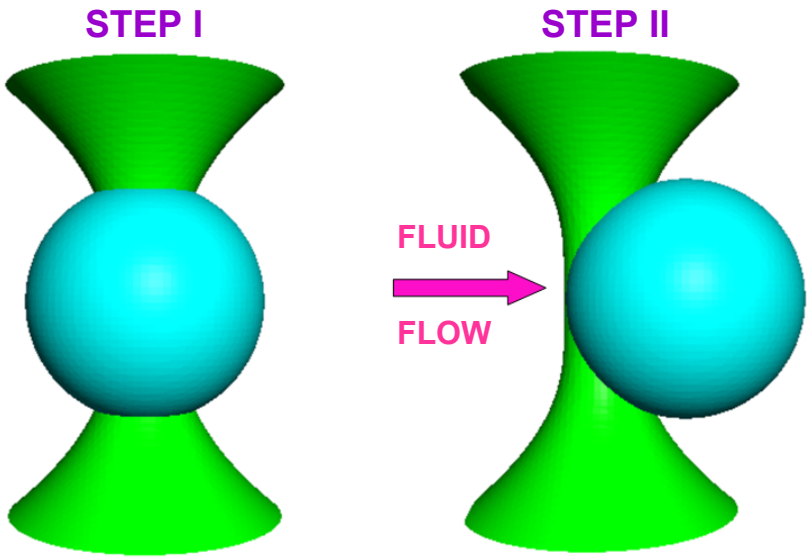

Figure 4.2: *Diagram of experimental procedure: Step I measures the bead trajectory in a static optical trap. Step II measures the displacement of the bead in response to a uniform fluid flow.*

The analysis of Step I provides (a) the trap stiffness (κ) - note that this has the added advantage of making the present method self-calibrated - and (b) the high-frequency viscoelastic properties of the material to a high accuracy. Step II has the potential to provide information about the viscoelastic properties of the material down to very low frequencies, limited only (at the bottom end) by the duration of the experiment. However, because of the harmonic nature of the optical trap, which tends not to transmit high-frequency applied forces to the bead, the material's high-frequency response can not be determined by this step. The full viscoelastic spectrum is thus resolved by combining the results obtained from Steps I and II.

The experimental procedure is analytically described through the analysis of the motion of a bead trapped in a stationary harmonic potential of force constant κ , where a uniform fluid flow field of

magnitude $\left|\vec{V}_s\right|$ can be exerted at time $t=0$. The equation describing the bead position $\vec{r}(t)\forall t$ can be derived by means of a generalised Langevin equation, which in three dimensions is:

$$m\vec{a}(t)=\vec{f}_R(t)-\int_{t_0}^{t}\zeta(t-\tau)\left[\vec{v}(\tau)-\vec{V}_s(\tau)\right]d\tau-\kappa\vec{r}(t) \tag{4.9}$$

where m is the mass of the particle, $\vec{a}(t)$ is its acceleration, $\vec{v}(t)$ is the bead velocity, $\vec{V}_s(t)$ is the fluid flow field velocity, and $\vec{f}_R(t)$ is the usual Gaussian white noise term, modelling stochastic thermal forces acting on the particle. The integral term represents the viscous damping of the fluid, which incorporates a generalised time-dependent memory function $\zeta(t)$ (as introduced by Mason and Weitz [4]). The term $\kappa\vec{r}(t)$ represents the optical trapping force acting on the bead.

We now show how Equation 4.5 evolves in the two cases mentioned above; when $\vec{V}_s(t)=\vec{0}$ (Step I) and $\vec{V}_s(t)\neq\vec{0}$ (Step II) respectively. In the first case, where $\vec{V}_s(t)=\vec{0}$, the measurement is effectively a static measurement, and can be analytically described by the same method introduced in the previous section, resulting in the complex shear modulus being calculated as in Equation 4.6.

The second step of the procedure, which experimentally follows the first, consists of the analysis of the induced bead displacement from the trap centre due to an imposed time-dependent uniform fluid flow field $\vec{V}_s(t)$ entraining the bead. In this case, Equation 4.9 yields, in the Laplace form, the mean velocity of the particle:

$$\left\langle\tilde{v}(s)\right\rangle=\frac{\tilde{\zeta}(s)\tilde{V}_s(s)}{ms+\tilde{\zeta}(s)+\kappa/s}\equiv s\left\langle\tilde{r}(s)\right\rangle \tag{4.10}$$

where the brackets $\langle....\rangle$ denote the average over several independent measurements (but not averaged over absolute time since time-translation invariance has been broken by the flow start-up at $t=0$). It is straightforward to show that, by analytical continuation from Equation 4.10, the complex modulus can be expressed directly in terms of both the imposed flow field and the induced bead displacement from the trap centre:

$$G^*(\omega)=s\tilde{\eta}(s)\big|_{s=i\omega}=\frac{(\kappa-m\omega^2)i\omega\left\langle\hat{r}(\omega)\right\rangle}{6\pi a\left[\hat{V}_s(\omega)-i\omega\left\langle\hat{r}(\omega)\right\rangle\right]} \tag{4.11}$$

where $\hat{V}_s(\omega)$ and $\left\langle\hat{r}(\omega)\right\rangle$ are the Fourier transforms of $\vec{V}_s(t)$ and $\left\langle\vec{r}(t)\right\rangle$, respectively. Note that, so far, the temporal form of $\vec{V}_s(t)$ is still undefined. Thus, Equation 4.11 represents the general solution for $G^*(\omega)$ independent of the temporal form of $\vec{V}_s(t)$ (*e.g.*, sinusoidal function

$\vec{V}_s \sin(\omega t)$ or, as in this work, Heaviside step function $\vec{V}_s H(t)$, where $\vec{V}_s(t) = \vec{0} \forall t < 0$ and $\vec{V}_s(t) = \vec{V}_s \forall t \geq 0$).

As before, Equation 4.11 (as with Equation 4.6) can be seen to be a simple expression relating the material complex modulus $G^*(\omega)$ to the observed time-dependent bead trajectory $\vec{r}(t)$ via the Fourier transform of $\vec{r}(t)$ itself. Once again, the evaluation of this Fourier transform, given only a finite set of data points over a finite time domain, is nontrivial since interpolation and extrapolation from those data can yield serious artefacts if handled carelessly. To express the Fourier transforms of Equation 4.11 in terms of the N experimental data points and $\left(t_k, \left\langle \vec{r}(t) \right\rangle_k\right)$ (where $k = 1.....N$), which extend over a finite range, exist only for positive t, and *need not* to be equally spaced, we adopt the analytical method introduced in Ref. [161] and shown in Equation 4.7. An identical formula can be written for $\left\langle \hat{r}(\omega) \right\rangle$, with g_k (being the finite set of data points of the time dependent quantity $g(t)$) being replaced with $\left\langle \vec{r} \right\rangle$.

4.2.2 Results and Discussion

In this section Equations 4.6 and 4.11 are tested (*via* Equation 4.7) by measuring both the viscosity of water and the viscoelastic properties of water-based solutions of polyacrylamide (PAM) (MW = 5-6×10^6 Da) using optical tweezers (as described in Chapter 3). The Brownian fluctuations of an optically trapped bead give rise to the time-dependent MSD, $\left\langle \Delta r^2(\tau) \right\rangle$, shown in Figure 4.3.

In the case of a bead immersed in a Newtonian fluid, it is expected that at short time intervals (thus small distances) the bead behaves as if it were free to diffuse. Indeed, the agreement between the observed MSD at short times of a trapped bead in water (circles) and the Einstein prediction for a freely diffusing bead (solid line) is good. As the time intervals increase the bead becomes influenced by the optical potential. This results in a plateau at large time intervals, where $\left\langle \Delta r^2(\tau) \right\rangle$ tends to $2\left\langle r^2 \right\rangle$ and we note that the ratio of these two quantities (the MSD and twice the variance of the positional distribution, as discussed in Chapter 4.1) is a dimensionless parameter that we call $\Pi(\tau)$, which is independent of both the optical trap stiffness and the bead radius. It thus allows an explicit comparison between the dynamics of the fluids under investigation as shown in Figure 4.4. Moreover, the onset point of the plateau region in Figure 4.4 indicates the bottom limit of the frequency range within which the moduli can be determined, which we define previously as the cut-off frequency (and will be discussed in greater detail in Chapter 5).

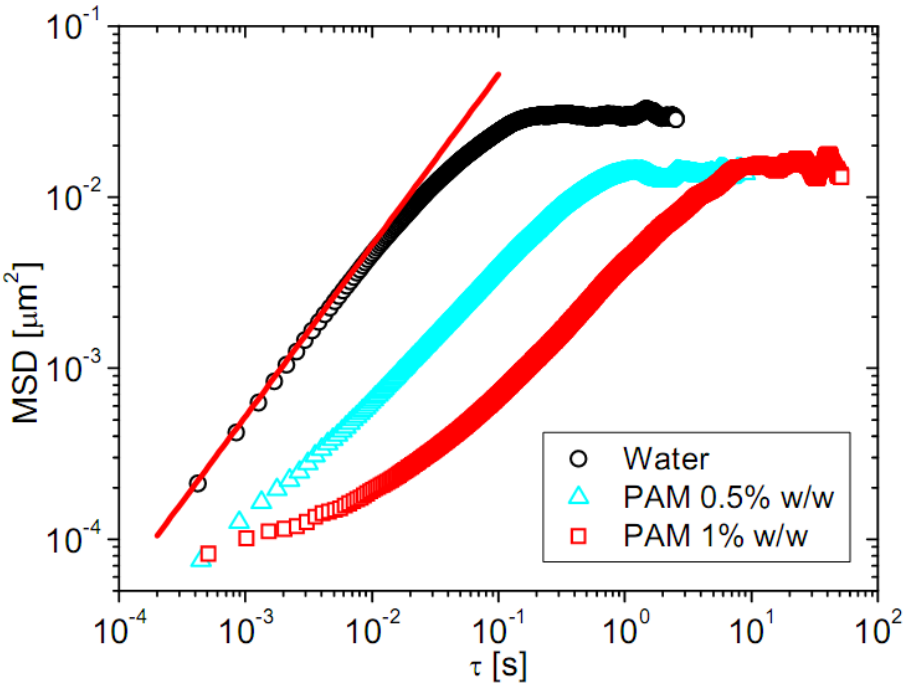

Figure 4.3: *The MSD* vs. *lag time of a 5μm diameter bead in water (with κ = 0.8 μN/m) and in two water-based solutions of PAM at concentrations of 0.5% and 1% w/w (both with κ = 1.7 μN/m). The line is the Einstein prediction of the MSD for 5μm diameter bead in water at 25 °C.*

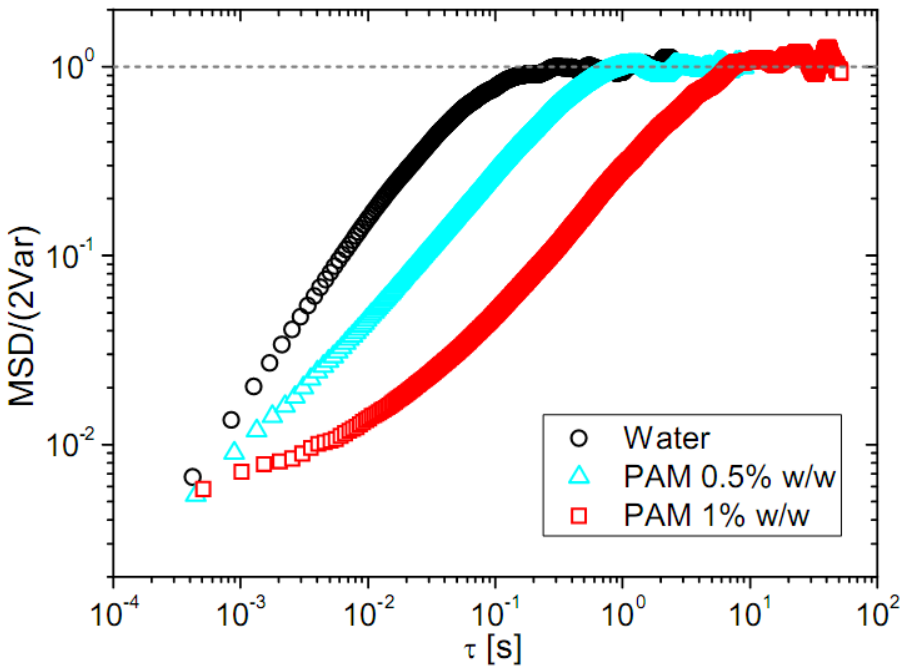

Figure 4.4: *The normalised MSD* vs. *lag time of a 5μm-diameter bead in water (with κ = 0.8 μN/m) and in two water-based solutions of PAM at concentrations of 0.5% and 1% w/w (both with κ = 1.7 μN/m).*

In Figure 4.5 we compare the responses of a 5μm diameter bead immersed in water (a Newtonian fluid) and in a water solution of PAM at 1% w/w (non-Newtonian fluid) due to the imposition of a uniform fluid flow field having temporal behaviour as a Heaviside step function $\vec{V}_s(t) = \vec{V}_s H(t)$,

with different magnitudes in the two measurements. Experimentally, the execution of a Heaviside step function is achieved by suddenly moving the motorized microscope stage at a predetermined speed and direction (here, parallel to the x axis). The experiment runs until a steady displacement (Δx) of the bead from the trap centre is reached (*i.e.* until all the material's characteristic relaxation times are exceeded).

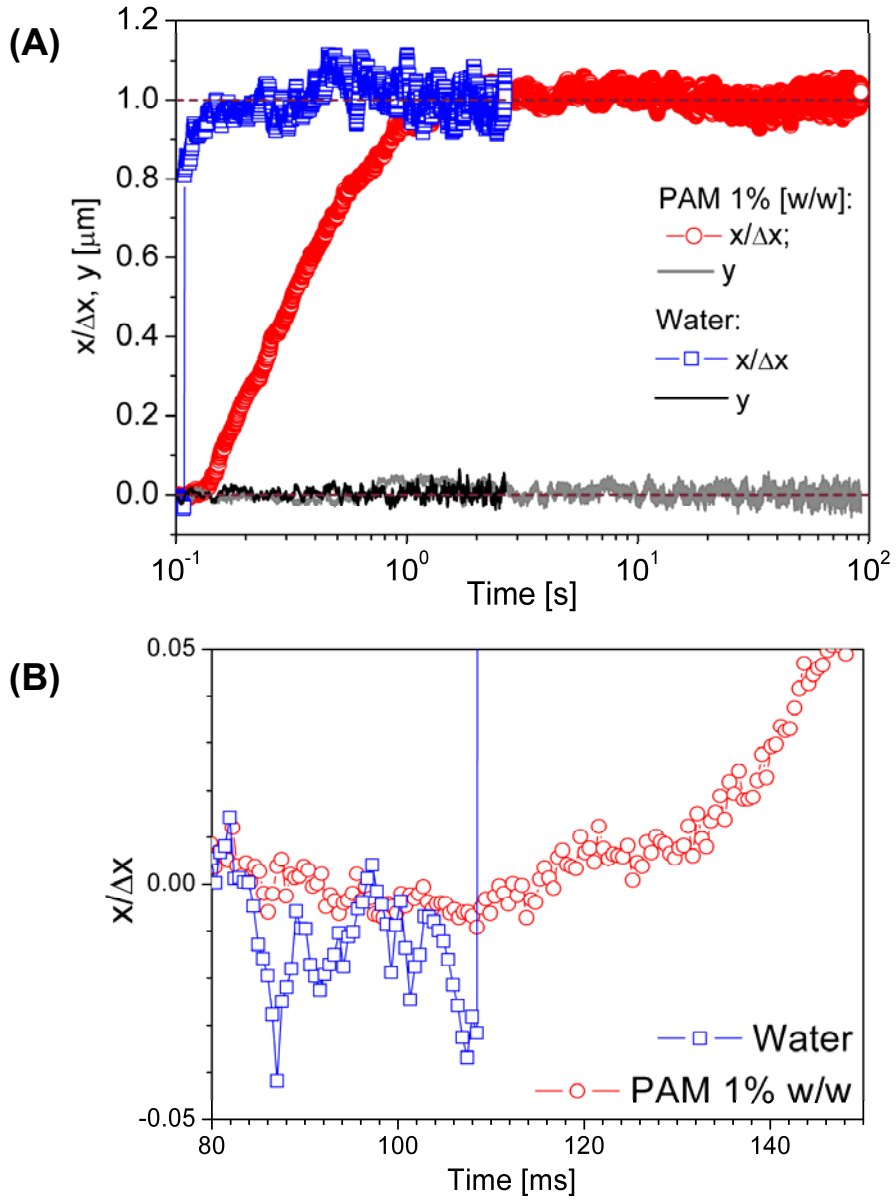

Figure 4.5: (A) *The coordinates of a 5μm diameter bead vs time for two different solutions and for two uniform fluid flow fields of different magnitudes* $\left|\vec{V}_s\right|$ *at 25 °C. In both cases the data was averaged over three measurements and the x coordinate has been normalised by the steady-state displacement* Δx *. In water* κ *= 1.7 μN/m,* $\left|\vec{V}_s\right|$ *= 20 μm/s, and* Δx *= 0.523 μm. In 1% w/w of PAM* κ *= 8.6 μN/m,* $\left|\vec{V}_s\right|$ *= 3 μm/s, and* Δx *= 1.115 μm. (B) The graph highlights the start-up behaviour of both the above systems.*

In Figure 4.5 the x component of the bead displacement has been normalised by Δx for a better comparison between the viscoelastic characters of the two samples. It is clear that while the Newtonian fluid reaches a steady value of the displacement almost instantaneously (as expected), the non-Newtonian fluid shows complex dynamics representative of its viscoelastic nature. It is important at this point to note that, because of the harmonic nature of the optical potential, at early times (*i.e.* for $t \to 0$ or equivalently for $\omega \to \infty$), the trapping force exerted on the bead is actually small (*i.e.* $\kappa\vec{r}(t) \to 0$); and the particle moves almost at the same speed as the imposed flow (*i.e.* $\vec{v}(t) \cong \vec{V}_s(t)$); this implies that Equation 4.11 becomes undefined at high frequencies.

The broadband microrheological measurement with optical tweezers is achieved by combining the frequency responses obtained from both the methods introduced above. In particular, the material's high-frequency response is determined by applying Equation 4.6 (*via* Equation 4.7 with $\left\langle \Delta r^2 \right\rangle_k$ replacing g_k) to the $\left\langle \Delta r^2(\tau) \right\rangle$ measurements, whereas the low-frequency response is resolved by applying Equation 4.11 (via Equation 4.7 with $\left\langle \vec{r} \right\rangle_k$ replacing g_k) to the data describing the bead's transient response to the applied flow field.

In the broadband response of water (not shown), a constant viscosity of $\eta = 8.69 \times 10^{-4} \pm 6 \times 10^{-6}$ Pa.s is measured over five frequency decades at 25°C. A typical result of this procedure for a non-Newtonian fluid (1% PAM) is shown in Figure 4.6.

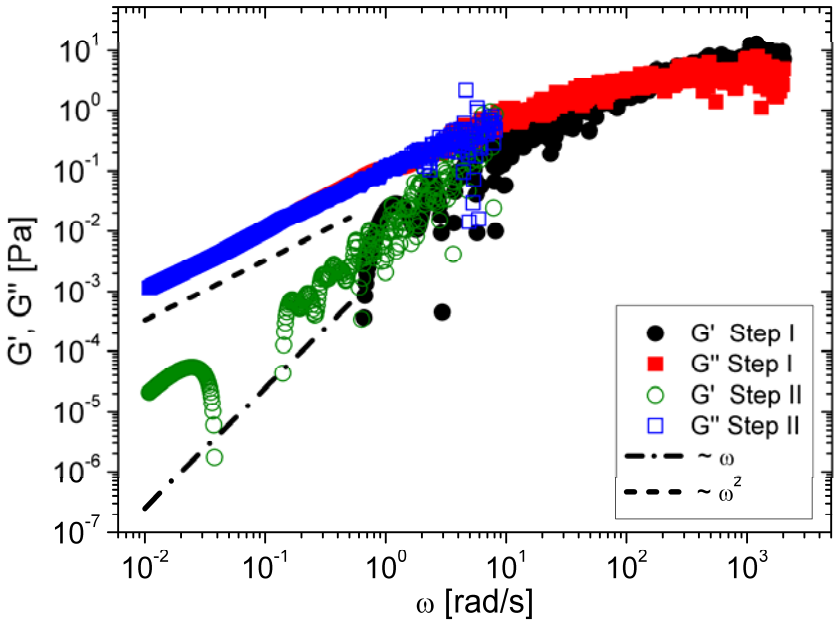

Figure 4.6: *Storage (circles) and loss (squares) moduli* vs. *frequency of a solution of 1% w/w of PAM in water measured by means of both Equation 4.6 (solid symbols at high frequencies) and Equation 4.11 (open symbols at low frequencies) applied directly to the experimental data presented in Figures. 4.4 and 4.5, respectively. The dotted lines are guides to the gradients.*

It is evident that, although there is some noise in the frequency domain that has propagated from genuine experimental noise in the time-domain data, there is a clear overlapping region of agreement between the two methods that makes the whole procedure 'self-consistent'. Moreover, it confirms the ease with which the low-frequency material response can be explored, right down to the terminal region (where $G' \propto \omega^2$ and $G'' \propto \omega$), which is the current limitation for microrheological measurements performed not only with stationary optical tweezers (as shown here by the high-frequency response in Figure 4.6, limited to frequencies above 10^0 s^{-1}), but also with PVPT and diffusing wave spectroscopy [6]. In particular, in PVPT microrheological measurements, the lowest accessible frequency is inversely proportional to both the fluid viscosity and the bead size; it is given by the inverse of the longest time for which the probe particle stays in focus (*i.e.* within the objective depth of field) during the experiment. For example, in water at 25°C a micron-sized bead, observed through a 100x objective with a depth of field of order 200nm, would remain in focus for a time of order 0.1s.

The experimental method presented here, on the other hand, has no fundamental restriction on the lowest achievable frequency. Indeed, with a suitable choice of the velocity of the applied fluid flow field (*e.g.*, $\left|\vec{V}_s\right| = 3\,\mu m/s$) and the sample holder geometry (*e.g.*, a 3-cm-long microfluidic channel), an experiment could be made to run for hours, thereby probing frequencies of order 10^{-4} s^{-1} or lower, without limit. Finally, in order to remove the genuine noise, a simple smoothing operation of the original data is sufficient and the results are shown in Figure 4.7.

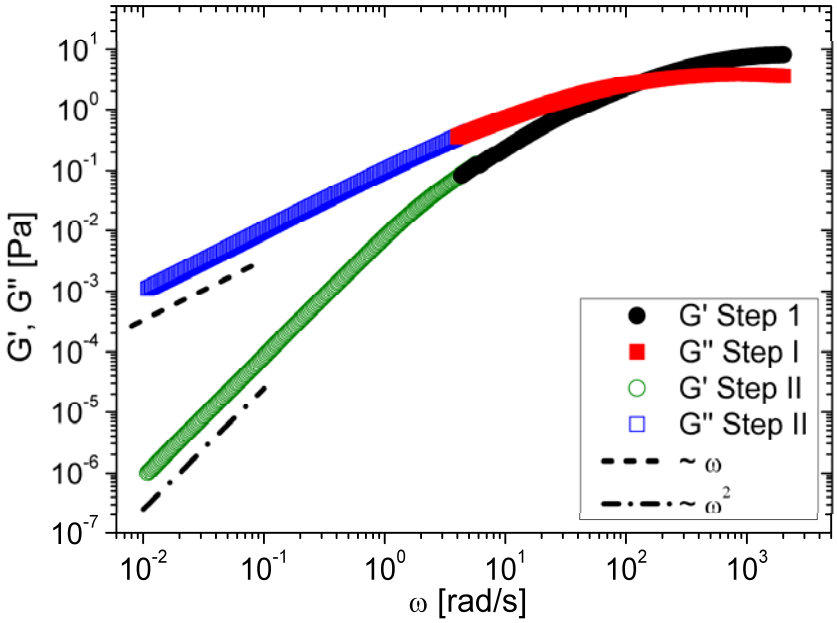

Figure 4.7: *Storage (circles) and loss (squares) moduli* vs. *frequency of a solution of 1% w/w of PAM in water measured by means of both Equation 4.4 (solid symbols at high frequencies) and Equation 4.9 (open symbols at low frequencies) applied directly to the experimental data presented in Figs. 4.4 and 4.5 but smoothed. The dotted lines are guides to the gradients.*

In summary, we have presented a 'self-consistent', 'self-calibrating' and simple experimental procedure, coupled with an analytical data analysis method, for determining the broadband viscoelastic properties of complex fluids with optical tweezers. This method extends the range of the frequency response achieved by conventional optical tweezers measurements down to the material's terminal region. In fact, the method has no lower limit on the accessible frequency, thus allowing microrheological measurements to be performed on complex fluids with very long relaxation times, such as those exhibiting soft glassy rheology [162], or composed of very high molecular weight polymers. Thus, the accessible frequency spectrum for small samples of complex fluids is now limited only by the patience of the observer.

4.3 Wideband microrheology with optical tweezers: 'Two trap' method

4.3.1 Analytical Method

The second method we present is an improved, efficient, self-consistent procedure for measuring the linear viscoelastic properties of materials, from non-oscillatory measurements, across the widest frequency range achievable with optical tweezers. Once again, in this case the experimental procedure consists of two steps: (I) measuring the thermal fluctuations of a trapped bead for a sufficiently long time; (II) measuring the transient displacement of a bead flipping between two optical traps (spaced at fixed distance D_0) that alternately switch on/off at a sufficiently low frequency (Figure 4.8). The analysis of Step I provides: (a) the trap stiffness ($\kappa_i, i = 1,2$) - note that, as for the fluid flow method, this has the added advantage of making the method self-calibrated - and (b) the high-frequency viscoelastic properties of the material, to a high accuracy. Step II has the potential to provide information about the material's viscoelastic properties over a very wide frequency range, which is only limited (at the top end) by the acquisition rate of the bead position ($\sim kH$) and (at the bottom end) by the duration of the experiment. However, because of the finite time required by the equipment to switch on/off (i.e. tens of milliseconds), the material's high-frequency response cannot be fully determined by this step. The full viscoelastic spectrum is thus resolved by combining the results obtained from steps I and II.

This method has various advantages over the flow field technique, namely it (a) is simpler to perform and (b) creates better statistics through flipping the traps multiple times, as described hereafter.

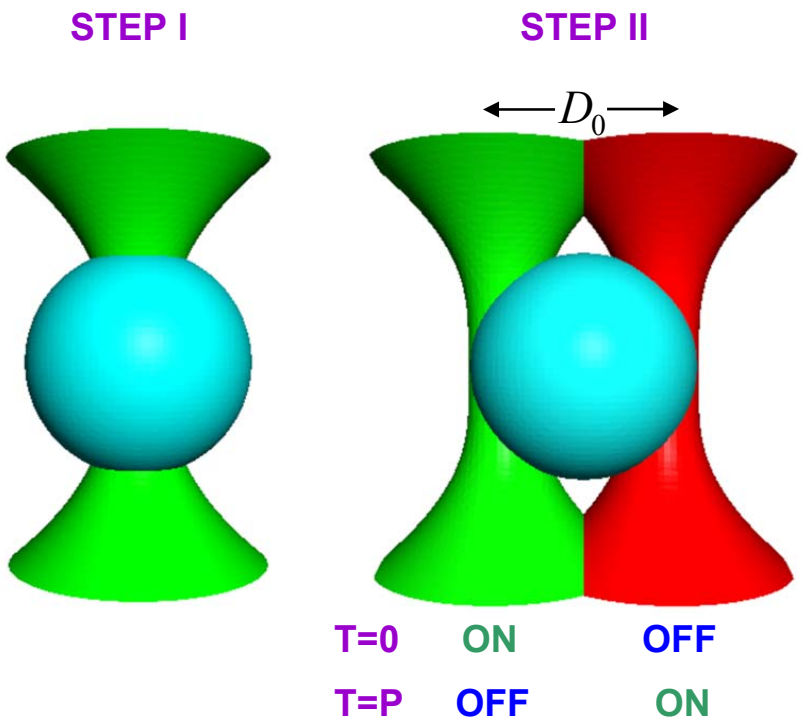

Figure 4.8: *Diagram of experimental procedure: Step I measures the bead trajectory in a static optical trap. Step II measures transient displacement of a bead flipping between two optical traps (spaced at fixed distance D_0) that alternately switch on/off.*

To understand the basis of the procedure, we consider the time-dependent position $\vec{r}(t)$ of a bead trapped by a stationary harmonic potential of force constant κ_i. Throughout the Step I of the procedure, the bead is always found close to the centre of the single trap which is switched on; it makes only small deviations $\vec{r}(t)$ (of a magnitude set by the thermal energy) away from the centre of the trap. During Step II of the procedure, the detours are considerably larger, of a magnitude set by the separation D_0 of the traps. $t_{||}$ is defined as the time at which Step II commences, *i.e.* the time at which the traps are first switched. Subsequently each trap remains on for a duration P before it is switched off and the other trap is switched on. Hence, the total period of the repeated sequence is therefore $2P$. At the instant immediately after the traps are switched ($t = t_{II} + nP, n = 0,1...N$) the bead is typically positioned at a distance $|\vec{r}(t)| \approx D_0$ from the centre of the currently active trap (i.e. close to the centre of the trap that has just been switched off). The coordinates are redefined so that the displacement of the bead, $\vec{r}(t)$, is always measured with respect to the centre of whichever trap is switched on.

The bead's position in three dimensions can be modelled by a generalised Langevin equation:

$$m\vec{a}(t) = \vec{f}_R(t) - \int_{t_0}^{t} \zeta(t-\tau)\vec{v}(\tau)d\tau - \kappa_i \vec{r}(t) \qquad (4.12)$$

where m is the mass of the particle, $\vec{a}(t)$ is its acceleration, $\vec{v}(t)$ is its velocity and $\vec{f}_R(t)$ is the usual Gaussian white noise term, modelling stochastic thermal forces acting on the particle. The integral, which incorporates a generalised time-dependent memory function $\zeta(t)$, represents viscoelastic drag from the fluid.

Note that the present method does not require the two traps to be equal. They can be independently, but not simultaneously, calibrated during step (I) by appealing to the principle of equipartition of energy, as described in the flow field method. Despite the variety of established methods for determining the stiffness of an optical trap (*e.g.* using the power spectrum or the drag force [34, 152]), the equipartition method is the only one independent of the viscoelastic properties of the material under investigation and is thus essential to the calibration of a rheological measurement.

Now, Equation 4.10 will be examined to see how it evolves in the two Steps, I and II. Step I is based on the statistical analysis of the thermal fluctuations of a trapped bead, as described in Chapter 4.1; however, here we present a alternative, yet equivalent, method of analysis.

During Step I, the thermal fluctuations of the trapped bead are investigated to determine the high-frequency viscoelastic properties of the material through analysis of the time dependence of the normalized position autocorrelation function A(τ) (NPAF):

$$A(\tau) = \frac{\left\langle \vec{r}(t_0)\vec{r}(t_0+\tau)\right\rangle_{t_0}}{\left\langle r(t_0)^2\right\rangle_{t_0}} \tag{4.13}$$

which, by time-translation invariance, is a function only of the time interval τ . Here, $\left\langle r(t_0)^2\right\rangle_{t_0}$ is the time-independent variance and the brackets $\left\langle ....\right\rangle_{t_0}$ denote an average over all initial times t_0. If we take the Laplace transfer of Equation 4.11, it gives:

$$m[s^2\tilde{r}(s) - s\tilde{r}(0) - v(0)] = \tilde{f}_R(s) - \tilde{\zeta}(s)[s\tilde{r}(s) - r(o)] - \kappa\tilde{r}(s) \tag{4.14}$$

Then, by multiplying both the sides of Equation 4.12 by $\vec{r}(t_0)$ and averaging over t_0, one obtains:

$$\tilde{A}(s) = \left(s + \frac{\kappa_i}{ms + \tilde{\zeta}(s)}\right)^{-1} \tag{4.15}$$

where $\tilde{A}(s)$ is the Laplace transform of $A(\tau)$, s is the Laplace frequency and it has been assumed that both the quantities $\left\langle \vec{r}(t_0)\vec{v}(t_0)\right\rangle_{t_0}$ and $\left\langle \vec{r}(t_0)\vec{f}_R(t_0+\tau)\right\rangle_{t_0}$ vanish for all τ .

We note that, for $ms << \tilde{\zeta}(s)$ (which is a good approximation up to MHz frequencies for micron-sized beads with a density of the order 1 g/cm^{3}in aqueous suspension) and for a Newtonian fluid (*i.e.* a liquid with time-independent viscosity η ,for which $\zeta = 6\pi a\eta$), Equation 4.12 recovers the well-known result for a massless particle harmonically trapped in a Newtonian fluid:

$$A(\tau) \to \exp(-\Gamma_i \tau) \tag{4.16}$$

where $\Gamma = \kappa_i / 6\pi a\eta$ is the characteristic relaxation rate of the system (*i.e.* optical tweezers, bead and fluid) and can be used to determine η once both κ_i and a are known.

In the general case of non-Newtonian fluids (*i.e.* materials with time-dependent viscosity $\eta(t)$) we adopt the relationship, first introduced by Mason and Weitz [4], between the bulk Laplace frequency-dependent viscosity of the fluid $\tilde{\eta}(s)$ and the microscopic memory function $\tilde{\zeta}(s) = 6\pi a\tilde{\eta}(s)$; so Equation 4.15 can be written as:

$$\tilde{\eta}(s) = \frac{\kappa}{6\pi a}\left[\frac{\tilde{A}(s)}{\left(1 - s\tilde{A}(s)\right)} - \frac{ms}{\kappa_i}\right] \tag{4.17}$$

Moreover, given that $G^*(\omega) \equiv s\tilde{\eta}(s)\big|_{s=i\omega}$, the complex viscoelastic modulus, $G^*(\omega)$, can be expressed directly in terms of the time-dependent NPAF:

$$G^*(\omega) = \frac{\kappa}{6\pi a}\left[\frac{i\omega\hat{A}(\omega)}{\left(1 - i\omega\hat{A}(\omega)\right)} + \frac{m\omega^2}{\kappa}\right] \tag{4.18}$$

where $\hat{A}(\omega)$ is the Fourier transform of $A(\tau)$ and, as mentioned before, the inertia term ($m\omega^2$) can be neglected for frequencies $\omega << MHz$.

It is interesting to highlight that Equation 4.18 is equivalent to Equation 4.6. Indeed, $A(\tau)$ is directly related to the quantity that we have defined as the normalised mean-square displacement (*i.e.* $\Pi(\tau) = \left\langle \Delta r^2(\tau) \right\rangle / 2\left\langle r^2 \right\rangle$) *via*:

$$\begin{aligned} \Pi(\tau) \equiv \frac{\left\langle \Delta r^2(\tau) \right\rangle}{2\left\langle r^2 \right\rangle} &= \frac{\left\langle r^2(\tau) \right\rangle + \left\langle r^2(t_0) \right\rangle - 2\left\langle \vec{r}(t_0)\vec{r}(\tau) \right\rangle}{2\left\langle r^2 \right\rangle} \\ &= 1 - A(\tau) \end{aligned} \tag{4.19}$$

By performing the Fourier transform of Equation 4.19 one obtains the relation:

$$\Pi(\tau) = \frac{1}{i\omega} - \hat{A}(\omega) \tag{4.20}$$

Note that the quantity $A(\tau)$ has the added advantage of having a well-controlled Fourier transform unlike the $MSD(\tau)$ as discussed hereafter.

The second step of the procedure consists of analysing the bead's transient displacements as it moves between two traps with separation D_0, that swap on and off at time $t = t_0 + nP$. Note that the duration of P must exceed all of the material's characteristic relaxation times. We can define the normalised mean position of the particle as:

$$D(t) = \frac{\left|\langle \vec{r}(t) \rangle\right|}{D_0} \tag{4.21}$$

where $\langle ... \rangle$ denotes the average over several independent measurements, but not over absolute time, since time translation invariance is broken by periodic switching. In this case, Equation 4.12 yields, in Laplace form, an identical expression to Equation 4.15, with $\tilde{A}(s)$ replaced by $\tilde{D}(s)$. Thus, as before, the complex modulus can therefore be expressed in terms of bead position:

$$G^*(\omega) = \frac{1}{12\pi a} \sum_{i=1,2} \left[\frac{\kappa_i i\omega \hat{D}(\omega)}{\left(1 - i\omega \hat{D}(\omega)\right)} + m\omega^2 \right] \tag{4.22}$$

where $\hat{D}(\omega)$ is the Fourier transform of $D(t)$, and the sum takes into account the linearity of the measurements performed with both traps. Note that $A(\tau)$ and $D(t)$ are expected to have the limits $A(0) = D(0) = 1$, $A(\infty) = D(\infty) = 0$, and $\dot{A}(\infty) = \dot{D}(\infty) = 0$. This turns out to be very useful when applying the Fourier transform during data processing.

In principle, Equations 4.18 and 4.22 are two simple expressions relating a materials complex modulus $G^*(\omega)$ to the observed time dependent bead trajectory $\vec{r}(t)$ via the Fourier transform of either $\vec{r}(t)$ itself (as in Equation 4.22) or the related NPAF (as in Equation 4.18). In practice, the evaluation of these Fourier transforms, given only a finite set of data points over a finite time domain, is non trivial since interpolation and extrapolation from these data can yield serious artefacts if handled carelessly. We deal with this in the same manner as the fluid flow method, by applying the equation derived by Ref. [161]. In this method, $\hat{g}(\omega)$ is replaced with $\hat{A}(\omega)$ or $\hat{D}(\omega)$ respectively. It is a strength of our new procedure that the extrapolated quantities $\dot{g}_\infty$ and $g(0^+)$ (which assumed the role of fitting parameters in Ref. [161]) in this case assume known values ($\dot{g}_\infty = 0$ and $g(0^+) = 1$) given by the limits of the functions $A(\tau)$ and $D(t)$. Like the

method presented in [161], the present procedure also has the advantage of removing the need for Laplace/inverse Laplace transform of experimental data [11].

4.3.2 Results and Discussion

We have validated the experimental procedure as described by Equations 4.16 and 4.20, *via* Equation 4.11, by measuring both the viscosity of water and the viscoelastic properties of water-based solutions of polyacrylamide (MW = 5-6×10^6 Da) using optical tweezers as described in Chapter 3. The normalized position autocorrelation functions, $A(\tau)$, measured from the stochastic fluctuations of beads optically trapped in two different fluids are shown in Figure 4.9, together with the function predicted for a simple Newtonian fluid. In the Newtonian case, it is expected that $A(\tau)$ decays as a single exponential with a characteristic relaxation rate related to the trap strength, bead size and fluid viscosity, *i.e.* Equation 4.16. The agreement between the data and prediction for water is good.

On the other hand, in the case of a non-Newtonian fluid, where the viscosity is time-dependent, it is not guaranteed that Equation 4.15 could be resolved (*i.e.* inverse-Laplace transformed) into a simple form like Equation 4.16. However, this is no hindrance since the viscoelastic moduli will be found via the analysis of the normalized position autocorrelation function.

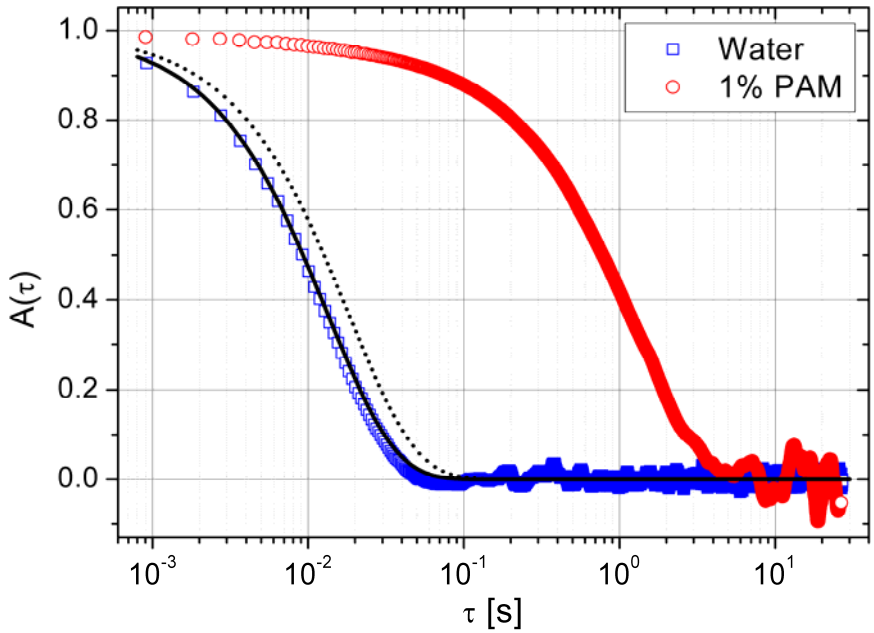

Figure 4.9: *The normalised position autocorrelation function vs. lag-time of a 5μm diameter bead (squares) in water (with $\kappa = 2.7\,\mu N/m$) and (circles) in a water-based solution of PAM at concentrations of 1 % w/w (with $\kappa = 2.2\,\mu N/m$). The continuous and dotted lines represent Equation 4.16 for a 5μm diameter bead in water at T = 25°C with $\kappa = 2.7\,\mu N/m$ and $\kappa = 2.2\,\mu N/m$, respectively.*

In Figure 4.10 we compare the impulse response (*i.e.* step (II) of the procedure) of a 5μm diameter bead suspended in water and in an aqueous solution of PAM at 1% w/w (a non-Newtonian fluid), with a duration between flips of $P = 20s$ and a trap centre-to-centre separation of $D_0 = 1.6\mu m$, giving $D_0 / a = 0.64$. In order to guarantee the linearity of the confining forces exerted by the two optical traps, the distance between them was always chosen to be no more than 80% of the bead radius, $D_0 \leq 0.8a$ [163]. Although Brownian statistical fluctuations appear in the figure, the difference between the viscoelastic natures of the two fluids is clear. Indeed, while a bead suspended in water flips from one trap to the other almost instantaneously, the same bead in the PAM solution takes much longer (a few seconds) to flip.

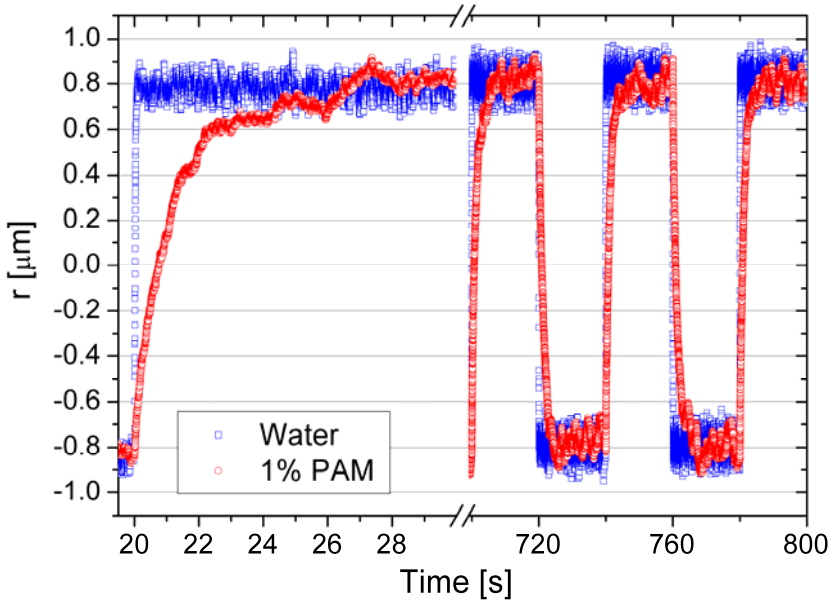

Figure 4.10: *The trajectory of a 5μm diameter bead flipping between two optical traps* κ_1 *(bottom) and* κ_2 *(top) repeatedly switching after a duration P = 20 s. The bead is suspended in (squares) water (with* $\kappa_1 = 2.7\mu N/m$ *and* $\kappa_2 = 2.5\mu N/m$*) and (circles) a water-based solution of PAM at concentrations of 1 % w/w (with* $\kappa_1 = 2.1\mu N/m$ *and* $\kappa_2 = 2.2\mu N/m$*).*

In order both to evaluate $D(t) = \left|\langle r(t)\rangle\right| / D_0$ (t) and to reduce noise caused by Brownian fluctuations, the transient measurements were averaged over twenty flips, with the resulting curves shown in Figure 4.11. Experimentally, the switching process of the two traps is controlled by means of a spatial light modulator (SLM) which alternately creates an optical trap in one of two positions. It is important at this point to note that there is a short but finite time for which both traps exist simultaneously [164], due to the finite time required by the SLM's display to update the holographic pattern. This makes the switching process not exactly binary. However, this will of course only affect the high-frequency results obtained during this step, which will ultimately be neglected in favour of the high-frequency response from Step (I).

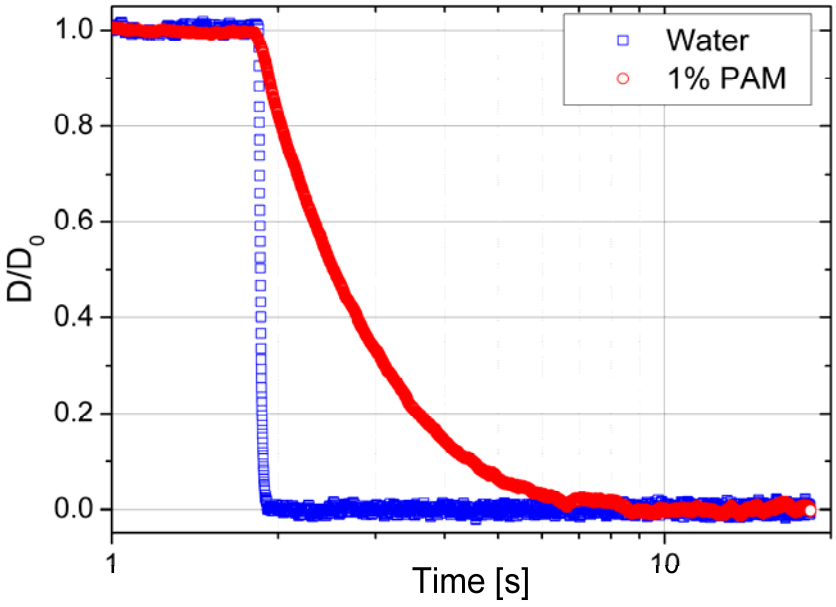

Figure 4.11: *The normalised mean position of all step-down data shown in Figure 4.10,* i.e. *when simultaneously trap 2 (top) switches off and trap 1 (bottom) switches on.*

Wideband microrheological measurement are obtained from the optical tweezers by combining the frequency responses obtained from both steps (I) and (II) of the procedure. In particular, the material's high-frequency response is determined by applying Equation 4.18 (*via* Equation 4.11 with A_k replacing g_k) to the $A(\tau)$ measurements (in which low-frequency information tends to be very noisy); whereas, the low-frequency response is resolved by applying Equation 4.22 (*via* Equation 4.11 with D_k replacing g_k) to the data describing the bead's transient response to the flipping traps (in which the high-frequency response is limited by the performance of the SLM).

Typical results for both Newtonian (water) and non-Newtonian (PAM) fluids are shown in Figures 4.12 and 4.13, respectively. As expected, the Newtonian example exhibits no elastic modulus other than what exists from the 'fingerprint' of the optical trap (which is a result both of the low number of flips that take place and of the non-perfect measurements – unless 1000s of flips are averaged this fingerprint will remain in evidence). In both the cases, it is evident that, although there is some noise in the frequency domain which comes from genuine experimental noise in the time-domain data, there is a clear overlapping region of agreement between the two methods which makes the whole procedure self-consistent. Moreover, it confirms the ease with which the low-frequency material response can be explored right down to the terminal region (where $G' \propto \omega^2$ and $G'' \propto \omega$). This is the current limitation for microrheological measurements.

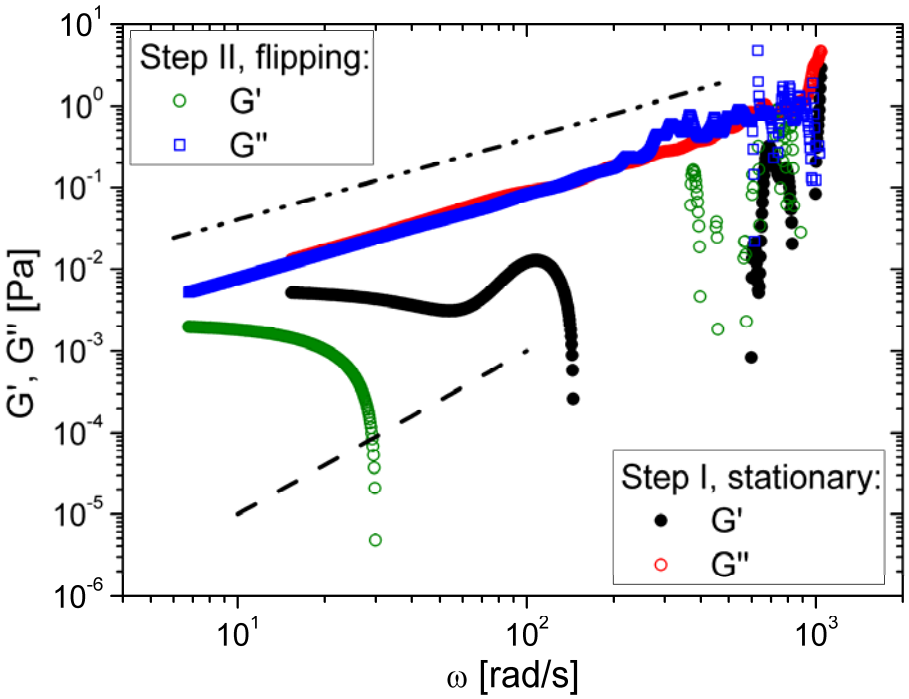

Figure 4.12: *Storage (G') and loss (G'') moduli of water vs. frequency, analysed using both Equation 4.18 (high frequencies) and Equation 4.22 (low frequencies) applied directly to the experimental data presented in Figure 4.9 and Figure 4.11, respectively. The lines represent the expected limiting behaviour of the moduli when the material reaches the terminal region:* $G'' \propto \omega$ *for a Newtonian fluid, and* $G' \propto \omega^2$ *and* $G'' \propto \omega$ *for a viscoelastic fluid.*

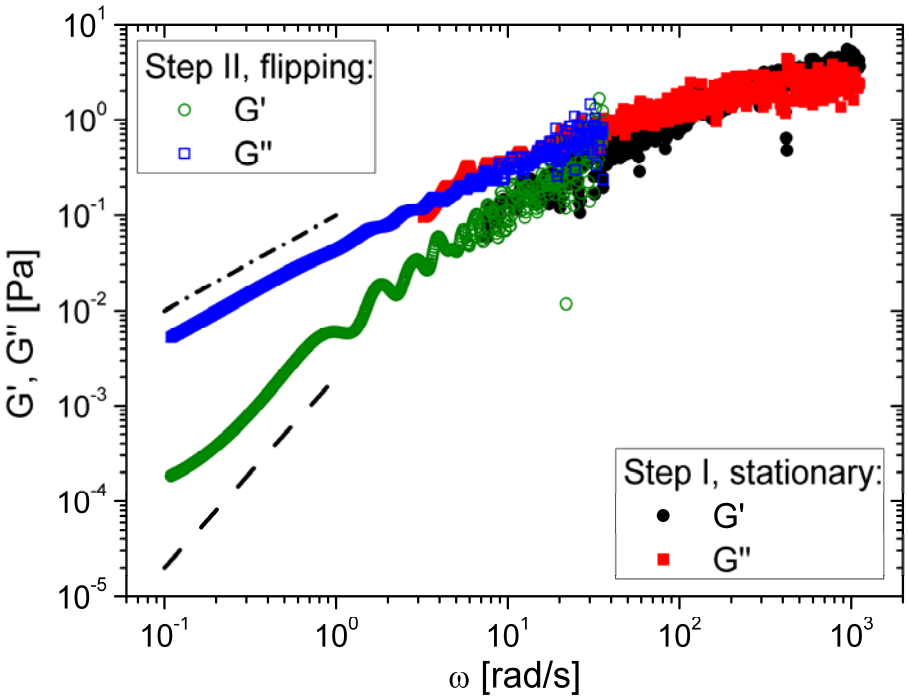

Figure 4.13: *Storage (G') and loss (G'') moduli vs. frequency of a solution of 1% w/w of PAM in water measured by means of both Equation 4.18 (high frequencies) and Equation 4.22 (low frequencies) applied directly to the experimental data presented in Figure 4.9 and Figure 4.11 respectively. The lines represents the expected limiting behaviour of the moduli when the material reaches the terminal region:* $G' \propto \omega^2$ *and* $G'' \propto \omega$.

In summary, we have presented another 'self-consistent', 'self-calibrating' and simple experimental procedure, coupled with a data analysis method, for determining the wide-band viscoelastic properties of complex fluids using optical tweezers. This method extends the range of the frequencies previously available to optical tweezers measurements. In fact, the accessible frequency range is limited only by the experiment length and by the maximum data acquisition speed (10s of MHz for a quadrant photo-diode). This allows access to the material's terminal region enabling micro-rheological measurements to be performed on complex fluids with very long relaxation times, such as those exhibiting soft glassy rheology [162]. The method provides a simple yet concrete basis on which future viscoelastic measurements may be made on both biological and non-biological systems using optical tweezers.

Chapter 5

CONCENTRATION SCALING LAWS IN POLYMER SOLUTIONS

It is of general interest in rheological studies to apply scaling laws to viscoelastic data in order to extract, for example, information about the concentration regimes into which the viscoelastic sample falls. In conventional rheology, these concentration scaling laws are derived either from the shear viscosity, or from the complex shear modulus, $G^*(\omega)$ in the frequency domain. Indeed, if we consider the model developed by Morse, we see that the any concentration dependences are presented with respect to the frequency-dependent moduli and their respective components (*i.e.* the tension, orientational and curvature stresses). Here, we present a new method of deriving the concentration scaling laws of polymer solutions directly from the time-dependent MSD, avoiding the need to Fourier transform the data.

Aside from biological samples, microrheological techniques have been applied to various systems, such as polymer gels [165], "worm-like" micelle gels and solutions [166] and associating polymer solutions [167]. These previous investigations indicate that a detailed study of the Brownian motion of spherical probes in simple flexible polymer solutions would provide an excellent method by which to interpret the Brownian motion in the more structurally complex systems - especially an investigation of the effect of polymer concentration on the observed Brownian motion [168]. Although some flexible polymer solutions have been investigated in limited detail previously, these earlier studies have not considered a wide range of polymer concentrations and have essentially been used to demonstrate the microrheological approach, specifically the agreement between the viscoelastic properties determined from microrheology and bulk rheometry [11, 13, 169]. Here, we present a detailed investigation of the Brownian motion of colloidal spheres in both water and aqueous polyacrylamide (PAM) as model Newtonian and non-Newtonian systems, respectively.

It is well established that the viscosity of a polymer solution depends on concentration and size (*i.e.* molecular weight) of the dissolved polymer, and here we will briefly discuss how this is of interest to this thesis. When a substance is added to a solvent, the viscosity of the solution will increase, the magnitude of which depends upon the size, shape and concentration of the solute. If we consider flexible polymers, then at low concentrations and in good solvents (*i.e.* where the polymer chain is more expanded) the polymers are roughly spherical. To good approximation, we can treat them as spheres, with an associated hydrodynamic radius. As the size or length (*i.e.* molecular weight) of the polymer increases, then the larger the sphere becomes. Indeed, statistical analyses have established a well defined relationship between the molecular weight of a molecule and its hydrodynamic radius [170].

One of the first studies on how the viscosity of a continuous phase solution changes with respect to the addition of non-interacting rigid spherical particles was conducted by Einstein [171]. Diluted suspensions of identical spherical particles show a Newtonian behaviour, and the distances between the particles are large enough that the thermal fluctuations of the particles predominate over the effect of inter-particle interactions for colloidal suspensions. Einstein derived an equation for the viscosity of highly diluted suspensions obtained in pure shear flow. He expanded the ratio of the solution viscosity to that of the solvent as a function of the volume fraction:

$$\frac{\eta}{\eta_s} = 1 + k_1\varphi + k_2\varphi^2 + O(\varphi^2) + \ldots \tag{5.1}$$

where η is the viscosity of the solution, η_s is the viscosity of the solvent, φ is the volume fraction and k_1 and k_2 are constants that are related to the particle in solution (k_1) and the interaction between particles (k_2). Einstein was the first to calculate that in solutions of rigid spheres $k_1 = 2.5$, thus k_1 is termed the Einstein viscosity coefficient. The order of approximation is denoted by the symbol $O(..)$.

The most common functions that are adopted to describe the contribution of the solute to viscosity of the system are shown in Equations 5.2 to 5.5. There exist several parameters that characterise the relationship between the solution viscosity, η, and the solvent viscosity, η_s. In particular, the:

Relative Viscosity
$$\eta_{rel} = \frac{\eta}{\eta_s} \tag{5.2}$$

Specific Viscosity
$$\eta_{sp} = \frac{\eta - \eta_s}{\eta_s} = \eta_{rel} - 1 \tag{5.3}$$

Reduced Viscosity
$$\eta_{red} = \frac{\eta_{sp}}{c} \tag{5.4}$$

Intrinsic Viscosity

$$[\eta] = \lim_{c \to 0} \frac{\eta_{sp}}{c} \tag{5.5}$$

where c is the concentration of solute.

Relative viscosity, η_{rel}, is the ratio between the viscosity of the solution and that of the solvent. Specific viscosity, η_{sp}, expresses the incremental viscosity due to the presence of the polymer in the solution. Dividing η_{sp} by concentration gives the reduced viscosity, η_{red}, which expresses the capacity of a polymer to cause the solution viscosity to increase; *i.e.* the incremental viscosity per unit concentration of polymer. The extrapolation of the reduced viscosity to zero concentration, gives us intrinsic viscosity, $[\eta]$. The intrinsic viscosity is adopted to measure the polymer's molecular weight *via* the Mark-Houwink equation :

$$[\eta] = KM^{\alpha} \tag{5.6}$$

where M is the molecular weight , and α and K are a fluid-dependent constants.

The intrinsic viscosity is, in fact, a generalisation of the Einstein coefficient for systems of rigid spheres. This, and the fact that rheological studies have related the volume fraction to the hydrodynamic radius, allows us to write Equation 5.1 in terms of the concentration and intrinsic viscosity as:

$$\frac{\eta}{\eta_s} = 1 + [\eta]c + k_H[\eta]^2 c^2 + ... \tag{5.7}$$

where c is the concentration and k_H is the Huggin's coefficient.

5.1 Analytical model and bench tests

The overall aim here is to extract the contribution of the solute (*i.e.* polymer) concentration to the solution viscosity, through the analysis of the time-dependent thermal fluctuations of a trapped bead. Before this can be done, however, it is important to first characterise the contribution made by the 'system', which may arise from the ensemble of the laser (*i.e.* the optical tweezers), the bead radius and the solvent viscosity. This was done by analysing an optically trapped bead in water, which is a Newtonian fluid with constant viscosity of 8.9 x 10^{-4} Pa.s at 25ºC. The Brownian fluctuations of an optically trapped bead give rise to the time-dependent MSD, $\langle \Delta r^2(\tau) \rangle$, shown in Figure 5.1.

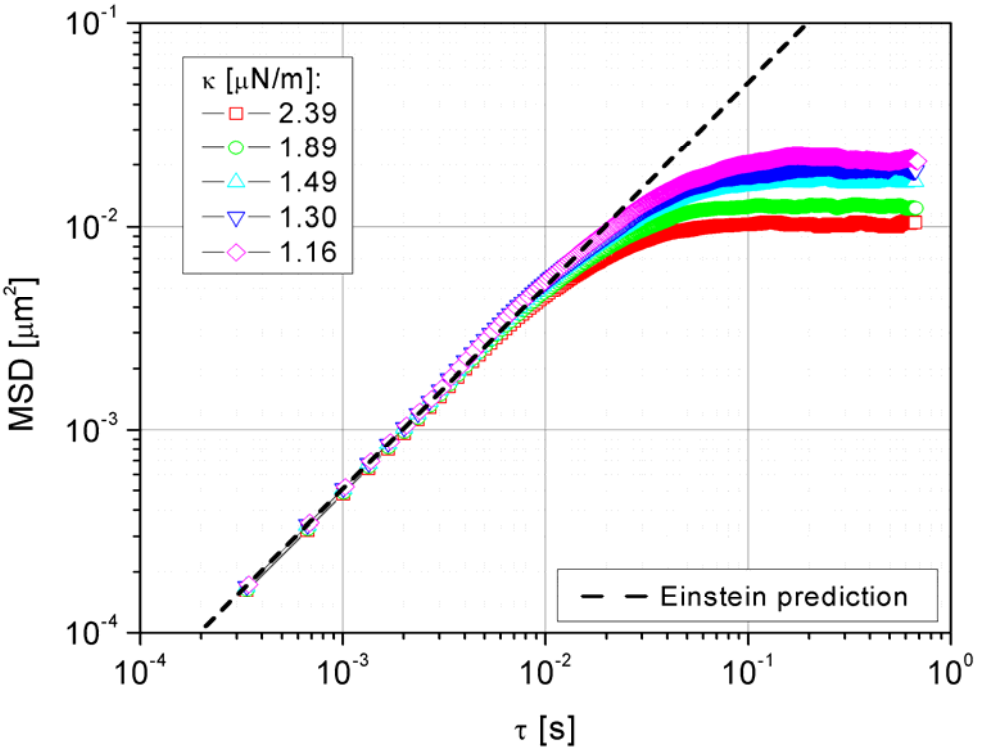

Figure 5.1: *MSD* vs. *lag time of a 5μm diameter bead for different optical trap strengths (κ) in water. The dotted line represents the Einstein prediction of the MSD of a freely diffusing 5μm bead in water at 25°C.*

At short time scales (high frequency) the bead behaves as if it was free to diffuse, as observed in the coincidence between the observed MSD and the Einstein prediction for a freely diffusing bead (from Equations 1.9 and 1.10). This is a result of the harmonic nature of the optical trap. The slope of the plot of the MSD against lag time, at high frequencies, gives the diffusion coefficient, D. At long time scales (low frequency) the MSD plateaus as the bead position becomes constrained by the force of the optical trap. The dependence upon trap power can be seen as a decrease in plateau height as the trapping power (and hence optical trap strength, κ) increases.

In this thesis we show for the first time that the correct asymptotic value (for large lag-times) of the mean-square displacement of a confined bead is equal to $2\langle \vec{r}^{\,2} \rangle$), where $\langle \vec{r}^{\,2} \rangle$ is the variance of the particle trajectory from the trap centre. Although we acknowledge that the limiting value of the MSD has been discussed before by Starrs *et al* [172], we also recognise that they did not obtain the correct constant of proportionality (i.e. the factor 2) between the MSD and the variance.

In order to characterise the plateau value more explicitly, let us once again discuss the normalised mean-square displacement, $\Pi(\tau)$, a dimensionless quantity that we discovered and introduced in Chapter 4. We observed experimentally that the MSD tends to twice the variance, $2\langle \vec{r}^{\,2} \rangle$, at long time intervals.

As proof of concept of the above result, let us consider a series of numbers flipping randomly between 1 and -1 for a sufficiently long period of time. The *mean* value of this series would be zero, and the variance, $\langle \vec{r}^2 \rangle$ (defined as $\sum (r-\mu)^2 / N$, where μ is the mean, and N is the number of measurements) would be equal to $\langle (\pm 1 - 0)^2 \rangle = 1$. The MSD for each point would be either 4 or 0, depending upon the specific event (1→-1, -1→1 or 1→1, -1→-1 respectively). Averaging over a statistically valid set of data would give a value of 2, which is twice the variance.

Thus for long time intervals, and for a confined bead, the following holds true:

$$\Pi(\tau) = \frac{\langle \Delta \vec{r}(\tau)^2 \rangle}{2\langle \vec{r}^2 \rangle} = 1 \quad \forall \tau >> \Gamma \tag{5.8}$$

where Γ is defined as the slowest relaxation rate of the system. In the case of optical tweezers, $\Gamma = \kappa / 6\pi a \eta$, as in Equation 4.16, where κ is the optical trap strength, a is the radius of the bead, and η is the zero-frequency viscosity of the solution. The nMSD is a dimensionless parameter that is neither dependent upon optical trap strength nor bead radius. Thus it provides a direct comparison between different fluids and viscosities. Figure 5.2 shows $\Pi(\tau)$ against lag time for 5μm beads in water.

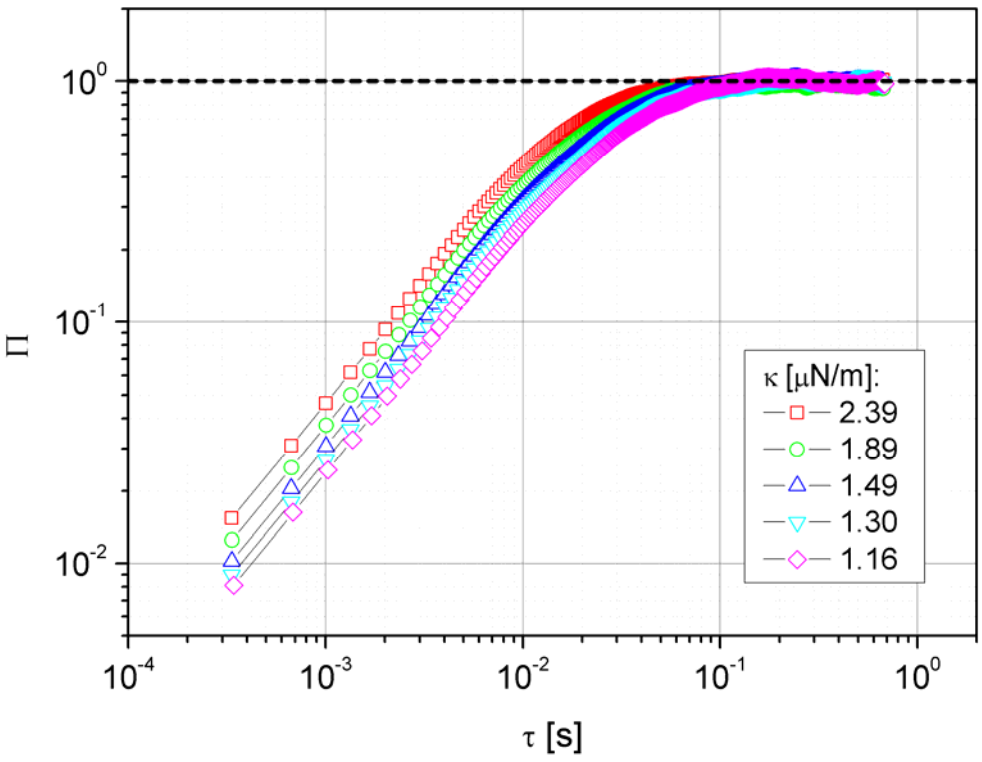

Figure 5.2: $\Pi(\tau)$ vs. *lag time for a 5μm diameter bead at different optical trap strengths (κ) in water. For long timescales* $\Pi(\tau)$ *reaches a constant value of 1.*

Figure 5.2 shows that the thermal fluctuations can be normalised on the vertical axis through use of the normalised MSD. In order to normalise the horizontal axis, we consider the Einstein equation, which defines the MSD of a freely diffusing bead as $\left\langle \Delta r^2(\tau) \right\rangle = 2dD\Delta t$. If both sides are divided by twice the variance, it is simple to show that (using the equipartition of energy theorem):

$$\Pi(\tau) = \frac{\kappa}{6\pi a \eta_s}\tau \tag{5.9}$$

where κ is the optical trap strength, a is the bead radius and η_s is the solvent viscosity.

It is then an easy step to show that the curves of Figure 5.2 can be collapsed onto a common curve when the normalised MSD, $\Pi(\tau)$, is plotted against the normalised lag time of Equation 5.9 (with η_s equal to the viscosity of water at 25ºC). This curve is presented in Figure 5.3.

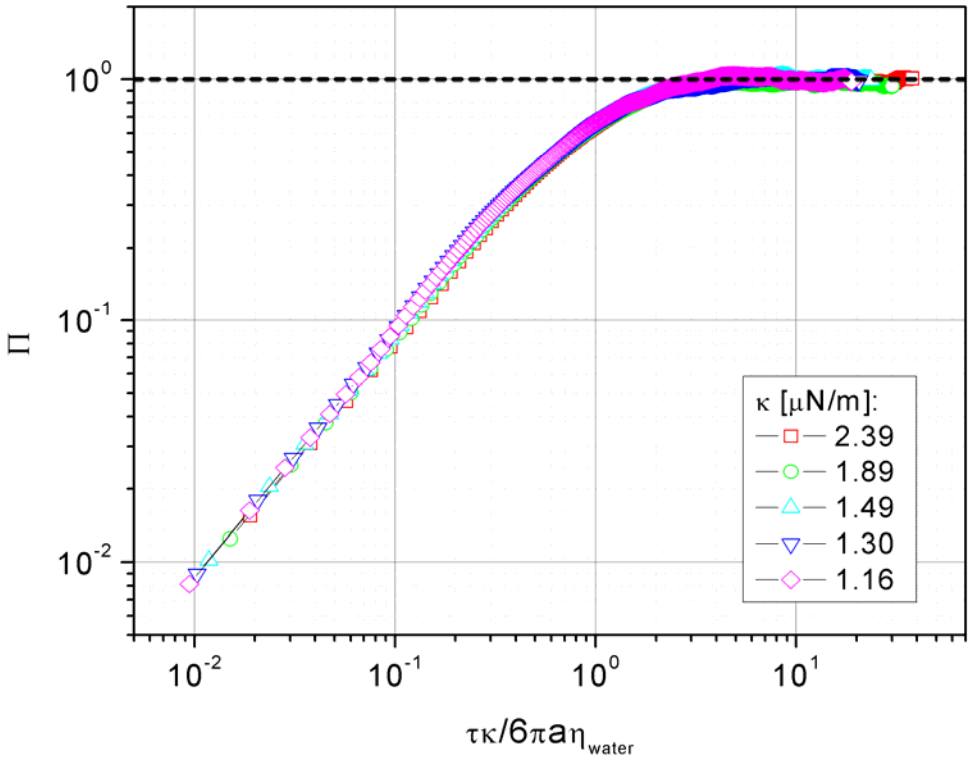

Figure 5.3: $\Pi(\tau)$ vs. *normalised lag time* ($\tau\kappa/6\pi a\eta_s$) *for a 5μm diameter bead at different optical trap strengths (κ) in water. After normalisation the curves collapse onto a master curve.*

The normalised lag time is a dimensionless parameter where $\kappa/6\pi a\eta_s$ represents the characteristic relaxation rate of the system made by the combination of trap strength, bead radius and solvent viscosity. The master curve proves that, given a solution, the contribution to the time behaviour of the MSD by the combination of trap strength, bead radius and solvent viscosity (if constant) can be separated from that provided by the solute itself.

The characteristic relaxation rate $\kappa/6\pi a\eta_s$ defines a cut-off frequency below which no viscoelastic information about the system can be obtained from measurements performed with stationary optical tweezers. If the MSD of an optically trapped bead in a Newtonian fluid is analysed by adopting the analytical model described by Mason & Weitz [3] for a freely diffusing bead (*i.e* one that is *not* optically trapped), one would expect that the measured storage modulus arises *only* from the elasticity of the optical trap. This is demonstrated in Figure 5.4, which shows the storage, $G'(\omega)$, and loss, $G''(\omega)$, moduli plotted for a bead optically trapped in water. The loss modulus has a slope of 1, consistent with a Newtonian fluid. The elastic response is a result of the optical trapping force and reiterates the fact that the trap only significantly affects the bead at low frequencies (as discussed in Chapter 4.1, Equation 4.5).

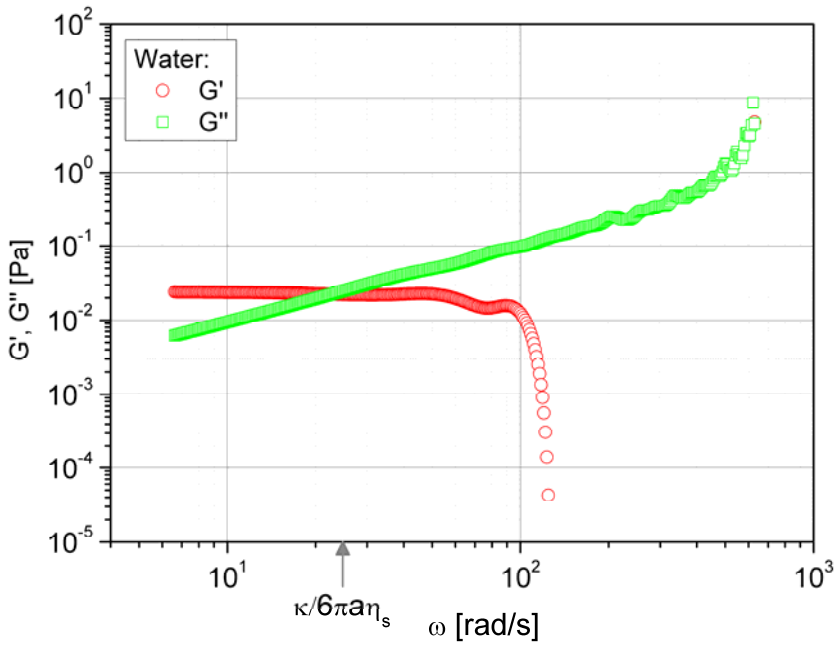

Figure 5.4: *Storage and loss moduli of an optically trapped 5μm bead in water analysed to show the elasticity ($G'(\omega)$) arising from the optical trap. The cut-off frequency $\kappa/6\pi a\eta_s$ defines the lowest frequency at which meaningful information can be extracted about the material properties. It dictates the crossover point at which $G'(\omega)$ and $G''(\omega)$ intersect.*

In rheology, the intersection points of the storage and loss moduli are always indicative of a characteristic relaxation time. For example, in Figure 2.4 (Chapter 2) the low frequency intersect of the moduli defines the reptation time, the slowest relaxation mode of a semiflexible polymer. Here, in Figure 5.4, the intersect point of $G'(\omega)$ and $G''(\omega)$ represents the single relaxation time of the system (the ensemble of laser, bead radius, and fluid viscosity), and is coincident with the value of $\kappa/6\pi a\eta_s$ (~ 26.2 for this particular sample with $\kappa = 1.06\times10^{-6}$ μN/m). The existence of this cut-off frequency can be understood from Figure 5.3, where at the time $\tau = (\kappa/6\pi a\eta_s)^{-1}$ the curves begin to diverge from a slope of 1, as the trapping force begins to dominate over the thermal energy. If

we normalise the $G'(\omega)$ and $G''(\omega)$ of Figure 5.4 by a factor of $\kappa/6\pi a$ and the frequency by a factor of $\kappa/6\pi a\eta_S$ then we see that the intersect of the moduli occurs at the point [1,1] (Figure 5.5).

For the case of a Newtonian fluid, the viscosity that defines the cut-off frequency must be the constant viscosity of the fluid. For a non-Newtonian fluid however, we can generically define the cut-off frequency as:

$$\omega_{coff} = \frac{\kappa}{6\pi a\eta_0} \tag{5.10}$$

where η_0 is the zero-shear viscosity of the fluid.

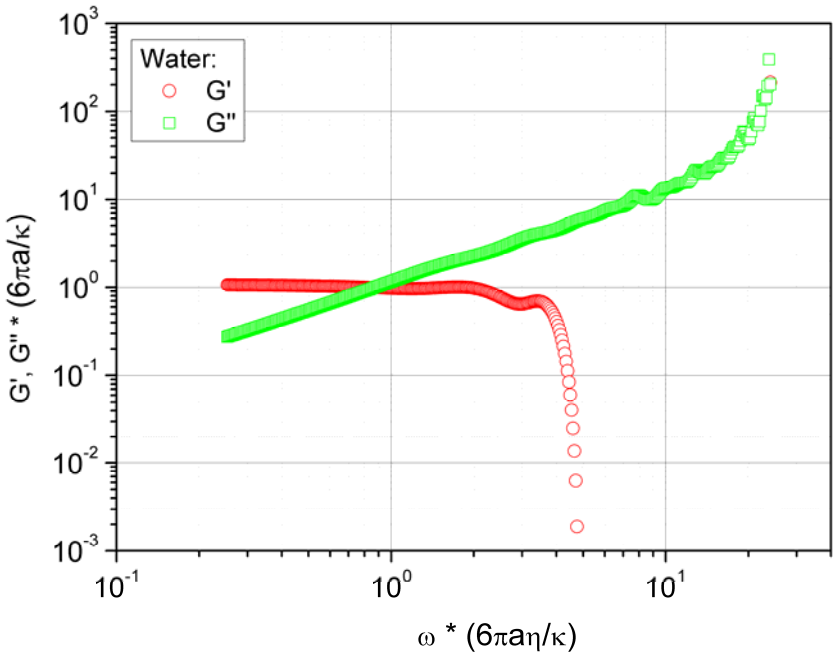

Figure 5.5: *Normalised storage and loss moduli of an optically trapped 5μm bead in water analysed to show the elasticity arising from the optical trap. The data is seen to be normalised (*i.e. *the intersect occurs at [1,1]) by applying a factor of* $6\pi a\eta_s/\kappa$ *to the frequency and a factor of* $6\pi a/\kappa$ *to the moduli.*

We have defined the contribution to the thermal fluctuations of a trapped bead that arise from the 'system' (*i.e.* laser, bead radius and solvent viscosity) itself. Now, let us define the relationship between the normalised MSD, $\Pi(\tau)$, and the viscosity of the solution. We have shown that both $\Pi(\tau)$ and the normalised position autocorrelation function, $A(\tau)$, can be arbitrarily adopted to describe the linear viscoelastic properties (*i.e.* $G^*(\omega)$) of a material by means of their Fourier transform (in Equations 4.6 and 4.18). At high frequencies Equation 4.18 recovers the generalised Stokes-Einstein equation (Equation 1.15) derived by Mason & Weitz for a freely diffusing particle [4]:

$$G^*(\omega) = \frac{k_B T}{\pi a\, i\omega \left\langle \Delta\hat{r}^2(\omega) \right\rangle} \left[* \frac{2\left\langle r^2 \right\rangle}{2\left\langle r^2 \right\rangle} \right] \equiv \frac{\kappa}{6\pi a} \frac{1}{i\omega \hat{\Pi}(\omega)} \tag{5.11}$$

Equation 1.15 Equation 4.18

where $\left\langle \Delta\hat{r}^2(\omega) \right\rangle$ is the Fourier transform of the mean-square displacement. The κ term in Equation 5.11 arises from the Equipartition of Energy theorem. It follows from the above relation that:

$$\hat{\eta}(\omega) = \frac{\kappa}{6\pi a} \frac{1}{\hat{\Pi}(\omega)} \frac{1}{(i\omega)^2} \tag{5.12}$$

where $\hat{\eta}(\omega)$ is the Fourier transform of $\eta(t)$.

As mentioned in the Introduction to this Chapter, a classical rheological parameter adopted to quantify the contribution to the solvent viscosity due to the addition of the solute itself, is the viscosity ratio, or relative viscosity, which is defined as the ratio between the solution viscosity, $\eta(t)$, and the solvent viscosity, $\eta_s(t)$. From this definition, and from Equation 5.12, it follows that:

$$\hat{\eta}_{rel}(\omega) = \frac{\hat{\eta}(\omega)}{\hat{\eta}_s(\omega)} = \frac{\hat{\Pi}_s(\omega)}{\hat{\Pi}(\omega)} \tag{5.13}$$

where $\hat{\eta}_{rel}(\omega)$ is the relative viscosity in the Fourier domain, $\hat{\eta}_s(\omega)$ is the Fourier transform of the solvent viscosity $\eta_s(t)$, and $\hat{\Pi}_s(\omega)$ is the Fourier transform of $\Pi_s(t)$, which is the normalised MSD experienced by the bead suspended into the solvent. Moreover, in Equation 5.13 it has been assumed that both the measurements of the normalised MSDs had the same constant of proportionality, $\kappa/6\pi a$.

Note that, although the non-trivial issue of evaluating the Fourier transform of a generic function given only a finite set of data points over a finite time domain, has been recently solved by Evans *et al.*[23] (as discussed in Chapter 4), we demonstrate that, in order to measure the concentration scaling laws, there is actually no need to evaluate the Fourier transforms in Equations 5.12 and 5.13, because we will show that Equation 5.13 holds also in the time-domain.

To do this, it is useful to remember a fundamental relationship between the shear modulus, $G(t)$, and the shear creep compliance, $J(t)$ [173]:

$$\int_0^t G(\tau)J(t-\tau)d\tau = t \tag{5.14}$$

which is the convolution integral between the above two time-dependent functions. An important property of the convolution integral between two functions is that its Fourier transform is equal to the product of the two Fourier transformed functions. This applies to Equation 5.14 and gives:

$$\hat{G}(\omega)\hat{J}(\omega) = \frac{1}{(i\omega)^2} \tag{5.15}$$

where $\hat{G}(\omega)$ and $\hat{J}(\omega)$ are the Fourier transforms of $G(t)$ and $J(t)$ respectively.

Let us now consider the definition of the complex modulus $G^*(\omega)$, which is given by the Fourier transform $(F[...])$ of the time derivative of the shear modulus $G(t)$:

$$G^*(\omega) = F\left[\frac{dG(t)}{dt}\right] = i\omega\hat{G}(\omega) \tag{5.16}$$

Thus, combining Equation 5.15 with Equation 5.16 it becomes clear how the complex modulus is related to the Fourier transform of the time-dependent creep compliance:

$$G^*(\omega) = \frac{1}{i\omega\hat{J}(\omega)} \tag{5.17}$$

Furthermore, since the material's linear viscoelastic properties are independent from the type of linear measurement performed to evaluate them, the combination of Equation 5.11 with Equation 5.17 provides, at high frequencies, the relationship between the Fourier-transformed compliance and the Fourier-transformed normalised MSD:

$$\hat{J}(\omega) = \frac{6\pi a}{\kappa}\hat{\Pi}(\omega) \tag{5.18}$$

It is important to highlight that, because the Fourier transform is a linear operator, the simple proportionality of Equation 5.13 holds also in the time-domain:

$$J(t) = \frac{6\pi a}{\kappa}\Pi(\tau) \tag{5.19}$$

Note that a similar result to Equation 5.19 was found by Mason *et al.* [173] in the case of a freely diffusing particle. They pointed out that: "the primary advantage of choosing $J(t)$ as the linear viscoelastic representation is that it is directly proportional to the measured MSD" (to the normalised MSD, in this case); "*no transformation to the frequency domain or fitting of the data are needed to properly report the material's linear viscoelastic response*".

In order to evaluate the concentration functionality of the shear modulus (or equivalently of the shear viscosity) it is convenient at this point to express the relationship between the concentration dependencies of both $G(t)$ and $J(t)$. In the general case of polymer solutions, both the above functions depend on the polymer concentration, c, and the time; and they can be expressed as follows:

$$G(t,c) = g(t/t_0(c))G_0(c) \tag{5.20}$$

where $g(t/t_0(c))$ and $G_0(c)$ represent the time and concentration dependent parts of $G(t,c)$ respectively and $t_0(c)$ is a characteristic time, which also depends on the polymer concentration. An identical formula can be written for $J(t,c)$ with g and G_0 being replaced with j and J_0 respectively. It is an easy step to show that by substituting Equation 5.20, written for both $G(t)$ and $J(t)$ into Equation 5.15, one obtains:

$$G_0(c)J_0(c) = \frac{u_0}{\int_0^{u_0} g(u)\,j(u_0 - u)du} \equiv constant \tag{5.21}$$

where $u_0 = t/t_0(c)$ and $u = \tau/t_0(c)$ are two arbitrary times. It can be seen that the left term of Equation 5.21 depends only on the polymer concentration and the central term depends only on time; indeed, once the solution concentration is fixed, both the terms are equal to an arbitrary constant, which we can fix equal to 1 for simplicity.

Finally, combining Equations 5.19 and 5.13, it is an easy step to show that, at high frequencies (or short lag-times), the relative viscosity in the time-domain is given by:

$$\eta_{rel}(t) = \frac{\eta(t)}{\eta_s(t)} \cong \frac{J_s(t)}{J(t)} = \frac{\Pi_s(\tau)}{\Pi(\tau)} \tag{5.22}$$

where the subscript ‘s’ denotes that the functions are related to the solvent. Also in this case, as for Equation 5.13, it has been assumed that the constant of proportionality $\kappa/6\pi a$ for both the solvent and the solution are equal.

Note that, so far, the viscoelastic nature of both the solvent and the solution has not been discussed. Indeed, both Equation 5.13 and Equation 5.22 are of general validity and can be applied to any fluid, whether the solvent is Newtonian or not. In the simplest and most common case of a Newtonian solvent, with time-independent viscosity η_s (as in this chapter; *i.e.* water), Equation 5.22 simply becomes:

$$\eta_{rel}(t) = \frac{\kappa}{6\pi a}\frac{\tau}{\eta_s}\frac{1}{\Pi(\tau)} \tag{5.23}$$

From the basic description of $J(t)$, in the absence of solute (*i.e.* $\eta_{rel}(t) = 1$), Equation 5.23 recovers Equation 5.9.

5.2 Scaling laws in flexible polymers

We have now shown both how to remove the contribution of the system from the analysis of the thermal fluctuations of a trapped bead and how the viscosity of the solution is related to the time-dependent normalised mean-square displacement of the bead. Now, we can develop test ideas to show how the bead fluctuations are related to the concentration of the solution. PAM is a well studied flexible polymer [65-68], and because of this is a useful tool for calibrating rheological measurements. Since we do not yet know the zero shear viscosity of the system, we instead use the viscosity of the solvent, water, to determine the characteristic relaxation time $\tau\kappa/6\pi a\eta_s$. This allows us to separate the viscosity contribution of the solvent from that of the solute at different concentrations.

In Figure 5.6, $\Pi(\tau)$ is plotted against normalised lag time, for a number of PAM concentrations (molecular weight 5-6 million Da).

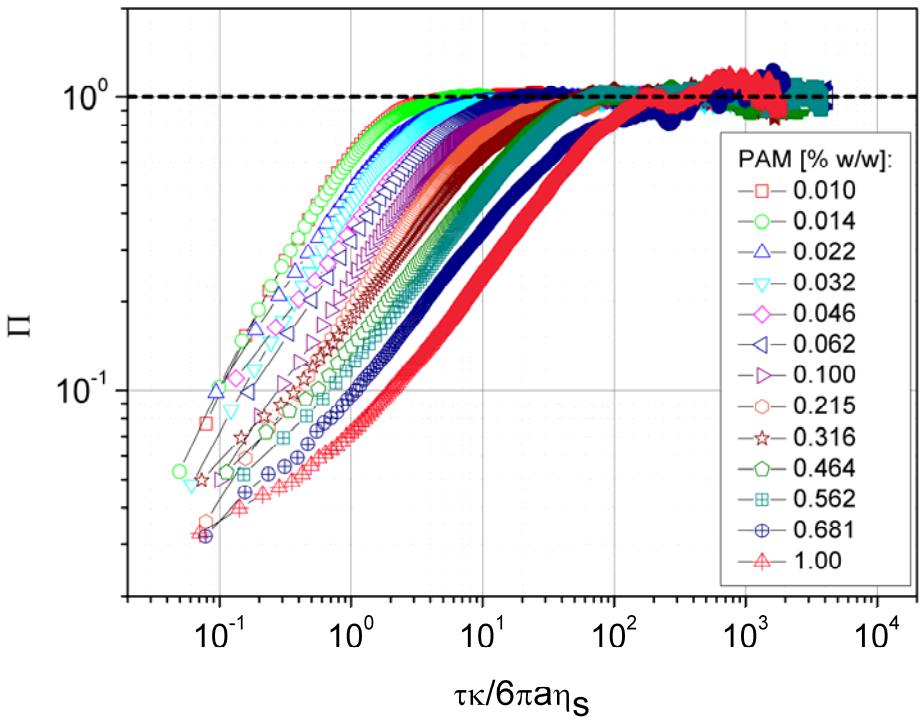

Figure 5.6: $\Pi(\tau)$ vs. *normalised lag time for a 5μm diameter bead in PAM (molecular weight 5-6 million Da) in concentrations ranging from 0.01-1.0% w/w. The normalised lag time uses the viscosity of the solvent, water.*

Since the viscosity contribution increases as the polymer concentration increases, the curves do not collapse in the same manner as a Newtonian fluid does. Indeed the solute contribution to the viscosity can be clearly seen in the increased time taken to reach the optical trap plateau (which itself is the fingerprint of the optical trap).

We have shown already that the concentration dependence of a fluid's linear viscoelastic properties can be extracted from the time-domain data. We therefore plot the concentration dependence at a value of $\tau\kappa/6\pi a\eta_s$ =0.5 (chosen to be well below the approximate cut-off frequency). It can be seen that the MSD (through $\Pi(\tau)$) varies approximately as $c^{-0.45}$. From the definition of the characteristic relaxation time, Equation 5.9, we know that $\eta \propto 1/\Pi$, thus $\eta \propto c^{0.45}$ (Figure 5.7).

The theoretical predictions for the concentration scaling laws of the viscosity of flexible polyelectrolytes are $\eta \propto c^{1/2}$, for $c \le c_e$ (where c_e is the entanglement concentration) and $\eta \propto c^{3/2}$ for $c \ge c_e$ [174]. The slope of $c^{-1/2}$ is included in Figure 5.7 as a guide, and it can be seen that this is very close to the actual measured slope.

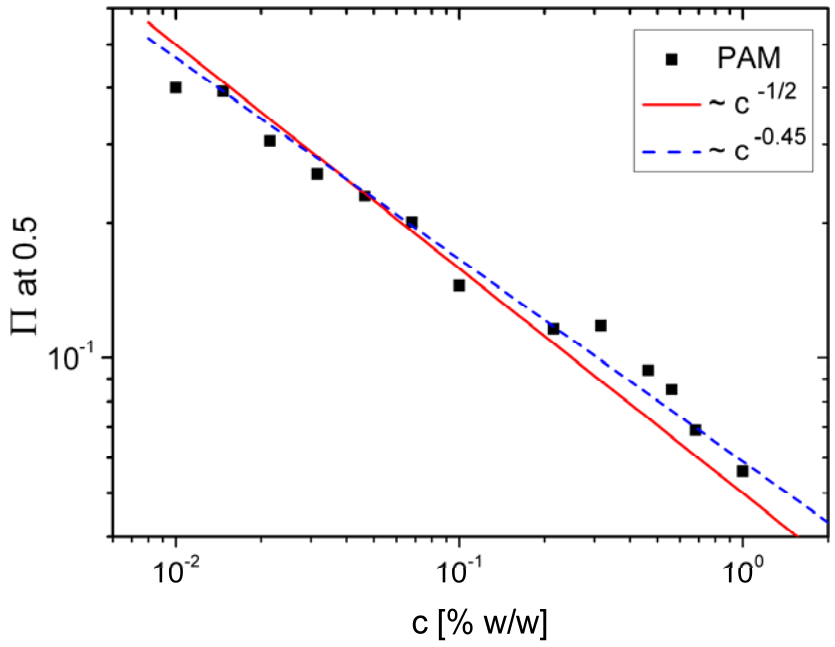

Figure 5.7: *Reliance of MSD on concentration for two points on* $\Pi(\tau)$ *(from Figure 5.6) for PAM (molecular weight 5-6 million Da) in concentrations ranging from 0.01-1.0% w/w. The lines are a guide to the gradient.*

In order to extract the concentration scaling laws of viscoelastic materials directly from the time domain, further steps can be taken, beginning with obtaining the relative viscosity, which was discussed in the introduction to the chapter, and is calculated as in Equation 5.20. By plotting $\eta_{rel}(t)$ against the characteristic relaxation time of Equation 5.21, the ratio of the solution to that of

the solvent can be obtained (Figure 5.8). Only a select number of concentrations have been plotted in order to make the graphs clearer.

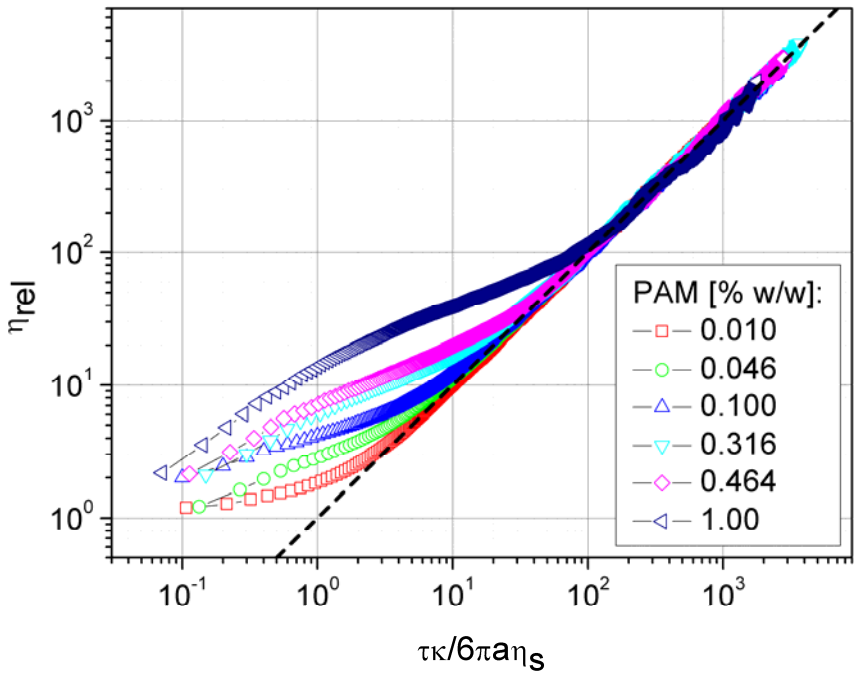

Figure 5.8: *Relative viscosity, η_{rel},* vs. *normalised lag time for PAM (molecular weight 5-6 million Da) in concentrations ranging from 0.01-1.0% w/w. The dotted line is a slope of 1.*

As expected, by reducing the solute (PAM) concentration the curves tend to 1 at short time intervals, as $\eta \rightarrow \eta_s$. There is a section of the graph - where the data falls along the dotted line - from which no information can be extracted. This is due to the optical trap plateau. From Figure 5.1 we know that a decrease in optical trap strength can increase the magnitude of the trap plateau, and thus the amount of information that can be obtained. Unfortunately the trap strength could not be reduced any less as the bead would drop from the focus point of the trap and the measurement of centre of mass proved problematic.

Following on from the relative viscosity, the specific viscosity, η_{sp}, (another dimensionless parameter, defined in the introduction) expresses the incremental viscosity due to the presence of the polymer in the solution. We plot the specific viscosity, $\eta_{sp}(t)$, against normalised lag time in Figure 5.9. As η tends towards η_s the specific viscosity should approach zero, which is consistent with the behaviour of the curves shown in Figure 5.9. The next stage in deriving the scaling laws involves plotting the reduced viscosity, η_{red} (with units of reciprocal concentration), which was defined in the introduction to this chapter, and which expresses the capacity of a polymer to cause the solution viscosity to increase; *i.e.* the incremental viscosity per unit concentration of polymer. The reduced viscosity, η_{red}, plotted against normalised lag time is presented in Figure 5.10.

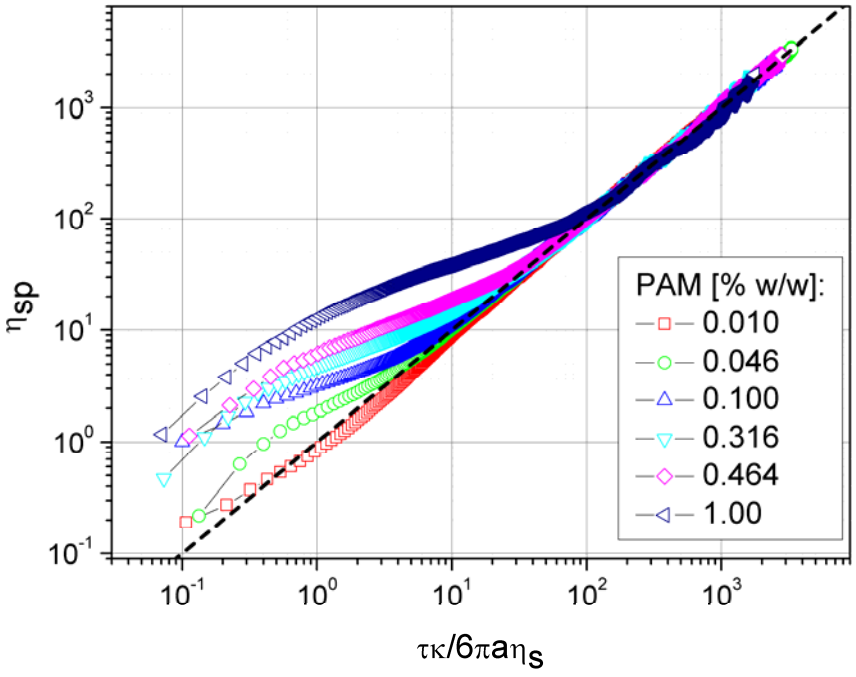

Figure 5.9: *Specific viscosity, η_{sp}, vs. normalised lag time for PAM (molecular weight 5-6 million Da) in concentrations ranging from 0.01-1.0% w/w.. The dotted line is a slope of 1.*

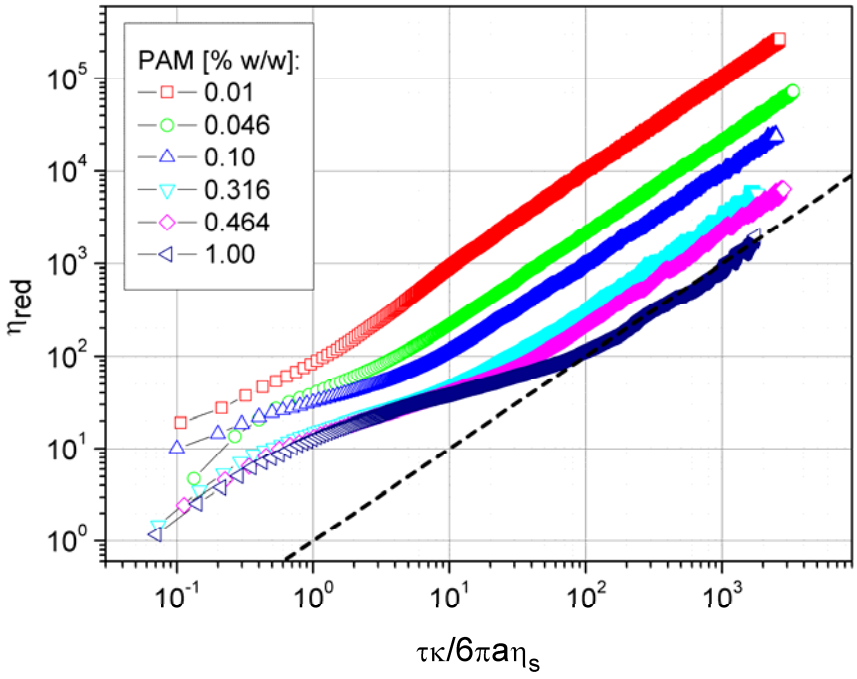

Figure 5.10: *Reduced viscosity, η_{red}, vs. normalised lag time for PAM (molecular weight 5-6 million Da) in concentrations ranging from 0.01-1.0% w/w. The dotted line is a slope of 1.*

We have applied the definition of the reduced viscosity as defined in Equation 5.4 in the Introduction. As observed in Figure 5.10, the data curves do not "collapse". Interestingly however, if we divide both axes (*i.e.* the specific viscosity and the normalised time) by $c^{3/2}$ we scale the higher concentration (0.1-1.0% PAM) data both vertically and horizontally onto a master curve (Figure 5.11). It is not immediately obvious why this uncovers the scaling factor of polyelectrolyte

solutions of $c \geq c_e$ (3/2) as opposed to the scaling factor of concentrations $c \leq c_e$ (1/2) that we discovered earlier in Figure 5.7. The two lowest concentration curves (0.01 and 0.0464 mg/ml) scale more accurately with a factor of c as shown in Figure 5.12.

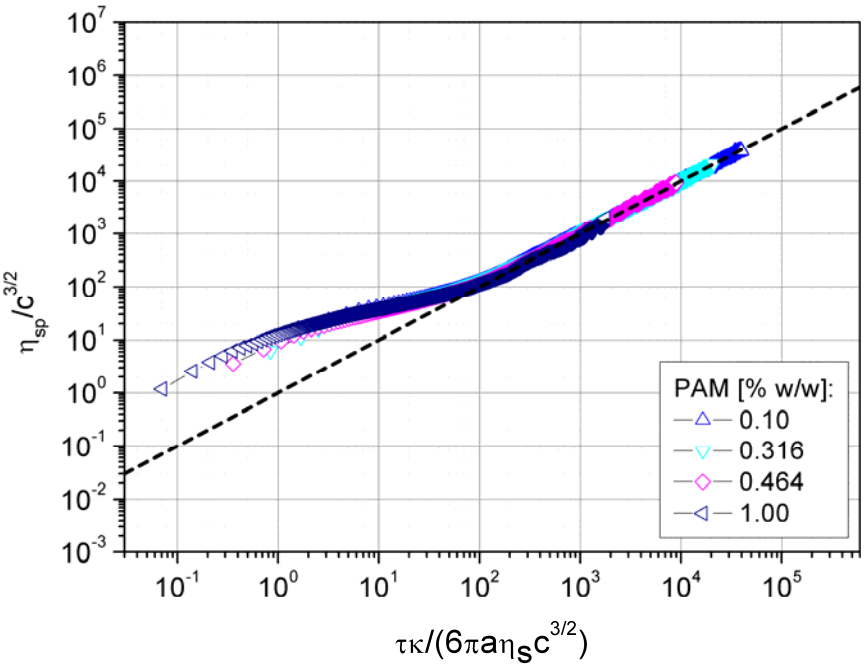

Figure 5.11: *Specific viscosity $\eta_{sp}/c^{3/2}$ vs. normalised lag time (taking into account $c^{3/2}$) for PAM (molecular weight 5-6 million Da) in concentrations ranging from 0.1-1.0% w/w. The dotted line is a slope of 1.*

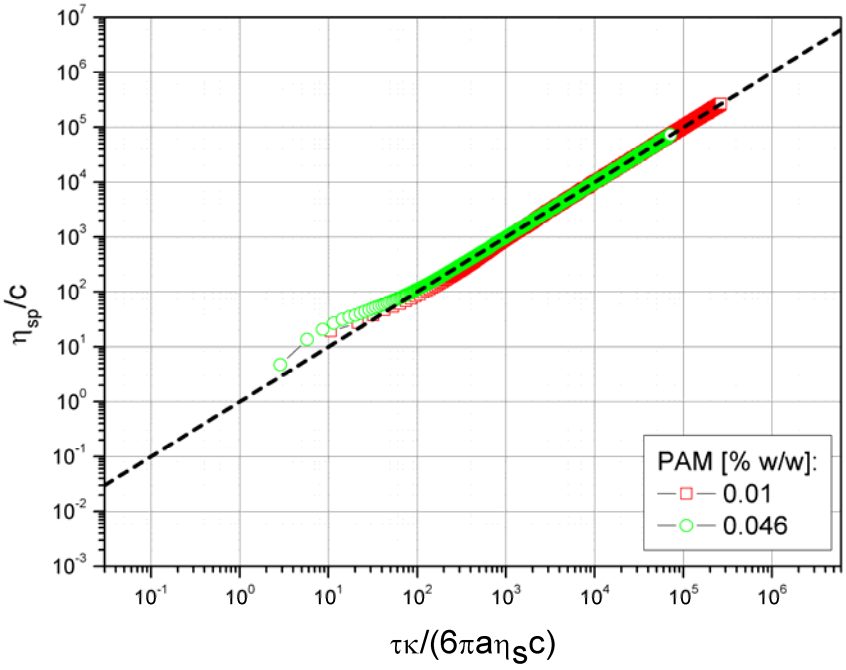

Figure 5.12: *Specific viscosity η_{sp}/c vs. normalised lag time (taking into account c) for PAM (molecular weight 5-6 million Da) in concentrations ranging from 0.01 and 0.0464% w/w. The dotted line is a slope of 1.*

We have obtained two concentration scaling factors for the time-dependent viscosity of the solution. Having already related the solution viscosity to the thermal fluctuations of a trapped bead

via Equation 5.23, the next logical step is to plot the nMSDs (*i.e.* the thermal fluctuations) of the beads (from Figure 5.6) against the concentration normalised lag times of Figure 5.11 and Figure 5.12. This is shown in Figure 5.13.

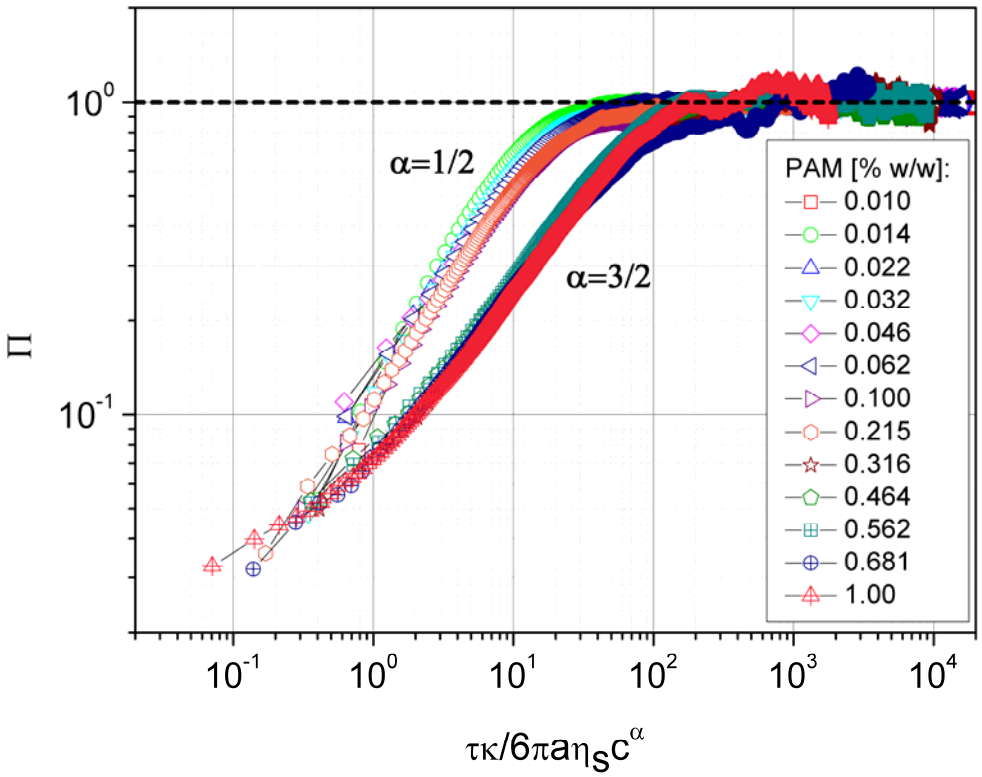

Figure 5.13: *Specific viscosity/c^{α}* vs. *normalised lag time/ c^{α} for PAM (molecular weight 5-6 million Da) in concentrations ranging from 0.01-1.0% w/w. For concentrations 0.01-0.215% PAM α=1/2, and for concentrations 0.316-1.0% PAM α=3/2. The dotted line is a slope of 1.*

As may be suggested by the graphs of Figs. 5.11 and 5.12, two scaling regimes are uncovered in Figure 5.13; a factor of 1/2 for PAM concentrations of 0.01-0.215%, and a factor of 3/2 for PAM concentrations of 0.316-1.0% (Figure 5.12). Although the low concentration scaling of 1/2 in Figure 5.13 differs from the scaling of 1 in Figure 5.12, it is possible that the data of Figure 5.12 is just too close to the dotted line (which represents the plateau value of the optical trap, and thus the section of the graph where information is hidden) for the scaling laws to be extracted properly. Indeed, a scaling law of 1/2 makes more sense rheologically, given that it is the predicted scaling of flexible polymers for concentrations beneath the entanglement concentration (as in Figure 5.7). In addition, the higher concentration (0.215-1.0%) scaling of 3/2 is the predicted scaling for flexible polymers in concentrations above the entanglement concentration.

We note that the higher concentration scaling of 3/2 was *not* detected in the concentration dependence of $\Pi(\tau)|_{\omega=0.5}$ shown in Figure 5.7, and here we discuss why this is so. In Figure 5.7 we plotted the nMSD at a specific frequency, which was an arbitrary value, albeit it was chosen to be well below the cut-off frequency defined in Equation 5.10. Instead of choosing this arbitrary

value we will show hereafter how the correct concentration scaling laws can be obtained by analysing the slope of the normalised MSD, $\Pi(\tau)$, close to zero.

We recall Equation 4.19 which relates the nMSD to the normalised autocorrelation function, $A(\tau)$, *via* $\Pi(\tau) = 1 - A(\tau)$. For a Newtonian fluid, the nPAF can be described by an exponential function, as in Equation 4.16. For a viscoelastic fluid, and in the case of an optically trapped bead, we can write the exponential as:

$$A(\tau) = e^{-\frac{\kappa\tau}{6\pi a \eta(t)}} \tag{5.24}$$

where κ is the trap strength and $\eta(t)$ is the viscosity of the solution. Although the theoretical basis for describing the nPAF of a viscoelastic fluid is not trivial to prove, we can see empirically that this is the case in Figure 5.14.

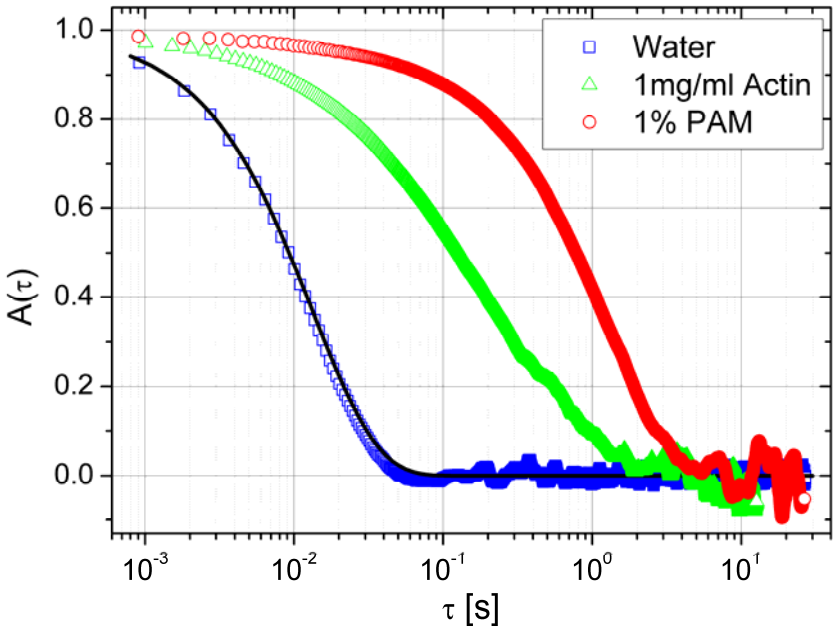

Figure 5.14: *Normalised position autocorrelation function vs. lag-time of a 5μm diameter bead in water, 1 mg/ml actin and 1% [w/w] PAM, showing the exponential shape of the function. The solid line is Eq. 5.24 plotted for a bead in water experiencing the same trap strength ($\kappa = 2.7\mu N/m$) as the experimental water measurement.*

If this exponential is expanded as a Taylor series around zero, it can be written (to 1st order) as:

$$A(\tau) = 1 - \left[e^{-\frac{\kappa\tau}{6\pi a \eta(t)}} \cdot \frac{\kappa}{6\pi a} \left(\frac{\eta(t) - \tau\eta'(t)}{\eta^2(t)} \right) \right]_{t=0} \tau \tag{5.25}$$

Equation 5.25 can be simplified to:

$$A(0) = 1 - \frac{\kappa\tau}{6\pi a \eta_0} \tag{5.26}$$

where η_0 is the viscosity at time zero. This in turn leads to a similar definition of the nMSD as in Equation 5.9:

$$\Pi(0) = \frac{\kappa}{6\pi a \eta_0}\tau \equiv \frac{1}{\eta_{rel(0)}} \cdot \frac{\kappa}{6\pi a \eta_s}\tau \tag{5.27}$$

The compliance $J(\tau)$ can then be written (from Equation 5.19) as:

$$J(\tau \to 0) \equiv J(0) = \frac{6\pi a}{\kappa}\Pi(0) = \frac{\tau}{\eta_0} \tag{5.28}$$

If we multiply both sides of Equation 5.28 by the viscosity of the solvent, η_s, we see that for $\Pi(\tau \to 0)$ the slope of the nMSD plotted against the normalised lag time $\kappa\tau / 6\pi a \eta_0$ is actually equal to $1/\eta_{rel}$ where η_{rel} is the relative viscosity (which is the ratio between the solution and solvent viscosities) at $\kappa/6\pi a \eta_s \, \tau \to 0$.

By plotting the reciprocal of the slope of the nMSD (when plotted against normalised lag time, when $[\kappa/6\pi a \eta_s \, \tau] \to 0$) against concentration, the correct concentration scaling laws (of 1/2 and 3/2), as predicted by the theory can be obtained, as shown in Figure 5.15.

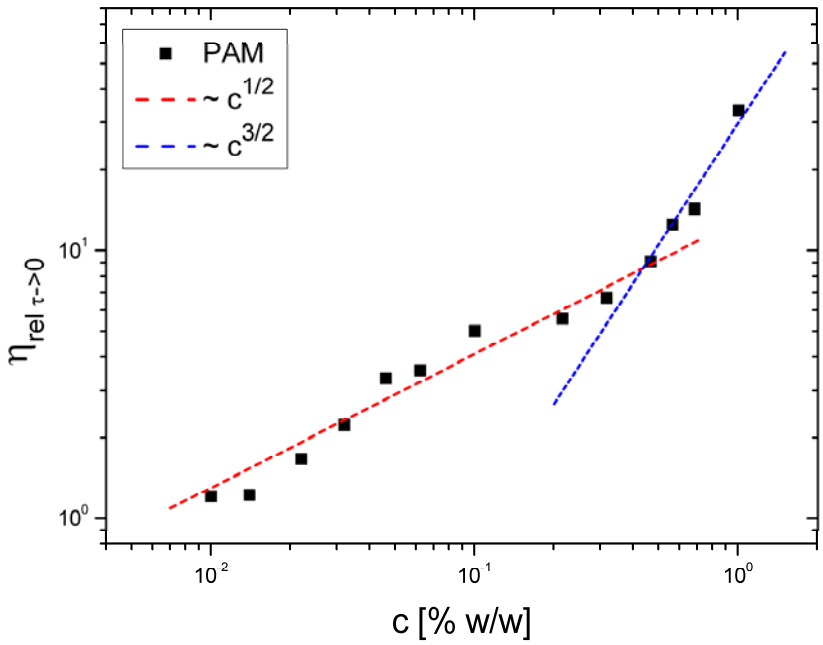

Figure 5.15: *The relative viscosity, η_{rel}, at $t \to 0$ plotted against concentration for PAM (molecular weight 5-6 million Da) in concentrations ranging from 0.01-1.0% w/w. The lines are a guide to the gradient.*

In this chapter we have discussed the usage of the normalised mean-square displacement, $\Pi(\tau)$, in deriving a characteristic relaxation rate of a system, $\kappa/6\pi a\eta_s$. This defines the single relaxation rate of a system composed of the ensemble of optical trap, bead radius, and solvent viscosity. In the case of a viscoelastic fluid, the normalisation factors allow the curves to be compared with respect to *only* the concentration. The concentration scaling laws can then be obtained in the time domain through manipulation of the relative viscosity and specific viscosity, without any need to perform a Fourier transform on the experimental data.

In addition, the factor of $\kappa/6\pi a\eta_s$ defines the cut-off frequency, below which the elastic nature of the trap masks any elastic component of the sample. This can be addressed by applying either of the two wideband methods introduced in Chapter 4, which use an extra step to obtain the low frequency viscoelastic response of the material.

Chapter 6

ACTIN NETWORKS

In this chapter the concentration scaling laws and viscoelasticity of *in vitro* reconstituted solutions of actin filaments are explored. Firstly, 'static' optical tweezer measurements are used (*via* the method described in Chapter 4.1) to analyse the normalised mean-square displacement, $\Pi(\tau)$, of micron-sized tracer probes in order to derive the concentration scaling laws of actin solutions in the time-domain. Following on from this, the storage and loss moduli of actin are examined and compared to the expected high frequency response of $\sim\omega^{3/4}$ as predicted by viscoelastic models [87, 175]. Next, the concentration dependence of the frequency-dependent viscoelastic response is compared to that of the time-dependent data; then finally, the 'two-trap' broadband technique for non-oscillating optical tweezers (presented in Chapter 4.4) is used to obtain a wideband frequency spectrum of the actin viscoelastic moduli.

6.1 Concentration scaling laws of actin networks

The dense actin filament networks that contribute to the mechanical properties of the cytoskeleton are difficult to measure *in vivo* and can be problematic to model theoretically as the structures and interactions involved are still not well understood. As actin is the main component of the cytoskeleton, studying the viscoelastic response of reconstituted actin networks will lead to a better understanding of cytoskeletal function.

Here, actin is obtained directly from fresh rabbit muscle and prepared as described in Chapter 3. We make use of the 'static' optical tweezer measurement described in Chapter 4.1 to study the high frequency viscoelastic response of actin solutions, and from these measurements we derive

concentration scaling laws of actin networks (and in the next Section, the related viscoelastic moduli) by analysing the normalised MSD, $\Pi(\tau)$. In Figure 6.1 are shown the normalised mean-square displacements against lag time for a range of actin concentrations, from 0.04-1.0 mg/ml.

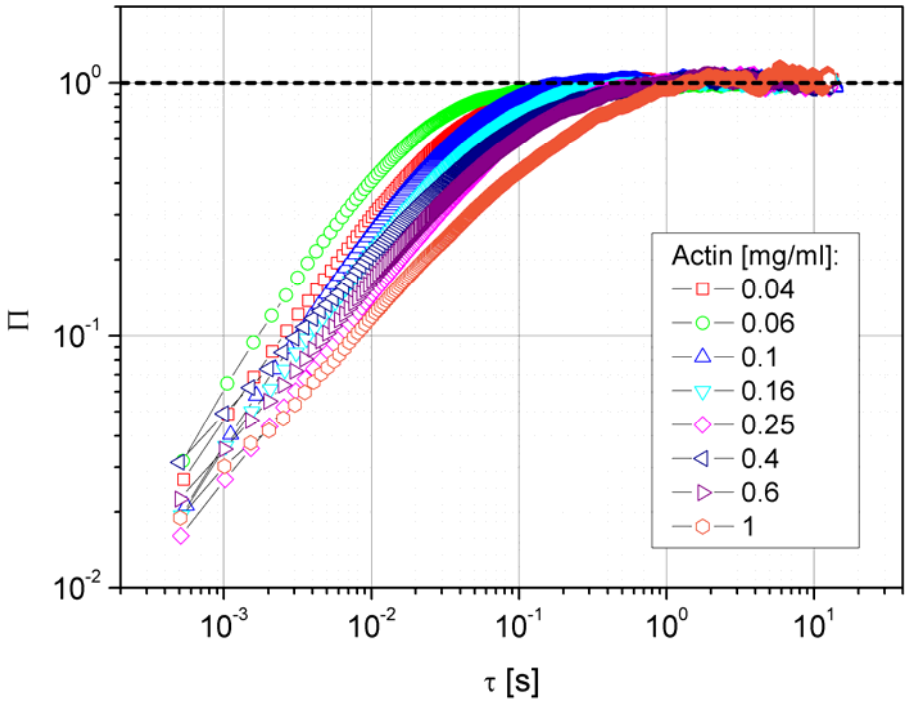

Figure 6.1: $\Pi(\tau)$ vs. *lag time for a 5μm diameter beads in actin solutions of concentrations ranging from 0.04-1 mg/ml.*

As expected, we see that the time taken to reach the plateau (where y→1) increases as the concentration increases. As introduced previously (Chapter 5) there exists a cut-off frequency, ω_{coff}, that dictates the timescale above which the elastic component of the solution is masked by the elastic component of the optical trap. This cut-off frequency is inversely proportional to the zero-shear viscosity of the system, thus as the actin concentration (and hence viscosity) increases, the cut-off frequency decreases and the time taken to reach the plateau is lengthened.

To present the results of Figure 6.1 more clearly the data has been split into two graphs, one from 0.04-0.25mg/ml (Figure 6.2 A) and one from 0.4-1.0mg/ml (Figure 6.2 B), both plotted against the characteristic relaxation time of the system (defined in the previous chapter) $\kappa\tau/6\pi a\eta_s$, where κ is the optical trap strength, τ is the lag time, a is the radius of the bead, and η_s is the viscosity of the solvent (in this case, water).

The dotted lines on the graphs are added as guidance for the slopes. Since viscous behaviour manifests itself as a slope of 1 (from Chapter 5) it is clear that sub-diffusive (*i.e.* elastic) behaviour (slope <1) is detected for all concentrations. In addition, it is observed that some data has a slope of

3/4, which is the predicted *frequency* dependence of the universal high-frequency limiting form of the complex modulus [85, 169]

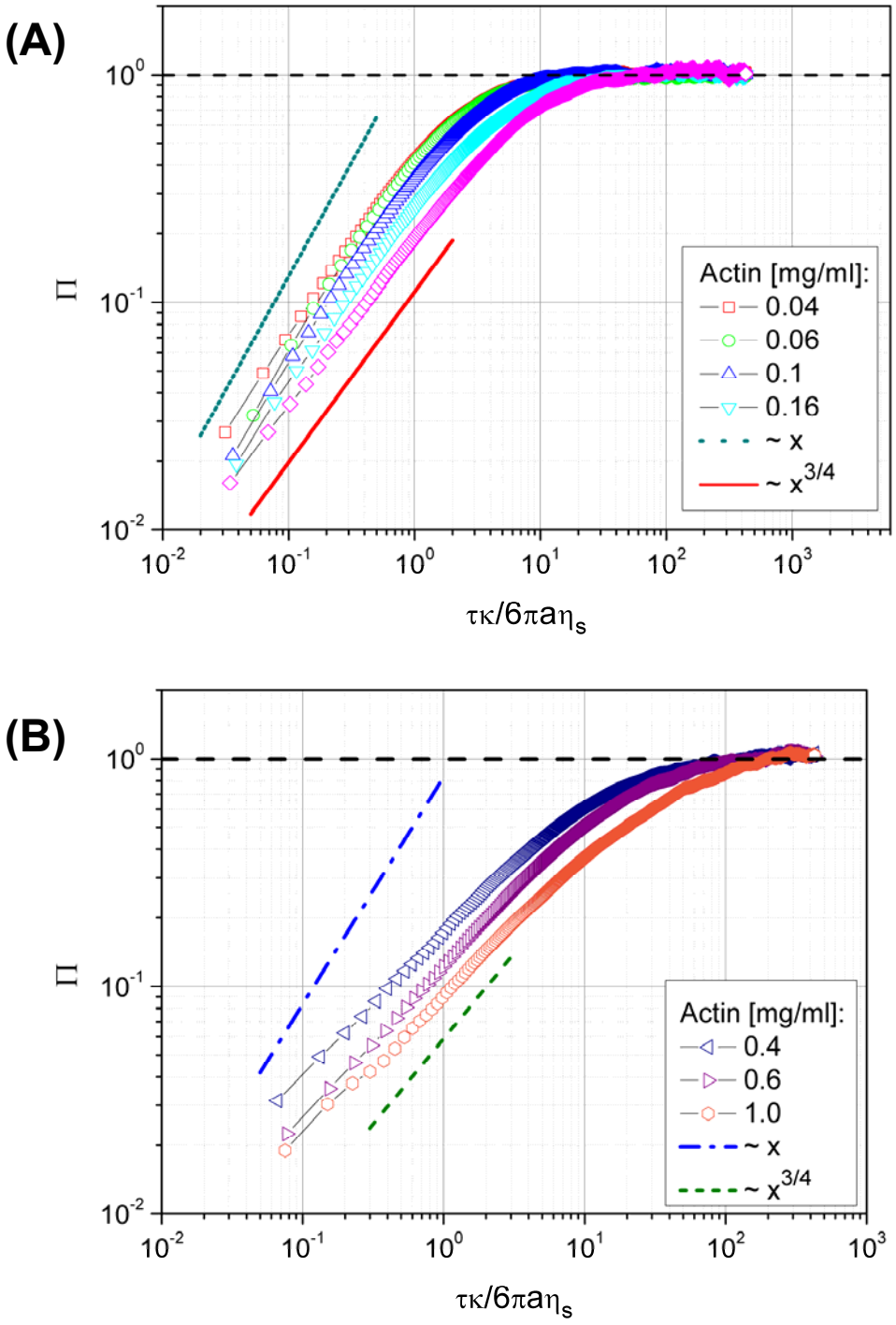

Figure 6.2: $\Pi(\tau)$ vs. *normalised lag time for a 5μm diameter bead in F- actin solutions in concentrations from (A) 0.04-0.25 mg/ml, and (B) 0.4-1.0 mg/ml. The lines are added as guide for the gradients.*

The derivation of the concentration scaling laws of biopolymer solutions can be addressed by the analytical methods employed in Chapter 5. The first technique makes use of the relative viscosity, $\eta_{rel}(\tau)$, specific viscosity, $\eta_{sp}(\tau)$ and reduced viscosity, $\eta_{red}(\tau)$. The relative viscosity is calculated *via* Equation 5.20, where we use the viscosity of water as the solvent viscosity, η_s. The relative, specific and reduced viscosities have all been plotted against the normalised lag time

($\tau\kappa / 6\pi a\eta_s$) in Figure 6.3. The relative viscosity (Figure 6.3A) represents the ratio of the solution viscosity to that of the solvent. The link between concentration and viscosity has already been discussed in Chapter 5, thus we see that as concentration of actin increases, so does the relative viscosity. Specific viscosity (Figure 6.3B) expresses the incremental viscosity due to the presence of the polymer in the solution. Dividing $\eta_{sp}(\tau)$ by concentration gives the reduced viscosity (Figure 6.3C), which expresses the capacity of a polymer to cause the solution viscosity to increase; *i.e.* the incremental viscosity per unit concentration of polymer.

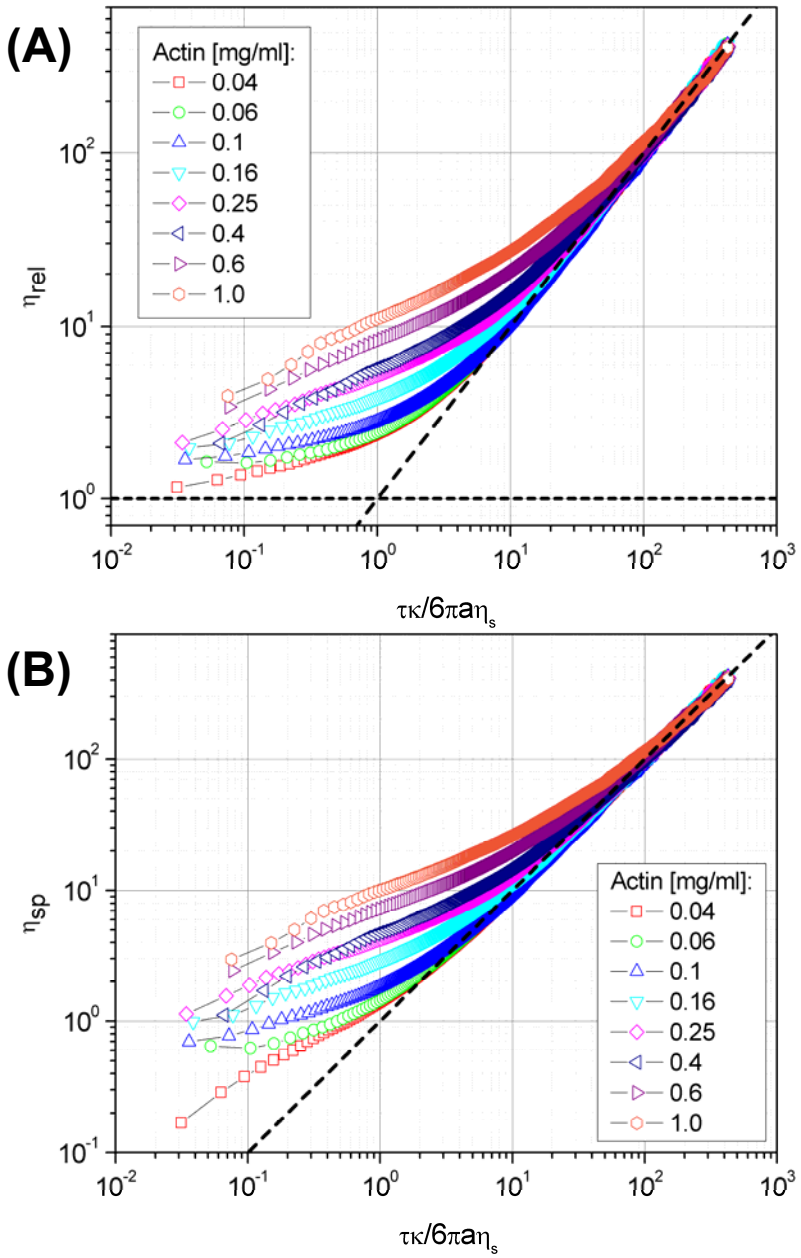

Figure 6.3 [A,B]: *(A) Relative viscosity, η_{rel},* vs. *normalised lag time and (B) specific viscosity, η_{sp}, vs. normalised lag time for a 5μm diameter bead in solutions of actin in concentrations from 0.04-1.0 mg/ml. The dotted lines are the lines of y=x (A and B) and y=1 (A).*

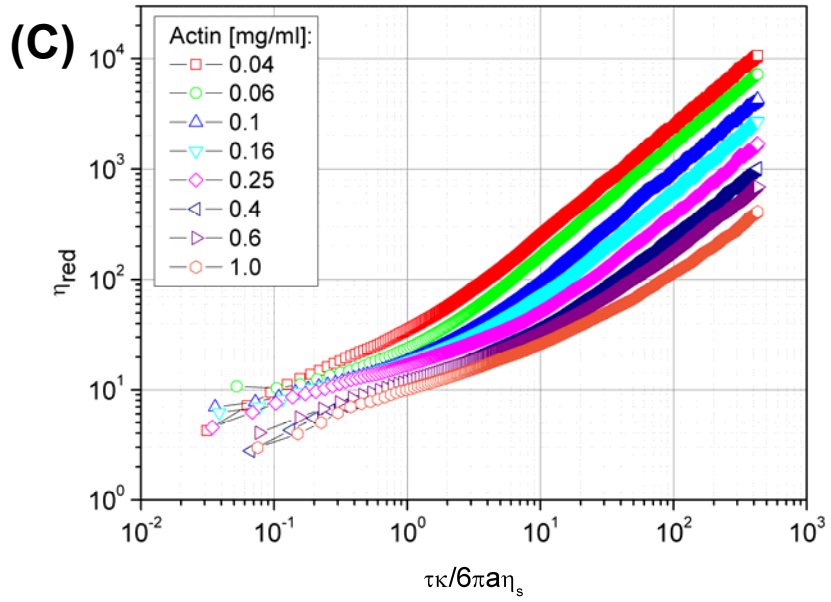

Figure 6.3 [C]: *Reduced viscosity,* Ω_{red}, vs. *normalised lag time for a 5µm diameter bead in solutions of actin in concentrations from 0.04-1.0 mg/ml.*

In order to make the reduced viscosity curves collapse onto a master curve, the concentration factor of the reduced viscosity (c) needs to be changed to $c^{4/3}$, and then this value must be used to normalise the time axis (Figure 6.4). This value of 4/3 corresponds to the scaling factor that Morse's model predicts for the concentration dependence of the curvature stress of the macroscopic plateau modulus (G'_0, Figure 2.4) of semiflexible polymers [85].

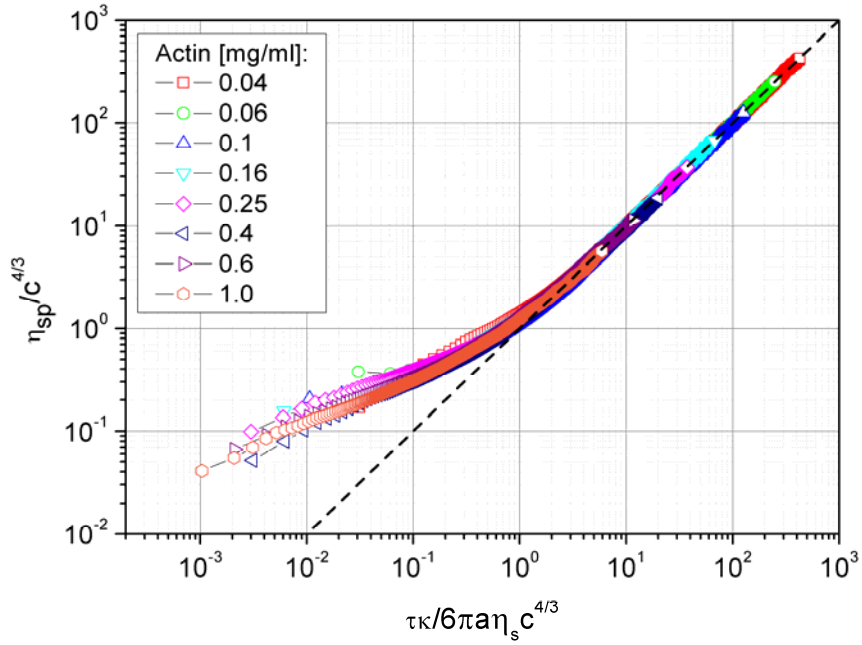

Figure 6.4: *Specific viscosity,* η_{sp} *divided by* $c^{4/3}$ vs. *normalised lag time multiplied by* $c^{4/3}$ *for a 5µm diameter bead in varying concentrations of actin. The dotted line is the slope of 1.*

It should be recalled that Morse's model expresses the intramolecular stress contribution (the main contribution to the viscoelastic properties of semiflexible chains) as a sum: $\sigma_{intra} = \sigma_{curve} + \sigma_{orient} + \sigma_{tens} - ck_BT\delta$. The curvature stress arises from the forces that oppose the transverse deformation or the rotation of chain segments. Tassieri *et al* [139] proved experimentally that the scaling factor of 4/3 was the correct concentration dependence of the curvature stress by measuring the persistence length, L_p, of actin filaments.

The second technique of extracting the concentration dependence of the time-dependent normalised MSD is by measuring the slope of the nMSD (when plotted against normalised lag time) close to zero. This slope is equal to $1/\eta_{rel}$, where η_{rel} is the relative viscosity of the solution. The relative viscosity is therefore plotted against concentration in Figure 6.5.

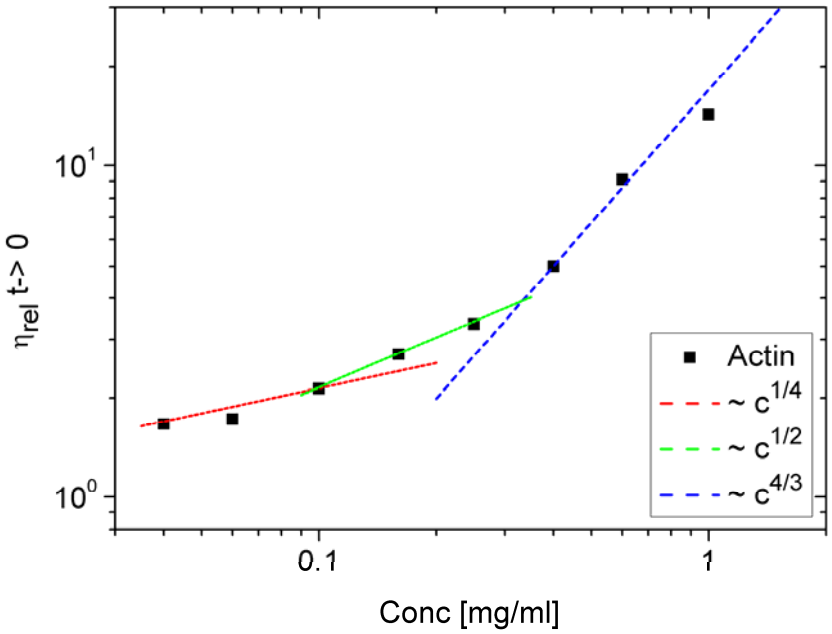

Figure 6.5: *The relative viscosity, η_{rel}, at $t \to 0$ plotted against concentration for actin in concentrations ranging from 0.04-1.0 mg/ml. The lines are a guide to the gradient.*

For this method, three scaling regimes are noted; a low concentration dependence of $c^{1/4}$, a high concentration dependence of $c^{4/3}$, and an intermediate regime of $c^{1/2}$. The 1/4 and 4/3 scaling factors are both predicted by Morse's model [87]; the 4/3 factor arises from the curvature stress as described above, and the 1/4 arises from the concentration dependence of the plateau modulus for semiflexible rods. These are exactly the same scaling factors as those that can be extracted from the frequency-dependent data, as will be shown in the next section.

We see, therefore, that it is possible to obtain scaling laws from the time-domain that were traditionally obtained from the frequency-domain. The frequency-dependent scaling factor of 3/4 (as described for the universal high-frequency limiting form for the complex modulus [87, 175]) is

apparent in the normalised MSDs in Figure 6.2 as $\sim \tau^{3/4}$, and the concentration dependences of 1/4 and 4/3 (as predicted for the concentration dependence of the plateau modulus in the frequency domain) can be extracted from the time-dependent normalised viscosity data of Figures 6.4 and 6.5. It may therefore not be strictly necessary to move to the frequency domain in order to extract scaling laws, such as the concentration dependence of a polymer solution; however, we will compare the results of this section to the concentration scaling of the frequency-dependent storage and loss moduli hereafter.

6.2 Viscoelasticity of actin solutions

To explore further the viscoelasticity of actin filaments the storage and loss moduli were calculated for actin solutions over a range of concentrations from 0.04-1.0 mg/ml. This was done by analysing the thermal fluctuations of a 5μm diameter silica bead in an optical trap. Morse's model describes the viscoelastic behaviour of 1mg/ml actin as shown in Figures 2.7 and 2.8. Figure 2.8 (for a polydisperse actin solution) has been repeated and modified below, in Figure 6.6.

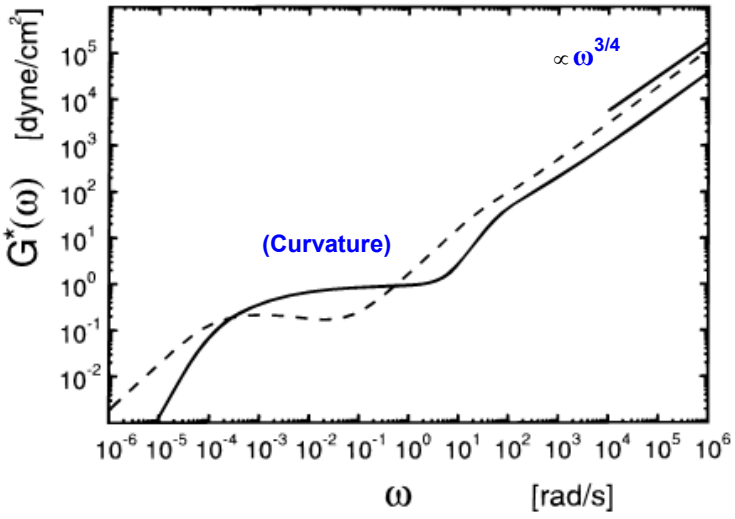

Figure 6.6: *(Taken from Ref. [87]) Calculated moduli $G'(\omega)$ (solid line) and $G''(\omega)$ (dotted line) for a polydisperse actin solution with $\overline{L}_c = 17\,\mu m$ and an exponential distribution of chain lengths. Morse's model predicts a frequency-independent plateau caused by the curvature stress and a high frequency dependence of $\propto\omega^{3/4}$.*

Indeed, many experimental studies have uncovered scaling laws predicted by Morse and others (*i.e* $G^*(\omega) \propto \omega^{3/4}$ at high frequencies) [87, 127], although there have also been experimental results that differ from this, and incorporate other scaling laws [120, 176]. Since the ultimate goal in actin cytoskeleton mechanics is to develop predictive physical models to characterise the mechanics of cellular physiology, work still needs to be done to fully elucidate what mechanisms these alternative scaling laws arise from, and to incorporate them into viscoelastic models.

Here, we measure the linear viscoelastic properties (*i.e.* $G^*(\omega)$) of a series of actin solutions using optical tweezers and the 'static' analytical method described in Chapter 4.1. The storage, $G'(\omega)$, and loss, $G''(\omega)$, moduli are plotted directly from the experimental data (*via* Equation 4.18), using Equation 4.7 to compute the Fourier transforms. Note that, this method of performing Fourier transforms of the normalised MSDs produces some scatter in the viscoelastic data at high frequencies and ripples in the low frequency portions of the curves. As explained in detail in Ref. [161], this method works directly on the experimental data points (*i.e.* $\{\tau_k, \Pi_k\}$, where $k = 1..N$) and therefore preserves genuine experimental noise.

As mentioned above, Equation 4.18 is used in order to calculate the complex shear modulus. This equation relates the normalised position autocorrelation function (nPAF) to complex shear modulus. The nPAF is related to the normalised MSD *via* $\Pi(\tau) + A(\tau) = 1$ and has the advantage of possessing a well defined Fourier transform. Note that Equation 4.6, which relates the complex shear modulus to the velocity autocorrelation function (VAF) is an equally valid method to use.

An important feature of using the nPAF to calculate the complex shear modulus, $G^*(\omega)$, is that the range over which the nPAF is analysed can greatly affect the resultant viscoelastic moduli. Next, we show specifically what range of data should be selected and what should be ignored.

The normalised autocorrelation function can be described by a simple exponential decay. By including in the data analysis the portion of the autocorrelation function that is close to zero (Figure 6.7, top left) a significant amount of high frequency noise is introduced into the calculation of the complex moduli (Figure 6.7, bottom left). This is due to the noise around zero which arises from poor statistics. By neglecting this portion of the nPAF graph (Figure 6.7, top right) the resulting moduli are much smoother (Figure 6.7, bottom right).

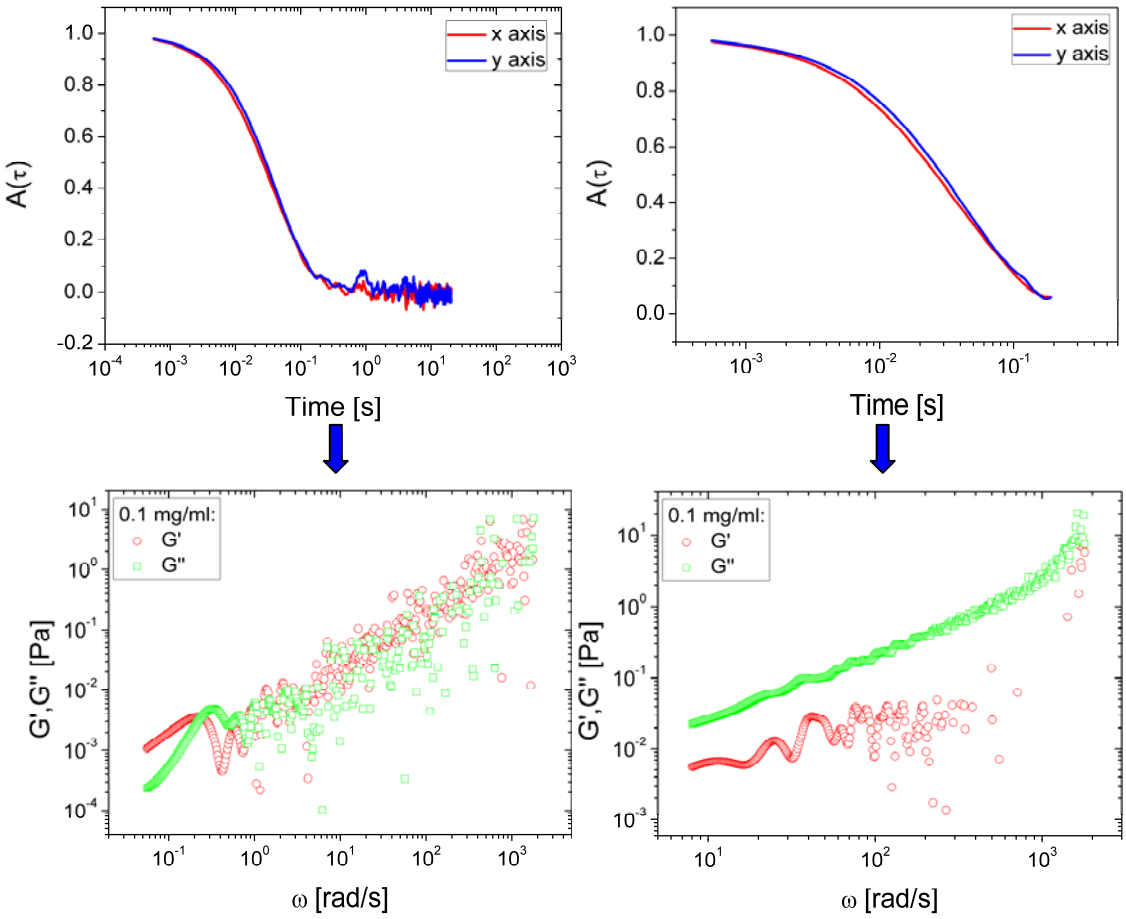

Figure 6.7: *Normalised position autocorrelation functions and resultant storage and loss moduli for 0.1 mg/ml actin. As the nPAF approaches zero a significant amount of noise becomes apparent in the measurement (top left). If this section of the data (i.e* $A(\tau) = 0$*) is selected to compute the complex shear modulus this noise is carried over into* $G^*(\omega)$ *(bottom left). A typical nPAF selection containing no noise (i.e* $A(\tau) \geq 0.1$*) (top right) produces moduli with much less noise (bottom right).*

Taking into account the correct nPAF selection, the storage and loss moduli of a series of actin concentrations are plotted below in Figure 6.8. Solid lines are a guide to the gradients.

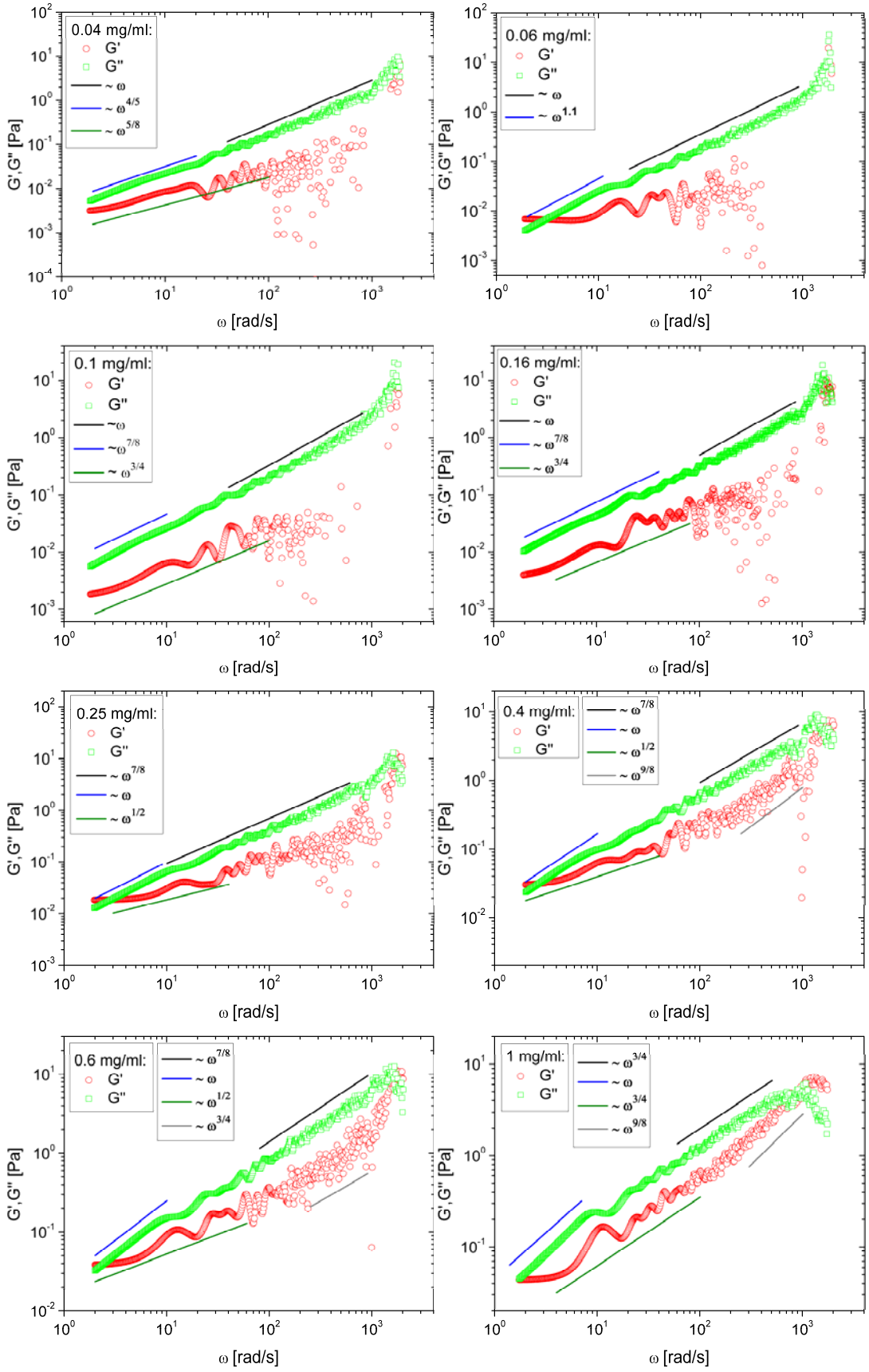

Figure 6.8: *Loss and storage moduli* vs. *frequency for varying concentrations of actin (0.1-1.0 mg/ml). The solid lines are a guide for the gradients.*

In Figure 6.8 we see that the storage and loss moduli of the higher concentration graphs are only just reaching a cross-over point at low frequencies (approaching 10^0 rad/s). Morse's model predicts

that this high frequency crossover point between the storage and loss moduli occurs at the entanglement frequency, τ_e^{-1}. The first point of note is that the dependence of $G^*(\omega) \propto (i\omega)^{3/4}$ at high frequencies (above the entanglement frequency) which has been predicted by Morse's model (amongst others *i.e.*[175]) and experimentally measured [177-180], can only be seen in the loss modulus of the 0.6 mg/ml and 1 mg/ml solutions, and in the storage modulus of the 0.1 and 0.16 and 1.0 mg/ml solutions.

Using Morse's model we now distinguish between the different stress contributions to the complex modulus, $G^*(\omega)$. This is done by extracting the concentration dependence of both the loss modulus, $G''(\omega)$, and storage modulus , $G'(\omega)$. In Figure 6.9 the loss modulus is plotted against concentration at two frequencies: 5 and 400 rad/s. Due to the oscillations present in Figure 6.8, the value of the moduli was obtained by applying a linear fit over a small range of frequencies in the log-log graph.

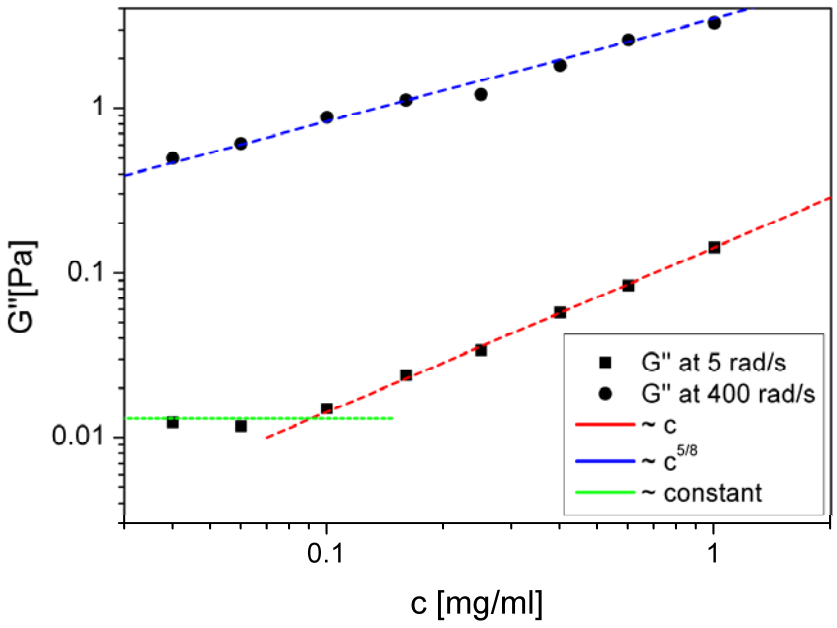

Figure 6.9: *The loss modulus* $G''(\omega)$ vs. *concentration extracted from the complex moduli of Figure 6.8, at frequency values of 5 rad/s and 400 rad/s. The lines are a guide for the gradient.*

The lower frequency of 5 rad/s in Figure 6.9 is designed to capture the $G''(\omega) \propto \omega$ dependence highlighted by the six higher concentrations (0.1-1mg/ml) in Figure 6.8. $G''(\omega)$ is found to vary linearly with concentration, $\propto c$, until the concentration drops to 0.1 mg/ml and below. Indeed the lower three concentration samples appear to exhibit no dependence upon concentration at 5 rad/s. This may be explained by the fact that the global rheological response of low actin concentrations is viscous at these concentrations and so the actin cannot resist shear deformations [181]. The scaling of $G''(\omega) \propto c$ would seem to demonstrate that the stress tension, σ_{tens}, provides the largest contribution to the loss modulus in this range of concentration, in good agreement with the

prediction of Morse's model, which calculates that $G_{tens}(\omega) \propto \rho$ (where ρ represents the concentration) for $\omega >> \tau_e^{-1}$. For frequencies greater than the entanglement frequency $G''(\omega)$ is expected to vary with $\omega^{3/4}$, which it clearly does *not* in the graphs of Figure 6.8 at frequencies surrounding 5 rad/s. Indeed, the slope of $G''(\omega)$ actually varies between $\omega^{4/5}$ and ω.

Given this discrepancy, we confirm that our measurements fall within the approximate magnitude range predicted by Morse's model by plotting the viscoelastic moduli of 1 mg/ml actin (from Figure 6.8) against Morse's three predictions for a 1 mg/ml actin solution (Figure 2.7). The best fit is found in the prediction for an actin solution with $L_c = L_p$ (for $L_p = 17\mu m$), as shown below in Figure 6.10. Note that the results from Figure 6.8 have been converted into Dynes/cm^2.

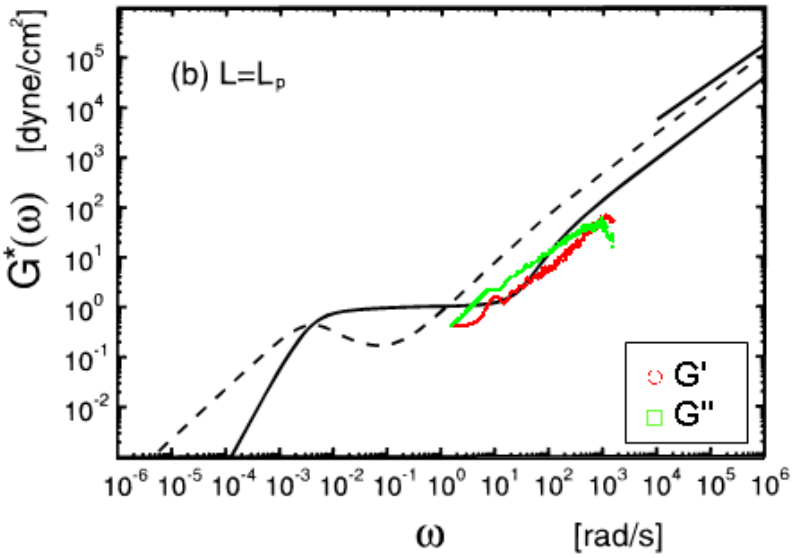

Figure 6.10: *(Taken from Ref. [87]) Morse's prediction for $G'(\omega)$ (solid line) and $G''(\omega)$ (dotted line) for a monodisperse solution of actin, $L_c = L_p$. The straight solid line in each figure has a slope of 3/4 and is the predicted high-frequency asymptote of $G''(\omega)$. The viscoelastic moduli (red circles: $G'(\omega)$; green squares: $G''(\omega)$) of 1 mg/ml actin from Figure 6.8 have been added as a comparison.*

The higher frequency of 400 rad/s in Figure 6.9 was also used to obtain a concentration dependence of $G''(\omega)$. At this frequency the loss modulus varies quite precisely with $c^{5/8}$. For this frequency (as for the lower frequency of 5 rad/s) it would be expected that $G''(\omega)$ varies linearly with concentration, since $G_{tens}(\omega)$ is still the main contributor to the stress relaxation. A scaling law of $G_{tens}(\omega) \propto c^{4/5}$ has been observed before however, by Tassieri *et al* [120]. This is shown in Figure 6.11, where the data of Tassieri *et al* [120] for 6.25 rad/s has been plotted next to the 5 rad/s data of Figure 6.9. Although slightly ambiguous, there it appears as it there may well exist a similar concentration independent plateau at low concentrations (<0.1 mg/ml).

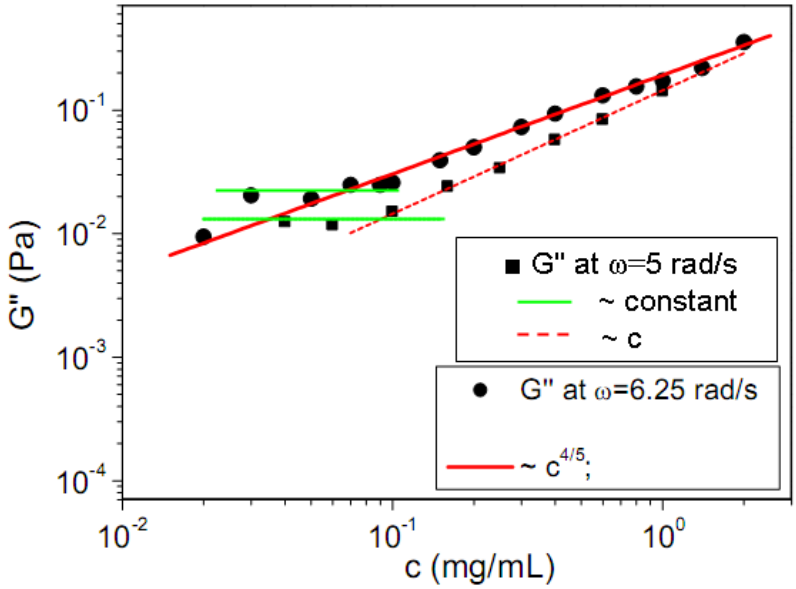

Figure 6.11: *The loss modulus* $G''(\omega)$ vs. *concentration at a frequency value of 5 rad/s (extracted from the complex moduli of Figure 6.8) compared to the loss modulus* vs. *concentration at a frequency of 6.25 rad/s (from Ref. [120]). The lines are a guide for the gradient.*

Morse's model predicts a concentration independent limiting form of the loss modulus at high frequency (the straight solid line in Figure 6.10). This high frequency asymptotic behaviour, $G''(\omega) \propto \omega^{3/4}$, is only evident in the viscoelastic moduli of Figure 6.8 in the concentrations of 0.6 and 1 mg/ml. The lower concentrations of 0.25-0.6 mg/ml scale with $\omega^{7/8}$ for $10 < \omega < 600$ and the concentrations of 0.04-0.16 mg/ml scale with ω for $30 < \omega < 800$. An explanation of this scaling linearly with ω, as previously mentioned, is that at low concentrations, the actin filaments cannot resist shear deformations, and their global rheological response is viscous [181].

Although the high frequency scaling of the loss moduli at lower concentrations (*i.e.* $G''(\omega) \propto \omega^{7/8}$ and $G''(\omega) \propto \omega$) are not predicted by Morse, the $\omega^{7/8}$ case has also been measured before for concentrations of actin ≤ 0.6 mg/ml [120]. Similar time scales have been discovered by Everaers *et al* [182] and Liverpool [176, 183] in studies of the longitudinal and transverse fluctuations of semiflexible filaments. They found that at high frequency (thus short times) the fluctuations perpendicular to the local axis of the polymer scale as $\left\langle r_{\perp}^2 \right\rangle \propto t^{3/4}$ (similar to Morse's Equation 2.24) but fluctuations parallel to the local axis scale instead as $\left\langle r_{\parallel}^2 \right\rangle \propto t^{7/8}$ and are correlated over a length $\ell_{\parallel} \propto t^{1/8}$. However, these studies are not addressed towards the viscoelastic properties of semiflexible polymers, rather they are focused more upon measuring the dynamics of filaments; therefore they do not provide any real insight into the relationship between these time scales and the viscoelastic parameters required to test these theories more rigorously.

Our results here indicate that the high frequency dependence of the viscous moduli moves from $\propto \omega$ at low concentrations (0.04-0.16 mg/ml) to a value of $\propto \omega^{3/4}$ at high concentrations (0.6-1.0 mg/ml). These discrepancies from the predicted scaling in the frequency-dependence moduli may explain why the high frequency concentration dependence also differs from the predicted value. Additionally, it should be noted that experimental measures of properties of actin solutions (specifically the modulus) suffer from wide variations, even on samples from the same source [184]. This variation may be the result of small numbers of cross-linking proteins that exist in the samples. Whilst it may be extremely useful to use a highly purified model, with carefully controlled filament length, to test the theoretical models, it may perhaps be even more important to develop a better understanding on how actin networks more typically behave.

We next plot the concentration dependence of the storage modulus, $G'(\omega)$, at two frequencies of 2 and 50rad/s (Figure 6.12). At the lower frequencies we recall (from Figure 6.8) that $G'(\omega)$ varies with frequency between $\omega^{1/2}$ and $\omega^{3/4}$, so we chose the frequency of 2 rad/s to capture this scaling. Note that the scaling of $\omega^{1/2}$ has been noted in bulk rheological measurements [185, 186] and in magnetic tweezer microrheology [25] for $10^{-1} < \omega < 10^{1}$ as an extension of the $G'(\omega)$ plateau.

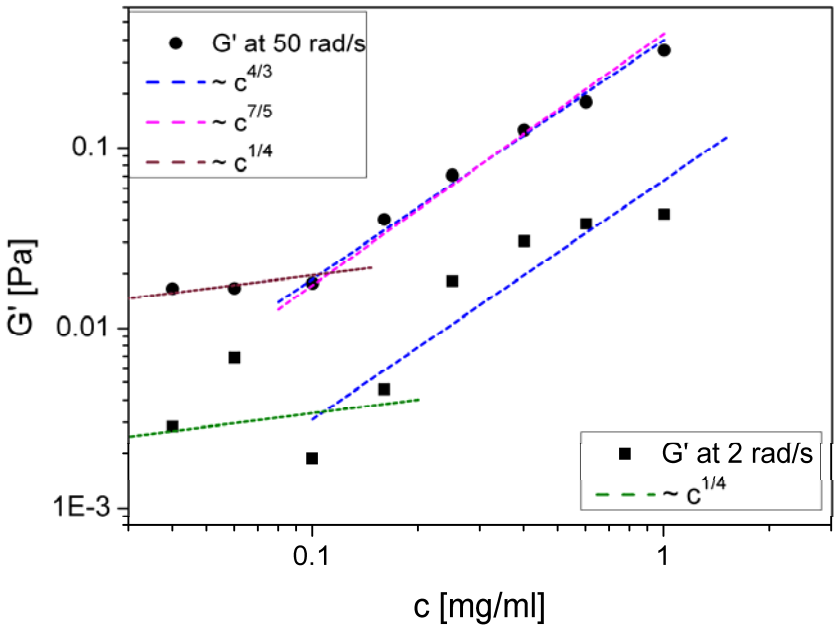

Figure 6.12: *The storage modulus* $G'(\omega)$ *vs. concentration extracted from the complex moduli of Figure 6.8, at frequency values of 2 rad/s and 50 rad/s. The dotted lines are a guide for the gradient. It has been shown experimentally [139] that the EMA is the most accurate scaling law for the macroscopic plateau modulus of semiflexible polymer solutions in the tightly entangled regime, although we provide slopes of both the EMA and BCA gradients. The slope of* $c^{4/3}$ *is a better fit for the data than* $c^{7/5}$*, agreeing with the EMA scaling.*

From Figure 6.12 it can be seen that the concentration dependence at the frequency of 2 rad/s is not well defined, although the values increase with concentration above a concentration of 0.1 mg/ml. Below 0.1 mg/ml they become more scattered, although arguably around a constant value. At the higher frequency of 50 rad/s the concentration dependence varies as $G'(\omega) \propto c^{4/3}$ for $0.1 < c < 1$, but is approximately constant with concentration for $c < 0.1$. Morse's model predicts that the stress curvature, σ_{curve}, contributes the most to the elastic modulus, thus Morse provides two scaling predictions for behaviour under this regime; i) $G_{curve}(\omega) \propto \rho^{7/5}$ by using the binary-collision approximation, and ii) $G_{curve}(\omega) \propto \rho^{4/3}$ by using the effective-medium approximation. We include lines of both these gradients in Figure 6.11 to highlight that merely plotting the concentration dependence alone cannot distinguish between the two scalings. Tassieri *et al* [139] calculated the persistence length of different actin solutions in order to prove that the EMA approximation is the correct one.

At low concentrations, Morse provides an alternative scaling of $G_{curve}(\omega)$. His model predicts that that upon entering the tightly-entangled regime, by increasing the concentration (or chain length) from a loosely entangled solution of semiflexible rods, one would expect to see the curvature-dominated power law regime predicted for loosely-entangled regimes, in which $G^*(\omega) \propto (i\omega)^{1/4}$, evolve into a curvature-dominated plateau, with a plateau modulus $G'(\omega) \propto \rho^{1/4}$. At higher concentrations, the behaviours become similar to that predicted for coil-like chains, $G'(\omega) \propto \rho^{4/3}$. The slope of $c^{1/4}$ has therefore been added as an alternative interpretation in Figure 6.12.

The scaling of $c^{1/4}$ for the storage modulus has also been discovered by Tassieri *et al* [120] at a frequency of 1 rad/s. This has been plotted against the 2 rad/s data (of Figure 6.12) in Figure 6.13.

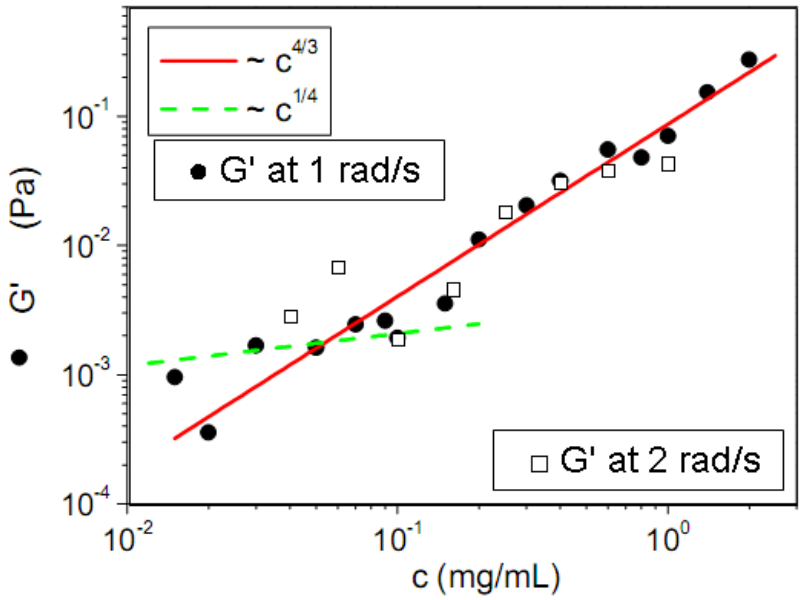

Figure 6.13: *The storage modulus* $G'(\omega)$ *vs. concentration at a frequency value of 2 rad/s (extracted from the complex moduli of Figure 6.8) compared to the storage modulus vs. concentration at a frequency of 1 rad/s (from Ref. [120]). The lines are a guide for the gradient.*

Note that these two scaling factors of 1/4 and 4/3 were also obtained from the time-dependent data, and shown in Figure 6.5.

For actin solutions the cross-over point between the loosely-entangled and tightly entangled regimes has been measured at ~0.1 mg/ml [127, 120, 139] and indeed Figures 6.10 and 6.12 both exhibit a change in scaling around these points (with the exception of the high frequency loss modulus).

Using the previous results from in Section 6.1, a comparison can now be made to see if similar concentration scaling occurs across the full spectrum of both the time-domain MSDs and the frequency-domain moduli. A scaling factor of 4/3 was used to normalise the time-dependent data, and this factor was also predicted by Morse's model for the concentration dependence of the curvature stress at the plateau modulus. In addition, this factor was discovered as the concentration scaling factor of the storage moduli in Figure 6.12. We find here that it can be used here to scale the higher concentration frequency-dependent data (*i.e.* neglecting the two lowest concentrations 0.04 and 0.06 mg/ml) specifically by dividing the storage modulus by $c^{4/3}$ (Figure 6.14).

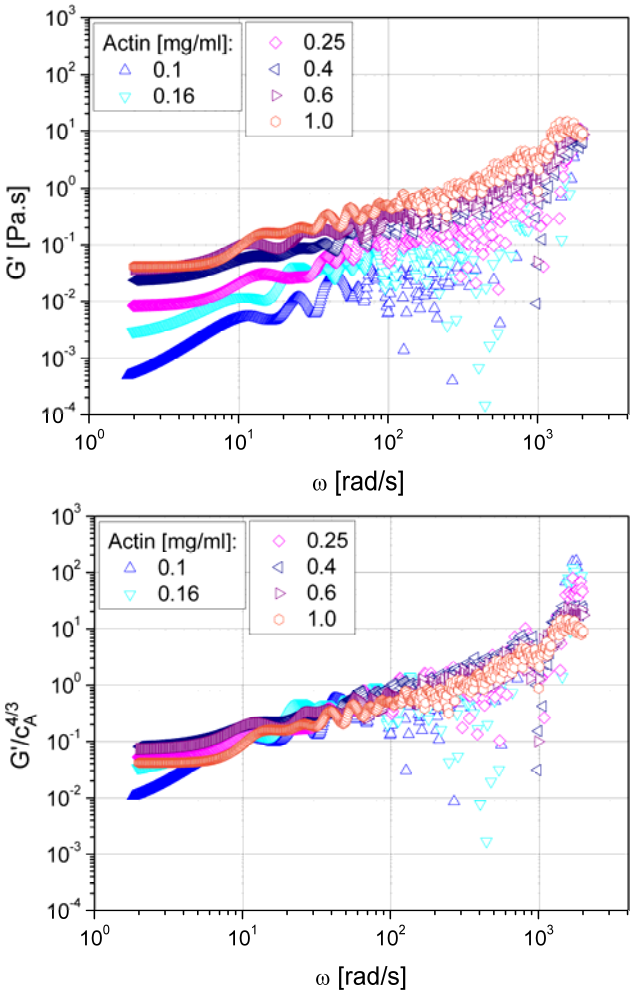

Figure 6.14: *G'(ω) (left) and normalised G'(ω) (right) for actin solutions in concentrations from 0.1-1.0mg/ml. The normalisation factor is a value of $c^{4/3}$.*

Figure 6.15 shows how the two lower concentrations (0.04 and 0.06 mg/ml) scale with the factor of $c^{1/4}$ discovered in the concentration dependence of the storage modulus (which was shown Figure 6.12) and also in the concentration dependence of the relative viscosity (which was shown in Figure 6.7).

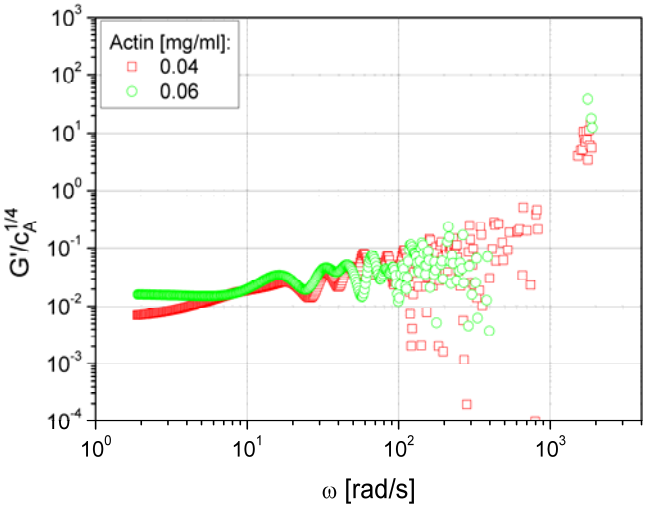

Figure 6.15: *Normalised G'(ω) for actin solutions in concentrations of 0.04 and 0.06 mg/ml. The normalisation factor is a value of $c^{1/4}$.*

Similarly, the frequency-dependent loss modulus can be scaled by the factor $c^{5/8}$ which was found in Figure 6.9 for the high frequency concentration dependence of the $G''(\omega)$ (Figure 6.16). Note that normalising by a factor of c – the low frequency concentration dependence of $G''(\omega)$ – does not cause the curves to collapse.

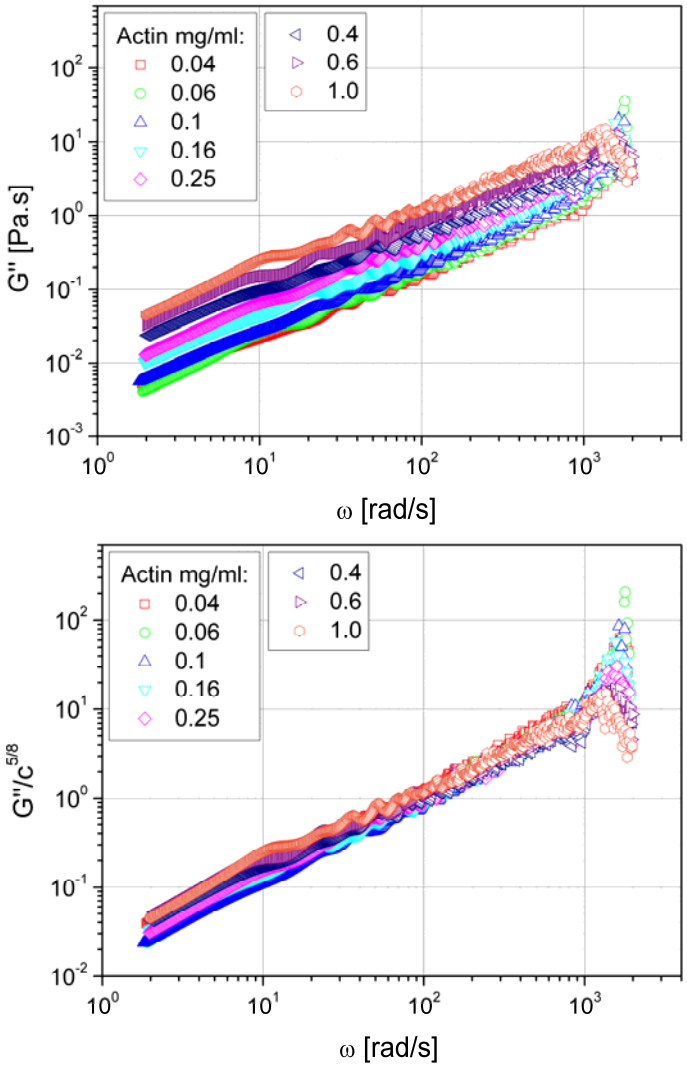

Figure 6.16: *$G''(\omega)$ (left) and normalised $G''(\omega)$ (right) for actin solutions in concentrations from 0.04-1.0mg/ml. The normalisation factor is a value of $c^{5/8}$.*

6.3 Wideband microrheology measurements of actin

We now adopt the 'two trap' broadband step procedure introduced in Chapter 4.3 in order to measure the viscoelasticity of actin over a larger frequency range than is accessible with a single trap. Usually microrheological measurements of viscoelastic materials are either limited to the high end of the frequency response [156, 158, 187] (omitting the low frequencies entirely) or account is taken of the low frequency response only by the use of complementary techniques such as rotational rheometry [71] or passive video particle tracking microrheology [72]. In both cases this has been done without showing an overlapping region, thus leaving a significant information gap. This technique was applied successfully to a single actin concentration of 0.04 mg/ml.

We recall from Chapter 4 that the broadband the procedure consists of two steps; namely measuring the thermal fluctuations of a trapped bead for a sufficiently long time to provide the trap stiffness and the high frequency viscoelastic properties (step I); followed by measuring the transient displacement of a bead flipping between two optical traps (spaced at fixed distance D_0) that alternately switch on/off at sufficiently low frequency (step II). This second step has the potential to provide information about the material's viscoelastic properties over a very wide frequency range, which is only limited by the acquisition rate of the bead position and by the duration of the experiment. However, because of the finite time required by the equipment to switch on/off (i.e. tens of milliseconds), the material's high-frequency response can not be fully determined by this step. The full viscoelastic spectrum is thus resolved by combining the results obtained from both steps.

Step I involves measuring the thermal fluctuations of an optically trapped bead in order to derive the normalised position autocorrelation function, $A(\tau)$ (Figure 6.17, together with the nPAFs predicted for a simple Newtonian fluid (*i.e.* water) with the same trap constant κ). In the Newtonian case, it is expected that $A(\tau)$ decays as a single exponential with a characteristic relaxation rate related to the trap strength, bead size and zero-shear viscosity *i.e.* the well-known result for a massless particle harmonically trapped in a Newtonian fluid, recovered from Equation 4.16, $A(\tau) \to \exp(-\Gamma_i \tau)$ where $\Gamma_i = \kappa / 6\pi a \eta$. If κ and a are known then the viscosity of the Newtonian fluid can be extracted.

On the other hand, in the case of a non-Newtonian fluid (where the viscosity is time-dependent) it is not guaranteed that Equation 4.16 can be resolved (*i.e.* inverse-Laplace transformed) into a simple form like the equation above, as shown in Chapter 4. However, this is no hindrance since we can calculate the viscoelastic moduli *via* the analysis of the nPAF, as in Equation 4.18.

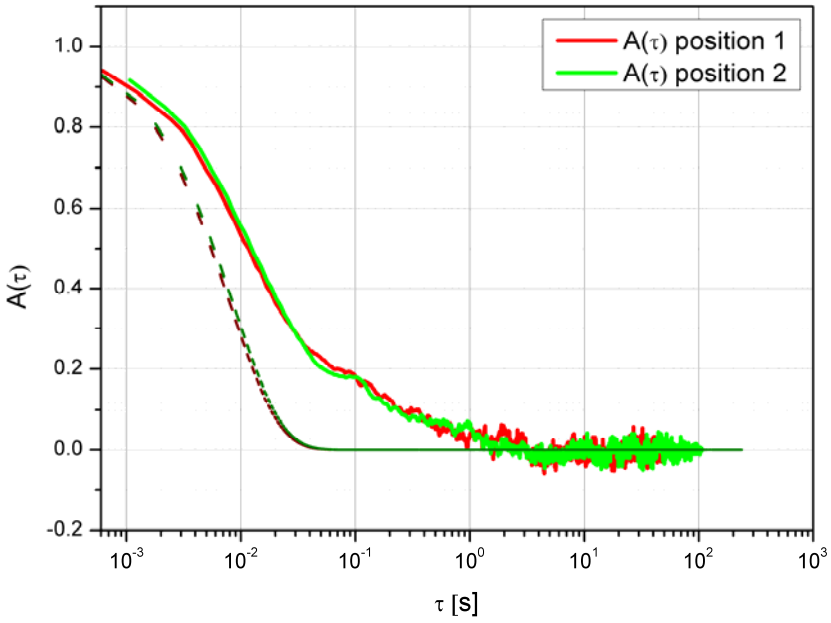

Figure 6.17: *The nPAF vs. lag-time of a 5μm diameter bead in actin at the two trap positions* $\kappa_1 = 5.34 \mu N/m$ *and* $\kappa_2 = 5.04 \mu N/m$. *The dotted lines represent the prediction for a 5μm diameter bead in water at T = 25°C with* $\kappa_1 = 5.34 \mu N/m$ *and* $\kappa_2 = 5.04 \mu N/m$, *respectively.*

In Figure 6.18 we display the impulse response (*i.e.* step II of the procedure) of a 5μm diameter bead suspended in a 0.04 mg/ml actin solution, with a duration between flips of $P = \sim 19s$ and a trap centre-to-centre separation of $D_0 = 1.6 \mu m$, giving $D_0/a = 0.64$. In order to guarantee the linearity of the confining forces exerted by the two optical traps, the distance between them was chosen to be no more than 80% of the bead radius, $D_0 \leq 0.8a$ [163].

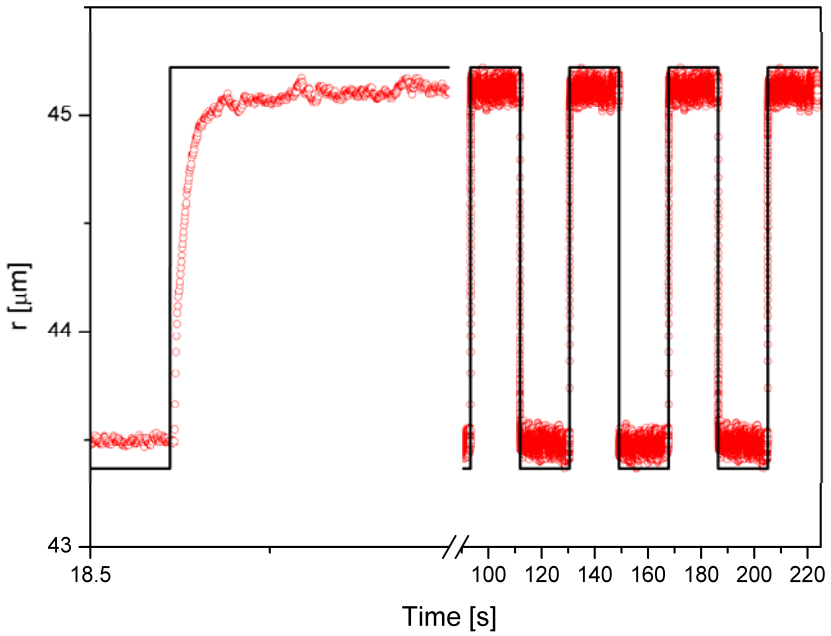

Figure 6.18: *The trajectory of a 5μm diameter bead flipping between two optical traps* κ_1 *(bottom) and* κ_2 *(top) repeatedly switching after a duration* $P = \sim 19s$. *The bead is suspended in actin (with* $\kappa_1 = 5.34 \mu N/m$ *and* $\kappa_1 = 5.34 \mu N/m$*).*

In order both to evaluate $D(t) = \left|\langle \vec{r}(t) \rangle\right| / D_0$ and to reduce noise caused by Brownian fluctuations, the transient measurements were averaged over twenty flips, with the resulting curves shown in Figure 6.19. Experimentally, the switching process of the two traps is controlled by means of a spatial light modulator (SLM) which alternately creates an optical trap in one of two positions. It is important at this point to note that there is a short but finite time for which both traps exist simultaneously [164], due to the finite time required by the SLMs display to update the holographic pattern. This makes the switching process not exactly binary. However, this will of course only affect the high-frequency results obtained during this step which will ultimately be neglected in favour of the high-frequency response from step I.

As in Chapter 5, wideband microrheological measurement are obtained from the optical tweezers by combining the frequency responses obtained from both steps I and II of the procedure. In particular, the material's high-frequency response is determined by applying Equation 4.18 (*via* Equation 4.7 with A_k replacing g_k) to the $A(\tau)$ measurements (in which low-frequency information tends to be very noisy); whereas, the low-frequency response is resolved by applying Equation 4.22 (*via* Equation 4.7 with D_k replacing g_k) to the data describing the bead's transient response to the flipping traps (in which the high-frequency response is limited by the performance of the SLM).

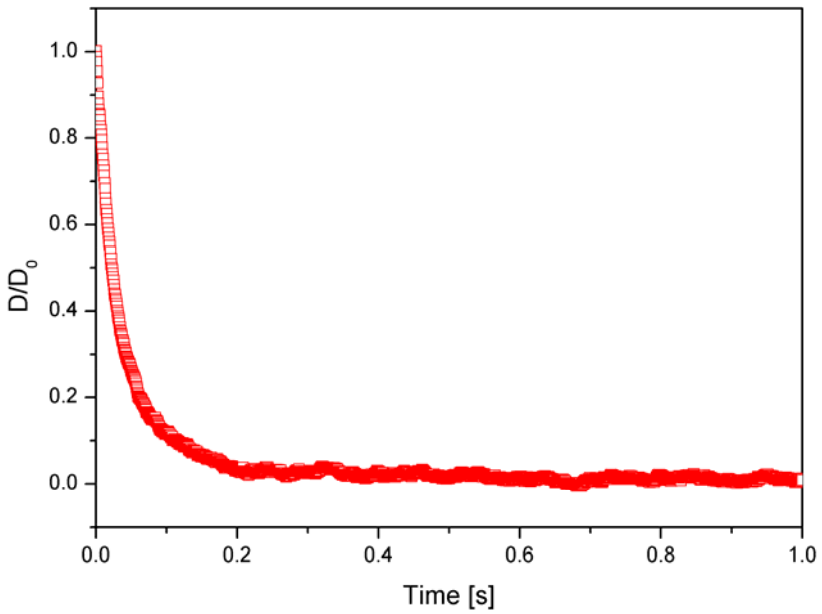

Figure 6.19: *The normalised mean position of all step-down data shown in Figure 6.18* i.e.*when simultaneously trap 2 (top) switches off and trap 1 (bottom) switches on.*

Typical results for actin are shown in Figure 6.20. It is evident that, although there is some noise in the frequency domain which comes from genuine experimental noise in the time-domain data (which can be reduced by increasing the number of flips), there is a clear overlapping region of agreement between the two methods, especially in the loss modulus, which makes the whole

procedure self-consistent. Moreover, it confirms the ease with which the low-frequency material response can be explored.

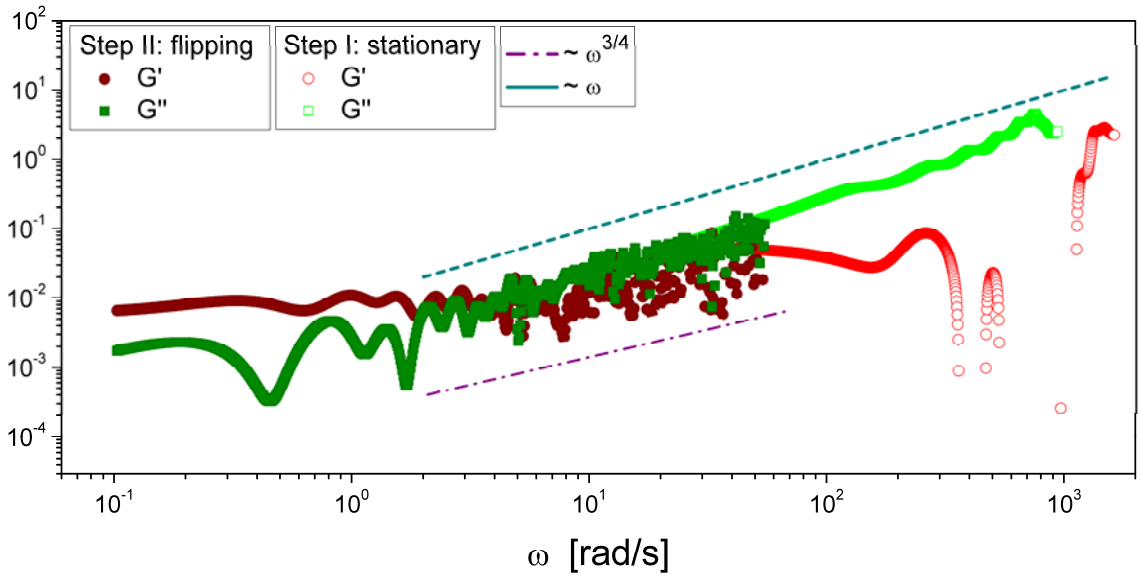

Figure 6.20: *Storage (G') and loss (G") moduli vs. frequency of a solution of 0.04mg/ml actin; measured by means of both Equation 4.18 (high frequencies) and Equation 4.22 (low frequencies) applied directly to the experimental data presented in Figure 6.17 and Figure 6.19, respectively.*

The loss modulus once again exhibits a steeper slope ($\sim\omega$) than described by Morse, but this is a result of the lower actin concentration used, as before. The storage modulus shows some agreement with the high frequency prediction of $\sim\omega^{3/4}$. The cross over between the storage and loss modulus at the entanglement frequency τ_e^{-1} can clearly be seen. This intersection was only just reached with the 'static' optical tweezer measurements in the previous section.

Note that actin can be up to 20μm long, thus it can have a reptation time is typically on the order of hours (since $\tau_{rep} \propto L_c^3$). It is therefore possible for $G'(\omega)$ to extend to very low frequencies. Indeed, Morse's model for semiflexible polymers with $L_c = 10L_p$ predicts a reptation time of around 100,000 seconds (~27 hours). Bulk rheometer studies of 1 mg/ml actin [177, 184] found that even at their lowest accessible frequency ($\sim 10^{-3}$ rad/s) $G'(\omega)$ was significantly larger than $G''(\omega)$, suggesting a very low terminal relaxation frequency. By using the two-trap method presented here optical tweezers have the potential to span a large frequency range; however, a measurement of these extremely low frequencies would involve monitoring the tracer bead position for over a day. This is problematic in terms of the sheer amount of data that would need to be collected and analysed. Indeed, this is the reason that we use a low concentration of actin for the two trap method. Although higher concentrations were attempted, it was found that the actin had still not relaxed completely between alternate flips of the traps. When the time between flips was extended

(~hours) the size of data sets collected (~millions of data points) prohibited analysis, and this is an issue that is still being dealt with.

To conclude, we have analysed the concentration scaling laws of actin solutions from both the time-dependent and frequency-dependent data. There are shown to be similar concentration scaling laws in both the frequency and time domains, which are coincident with those predicted by theoretical models. In addition, we have applied the wideband microrheological method described in Chapter 4 to an *in vitro* reconstituted solution of actin.

Chapter 7

ACTIN AND MYOSIN NETWORKS

It has been observed that single cells possess viscoelastic moduli with a much higher absolute value than those observed in reconstituted actin solutions alone [188-191]. This can be attributed to the huge variety of proteins that actin interacts with as it undergoes its normal routine. The biochemical differences between these proteins are exploited by the cell so as to adapt to as many environments and conditions as possible. Many actin-binding proteins possess the ability to significantly influence the structure of the actin cytoskeleton, and may therefore affect the viscoelastic properties of an actin network. For a small number of actin-binding proteins the viscoelastic change they produce within an actin network has been quantified *e.g.* fascin [192], myosin filaments [193], HMM [194], α-actinin [195], scruin [196] and filamin [197].

One of the most ubiquitous of these actin binding proteins is the motor protein myosin, of which the myosin-II isoform found in skeletal muscle cells has been extensively characterised in terms of its biophysical and kinetic properties [38, 89, 99, 198]. In practice however, the thick myosin-II filaments that occur naturally in muscle cells are problematic to work with. A common alternative to these filaments are the protolytically produced fragments that are soluble and enzymatically active. The S1 fragment is comprised of a single head domain attached to a part of the myosin-II heavy chain. It retains the ability to bind to actin; indeed, if ATP is present in solution the head domain alone can generate movement [98, 99]. Heavy meromyosin (HMM) contains two head domains and a portion of the heavy chain, as described in detail in Chapter 1.

The rigor properties (*i.e.* with no adenosine triphosphate (ATP) present) of HMM networks have been well studied [199-201]. For example, Tharmann *et al.* [200] demonstrated experimentally that

the linear elastic response of the cross-linked rigor networks is of entropic origin and fully determined by the distance between the cross-linked points (hence, the cross-link concentration).

In the general behaviour of polymer networks, recall that distinct molecular mechanisms can lead to a relaxation of an external or internal stress on different time scales, producing either elastic or viscous behaviour depending on whether energy is stored or dissipated. Many synthetic polymer networks contain cross-links that are covalent in nature, which causes a predominantly elastic response over a wide frequency range, as discussed in Chapter 2. This is a result of the *covalent* cross-links suppressing the single polymer diffusion that exists in entangled solutions; which in turns means that reptation is repressed and the low frequency viscoelastic behaviour of a covalently cross-linked polymer network is expected to reach a constant level of elasticity whilst viscous effects become negligible.

Transient cross-links can be defined as those based on electrostatic interactions or Van der Waals forces, as is the case with actin and myosin [194]. These cross-links are different to purely covalent bonds; in particular, transiently cross-linking proteins can be characterised by an off-rate k_{off}, which typically corresponds to frequencies in the intermediate regime of several mHz up to a few Hz [202, 203]. A molecular understanding of the mechanisms responsible for the behaviour of transiently cross-linked cytoskeletal networks is needed to quantify the mechanical properties of living cells.

In contrast to covalently cross-linked filaments (as discussed in Chapter 2, for the model presented by Morse [87]), if transient cross-links are present, a pronounced minimum and maximum in the viscous loss moduli is observed at low frequency [194, 202] (Figure 7.1). In the case of rigour-HMM, this viscous maximum occurs around $f_{\max} \approx 0.03Hz$ [194], and this time scale is independent of the cross-link density. Alongside this feature in the loss modulus there is always a decrease in elasticity at low frequencies, although the elastic response is still the dominant one. The magnitude of the storage modulus is dependent upon cross-link density, and this is not affected by frequency.

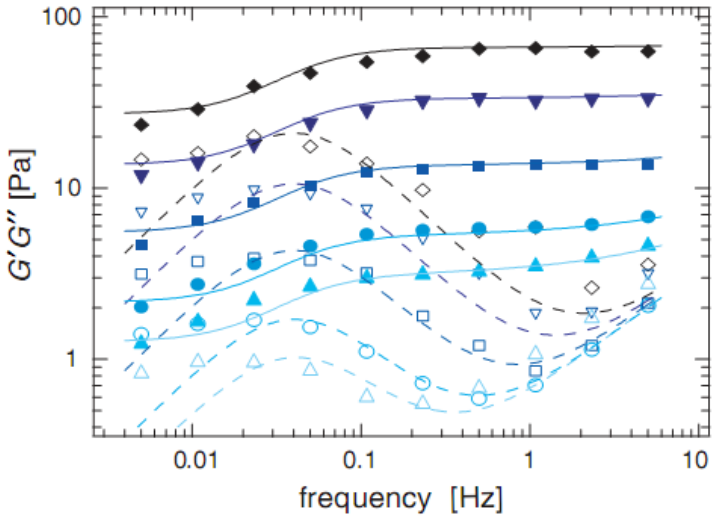

Figure 7.1: *(Taken from Ref. [194]) Elastic (solid symbols) and viscous (open symbols) response for actin-rigor-HMM networks as a function of frequency [c_{ACTIN}=19μM, Ratio of HMM/actin =0.0076 (upright triangles) up to R= 0.143 (diamonds)]. The solid and dashed lines represent a global best fit of the model described in the study.*

In contrast to HMM, the S1 molecule has only a single actin-binding domain and cannot cause cross-linking between filaments, and its effect on actin networks has not been well studied; indeed, to the best of our knowledge, only one rheological study has been carried out by Le Goff *et al.* [204] which focused on the very high (>1000 Hz) frequency response obtained using DWS.

In this chapter we aim to explore the dynamics of *active* actin and HMM or S1 networks (*i.e.* networks experiencing an excess of ATP), and the viscoelastic properties of *active* actin/S1 networks at 'medium' frequencies, which we class as between the 'low' frequency (0.01-10 Hz) work of Lieleg *et al* [194], and the 'high' frequency (10^3-10^6 Hz) data of Goff *et al* [204]. Note that, the highest frequency we can access with optical tweezers (~1000Hz) corresponds to a timescale that is relevant to the myosin power-stroke duration (as described in Chapter 1) inferred from biochemical assays (~1ms) [204].

A major line of work in recent years has been to address the issue of how 'active' systems in non-equilibrium should be treated [205-208]. Active systems may be described as ones where some driven process occurs, for example, the interaction of actin with myosin molecules in the presence of adenosine triphosphate. The fluctuation-dissipation theorem (FDT) dictates that the same random 'kicks' of molecules in a system cause both Brownian diffusion motion and viscous dissipation, or equivalently that the response of a system in thermodynamic equilibrium to a small applied force is the same as its response to a spontaneous fluctuation [209]. If non-thermal forces are present within a system, then the fluctuations are greater than can be described thermally, and the FDT breaks down. This renders the Einstein component of the Einstein-Stokes relationship invalid, because the Einstein description of Brownian motion is violated.

One of the studies that instigated this branch of research was by Mizuno *et al* [205], who evaluated active and passive microrheology of *in vitro* actin filaments and myosin mini-filament networks. They found low-frequency discrepancies in the passive microrheology measurements when compared to the active microrheology. These non-thermal fluctuations were attributed to the myosin mini-filaments changing from a non-progressive to a progressive state at low ATP concentrations, whereby they increased the tension in the actin network, as shown in a change of scaling law of the elastic modulus from $\omega^{3/4}$ to $\omega^{1/2}$ [210]. However, we must highlight that there were two conditions that needed to be satisfied in order for these non-active fluctuations to be observed, namely that the ATP levels were low (≤60μM), either through ATP hydrolysis or through low initial conditions, and that the system was studied at a frequency <10Hz. If the ATP levels were kept at 1mM (using an ATP regeneration system as we have used in this thesis) then there was *no difference* from actin networks without myosin.

Notwithstanding, the system studied here differs substantially from that of Mizuno *et al* because (I) we use a higher ATP concentration higher than 60 μM; (II) our experiments are conducted at a higher frequency (>10Hz), and (III); we do not use myosin filaments, instead we use double headed (HMM) and single headed (S1) myosin fragments. Single S1 molecules possess the ability to process along an actin filament [98] but they cannot cross-link filaments and therefore cannot increase tension in a manner comparable to myosin mini-filaments. Since HMM *does* possess the ability to cross-link actin filaments, we only study the dynamics of actin and HMM solutions in the time-domain, through the MSD and the concentration scaling laws.

To explore the dynamics and viscoelasticity of *in vitro* reconstituted solutions of actin and myosin networks 'static' optical tweezer measurements are used (*via* the method described in Chapter 4.1) to analyse the normalised mean-square displacement, $\Pi(\tau)$, of micron-sized tracer probes in order to derive the concentration scaling laws of actin and S1/HMM solutions from the time-domain. Following on from this, the storage and loss moduli of actin/S1 are examined and the concentration dependence of the frequency-dependent viscoelastic response is compared to that of the time-dependent data.

7.1 Concentration scaling laws of actin and myosin networks

To derive the concentration scaling laws of active actin/HMM and actin/S1 networks, the Brownian trajectory of optically trapped beads embedded in both the materials were analysed, *via* the normalised MSD, $\Pi(\tau)$. S1 and HMM were added to actin (0.04mg/ml) in ratios of one molecule per actin filament (1:1) and four molecules per actin filament (4:1); both in the presence of excess ATP. In addition, a control sample of 'dead' or inactive HMM was analysed. The nMSD is plotted against normalised lag time in Figure 7.2. All results were averaged over a number of measurements N [(a) actin N=3, (b) dead HMM/actin N=2, (c) S1/actin (1:1) N=5, (d) HMM/actin (1:1) N=4, (e) S1/actin (4:1) N=4, (f) HMM/actin (4:1) N=5] taken from multiple samples over a period of three days. The error bars (representing the standard deviation) have been omitted from Figure 7.2 for ease of viewing, but have been plotted in Figure 7.3.

The error bars are relatively small, although the errors for HMM/actin (1:1) are slightly larger as they exceed the errors of the HMM/actin (4:1) at very high frequency. At lower frequencies (longer timescales) this overlapping disappears. The normalised MSD, $\Pi(\tau)$, of the dead HMM control sample is indistinguishable from that of the pure actin solution, and has a marked difference from the HMM/actin (1:1) sample, showing that no chemical interaction is taking place. Thus, steric interactions between actin and HMM are not enough to produce a marked behavioural change in the actin network. The S1/actin (1:1) sample is also virtually the same as that of the pure actin, whereas the HMM/actin solutions in both low and high ratio show a distinct change from that of actin alone. Interestingly the higher ratio (4:1) of the S1/actin sample actually lies above the $\Pi(\tau)$ curve of actin, and thus closer to the curve of water (slope of 1) implying the solution possesses reduced viscoelasticity when compared to that of actin.

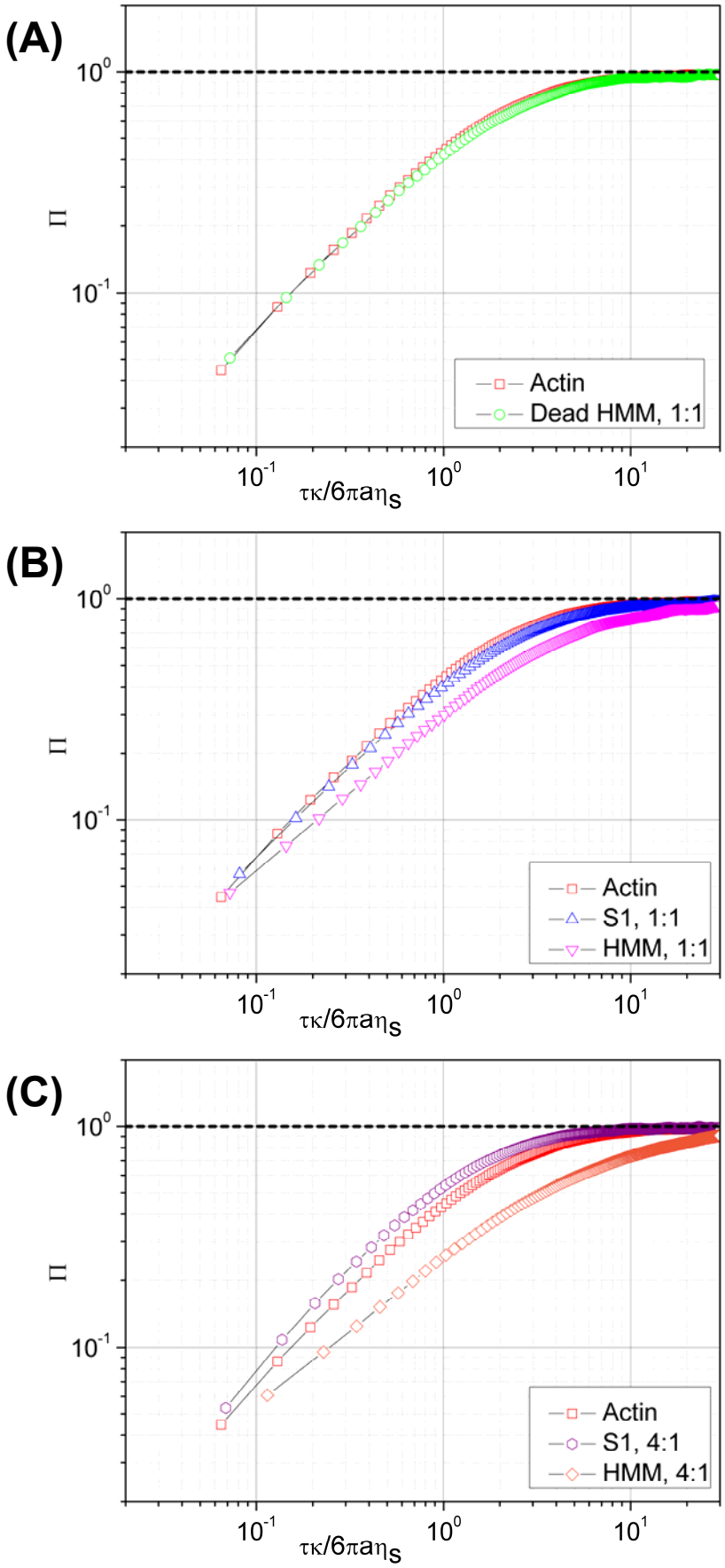

Figure 7.2: $\Pi(\tau)$ vs. *normalised lag time for a 5μm diameter bead in (A) pure actin or actin with dead HMM, (B) actin with single (S1) or double (HMM) headed myosin fragments in the ration 1:1, and (C) actin with single (S1) or double (HMM) headed myosin fragments in the ration 4:1.*

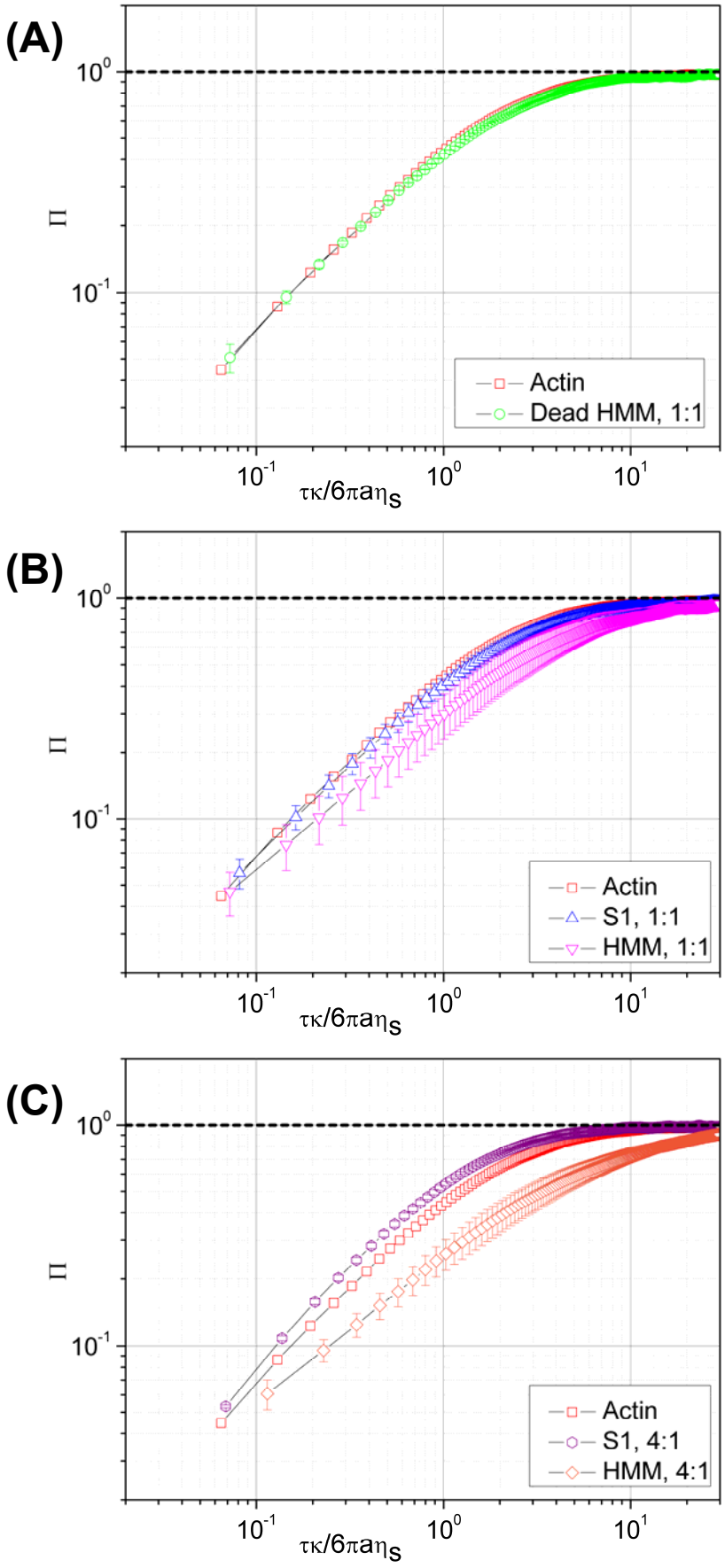

Figure 7.3: $\Pi(\tau)$ vs. *normalised lag time (with error bars) for a 5μm diameter bead in (A) pure actin or actin with dead HMM, (B) actin with single (S1) or double (HMM) headed myosin fragments in the ration 1:1, and (C) actin with single (S1) or double (HMM) headed myosin fragments in the ration 4:1. Error bars represent the standard deviation.*

As discussed in Chapters 5 and 6, we have found that concentration scaling laws of polymer solutions can be obtained directly from the time-domain, with no need to convert the experimental data to the frequency-domain, through the use of a Fourier transform. The first method of doing this is by analysing the relative viscosity, $\eta_{rel}(\tau)$ (Figure 7.4) and specific viscosity $\eta_{sp}(\tau)$ (Figure 7.5).

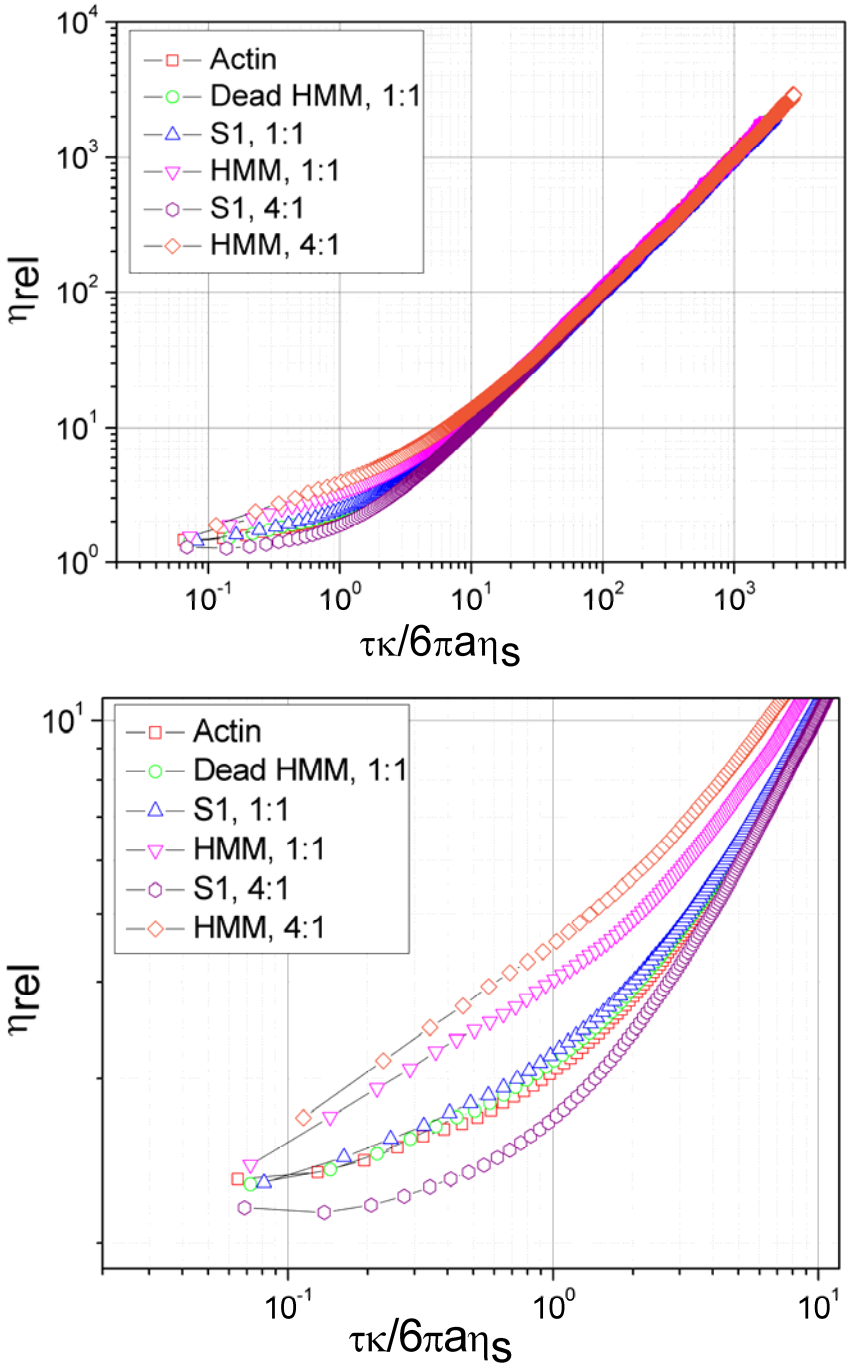

Figure 7.4: *Relative viscosity, $\eta_{rel}(\tau)$, vs. normalised lag time for actin (0.04mg/ml), and for actin with dead myosin, single headed (S1) myosin fragments (Ratio of myosin:actin of 1:1 and 4:1) or double headed (HMM) myosin fragments (Ratio of myosin:actin of 1:1 and 4:1). Inset is a magnified section of the graph (at short times).*

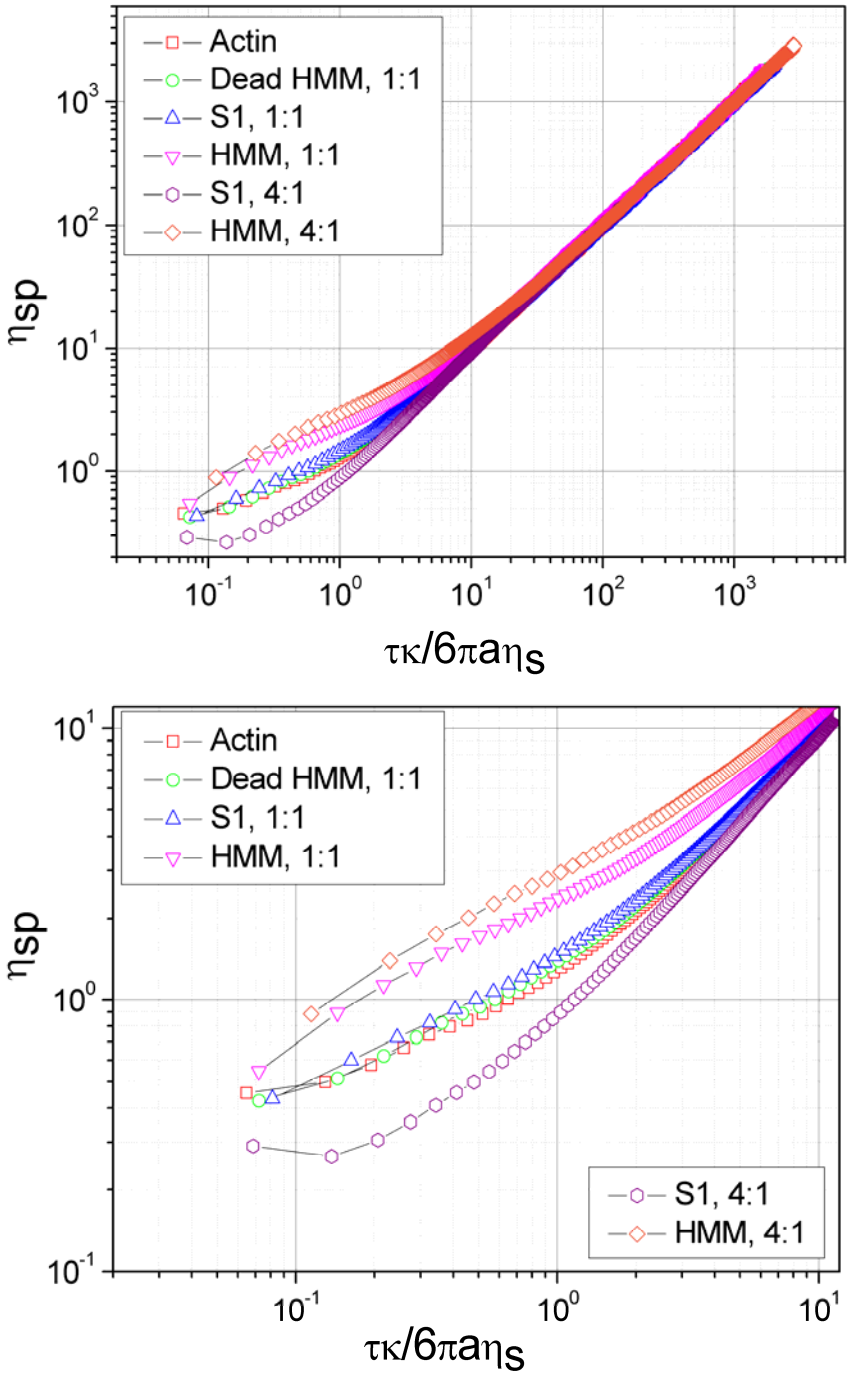

Figure 7.5: *Specific viscosity, $\eta_{sp}(\tau)$, vs. normalised lag time for actin (0.04mg/ml), and for actin with dead myosin, single headed (S1) myosin fragments (Ratio of myosin:actin of 1:1 and 4:1) or double headed (HMM) myosin fragments (Ratio of myosin:actin of 1:1 and 4:1). Inset is a magnified section of the graph (at short times).*

The next step in deriving the concentration scaling factors is to uncover a factor that normalises the specific viscosity. In this case, the scaling factor is obtained by first dividing the specific viscosity by the number of myosin heads per molecule (*i.e.* 1 for S1, and 2 for HMM), then by the square route of the concentration of the myosin fragments. If this normalisation factor is also applied to the normalised time, it produces a master curve for the HMM/actin solutions and the lower ratio of S1/actin, as shown in Figure 7.6.

The S1/actin (4:1) data does not collapse onto the same curve as the other networks under these normalisation conditions. This can be explained by the different mechanisms by which the two molecules interact with actin *i.e.* the cross-linking capabilities of HMM *vs* .the single actin binding domain of S1. The fact that the S1/actin (1:1) curve collapses onto the master curve shows that at low S1 concentrations the viscoelastic response is similar to that of low concentrations of HMM, but for the higher concentrations the two responses diverge.

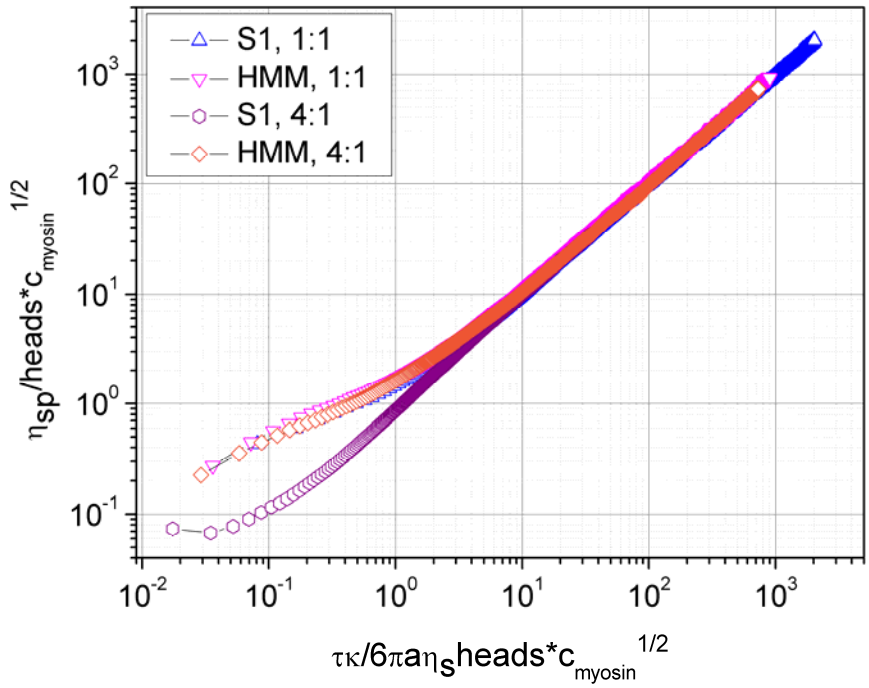

Figure 7.6: *Specific viscosity normalised by a factor of (no. of heads x $c_{myosin}^{1/2}$)* vs. *normalised lag time (no. of heads x $c_{myosin}^{1/2)}$ for actin (0.04mg/ml) with single headed (S1) myosin fragments (Ratio of myosin:actin of 1:1 and 4:1) or double headed (HMM) myosin fragments (Ratio of myosin:actin of 1:1 and 4:1)*

The factor of $c_{myosin}^{1/2}$ is different from that found in pure actin networks ($c_{actin}^{4/3}$). As far as we are aware, this scaling factor is not predicted anywhere in the literature.

A corollary of this normalisation is that normalising both the specific viscosity and time with regards to only the number of heads per molecule (one for S1, and two for HMM) for the low concentration 1:1 ratio measurements also causes the curves to collapse, as in Figure 7.7.

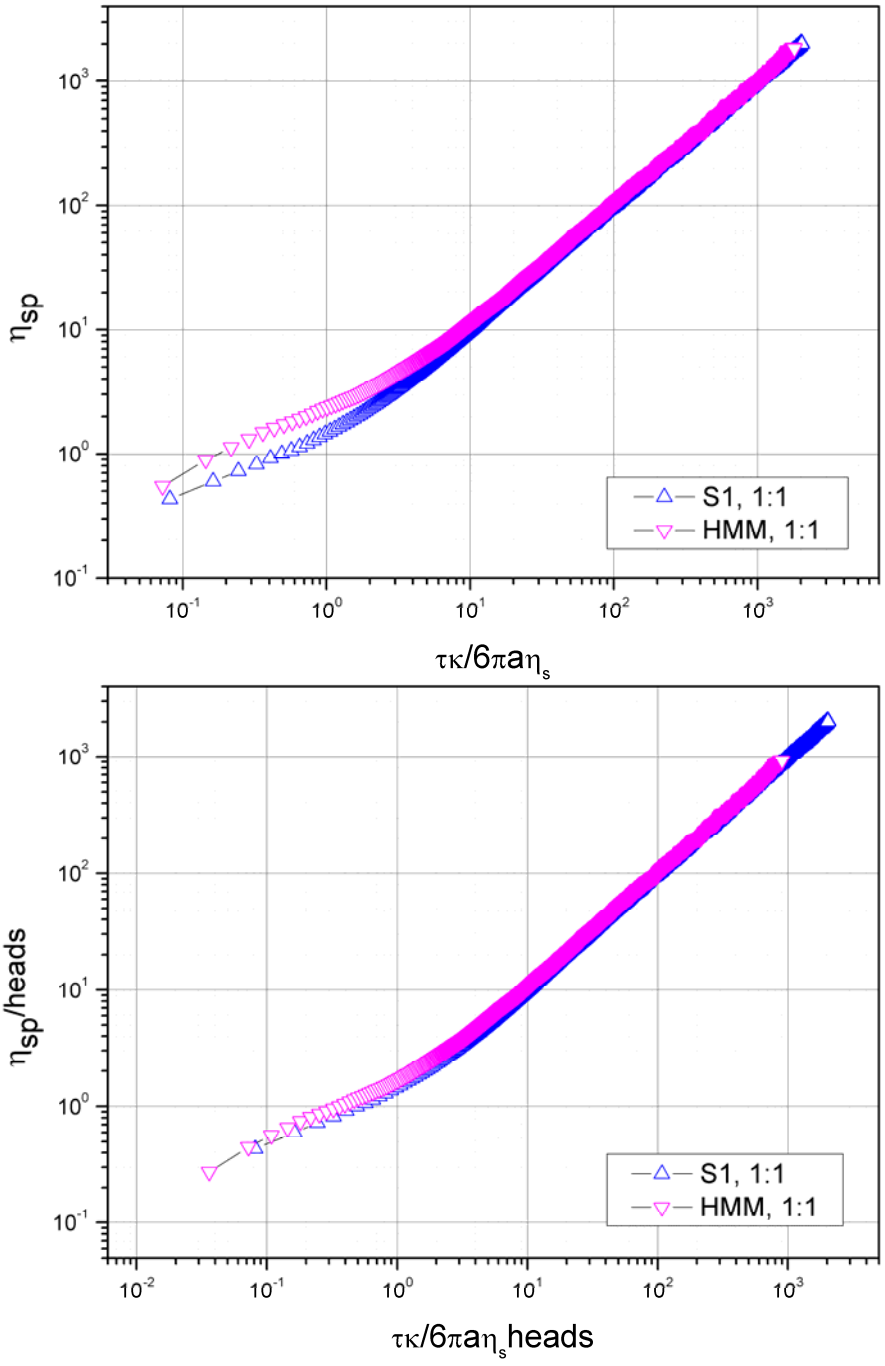

Figure 7.7: *Specific viscosity normalised by number of molecular heads* vs. *normalised lag time (taking into account number of molecular heads) for actin (0.04 mg/ml) and S1 or HMM in 1:1 ratio.*

The concentration dependence can also be obtained by analysing the slope of the nMSD *vs.* normalised time close to zero. This value is equal to $1/\eta_{rel}$ (where η_{rel} is the relative viscosity) and it was shown in Chapter 5 that plotting the η_{rel} against concentration ratio (R) for PAM solutions produced the concentration scaling factors predicted in the literature. If the η_{rel} of the actin and myosin solutions are plotted against the concentration ratio (Figure 7.8), it can be seen that two very approximate scaling regimes are uncovered: an increasing η_{rel} for actin/HMM and a decreasing η_{rel} for actin/S1.

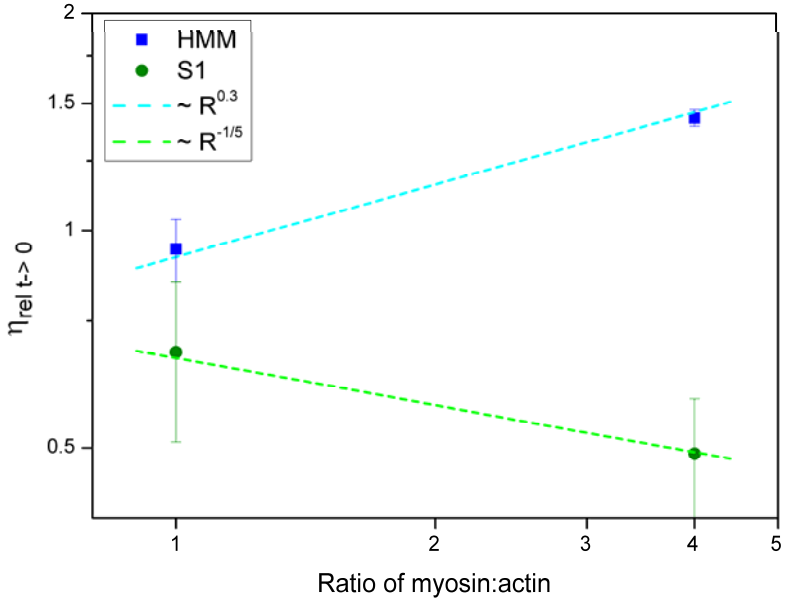

Figure 7.8: *The relative viscosity, η_{rel}, at $t \to 0$ plotted against actin/myosin ratio for actin/HMM (squares) and actin/S1 (circles). The lines are a guide to the gradient.*

Whilst there are obvious limitations to obtaining accurate slopes from graphs with only two points, the error bars are small enough that the general trends can still be hinted at. In Section 7.2.2 actin/S1 networks are studied in greater detail and similar scaling laws are found as in Figure 7.8.

7.2 Viscoelasticity of actin-S1 networks

In order to elucidate further the effect of adding S1 molecules to actin networks, we probe the linear viscoelastic properties of a number of additional active S1 and actin solutions. The storage, $G'(\omega)$, and loss, $G''(\omega)$, moduli were once again calculated from measuring the trajectory of an optically trapped bead in a series of concentrations of S1 and actin (in the presence of ATP). An average was taken of the complex moduli of N measurements per concentration ratio [N=5-7 for all data sets] (Figure 7.9, A-G).

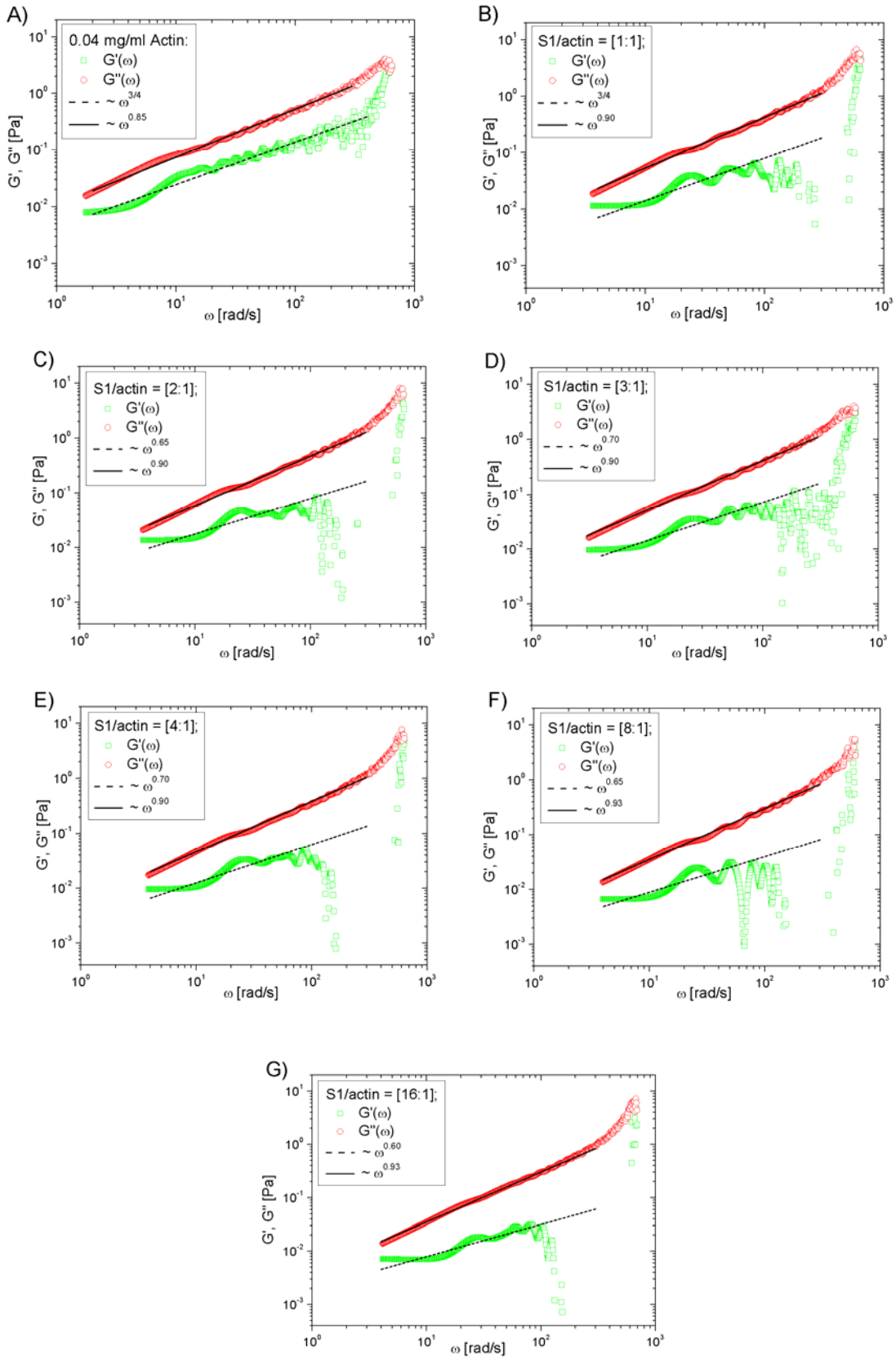

Figure 7.9 [A-G]: *Loss and storage moduli vs. frequency for (A) pure actin (0.04mg/ml) or actin with single head myosin fragment (S1) in ratios of: (B) S1/actin 1:1, (C) 2:1, (D) 3:1, (E) 4:1, (F) 8:1 and (G) 16.1. The solid and dotted lines are a guide for the gradients.*

For the pure actin sample (Figure 7.9A), we see that the storage modulus scales with $\omega^{0.85}$ and the loss modulus with $\omega^{3/4}$. The scaling of 3/4 is as described by Morse [87] and as discussed in previous chapters, whereas the scaling of 0.85 is between the values of 7/8 and 1, as measured for other low concentration actin samples in Chapter 6. The most obvious change that the addition of S1 produces in the network is the immediate decrease in the storage modulus at high frequencies, opposed to HMM, which produces an increase [201]. Indeed, apart from in the 3:1 ratio (Figure 7.9D), the elastic component practically vanishes for all frequencies > 100 rad/s, leaving only some high frequency noise.

The study by Le Goff *et al.* found that S1 decreased the elastic modulus at very high frequencies (>1000Hz), as well as changing the scaling factor of the shear modulus amplitude (G_d) from $G_d \sim \omega^{3/4}$ to $G_d \sim \omega^{7/8}$, indicating dominance of the longitudinal modes of fluctuation [204]. We find here that S1 also decreases the elastic modulus at lower frequencies (4-1000Hz), but we do not see the concomitant change in scaling law.

To extract further information, the concentration dependence of the loss and storage moduli are plotted for frequencies of 80 and 400 rad/s for the loss modulus, (Figure 7.10) and 50 rad/s for the storage modulus (Figure 7.11). Both the loss and storage moduli have been normalised by the value for pure actin.

The loss moduli graphs have been shown in both linear (Figure 7.10, A) and log-log (Figure 7.10, B) form. The added lines on the log-log graph are designed to extract the actual dependence of the concentration.

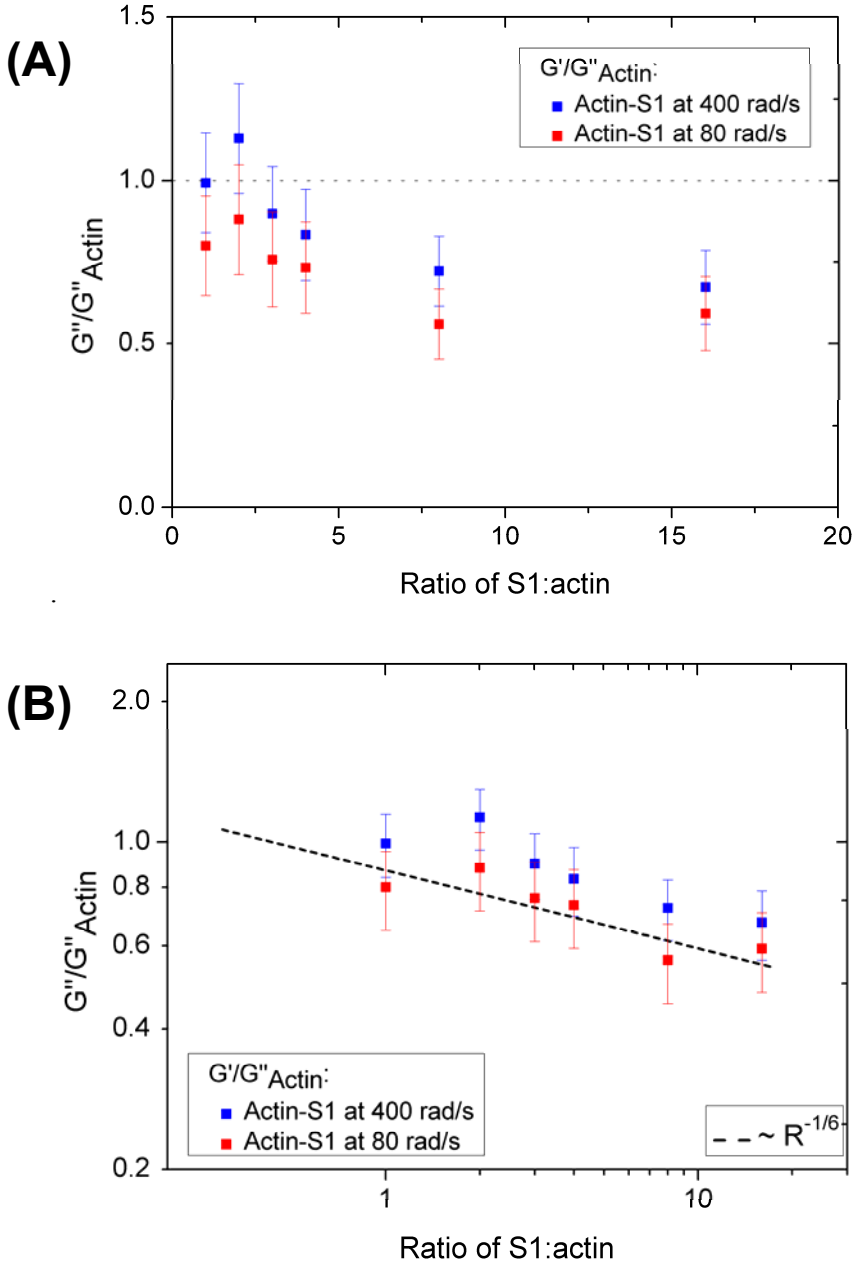

Figure 7.10: *The normalised loss modulus* $G''(\omega)/G''_{Actin}(\omega)$ *vs. ratio of myosin:actin (for data extracted from the complex moduli of Figure 7.9) for actin/S1 samples at a frequency of 80 and 400 rad/s, and at S1:actin ratios of 1:1→16:1 .(A) Linear graph: The lines have been added to demonstrate the general trends of the concentration dependence. (B) Log-log graph: The dotted lines are a guide for the gradient.*

The data in Figure 7.10 confirms the trend first noticed in Figure 7.8, where the loss modulus decreases as the S1 concentration increases. At both frequencies in Figure 7.8 the loss modulus scales with $\sim R^{-1/6}$. From this it can be inferred that the S1 molecules suppress the viscous dissipation of the actin filament. If we assume that (for the frequencies measured here) that the tension stress contributes the most to the response of the complex shear modulus, then from Equation 2.24 (Morse's equation for the limiting value of $G^*_{tens}(\omega)$,) we see that the stress is proportional to the persistence length (as $L_p^{5/4}$, which is also predicted by MacKintosh [130]). The

persistence length of actin filaments interacting with S1 molecules has been measured to be less than that of an actin filament [204], which would correspond to a decreasing tension stress contribution to the high frequency moduli.

The scaling uncovered here for the concentration ratio dependence of the loss modulus is similar to the scaling factor of -1/5 seen in Figure 7.8, where the relative viscosity was plotted against concentration. From Chapter 5, the relative viscosity can be related to the complex shear modulus *via* Equations 5.23 and 4.18, thus it is valid to compare the scaling laws of both quantities.

Figure 7.11 shows the relationship between the concentration and the storage modulus, where the data is shown in linear (Figure 7.11A) and log-log (Figure 7.11B) form. It can be seen that the concentration dependence of the storage modulus at a frequency of 50 rad/s is approximately $R^{-1/3}$, which is a stronger dependence than measured for the relative viscosity in Figure 7.8.

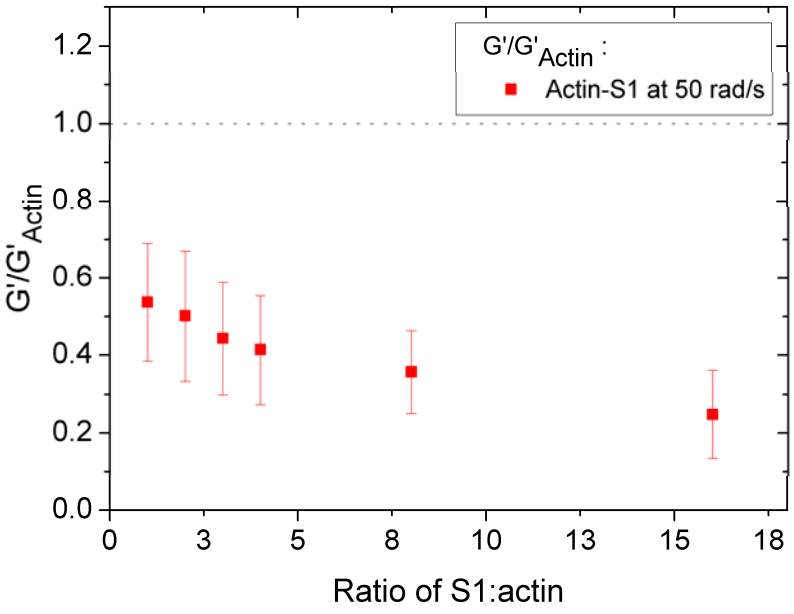

Figure 7.11 [A]: *The normalised storage modulus* $G''(\omega)/G''_{Actin}(\omega)$ vs. *ratio of myosin:actin (for data extracted from the complex moduli of Figure 7.19) for actin/S1 samples at a frequency of 50 rad/s, and at S1:actin ratios of 1:1→16:1. The data is shown on a linear plot where the lines are added simply to illustrate the shape of the concentration dependence.*

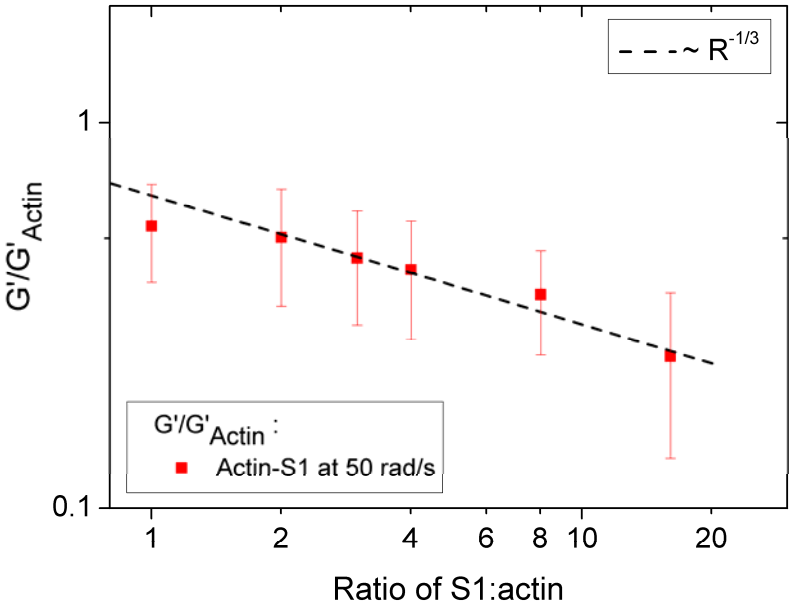

Figure 7.11 [B]: *The normalised storage modulus* $G''(\omega)/G''_{Actin}(\omega)$ vs. *ratio of myosin:actin (for data extracted from the complex moduli of Figure 7.9) for actin/S1 samples at a frequency of 50 rad/s, and at S1:actin ratios of 1:1→16:1. The data is shown on a log-log plot where the dotted lines are a guide for the gradient.*

What is striking about the effect of S1 upon actin networks is that the observed decrease in network elasticity is similarly observed in active solutions of actin and myosin *filaments.* Humphrey *et al*. [211] studied active actin and myosin-II mini-filaments (short versions of the myosin 'thick' filaments) and discovered a similar reduction in storage (and a small reduction in loss modulus) when compared to pure actin. Using a ratio of myosin to actin of 15:1, they showed that when no ATP was present, the myosin filaments act as a cross-linker (similar to HMM samples that were discussed earlier in the chapter), thus increasing the elastic plateau modulus. Once ATP was added however, the storage modulus decreased to $40\% \pm 10\%$ of actin alone (a value close to the $25\% \pm 11\%$ for the 16:1 sample of Figure 7.13). A simple tipping of a cuvette demonstrated that the presence of myosin caused the actin solution to flow, confirming that it became more fluid-like. A subsequent fluorescence comparison of filaments with and without myosin motors highlighted differences in both speed and directionality; in the absence of myosin motors, the filament undergoes random Brownian motion confined by the surrounding unlabelled actin filaments; in the presence of myosin filaments, the myosin induces longitudinal sliding of the actin filaments (in the presence of ATP); thus, they found that the average reptation time of the network decreased from 500 ± 100 seconds to 8 ± 0.4s when myosin was added.

The difference between the myosin mini-filaments and the S1 molecules studied in this chapter lies in the timescales upon which they modify the actin behaviour. In the case of the mini-filaments $G'(\omega)$ is only much less than $G''(\omega)$ (*i.e.* the material *flows*) for frequencies lower than τ_{rep}^{-1}

(approximately 1/8 rad/s in this case) whereas for the S1 molecules $G'(\omega)$ is decreased at high frequencies when compared to actin alone, due to the increase in persistence length.

In this Chapter we have investigated the effect of two types of myosin fragments upon the dynamics or viscoelasticity of actin networks. In particular, we have presented a direct comparison between HMM and S1 molecules in order to highlight the different ways in which they modify the relative viscosity of actin solutions.

Chapter 8

MEASURING THE MECHANICS OF SINGLE CELLS

Measuring the properties of protein networks *in vitro* has great importance in understanding cell mechanics, but being able to measure cytoskeletal properties *in situ* within a live cell takes us a step closer to seeing the 'bigger picture' of cell behaviour. Many more variables come into play during an *in vivo* experiment and being able to accurately and sensitively decipher the viscoelastic changes requires a more careful interpretation than for protein networks. As many authors have noted, the mechanical properties of a cell's cytoskeleton can influence factors such as growth, apoptosis, motility, signal transduction, gene expression *etc* [89, 212, 213]. Related to this is a desire to be able to provide a theological interpretation of the cell's viscoelastic response that has the potential to yield quantitative information on the cell's cytoskeletal structure. Consequently, we have developed a means of passive video particle-tracking microrheology measurements that quantitatively measure changes in the time-dependent and viscoelastic properties of a cell as a consequence (in this case) of simple changes in its external environment *i.e* subjecting a cell to hypo-osmotic shock. In the process, we identify scaling laws that differ from the expected high-frequency cell response of $\sim\omega^{3/4}$, which we attempt to describe rheologically as well as biologically.

Osmotic regulation and the transport of osmotically active molecules are fundamental to both metabolic processes and homeostasis of cells and require a precise regulation and maintenance of intracellular water homeostasis [214]. The ability of many cells to regulate their volume, *via* internal restructuring, in response to osmotic changes in their environment is an essential component of normal cellular function. This regulatory volume change is linked to a reorganization of the cytoskeletal actin networks [215-218]. Figure 8.1 is taken from Ref. [218] and provides a good example of how the actin structures in a cultured astrocyte cell can change under

exposure to various osmotic conditions. Cells thrive in iso-osmotic conditions where their environment contains physiological salt levels. Exposure to a hypotonic solution typically induces an initial swelling followed by a compensatory cell shrinkage, which occurs over a slower timescale of several minutes. The modulation of the actin dynamics and polymerisation that accompanies these regulatory volume changes has been shown in various cell types by methods such as DNase I inhibition assay, fluorescence measurements of phalloidin-labelled actin, and immunoblot analysis [219].

In this thesis we have developed a video particle-tracking tool to study the microrheology of cells, using a Jurkat lymphocyte cell line as a model system. In general, lymphocytes have been shown to have a response to hypo-osmotic solutions that is influenced by tyrosine kinase activity [220] and cytoskeleton (actin) participation in ion channel activation has been demonstrated [221]. Furthermore, the interest in T-cells stems from their important role in the regulation of immune responses. In particular, Jurkat cells, as used here, are CD4+ T-lymphoma cells that are often utilised in the study of T-cell signalling [145] and HIV-1 dissemination in viral pathogenesis [146]. In addition, they are non-adherent spherical cells that retain their spherical shape throughout their lifetime, and experience no spreading or migration when settled on a glass coverslip.

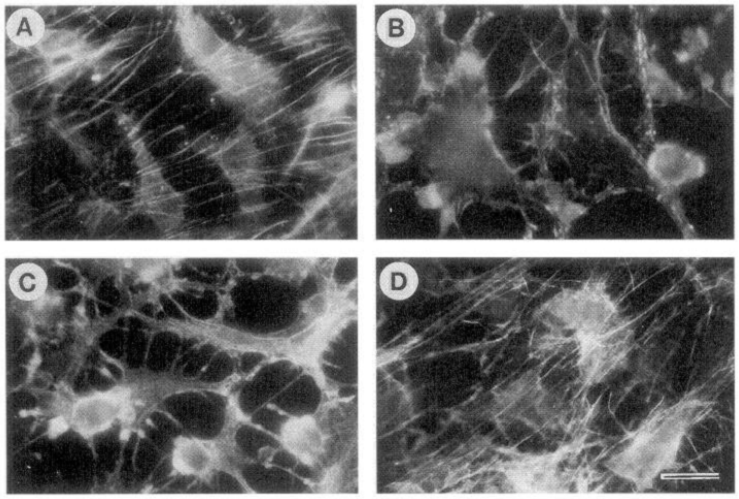

Figure 8.1: *(Taken from Ref. [218]). Distribution of actin in astrocyte cells under different osmotic conditions. Cells were incubated in Krebs-HEPES medium of different osmolarities and then fixed and stained with rhodamine-phalloidin. Actin was visualised by fluorescence microscopy. (A): cells in iso-osmotic medium; (B): cells maintained in 50% hypo-osmotic medium for 2 min; (C): cells maintained in 50% hypo-osmotic medium for 15 min; (D): cells maintained in 50% hypo-osmotic medium for 2 hours.*

The linear viscoelastic properties of a material can be represented by the frequency-dependent dynamic complex modulus, $G^*(\omega)$, which provides information on both the viscous and elastic nature of the material. The standard method of measuring $G^*(\omega)$ is based on the imposition of an oscillatory stress, $\sigma(\omega,t)$, and the measurements of the resulting oscillatory strain, $\gamma(\omega,t)$, or *vice*

versa. The amplitudes of in-phase and out-of-phase components are proportional to the stress amplitude, with constants of proportionality defining, respectively, the storage and loss moduli.

The aim here is to present a straightforward procedure for measuring the *in vivo* mechanical properties of single cells *via* passive video particle tracking microrheology of single beads attached to the cells' exterior. This method has advantages over both complicated active microrheology techniques, where complex experimental set-ups are necessary to exert an external force for performing stress-controlled measurements; and invasive passive video particle tracking of submicron-probes embedded (either via endocytosis or micropipette injection) within the cell's cytoskeleton (*e.g.* [14, 26, 108, 222-224]).

In particular, the procedure consists of measuring the thermal fluctuations of a bead chemically bound to a cell (Figure 8.3) for a sufficiently long time. Under these circumstances the cell acts as a trap, creating normalised MSD profiles very similar to those of optically constrained beads as shown in Figure 8.2. The time-dependent mechanical properties of the cell can then potentially be analysed similarly to the OT tweezer experiments in previous chapters.

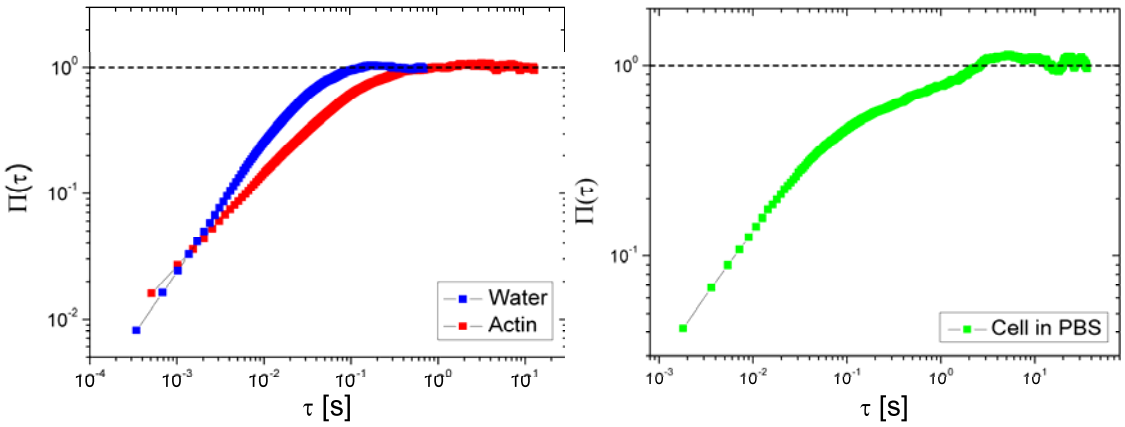

Figure 8.2: *Normalised MSDs of optically trapped beads in water (blue) and actin (red) (left) and of a bead stuck to a cell (right).*

A generalised Langevin equation is adopted to relate the time-dependent bead trajectory, $\vec{r}(t)$, to the frequency-dependent moduli of the cell. Notably, the procedure presented here represents an alternative methodology that can be extended to many experimental formats and provides a simpler addition to cellular physiology studies (*e.g.* those monitoring cell pharmacological response) than existing single cell viscoelasticity assays. Indeed, when compared to single cell viscoelasticity assays such as magnetic tweezers, atomic force microscopy and optical stretcher, as employed in [14, 26, 108, 222-224], our method has the advantage of revealing the changes of the cell's viscoelastic properties over a wide range of frequencies (here from ~0.6 Hz up to ~600 Hz), to a high level of accuracy, whilst it experiences an induced physiological process.

As discussed in Chapter 7, when carrying out microrheology on 'active' systems, there arise some open questions that need to be addressed. Predominantly these deal with whether or not it is valid to apply Einstein's equation for the MSD (Eq. 1.14) to a system where active fluctuations may be measureable, because Einstein's equation is valid only for Gaussian distributions [171]. To recap, Mizuno *et al* [205] discovered that at low ATP conditions, non-thermal low frequency fluctuations were measureable in *in vitro* solutions of actin and myosin mini-filaments, causing the fluctuation dissipation theorem (FDT) to break down.

Some studies have shown that these non-thermal fluctuations are important in cell microrheology [206-208], with beads undergoing two different types of movement in cells, depending upon the time-scale under observation. Indeed, Rogers *et al* [225] highlight that intracellular probes can experience two different regimes of behaviour; sub-diffusive behaviour at short time scales, indicative of thermal motion in a viscoelastic medium; and a super-diffusive regime at longer time-scales, indicative of active motion. In the experiment we present here, the beads are prohibited by experiencing this super-diffusive regime because they are neither intracellular, nor are they free to diffuse on long time scales, as the cell itself acts as an anchor, restricting the beads' long term motion.

Moreover, there is another set of studies [206, 226] which have found that even though active fluctuations clearly have a place in the physiology of a cell, they do not interfere with cellular rheology measurements, and indeed the displacement of beads within or on cells can be treated as Gaussian; thus Einstein's equation is valid. The work of Massiera *et al* [226] on epithelial cells directly conflicts with the study performed by Bursac *et al* [208] on muscle cells. Massiera *et al* found that for short lag times only a small non-Gaussian parameter exists in the distribution of the thermal fluctuations of a bead attached to the epithelial cell membrane, as opposed to the finding of Bursac *et al* that a large non-Gaussian parameter is apparent in muscle cells. It may be that the large bead excursions seen in muscle cells are due to cell-scale contractile activity, which is not relevant in non-contractile epithelial cells [226]. Importantly, this highlights the differences that exist between each cell type, and the care that must be taken when comparing cell mechanics across different kinds of cells.

To calculate the linear viscoelastic properties of the cell from the time-dependent bead MSD, Massiera *et al* truncate data at long lag times from their measurements, thus removing any bead behaviour that may be considered super-diffusive [226]. This is similar to the approach which we adopt here, although we do not truncate the data; instead, the cell constrains the movement of the bead at long times, acting in the same way as an optical trap and restricting the bead's long time-scale diffusion. Accordingly, as in previous Chapters, we first analyse the time-dependent trajectory of the bead using the mean square displacement. Then, using only the data at short times,

and treating the system as 'quasi-static' (as discussed further in a later section), we calculate the linear viscoelastic properties of the cell.

8.1 Experimental Details

Jurkat cells were obtained from ATCC (clone E6-1, TIB-152) and maintained in RPMI 1640 (1x) media containing L-Glutamine and 25mM HEPES [Gibco, Invitrogen]. Prior to experiments they were suspended in PBS [Gibco, Invitrogen] with an osmolarity of 275-304 mOsm then, mixed with functionalised beads and allowed to equilibrate for ~ 10min.

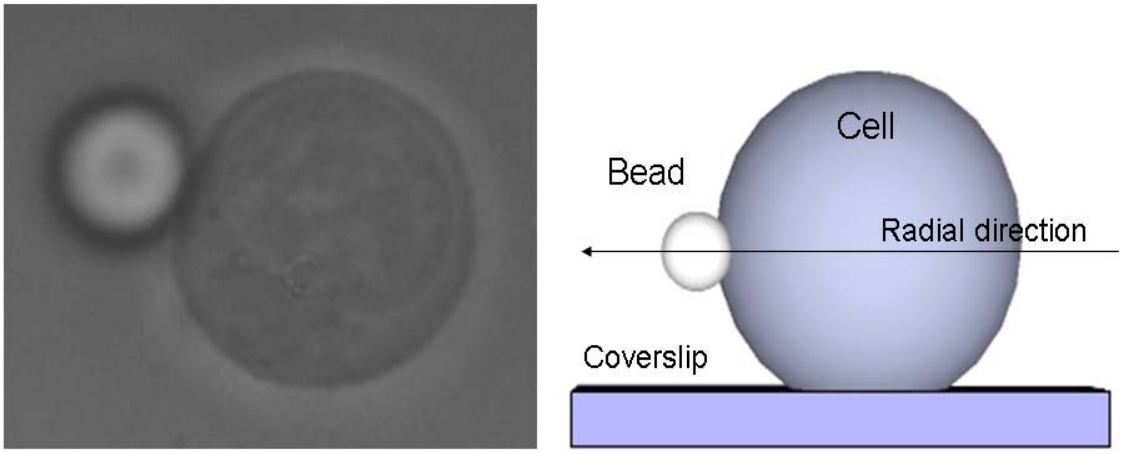

Figure 8.3: *(Left) Top view of a 5μm diameter silica bead chemically bound to the surface of a Jurkat cell and (Right) Side view of left image.*

Silica beads were functionalised with anti-CD4+ (as described in Chapter 3); chosen so as to bind to the CD4 protein expressed on the surface of Jurkat cells. These beads were optically trapped and moved to the equatorial plane of the cell, where they were held for a sufficient time (≈ 2min) until the bonding process was completed (Figure 8.3). This was judged by switching the trap off and confirming that the bead stayed in the same position.

The bead trajectory was measured in real time, at up to ≈ 600Hz, by using our own suite of image analysis software written in LabVIEW, which is based on the analytical method (the static optical tweezer measurements) described in Chapter 4. Measurements were taken first in phosphate-buffered saline (PBS), a common buffer for biological studies because it provides cells with optimal isotonic conditions similar to what would be experienced in the body. 10% (v/v) of distilled water was then added in order to change the osmolarity of the solution and to induce a regulatory volume change in the cell.

8.2 Analysis of the mean square displacements

It is anticipated that there are two major physiological processes that accompany the changes in osmolarity of the solution surrounding the Jurkat cell: firstly, there is an actin cytoskeleton reorganisation; and secondly there is an increase of the cell volume as the solution becomes hypo-osmotic. In order to quantify the changes in cell volumes, we assumed that the cells were spherical (Figure 8.3). In particular, Figure 8.4 shows the relative volume changes <20% when the surrounding PBS solution was made hypo-osmotic by addition of 10% [v/v] distilled water.

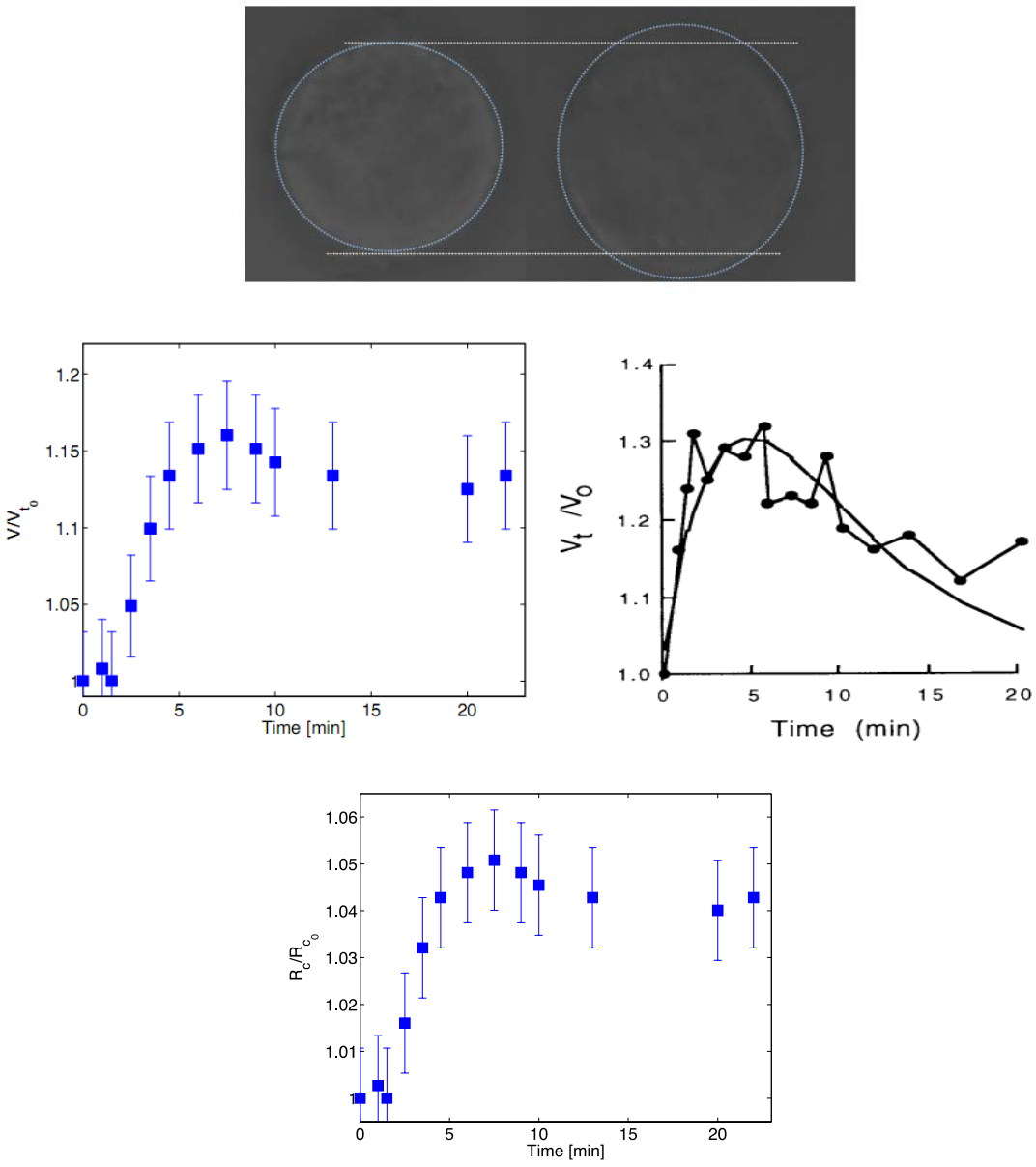

Figure 8.4: *(Top) Change in volume measured for a single Jurkat cell, with left image showing the cell in the isotonic solution, and the right image showing the cell 7 minutes after the solution was made hypotonic. (Middle left) Volume change of a Jurkat cell plotted as a function of time in our experiment and in (Middle right) Ref. [227] for a human melanoma cell.(Bottom) The volume change plotted as a function of the radius.*

The data in Figure 8.4 shows that, after an initial swelling, the cells contract to a still swollen state that is ~15% larger than when they were in isotonic PBS. These results correspond to a change of <6% and ~5% in the cell radius, respectively (Figure 8.4, bottom). The shape of the volume graph we obtain (middle left in Figure 8.4) compares favourably with other measurements of hypotonically induced regulatory volume changes already existing in the literature (middle right in Figure 8.3, taken from Ref. [227]). In this example the authors fitted an exponential decay to the curve, however it appears that the data diverges from the curve at long time, which is similar to our results. Based on these observations, in this study we assume that these small radius changes do not affect the dynamics of the system appreciably. To study how the dynamics of Jurkat cells vary with the osmolarity of the solution, we first analyse the difference time regimes in the time-dependent normalised mean-square displacement, $\Pi(\tau)$, which has the potential to reveal information both on the pure elastic component of the cell (at long time intervals or low frequencies) and on the fast dynamics occurring at small length scales (*e.g.* those related to the transverse bending modes of single actin filaments in the cytoskeleton).

In Figure 8.5, the $\Pi(\tau)$ curves are derived from measurements that were collected at fixed time intervals after the solution was made hypotonic and compared with the normalised MSD of the same cell in phosphate buffered saline (PBS) solution, prior to hypotonic exposure Note that in order to more easily discern visually the changes in $\Pi(\tau)$ caused by the hypo-osmolarity, the normalised MSD for the cell in PBS is plotted in each of the panels.

During hypo-osmotic shock the analysis of the MSD uncovers the changes in the dynamical response of the cell, as shown in Figure 8.5. 2 minutes after exposure to a hypo-osmotic condition the cell behaves similarly to the control conditions in PBS (Figure 8.5A). However, after 7 minutes exposure the MSD moves upwards when compared to the cell in PBS (Figure 8.5B), indicating an increase in elasticity (as demonstrated in Figure 1.6 in the Introduction). As time passes the cell then begins to equilibrate its osmolarity, and both the slope and time dependence of the MSD change and revert back to once again behaving in an equivalent way to the cell in PBS. Importantly, it should be noted that in Figure 8.5 there is no evidence of a super-diffusive bead motion at long times. This is, we believe, because the cell acts as an anchor, meaning that long term diffusion modes are prohibited.

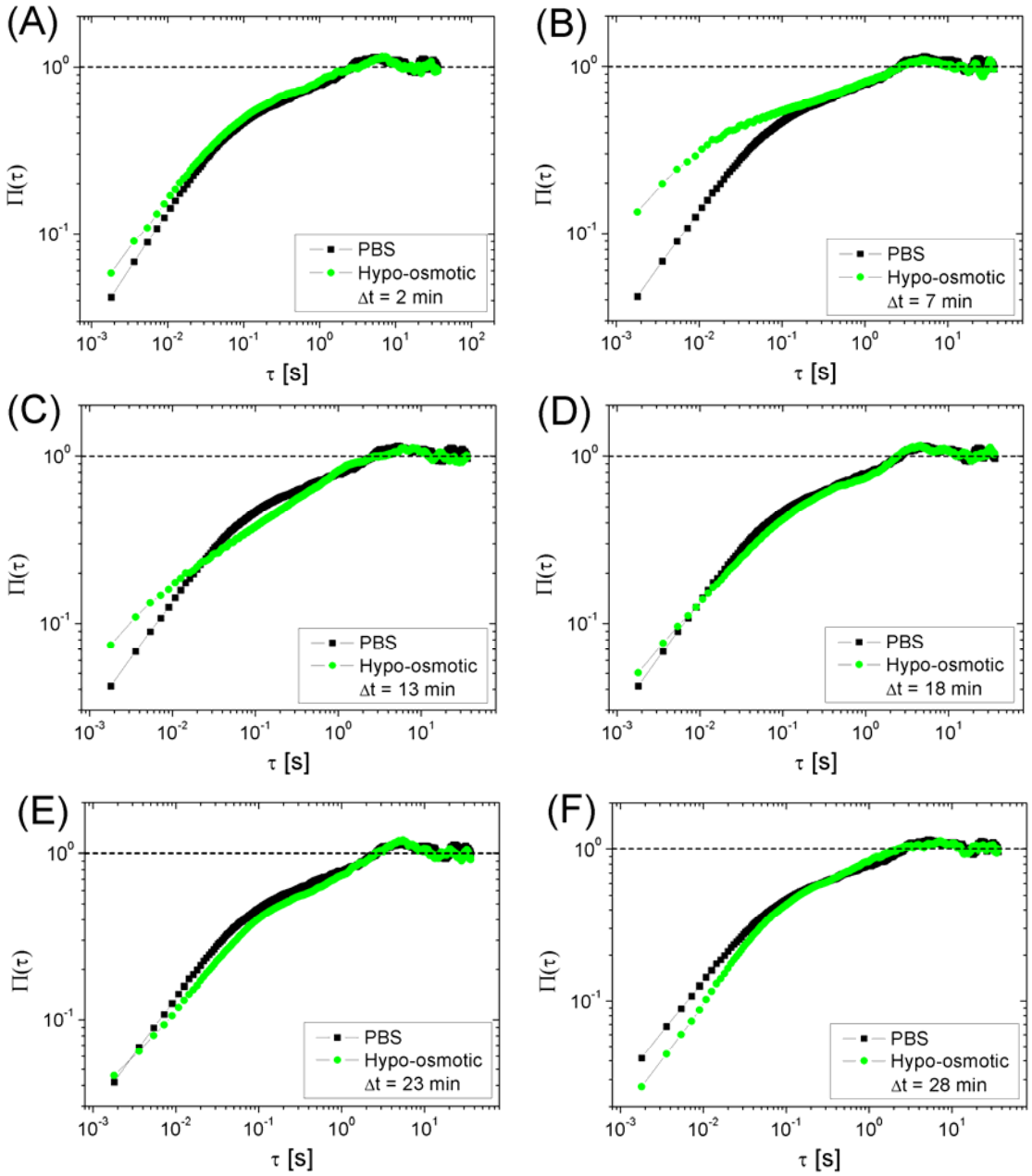

Figure 8.5 [A-F]: *The $\Pi(\tau)$ vs. lag-time of a 5μm diameter silica bead chemically bound to a Jurkat cell in iso-osmotic (PBS) solution (squares) and in hypo-osmotic solution (circles) after addition of 10% v/v distilled water to the PBS buffer, and measured at time intervals (Δt) of (A) 2 min, (B) 7 min, (C) 12 min, (D) 18 min, (E) 23 min and (F) 28 min respectively.*

8.3 Cell viscoelasticity model, results and discussion

We now analyse the linear viscoelastic properties of the cell *via* a Langevin equation, which relates the time-dependent bead position to the viscoelastic moduli of the cell. As discussed earlier, there is some debate about the conditions under which the Stokes-Einstein relation can be applied to active materials. The condition of 'quasi-steady' is required for the FDT to be applicable, and is described by Mason and Squires as when 'changes occur slowly compared to sampling times' [228]. As can be seen in Figures 8.2 and 8.5, the plateau region of the MSD, where no diffusion modes are apparent, is reached within a few seconds. It is therefore reasonable, given the quick sampling time (where each measurement takes on average 2 minutes), to assume that the cell is in a quasi-steady state, as the broad cytoskeletal restructuring (in response to hypo-osmotic shock) takes place on a time-scale of ~ 30 minutes.

The experimental procedure is analytically described through the analysis of the time-dependent trajectory $\vec{r}(t)$ of a bead, chemically bound to the cell membrane. The equation describing the bead position $\vec{r}(t)\ \forall t$ can be derived by means of a generalised Langevin equation, which in three dimensions is:

$$m\vec{a}(t) = \vec{f}_R - \int_0^t \left[\zeta_c(t-\tau) + \zeta_s(t-\tau)\right]\vec{v}(\tau)d\tau \tag{8.1}$$

where m is the mass of the particle, $\vec{a}(t)$ is the acceleration, $\vec{v}(t)$ is the bead velocity and $\vec{f}_R$ is the usual Gaussian white noise term, modelling stochastic thermal forces acting on the particle. The integral term represents the total viscous damping force acting on the bead, which, based on the superposition principle, incorporates two generalised time-dependent memory functions, $\zeta_c(t)$ and $\zeta_s(t)$, that are representative of the viscoelastic nature of both the cell and the solvent respectively. These memory functions are directly related to the materials' complex modulus as shown below.

In the case of the solvent, which in this work is the media surrounding the cell, the relationship between the memory function and the complex modulus is straightforward. Indeed, to a first approximation, using the assumptions adopted by Mason & Weitz [4] when studying the motion of thermally excited free particles at thermal equilibrium, the complex modulus of the solvent is related to $\zeta(t)$ by the expression:

$$G_s^*(\omega) = \frac{i\omega\hat{\zeta}_s(\omega)}{6\pi R} \tag{8.2}$$

where R is the bead radius and $\hat{\zeta}_s(\omega)$ is the Fourier transform of $\zeta_s(t)$. In the case of the cell, we assume a similar relationship between $G_c^*(\omega)$ and $\zeta_c(t)$ to that given above for the solvent, but with a different constant of proportionality, yet unknown, that we will call β:

$$G_c^*(\omega) = \frac{i\omega\hat{\zeta}_c(\omega)}{\beta} \tag{8.3}$$

Note that, β may vary between different cells because it depends on (i) the cell radius (R_c), (ii) the number of the chemical bonds between the bead and the cell, (iii) the contact area between the cell and the glass coverslip, and (iv) the relative position of the bead with respect to both the cell's equatorial plane and the glass coverslip. However, in this study we will focus only on the changes in dynamics due to variations in osmolarity. This can be achieved since all the above parameters, with the exception of R_c, are (in good approximation) time-independent, and will not change significantly during the course of a set of measurements (as shown hereafter in Figure 8.4 for cells performed in iso-osmotic conditions). In addition, it is important to highlight that the cells maintained a spherical shape well beyond the duration of the experiment. Moreover, the cells adhered to the cover-slip and no drift was observed during the experiment. Finally, given that we measure an increase of the cell radius (R_c) of $\leq$5% for the hypo-osmolarity experiments described below, we make the assumption that this small change does not affect the dynamics of the system appreciably.

Importantly, β also incorporates the boundary conditions of the Stokes part of the Stokes-Einstein relation. Moving a bead close to a surface boundary requires a correction factor to be applied, in comparison to when the bead is far from a boundary in solution. Although we cannot quantify this factor, it can be neglected here provided it stays constant throughout the experiment, because our results will be shown to include a ratio of two functions proportional to β.

We now describe how the thermal fluctuations of a bead, chemically bound to a cell, can be investigated to determine the viscoelastic properties of the cell through the analysis of the time dependence of the bead's mean-square displacement $\left\langle \Delta r^2(\tau) \right\rangle \equiv \left\langle \left[\vec{r}(t+\tau) - \vec{r}(t)\right]^2 \right\rangle_t$ in the radial direction of the cell; where t is the absolute time and τ is the lag time (*i.e.* time interval). The average is taken over all initial times t. Under these circumstances, it is an easy step to show that, at thermal equilibrium, Equation 8.1 can be reorganized to express $\zeta_c(\omega)$ as function of the $\mathrm{MSD}(\tau)$:

$$\hat{\zeta}_c(\omega) = -mi\omega - \frac{6k_BT}{\omega^2\left\langle \Delta\hat{r}^2(\omega) \right\rangle} - \hat{\zeta}_s(\omega) \tag{8.4}$$

where $\left\langle \Delta\hat{r}^2(\omega) \right\rangle$ is the Fourier transform of $\left\langle \Delta r^2(\tau) \right\rangle$, $i\omega$ is the Fourier frequency, k_B is the Boltzmann constant and T is the absolute temperature. From Equation 8.4, it follows that:

$$\frac{G_c^*(\omega)}{G'_0} = \frac{1}{i\omega\hat{\Pi}(\omega)} + \frac{m\omega^2}{\beta G'_0} - \frac{6\pi R G_s^*(\omega)}{\beta G'_0} \tag{8.5}$$

where G'_0 is the limiting value, for vanishing frequencies, of the elastic modulus of the whole system (*i.e* cell *plus* solvent), which in this work is $G'_0 \equiv G'_c(\omega)$ for $\omega \to 0$; and $\hat{\Pi}(\omega)$ is the Fourier transform of $\Pi(\tau) = \left\langle \Delta r^2(\tau) \right\rangle / 2\left\langle r^2 \right\rangle$ as before, where $\left\langle r^2 \right\rangle$ is the variance of $\vec{r}(t)$ measured for sufficiently long time. It has been shown (in Chapter 5) that for a constrained bead $\Pi(\tau) = 1$ at large time intervals. It is important to highlight that the term $\beta G'_0$ (representing the coefficient of the elastic restoring force) can be determined by means of the principle of equipartition of energy, which in one dimension, is written:

$$k_B T = \beta G'_0 \left\langle r^2 \right\rangle \tag{8.6}$$

Usefully, two further simplifications can be applied here; namely that for micron-sized silica beads, the inertia term $m\omega^2$ is negligible up to frequencies on the order of MHz, and that for solvents having a frequency-independent viscosity η_s (*e.g.* water), $G_s^*(\omega)$ simplifies to $i\omega\eta_s$. Thus, Equation 8.5 provides the linear viscoelastic properties of the cell (scaled by G'_0) over a range of frequencies that is limited at the top end by the rate of acquisition of images to determine the bead position, and at the bottom end by a cut-off frequency given by:

$$\omega_{coff} = \frac{\beta G'_0}{\eta_0} \tag{8.7}$$

where η_0 is the limiting value, for vanishing frequencies, of the viscosity of the whole system.

Finally, in order to evaluate the Fourier transform in Equation 8.5 we adopt the analytical method introduced by Evans *et al* [161], discussed in Chapter 4, which is applied directly to the experimental data points and has the advantage of removing the need for Laplace and inverse-Laplace transformations of experimental data.

(I) Elastic properties of the cell derived from $\Pi(\tau)$.

The first result that can be obtained through the analysis of the thermal fluctuations of the bound bead is the relative change of the cell's low-frequency elastic plateau modulus, $G_c^{'}(0)$, shown in Figure 8.6. This can be evaluated from the time-dependent variance, $\left\langle r^2 \right\rangle$, of the constrained bead in the radial direction of the cell, by adopting the principle of equipartition of energy as in

Equation 8.6. Based on the assumption of the cell being in a quasi-static state, we define this low frequency modulus (multiplied by the factor β) as analogous to the optical trap strength in optically trapped bead experiments, and it can be seen as being defined by the plateau value of the MSD graphs in Figure 8.5.

In addition, experiments were carried out on cells treated with blebbistatin, an inhibitor of the actin and myosin interaction mechanism. If the low-frequency modulus was measuring any non-thermal fluctuations caused by actin-myosin contractility, it would be expected that this would be shown in differences between control cells and cells in which the contractility is inhibited; however, no statistical difference was found between the low-frequency elastic modulus of blebbistatin treated cells when compared to the control cells in PBS (results not shown in this thesis).

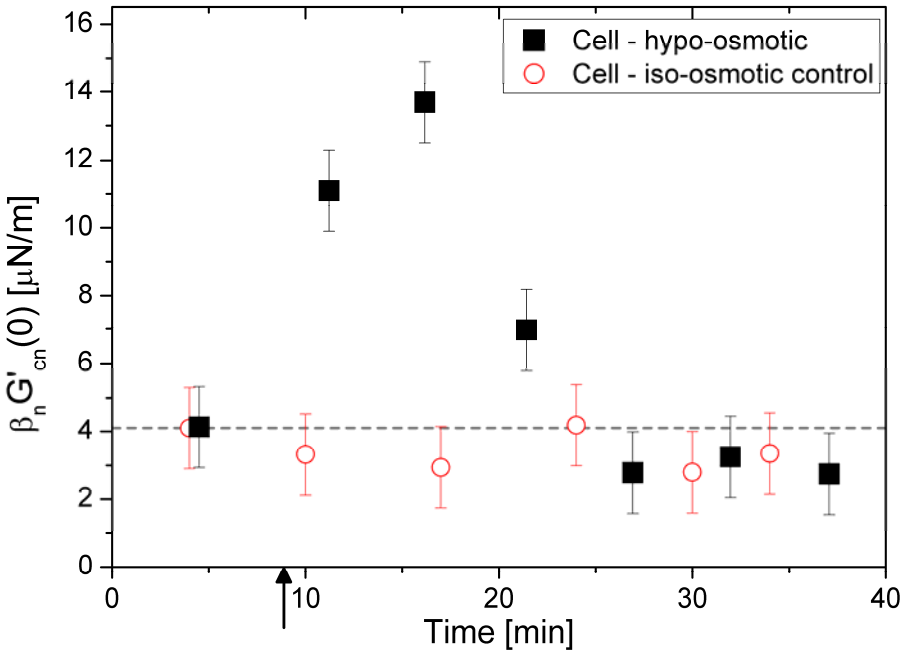

Figure 8.6: *The absolute value of $\beta_n G'_{cn}(0)$ measured in PBS and in 10% hypotonic solution (squares) or in isotonic PBS solution (circles). The arrow indicates the time at which the PBS solution is made hypotonic by the addition of water. The single PBS measurement at 4.5 minutes was an average of three PBS measurements, and the standard deviation was used as the error in all readings. The dotted line is to compare later hypotonic measurements with the initial measurement in PBS.*

Although the absolute value of $G'_c(0)$ cannot be determined because of the unknown factor , β , the relative change between the different values of $\beta G'_c(0)$, obtained from n sequential measurements performed on the same cell, differ from each other only because of the small increase of the cell radius (measured as ~5%) and the variation of $G'_c(0)$. Thus, from Figure 8.6 it is clear that a change of 10% in osmolarity towards hypo-osmolarity, which occurs at t ~ 9min through the addition of distilled water to the isotonic solution, induces a temporary increase of

$\beta G_c^{'}(0)$ that lasts for approximately 15-30 min. At its greatest, this change in the low frequency elastic modulus dependent term, $\beta G_c^{'}(0)$, is over 3 fold in magnitude. Figure 8.5 also portrays the values of $\beta G_c^{'}(0)$ for a control cell that was kept in isotonic PBS for a similar length of time as the hypo-osmotic cell. No significant change in $\beta G_c^{'}(0)$ can be seen for the control cell.

The explanation for such a large increase may in part be due to the change in radius; however, if this were solely responsible, it would be expected that $\beta G_c^{'}(0)$ would remain significantly above its original value, as the cells do not regain their original radius. Thus, since $\beta G_c^{'}(0)$ *does* return to close to the original value (at t ~ 25 min), consideration should be given to a temporary increase in cytoskeletal tension due to the reduction in ionic strength of the solution (*i.e.* a reduction in screening of the charges of the cytoskeletal molecules by solution based ions). This would cause the elastic modulus to increase as predicted by Granek [210]. This latter phenomenon would also alter the cell's viscoelastic properties and any resulting actin cytoskeleton rearrangement may be seen as part of an attempt of the cell to re-equilibrate the solution osmolarity.

Moreover, a >3 fold increase in the cell's elastic plateau modulus could be explained by an increase of biomolecular interactions (*i.e.* electrostatic interactions) that would have the effect of forming bundles of actin filaments and reshaping the isotropic cytoskeleton structure. This scenario is in good agreement with confocal microscopy results already reported for multiple cell lines (as shown in Figure 8.1) and the observations that actin forms bundles aortic bovine endothelial cells after hypotonic exposure [229].

(II) Fast dynamics of the cell derived from $\Pi(\tau)$

In order to study the high frequency behaviour of cells, we analyse the elastic ($G'(\omega)$) and viscous, ($G''(\omega)$) components of the viscoelastic modulus, $G^*(\omega)$, derived from the measurements shown in Figure 8.5 are shown in Figure 8.7 (scaled by the plateau modulus $G'_c(0)$). It is clear that, in PBS (Figure 8.7A), the high frequency behaviour of the cell's elastic and viscous moduli both show a frequency dependence of $\propto \omega^{3/4}$, which is characteristic of concentrated isotropic actin filament solutions [139, 175]

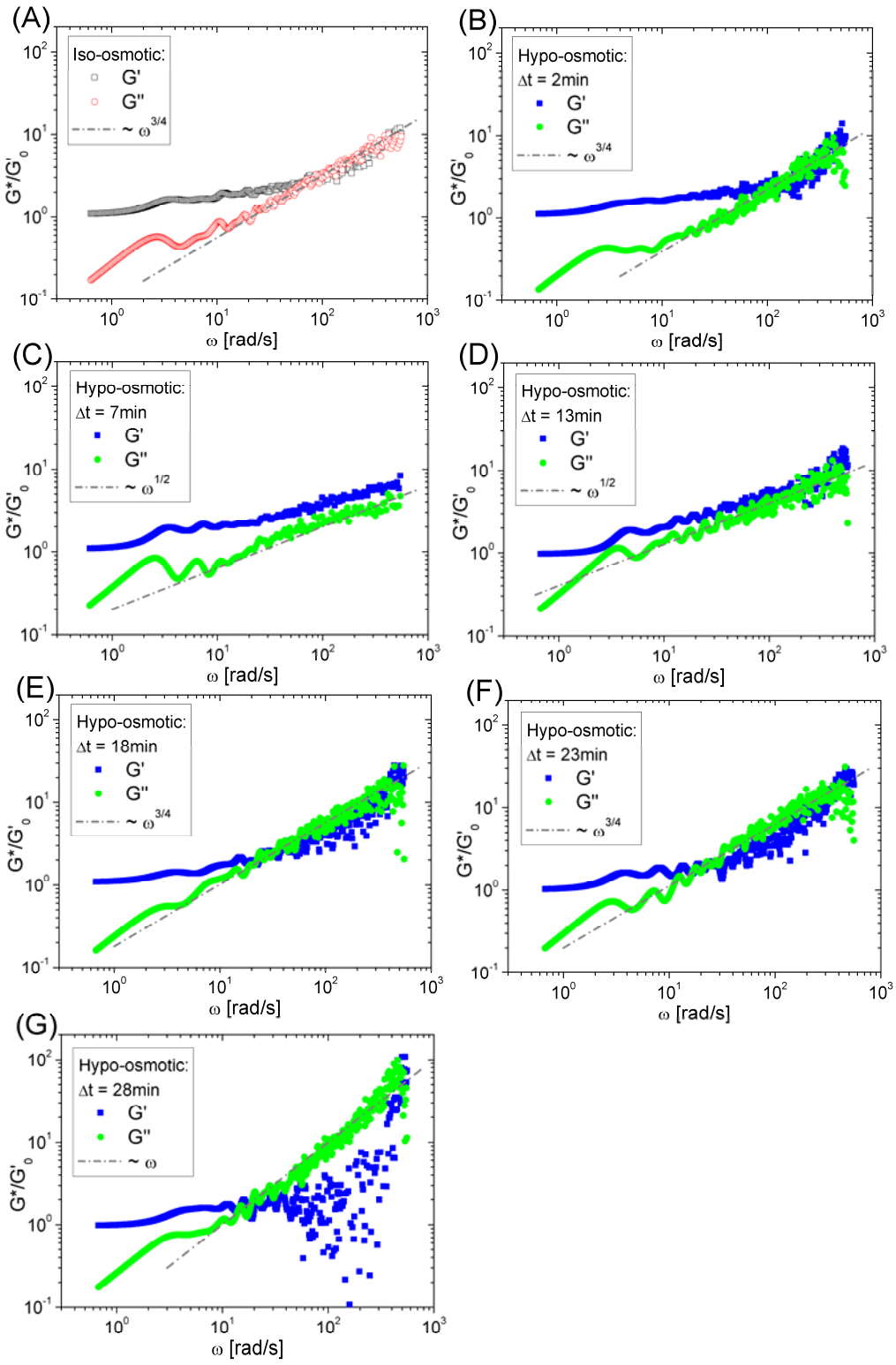

Figure 8.7: *The real (storage, $G'_c(\omega)$) and the imaginary (loss, $G''_c(\omega)$) parts of the complex modulus ($G^*_c(\omega)$) scaled by G'_0 vs. frequency, of a Jurkat cell in iso-osmotic (PBS) solution (A) and in hypo-osmotic solution (B-G) after the addition of 10% v/v distilled water to the PBS buffer and measured at time intervals (Δt) of (A) 2 min, (B) 7 min, (C) 12 min, (D) 18 min, (E) 23 min and (F) 28 min, respectively. The moduli have been evaluated by using Equation 8.3 on the normalised MSD data shown in Figure 8.5. The lines are guides for the gradients.*

As the solution is made hypo-osmotic, the cell cytoskeleton starts to reorganise and the frequency behaviour of the moduli drastically change as (sequentially) shown in Figure 8.7. Specifically, after ~ 10min in the hypo-osmotic solution both moduli tend to assume a high frequency behaviour $\propto \omega^{1/2}$ (Figures 8.7C and 8.7D). This change in the degree of elasticity may be explained by two alternative (and possibly concomitant) processes: (i) an increase in cytoskeletal tension as response to a stretching force caused by the cell swelling and (ii) the consequent formation of actin bundles (Figure 8.1), generated during the reorganisation process of the cell cytoskeleton. However, whilst the increase in cytoskeletal tension would explain both the initial increase of the cell stiffness and the change in the frequency scaling laws of the moduli (*i.e.* from $\propto \omega^{3/4}$ to $\propto \omega^{1/2}$), as predicted by Granek [210] it would fail to explain the softening process occurring during the cell volume re-equilibration, which ends with a breakdown, at high frequency, of the cell's elastic modulus (Figure 8.7G).

Finally, it is important to highlight that the results that have been obtained here using a video particle tracking method are in good agreement with those presented in the review written by Papkonstanti & Stournaras [219], where a set of assessments of actin cytoskeleton dynamics and actin architecture in cell volume regulation are summarised. However, none of the techniques that have been reviewed [219] are able to provide quantitative information on the cell viscoelasticity, as is the case here.

In summary, we have presented a straightforward experimental procedure, coupled with a new analytical method to interpret the data, which leads to quantitative determination of the *in vivo* viscoelastic properties of cells in the frequency-domain. The method has the potential to monitor, in real-time, the internal dynamics and re-organisation of the actin cytoskeleton up to frequencies on the order of *kHz*, representing a valuable addition to studies that address cellular physiology and pharmacological response. Indeed, in this thesis we report, *for the first time*, a real-time observation of the high frequencies (up to $\sim 600Hz$) changes of the Jurkat cells' viscoelastic spectrum from $\propto \omega^{3/4}$ to $\propto \omega^{1/2}$, as response to a change in osmolarity of the solution. The rheological interpretation of the results gives a direct insight of the cell cytoskeleton structure and its re-organisation. In the future, it is envisaged that these interpretations could be coupled with advanced molecular biology techniques to resolve the detailed interactions underlying these rheological changes and that faster dynamics could be studied by means of a quadrant photo-diode based tracking system.

Chapter 9

CONCLUSIONS

In this thesis optical tweezers and passive video particle tracking microrheology have been used to study the viscoelastic properties of both biopolymer solutions and cells.

In particular,

- Two new self-consistent and self-calibrating wideband microrheological techniques have been developed for measuring the linear viscoelastic properties of fluids across the widest frequency range achievable with optical tweezers (*Phys.Review E.* (2010) 81:2, and *J. Optics* (2011) 13:4). These methods extend the range of accessible frequencies previously available to optical tweezers measurements. The wideband optical tweezers methods were applied to synthetic and biopolymer solutions, demonstrating that it is possible to measure the material's viscoelastic properties down to the terminal region (*i.e.* low frequency), where the material's longest characteristic relaxation time is exceeded.

- New methods for data analysis were developed to derive the concentration scaling laws of polymer and biopolymer solutions from microrheological measurements with optical tweezers. It has been shown that concentration scaling laws derived from time-dependent functions were in good agreement with those predicted for the concentration scaling of related functions but in the frequency-domain. In particular, the theoretical predictions for the concentration scaling laws of the viscosity of polyacrylamide (PAM) solutions (*i.e.* $\eta \propto c^{1/2}$ and $\eta \propto c^{3/2}$) were calculated directly from the thermal fluctuations of optically trapped beads. For solutions of actin (a semiflexible polymer), the predicted concentration scaling law of the elastic modulus, *i.e.* $G'_0 \propto c^{4/3}$, was obtained.

- The concentration scaling laws of actin/myosin samples were measured, giving rise to new scaling regimes not predicted by any current semiflexible polymer models. A direct comparison was made between the relative viscosity measured after the addition of either two-headed myosin fragment (HMM) or single-head myosin fragment (S1) to action networks.

- A straightforward procedure was presented for measuring the *in vivo* mechanics and linear viscoelastic properties of single cells *via* passive video particle tracking microrheology of single beads attached to the cells' exterior. Notably, the procedure presented here represents an alternative methodology that can be extended to many experimental formats and provides a simple addition to existing cellular physiology studies (e.g. those monitoring cell pharmacological response).

- The first real time observation of the changes of the Jurkat cells' viscoelastic spectrum at high frequencies (up to $\sim 600Hz$) was reported. This highlighted a scaling in the viscoelastic moduli from $\propto \omega^{3/4}$ to $\propto \omega^{1/2}$, as a response to a change in osmolarity of the solution. The rheological interpretation of the results gave a direct insight into the cell cytoskeleton structure and its reorganisation.

Chapter 10

FUTURE WORK

There are a number of avenues that future work can focus on, based upon the results of this thesis.

In particular,

- The accessible frequency range of the wideband experiments is defined on one extreme by the experiment length and on the other by the maximum data acquisition speed (which can reach 10s of MHz for a quadrant photo-diode). This allows access to the material's terminal region and enables microrheological measurements to be performed on complex fluids with very long relaxation times. For some materials, specifically actin, a very long measurement (on the order of hours) is required so that the longest relaxation time (predicted to range from 10^3 to 10^6 sec) can be observed. However, lengthy measurements generate extremely large data files and the analysis of these becomes problematic; *i.e*. the software struggles to handle large data files, causing the operating system to crash. Once this data processing issue has been addressed, there is no reason why the reptation time (*i.e.* the longest relaxation time) of actin filaments cannot be measured using optical tweezers.

- In the course of deriving the methodology of the concentration scaling laws and carrying out microrheological experiments with optical tweezers we also defined the quantity that we call the normalised mean-square displacement (equal to the MSD divided by twice the variance of the bead fluctuations) which is fundamental in defining the characteristic relaxation rate of the system. This is noteworthy simply because to our knowledge, in more than 30 years of optical trapping, no-one has defined, in this way, the long time asymptotic value of the bead's MSD. Given this fact, it is likely that both the nMSD and

the scaling factor $\kappa / 6\pi a\eta_s$ can be exploited in more ways than have been identified within this thesis.

- With regards to the actin networks, it would be useful to draw on the results obtained here, along with other studies, as the basis for a more comprehensive investigation into the scaling regimes of *in vitro* reconstituted actin solutions. Although the properties of actin solutions are, on the whole, compliant with theoretical models [2-4] there are still some discrepancies that need to be understood. It is not completely clear whether these discrepancies stem from impurities in the actin solutions, or whether the theoretical predictions need to be modified to include a description of actin behaviour at other concentrations.

- The actin and myosin network studies would benefit from study at more concentrations, and with varying actin concentrations. An interesting extension of the actin/myosin research would be to determine whether actin polymers interacting with S1 molecules display properties of 'comb-polymers' (whereby actin forms the backbone of the polymer, and S1 forms the combs) because models governing the viscoelasticity of semi-flexible polymers are sparse.

- It would be of interest to see if the osmolarity induced changes observed in the viscoelasticity of Jurkat cells could be recreated *in vitro* with actin solutions and/or actin-binding proteins. This would help create a more detailed model of the processes governing the actin reorganisation of the cell cytoskeleton in response to induced changes.

- The passive video-particle tracking method for determining the dynamics and linear viscoelastic changes in singles cells has the potential to be applied to a wide range of studies, especially those that involve a change in cellular physiology; for example, the response of the cell to different pharmacological agents. In the future, it is envisaged that rheological interpretations of the cell's behaviour could be coupled with advanced molecular biology techniques to resolve the detailed interactions underlying viscoelastic changes and that faster dynamics could be studied by means of a quadrant photo-diode based tracking system.

BIBLIOGRAPHY

1. Brown, R., *A brief account of microscopical observations on the particles contained in the pollen of plants; and on the general existence of active molecules in organic and inorganic bodies.* Edinburgh New Philosophical Journal 1828. July-Sep p. 358-371.

2. Einstein, A., *Investigations on the theory of the Brownian movement*. 1905, Translated 1926: Dover Publications.

3. Smolochowski, M., *Zur kinetischen theorie der brownschen molekularbewegung und der suspensionen.* Annalen Der Physik, 1906. 21: p. 756-780.

4. Mason, T.G. and D.A. Weitz, *Optical measurements of frequency-dependent linear viscoelastic moduli of complex fluids.* Physical Review Letters, 1995. 74(7): p. 1250-1253.

5. Liu, A.P. and D.A. Fletcher, *Biology under construction: in vitro reconstitution of cellular function.* Nat Rev Mol Cell Biol, 2009. 10(9): p. 644-650.

6. Waigh, T.A., *Microrheology of complex fluids.* Reports on Progress in Physics, 2005. 68: p. 685-742.

7. MacKintosh, F.C. and C.F. Schmidt, *Microrheology.* Current Opinion in Colloid & Interface Science, 1999. 4(4): p. 300-307.

8. Gardel, M.L., Valentine, M.T, Weitz, D.A., *Microrheology*. Microscale Diagnostic Techniques, ed. K.Breuer. 2005: Springer Verlag.

9. Murray, C.A. and D.G. Grier, *Video microscopy of monodisperse colloidal systems.* Annual Review of Physical Chemistry, 1996. 47: p. 421-462.

10. Tseng, Y. and D. Wirtz, *Mechanics and multiple-particle tracking microheterogeneity of alpha-actinin-cross-linked actin filament networks.* Biophysical Journal, 2001. 81(3): p. 1643-1656.

11. Mason, T.G., Ganesan, K, van Zatten, J.H, Wirtz, D, Kuo, S.C., *Particle tracking microrheology of complex fluids.* Physical Review Letters, 1997. 79(17): p. 3282-3285.

12. Corrigan, A.M. and A.M. Donald, *Particle tracking microrheology of gel-forming amyloid fibril networks.* European Physical Journal E, 2009. 28(4): p. 457-462.

13. Xu, J., V. Viasnoff, and D. Wirtz, *Compliance of actin filament networks measured by particle-tracking microrheology and diffusing wave spectroscopy.* Rheologica Acta, 1998. 37(4): p. 387-398.

14. Wirtz, D., *Particle-Tracking Microrheology of Living Cells: Principles and Applications.* Annual Review of Biophysics, 2009. 38(1): p. 301-326.

15. Palmer, A., Mason, T. G, Xu, J. Y, Kuo, S. C, Wirtz, D., *Diffusing wave spectroscopy microrheology of actin filament networks.* Biophysical Journal, 1999. 76(2): p. 1063-1071.

16. Pine, D.J., Weitz, D. A, Chaikin, P. M, Herbolzheimer, E., *Diffusing-wave spectroscopy.* Physical Review Letters, 1988. 60(12): p. 1134-1137.

17. Meglinskii, I. and A. Korolevich, *Use of diffusion wave spectroscopy in diagnostics of blood.* Journal of Applied Spectroscopy, 2000. 67(4): p. 709-716.

18. Ninck, M., M. Untenberger, and T. Gisler, *Diffusing-wave spectroscopy with dynamic contrast variation: disentangling the effects of blood flow and extravascular tissue shearing on signals from deep tissue.* Biomed. Opt. Express. 1(5): p. 1502-1513.

19. Liu, S.Y. and Y.F. Wang, *Application of AFM in Microbiology: A Review.* Scanning. 32(2): p. 61-73.

20. Muller, D.J., Helenius, J, Alsteens, D, Dufrene, Y. F., *Force probing surfaces of living cells to molecular resolution.* Nature Chemical Biology, 2009. 5(6): p. 383-390.

21. Baclayon, M., G.J.L. Wuite, and W.H. Roos, *Imaging and manipulation of single viruses by atomic force microscopy.* Soft Matter. 6(21): p. 5273-5285.

22. Wright, C.J., Shah, M. K, Powell, L. C, Armstrong, I., *Application of AFM From Microbial Cell to Biofilm.* Scanning. 32(3): p. 134-149

23. Okajima, T., Arakawa, H, Alam, M. T, Sekiguchi, H, Ikai, A., *Dynamics of a partially stretched protein molecule studied using an atomic force microscope.* Biophysical Chemistry, 2004. 107(1): p. 51-61.

24. Ziemann, F., Schmidt, F, Baermann, M, Sackmann, E., *Magnetic tweezers: A new tool for local measurements of viscoelastic parameters, force fields and reptation dynamics of single filaments within actin networks.* Biophysical Journal, 1995. 68(2 PART 2): p. A285.

25. Ziemann, F., J. Radler, and E. Sackmann, *Local measurements of viscoelastic moduli of entangled actin networks using an oscillating magnetic bead micro-rheometer.* Biophysical Journal, 1994. 66(6): p. 2210-2216.

26. Deng, L.H., Trepat, X, Butler, J. P, Millet, E, Morgan, K. G, Weitz, D.A, .Fredberg, J. J., *Fast and slow dynamics of the cytoskeleton.* Nature Materials, 2006. 5(8): p. 636-640.

27. Wilhelm, C., *Out-of-Equilibrium Microrheology inside Living Cells.* Physical Review Letters, 2008. 101(2): p. 028101.

28. Massiera, G., Van Citters, K. M, Biancaniello, P. L, Crocker, J. C., *Mechanics of single cells: Rheology, time depndence, and fluctuations.* Biophysical Journal, 2007. 93: p. 3703-3713.

29. Ashkin, A., *Acceleration and Trapping of Particles by Radiation Pressure.* Physical Review Letters, 1970. 24(4): p. 156

30. Ashkin, A. and J.M. Dziedzic, *Optical Levitation by Radiation Pressure.* Applied Physics Letters, 1971. 19(8): p. 283-&.

31. Ashkin, A., Dziedzic, J. M, Bjorkholm, J. E, Chu, S., *Observation of a Single-Beam Gradient Force Optical Trap for Dielectric Particles.* Optics Letters, 1986. 11(5): p. 288-290.

32. Ashkin, A. and J.M. Dziedzic, *Optical Trapping and Manipulation of Viruses and Bacteria.* Science, 1987. 235(4795): p. 1517-1520.

33. Gittes, F. and F.C. MacKintosh, *Dynamic shear modulus of a semiflexible polymer network.* Physical Review E, 1998. 58(2): p. R1241-R1244.

34. Neuman, K.C. and S.M. Block, *Optical trapping.* Review of Scientific Instruments, 2004. 75(9): p. 2787-2809.

35. Sheetzed, M., *Laser tweezers in cell biology*. Methods in cell biology, ed. L.a.M. Wilson, P. Vol. 55. 1998, San Diego: Academic Press.

36. Wright, W.H., Sonek, G. J, Tadir, Y, Berns, M. W., *Laser trapping in cell biology.* Ieee Journal of Quantum Electronics, 1990. 26(12): p. 2148-2157.

37. Block, S.M., D.F. Blair, and H.C. Berg, *Compliance of Bacterial Flagella Measured with Optical Tweezers.* Nature, 1989. 338(6215): p. 514-518.

38. Finer, J.T., R.M. Simmons, and J.A. Spudich, *Single myosin molecule mechanics – picoNewton forces and nanometer steps.* Nature, 1994. 368(6467): p. 113-119.

39. Wang, M.D, Yin, H, Landick, R, Gelles, J, Block, S. M., *Stretching DNA with optical tweezers.* Biophysical Journal, 1997. 72(3): p. 1335-1346.

40. Yoon, Y.Z., Kotar, J, Brown, A. T, Cicuta, P., *Red blood cell dynamics: from spontaneous fluctuations to non-linear response.* Soft Matter. 7(5): p. 2042-2051.

41. Tskhovrebova, L., Trinick, J, Sleep, J. A, Simmons, R. M., *Elasticity and unfolding of single molecules of the giant muscle protein titin.* Nature, 1997. 387(6630): p. 308-312.

42. Mehta, A.D., Rief, M, Spudich, J.A, Smith, D.A, Simmons, R.M., *Single-Molecule Biomechanics with Optical Methods.* Science, 1999. 283(5408): p. 1689-1695.

43. Block, S.M., L.S.B. Goldstein, and B.J. Schnapp, *Bead movement by single kinesin molecules studied with optical tweezers.*. Nature, 1990. 348(6299): p. 348-352.

44. Fournier, J.M.R., M.M. Burns, and J.A. Golovchenko, *Writing diffractive structures by optical trapping.* Practical Holography Ix, 1995. 2406: p. 101-111.

45. Dufresne, E.R. and D.G. Grier, *Optical tweezer arrays and optical substrates created with diffractive optics.* Review of Scientific Instruments, 1998. 69(5): p. 1974-1977.

46. Hayasaki, Y., Itoh, M, Yatagai, T, Nishida, N., *Nonmechanical optical manipulation of microparticle using spatial light modulator.* Optical Review, 1999. 6(1): p. 24-27.

47. Liesener, J., Reicherter, M, Haist, T, Tiziani, H. J., *Multi-functional optical tweezers using computer-generated holograms.* Optics Communications, 2000. 185(1-3): p. 77-82.

48. Curtis, J.E., B.A. Koss, and D.G. Grier, *Dynamic holographic optical tweezers.* Optics Communications, 2002. 207(1-6): p. 169-175.

49. Gibson, G.M., Leach, J, Keen, S, Wright, A. J, Padgett, M. J., *Measuring the accuracy of particle position and force in optical tweezers using high-speed video microscopy.* Optics Express, 2008. 16(19): p. 14561-14570.

50. Keen, S., Leach, J, Gibson, G, Padgett, M. J., *Comparison of a high-speed camera and a quadrant detector for measuring displacements in optical tweezers.* Journal of Optics a-Pure and Applied Optics, 2007. 9(8): p. S264-S266.

51. Di Leonardo, R., Ruocco, G, Leach, J, Padgett, M. J, Wright, A. J, Girkin, J. M, Burnham, D. R, McGloin, D., *Parametric resonance of optically trapped aerosols (vol 99, art no 010601, 2007).* Physical Review Letters, 2007. 99(2).

52. Crocker, J.C. and D.G. Grier, *Microscopic measurement of the pair interaction potential of charge-stablized colloid.* Physical Review Letters, 1994. 73(2): p. 352-355.

53. Dinsmore, A.D., A.G. Yodh, and D.J. Pine, *Entropic control of particle motion using passive surface microstructures.* Nature, 1996. 383(6597): p. 239-242.

54. Crocker, J.C., *Measurement of the hydrodynamic corrections to the Brownian motion of two colloidal spheres.* Journal of Chemical Physics, 1997. 106(7): p. 2837-2840.

55. Meiners, J.C. and S.R. Quake, *Direct measurement of hydrodynamic cross correlations between two particles in an external potential.* Physical Review Letters, 1999. 82(10): p. 2211-2214.

56. Di Leonardo, R., Keen, S, Leach, J, Saunter, C. D, Love, G. D, Ruocco, G, Padgett, M. J., *Eigenmodes of a hydrodynamically coupled micron-size multiple-particle ring.* Physical Review E, 2007. 76(6).

57. Yao, A.M., Keen, S. A, Burnham, D. R, Leach, J, Di Leonardo, R, McGloin, D, Padgett, M. J., *Underdamped modes in a hydrodynamically coupled microparticle system.* New Journal of Physics, 2009. 11.

58. Dholakia, K., Lee, W. M, Paterson, L, MacDonald, M. P, McDonald, R, Andreev, I, Mthunzi, P, Brown, C. T. A, Marchington, R. F, Riches, A. C., *Optical separation of cells on potential energy landscapes: Enhancement with dielectric tagging.* Ieee Journal of Selected Topics in Quantum Electronics, 2007. 13(6): p. 1646-1654.

59. Milne, G., Rhodes, D, MacDonald, M, Dholakia, K., *Fractionation of polydisperse colloid with acousto-optically generated potential energy landscapes.* Optics Letters, 2007. 32(9): p. 1144-1146.

60. Smith, R.L., Spalding, G. C, Dholakia, K, MacDonald, M. P., *Colloidal sorting in dynamic optical lattices.* Journal of Optics a-Pure and Applied Optics, 2007. 9(8): p. S134-S138.

61. Leach, J., Mushfique, H, di Leonardo, R, Padgett, M, Cooper, J., *An optically driven pump for microfluidics.* Lab on a Chip, 2006. 6(6): p. 735-739.

62. Mushfique, H., Leach, J, Di Leonardo, R, Padgett, M. J, Cooper, J. M., *Optically driven pumps and flow sensors for microfluidic systems.* Proceedings of the Institution of Mechanical Engineers Part C-Journal of Mechanical Engineering Science, 2008. 222(5): p. 829-837.

63. Mushfique, H., Leach, J, Yin, H. B, Di Leonardo, R, Padgett, M. J, Cooper, J. M., *3D mapping of microfluidic flow in laboratory-on-a-chip structures using optical tweezers.* Analytical Chemistry, 2008. 80(11): p. 4237-4240.

64. Guck, J., Ananthakrishnan, R, Cunningham, C. C, Kas, J., *Stretching biological cells with light.* Journal of Physics-Condensed Matter, 2002. 14(19): p. 4843-4856.

65. Guck, J., Ananthakrishnan, R, Mahmood, H, Moon, T. J, Cunningham, C. C, Kas, J., *The optical stretcher: A novel laser tool to micromanipulate cells.* Biophysical Journal, 2001. 81(2): p. 767-784.

66. Guck, J.R., Ananthakrishnan, R, Moon, T. J, Cunningham, C. C, Kas, J. A., *The optical stretcher - Shedding new light on the cytoskeleton.* Molecular Biology of the Cell, 2000. 11: p. 1818.

67. Guck, J., *et al*., *Optical deformability as an inherent cell marker for testing malignant transformation and metastatic competence.* Biophysical Journal, 2005. 88(5): p. 3689-3698.

68. Lincoln, B., *et al*., *Reconfigurable microfluidic integration of a dual-beam laser trap with biomedical applications.* Biomedical Microdevices, 2007. 9(5): p. 703-710.

69. Lincoln, B., Wottawah, F, Schinkinger, S, Ebert, S, Guck, J., *High-throughput rheological measurements with an optical stretcher.* Cell Mechanics, 2007. 83: p. 397-423.

70. Image taken from the webpages of the Sevick Group, Australian National University, *Animations*. 2011.

71. Pesce, G., De Luca, A. C, Rusciano, G, Netti, P. A, Fusco, S, Sasso, A., *Microrheology of complex fluids using optical tweezers: a comparison with macrorheological measurements.* Journal of Optics a-Pure and Applied Optics, 2009. 11(3).

72. Tolic-Norrelykke, I.M., Munteanu, E. L, Thon, G, Oddershede, L, Berg-Sorensen, K., *Anomalous diffusion in living yeast cells.* Physical Review Letters, 2004. 93(7): p. 4.

73. Stevenson, D.J., F. Gunn-Moore, and K. Dholakia, *Light forces the pace: optical manipulation for biophotonics.* Journal of Biomedical Optics. 15(4): p. 21.

74. Lang, M.J., Fordyce, P. M, Engh, A. M, Neuman, K. C, Block, S. M., *Simultaneous, coincident optical trapping and single-molecule fluorescence.* Nature Methods, 2004. 1(2): p. 133-139.

75. Dholakia, K., P. Reece, and M. Gu, *Optical micromanipulation.* Chemical Society Reviews, 2008. 37(1): p. 42-55.

76. Yao, A., Tassieri, M, Padgett, M, Cooper, JM., *Microrheology with optical tweezers.* Lab Chip, 2009. 9(17): p. 2568-75.

77. Image taken from the JackFruit Recipes website, 2011.

78. Image taken from the Scientia Press website, 2011.

79. Ferry, J., *Viscoelastic properties of polymers*. 1980: Wiley, John & Sons.

80. Grimm, M., S. Jeney, and T. Franosch, *Brownian motion in a Maxwell fluid.* Soft Matter. 7(5): p. 2076-2084.

81. Boon, J.P.and Yip.S., *Molecular hydrodyamics*. 1991 New York: Dover Publications.

82. Doi, M and . Edwards, S.F., *The theory of polymer dynamics*. International series of monographs on physics. 1988: Oxford science publications.

83. Kas, J., H. Strey, and E. Sackmann, *Direct imaging of reptation for semiflexible actin filaments.* Nature, 1994. 368(6468): p. 226-229.

84. Gittes, F., Mickey, B, Nettleton, J, Howard, J., *Flexural rigidity of microtubules and actin filaments measured from thermal fluctuations in shape.* Journal of Cell Biology, 1993. 120(4): p. 923-934.

85. Taylor, W.H. and P.J. Hagerman, *Application of the method of phage-T4 DNA ligase-catalyzed ring-closure to the study of SNA structure 2. NaCl-dependence of DNA flexibility and helical repeat.* Journal of Molecular Biology, 1990. 212(2): p. 363-376.

86. Morse, D.C., *Viscoelasticity of concentrated isotropic solutions of semiflexible polymers. 1. Model and stress tensor.* Macromolecules, 1998. 31(20): p. 7030-7043.

87. Morse, D.C., *Viscoelasticity of concentrated isotropic solutions of semiflexible polymers. 2. Linear response.* Macromolecules, 1998. 31(20): p. 7044-7067.

88. Morse, D.C., *Viscoelasticity of concentrated isotropic solutions of semiflexible polymers. 3. Nonlinear rheology.* Macromolecules, 1999. 32(18): p. 5934-5943.

89. *Molecular Biology of the Cell, 4th edition*, Ed. A. B.A., Johnson, J. Lewis, M. Raff, K. Roberts, and P.Walter. 2002, New York: Garland Science.

90. Gardel, M.L., Valentine, M. T, Crocker, J. C, Bausch, A. R, Weitz, D. A., *Microrheology of entangled F-actin solutions.* Physical Review Letters, 2003. 91(15).

91. *Molecular Interactions of Actin: Actin Structure and Actin-Binding Proteins*, Ed. C.G. dos Remedios. 2001, Springer.

92. Straub, F.B., *Actin.* Actin Stud Inst Med Chem Univ Szeged Hung, 1942. 2-3: p. 3-37.

93. Image taken from the Allegheny College website, 2011.

94. Basaraba, R.J., *et al*., *Actin enhances the haemolytic activity of Escherichia coli.* Microbiology – SGM, 1998. 144: p. 1845-1852.

95. Janmey, P.A., Lamb, J. A, Ezzell, R. M, Hvidt, S. Lind, S. E., *Effects of actin-filaments on fibrin clot structure and lysis.* Blood, 1992. 80(4): p. 928-936.

96. Vasconcellos, C.A., *et al*., *Reduction in viscosity of cystic-fibrosis sputum in-vitro by gelsolin.* Science, 1994. 263(5149): p. 969-971.

97. Foth, B.J., M.C. Goedecke, and D. Soldati, *New insights into myosin evolution and classification.* Proceedings of the National Academy of Sciences of the United States of America, 2006. 103(10): p. 3681-3686.

98. Molloy, J.E., Burns, J. E, Kendrickjones, J, Tregear, R. T, White, D. C. S., *Movement and force production by a single myosin head.* Nature, 1995. 378(6553): p. 209-212.

99. Molloy, J.E., *et al*., *Single-molecule mechanics of heavy-meromyosin and S1 ineracting with rabbit or drosophila actins using optical tweezers.* Biophysical Journal, 1995. 68(4): p. S298-S305.

100. Veigel, C., Molloy, J. E, Schmitz, S, Kendrick-Jones, J., *Load-dependent kinetics of force production by smooth muscle myosin measured with optical tweezers.* Nature Cell Biology, 2003. 5(11): p. 980-986.

101. Guilford, W.H., *et al*., *Smooth muscle and skeletal muscle myosins produce similar unitary forces and displacements in the laser trap.* Biophysical Journal, 1997. 72(3): p. 1006-1021.

102. Hoffman, B.D., Massiera, G, Van Citters, K. M, Crocker, J. C., *The consensus mechanics of cultured mammalian cells.* Proceedings of the National Academy of Sciences of the United States of America, 2006. 103(27): p. 10259-10264.

103. Yamada, S., D. Wirtz, and S.C. Kuo, *Mechanics of living cells measured by laser tracking microrheology.* Biophysical Journal, 2000. 78(4): p. 1736-1747.

104. Fabry, B., *et al*., *Scaling the microrheology of living cells.* Physical Review Letters, 2001. 87(14).

105. Bausch, A.R., W. Moller, and E. Sackmann, *Measurement of local viscoelasticity and forces in living cells by magnetic tweezers.* Biophysical Journal, 1999. 76(1): p. 573-579.

106. Lau, A.W.C., Hoffman, B. D, Davies, A, Crocker, J. C, Lubensky, T. C., *Microrheology, stress fluctuations, and active behavior of living cells.* Physical Review Letters, 2003. 91(19).

107. Laurent, V.M., *et al*., *Assessment of mechanical properties of adherent living cells by bead micromanipulation: Comparison of magnetic twisting cytometry vs optical tweezers.* Journal of Biomechanical Engineering-Transactions of the Asme, 2002. 124(4): p. 408-421.

108. Lu, Y.B., *et al*., *Viscoelastic properties of individual glial cells and neurons in the CNS.* Proceedings of the National Academy of Sciences of the United States of America, 2006. 103(47): p. 17759-17764.

109. Kole, T.P., Tseng, Y, Huang, L, Katz, J. L, Wirtz, D., *Rho kinase regulates the intracellular micromechanical response of adherent cells to rho activation.* Molecular Biology of the Cell, 2004. 15(7): p. 3475-3484.

110. Morse, D.C., *Tube diameter in tightly entangled solutions of semiflexible polymers.* Physical Review E, 2001. 63(3).

111. Edwards, S.F. and T.A. Vilgis, *The tube model theory of rubber elasticity.* Reports on Progress in Physics, 1988. 51(2): p. 243-297.

112. Degennes, P.G., *Reptation of a polymer chain in presence of fixed obstacles.* Journal of Chemical Physics, 1971. 55(2): p. 572

113. Doi, M. and S.F. Edwards, *Dynamics of concentrated polymer systems 1. Brownian motion in equilibrium state.* Journal of the Chemical Society-Faraday Transactions Ii, 1978. 74: p. 1789-1801.

114. Doi, M. and S.F. Edwards, *Dynamics of concentrated polymer systems 2. Molecular motion under flow.* Journal of the Chemical Society-Faraday Transactions Ii, 1978. 74: p. 1802-1817.

115. Doi, M. and S.F. Edwards, *Dynamics of concentrated polymer systems 3. Constitutice equation.* Journal of the Chemical Society-Faraday Transactions Ii, 1978. 74: p. 1818-1832.

116. Doi, M. and S.F. Edwards, *Dynamics of concentrated polymer systems 4. Rheological properties.* Journal of the Chemical Society-Faraday Transactions Ii, 1979. 75: p. 38-54.

117. Doi, M. and S.F. Edwards, *Dynamics of rod-like macromolecules in concentration solution 1.* Journal of the Chemical Society-Faraday Transactions Ii, 1978. 74: p. 560-570.

118. Doi, M. and S.F. Edwards, *Dynamics of rod-like macromolecules in concentration solution 2.* Journal of the Chemical Society-Faraday Transactions Ii, 1978. 74: p. 918-932.

119. Zimm, B.H., *Dynamics of polymer molecules in dilute solution – viscoelasticity, flow birefringence and dielectric loss.* Journal of Chemical Physics, 1956. 24(2): p. 269-278.

120. Tassieri, M., *Microrheology of Semiflexible Polymers*, Thesis, School of Physics and Astronomy. 2007, University of Leeds.

121. Khokhlov, A.R. and A.N. Semenov, *Liquid-crystalline ordering in the solution of long persistent chains.* Physica A, 1981. 108(2-3): p. 546-556.

122. Semenov, A.N. and A.R. Khokhlov, *Statistical physics of liquid-crystalline polymers.* Uspekhi Fizicheskikh Nauk, 1988. 156(3): p. 427-476.

123. Onsager, L., *The effects of shape on the interaction of colloidal particles.* Annals of the New York Academy of Sciences, 1949. 51(4): p. 627-659.

124. Kramers, H.A., *The behaviour of macromolecules in inhomogenous flow.* Journal of Chemical Physics, 1946. 14(7): p. 415-424.

125. Kirkwood, J.G. and J. Riseman, *The intrinsic viscosities and diffusion constants of flexible macromolecules in solution.* Journal of Chemical Physics, 1948. 16(6): p. 565-573.

126. Isambert, H. and A.C. Maggs, *Dynamics and Rheology of Actin Solutions.* Macromolecules, 1996. 29(3): p. 1036-1040.

127. Maggs, A.C., *Two plateau moduli for actin gels.* Physical Review E, 1997. 55(6): p. 7396-7400.

128. Semenov, A.N., *Dynamics of concentrated solutions of rigid-chain polymers 1. Brownian motion of persistent macromolecules in isotropic solution.* Journal of the Chemical Society-Faraday Transactions Ii, 1986. 82: p. 317-329.

129. Odijk, T., *On the statistics and dynamics of confined or entangled stiff polymers.* Macromolecules, 1983. 16(8): p. 1340-1344.

130. Mackintosh, F.C., J. Kas, and P.A. Janmey, *Elasticity of semiflexible biopolymer networks.* Physical Review Letters, 1995. 75(24): p. 4425-4428.

131. Rouse, P.E., *A theory of the linear viscoelastic properties of dilute solutions of coiling polymersS.* Journal of Chemical Physics, 1953. 21(7): p. 1272-1280.

132. Adam, M. and M. Delsanti, *Viscosity and longest relaxation time of semi-dilute polymer solutions 1. Good solvent.* Journal De Physique, 1983. 44(10): p. 1185-1193.

133. Adam, M. and M. Delsanti, *Viscosity of semi-dilute polymer solutions.* Journal De Physique, 1982. 43(3): p. 549-557.

134. Adam, M. and M. Delsanti, *Viscosity and longest relaxation time of semi-dilute polymer solutions 2. Theta solvent.* Journal De Physique, 1984. 45(9): p. 1513-1521.

135. Roychowdhury, P. and V.D. Deuskar, *Rheological properties of concentrated polymer solution – polybutadiene in good and O-solvents.* Journal of Applied Polymer Science, 1986. 31(1): p. 145-161.

136. Colby, R.H. and M. Rubinstein, *2-Parameter scaling for polymers in theta-solvents*Macromolecules, 1990. 23(10): p. 2753-2757.

137. Fixman, M., *Entanglements of semi-dilute polymer rods.* Physical Review Letters, 1985. 54(4): p. 337-339.

138. Bitsanis, I., H.T. Davis, and M. Tirrell, *Brownian dynamics of non-dilute solutions fo rod-like polymers 1. Low concentrations.* Macromolecules, 1988. 21(9): p. 2824-2835.

139. Tassieri, M., *et al*., *Dynamics of Semiflexible Polymer Solutions in the Highly Entangled Regime.* Physical Review Letters, 2008. 101(19).

140. Pardee, J.D. and J.A. Spudich, *Purification of muscle actin.* Methods in Cell Biology, 1982. 24: p. 271-289.

141. Kas, J., *et al*., *F-actin, a model polymer for semiflexible chains in dilute, semidilute, and liquid crystalline solutions.* Biophysical Journal, 1996. 70(2): p. 609-625.

142. Liston, A., A. Enders, and O.M. Siggs, *Unravelling the association of partial T-cell immunodeficiency and immune dysregulation.* Nat Rev Immunol, 2008. 8(7): p. 545-558.

143. Gischel, M.E., C. Beck, and M. Hall, *A Mystery Diagnosis: Immune Dysregulation, Polyendocrinopathy, Enteropathy, X-Linked Recessive.* Labmedicine, 2009. 40(5): p. 303-306.

144. Koguchi, K., *et al*., *Dysregulated T cell expression of TIM3 in multiple sclerosis.* Journal of Experimental Medicine, 2006. 203(6): p. 1413-1418.

145. Abraham, R.T. and A. Weiss, *Jurkat T cells and development of the T-cell receptor signalling paradigm.* Nat Rev Immunol, 2004. 4(4): p. 301-308.

146. Cheng-Mayer, C., Iannello, P, Shaw, K, Luciw, PA, Levy, JA., *Differential effects of nef on HIV replication: implications for viral pathogenesis in the host.* Science, 1989. 246(4937): p. 1629-1632.

147. Kulin, S., Kishore, , Hubbard, J.B, Helmerson, K., *Real-Time Measurement of Spontaneous Antigen-Antibody Dissociation.* Biophysical Journal, 2002. 83(4): p. 1965-1973.

148. Padgett, M. and R. Di Leonardo, *Holographic optical tweezers and their relevance to lab on chip devices.* Lab on a Chip. 11(7): p. 1196-1205.

149. Misawa, H., Sasaki, K, Koshioka, M, Kitamura, N, Masuhara, H., *Multibeam laser manipulation and fixation of microparticles.* Applied Physics Letters, 1992. 60(3): p. 310-312.

150. Sasaki, K., Koshioka, M, Misawa, H, Kitamura, N, Masuhara, H., *Pattern formation and flow-control of fine particles by laser-scanning micromanipulation.* Optics Letters, 1991. 16(19): p. 1463-1465.

151. Visscher, K., S.P. Gross, and S.M. Block, *Construction of multiple-beam optical traps with nanometer-resolution position sensing.* Ieee Journal of Selected Topics in Quantum Electronics, 1996. 2(4): p. 1066-1076.

152. Berg-Sorensen, K. and H. Flyvbjerg, *Power spectrum analysis for optical tweezers.* Review of Scientific Instruments, 2004. 75(3): p. 594-612.

153. Tolic-Norrelykke, S.F., *et al*., *Calibration of optical tweezers with positional detection in the back focal plane.* Review of Scientific Instruments, 2006. 77(10).

154. Tassieri, M., Gibson, G. M, Evans, R. M. L, Yao, A. M, Warren, R, Padgett, M. J, Cooper, J. M., *Measuring storage and loss moduli using optical tweezers: Broadband microrheology.* Physical Review E, 2010. 81(2): p. 5.

155. Preece, D., Warren, R, Tassieri, M, Evans, R.M.L, Gibson, G.M, Padgett, M.J, Cooper, J.M., *Optical tweezers: wideband microrheology.* Journal of Optics. 13(4).

156. Starrs, L. and P. Bartlett, *One- and two-point micro-rheology of viscoelastic media.* Journal of Physics-Condensed Matter, 2003. 15(1): p. S251-S256.

157. Atakhorrami, M. and C.F. Schmidt, *High-bandwidth one- and two-particle microrheology in solutions of wormlike micelles.* Rheologica Acta, 2006. 45(4): p. 449-456.

158. Nijenhuis, N., Mizuno, D, Spaan, J. A. E, Schmidt, C. F., *Viscoelastic response of a model endothelial glycocalyx.* Physical Biology, 2009. 6(2).

159. Valentine, M.T., L.E. Dewalt, and H.D. OuYang, *Forces on a colloidal particle in a polymer solution: A study using optical tweezers.* Journal of Physics-Condensed Matter, 1996. 8(47): p. 9477-9482.

160. Hough, L.A. and H.D. Ou-Yang, *Viscoelasticity of aqueous telechelic poly(ethylene oxide) solutions: Relaxation and structure.* Physical Review E, 2006. 73(3): p. 8.

161. Evans, R.M.L., Tassieri, M, Auhl, D, Waigh, T. A., *Direct conversion of rheological compliance measurements into storage and loss moduli.* Physical Review E, 2009. 80(1).

162. Fielding, S.M., P. Sollich, and M.E. Cates, *Aging and rheology in soft materials.* Journal of Rheology, 2000. 44(2): p. 323-369.

163. Ashkin, A., *Forces of a Single-Beam Gradient Laser Trap on a Dielectric Sphere in the Ray Optics Regime.* Biophysical Journal, 1992. 61(2): p. 569-582.

164. Preece, D., *et al*., *Increasing trap stiffness with position clamping in holographic optical tweezers.* Optics Express, 2009. 17(25): p. 22718-22725.

165. Narita, T., Knaebel, A, Munch, J. P, Candau, S. J., *Microrheology of poly(vinyl alcohol) aqueous solutions and chemically cross-linked gels.* Macromolecules, 2001. 34(23): p. 8224-8231.

166. van Zanten, J.H. and K.P. Rufener, *Brownian motion in a single relaxation time Maxwell fluid.* Physical Review E, 2000. 62(4): p. 5389-5396.

167. van der Gucht, J., Besseling, N. A. M, Knoben, W, Bouteiller, L, Stuart, M. A. C., *Brownian particles in supramolecular polymer solutions.* Physical Review E, 2003. 67(5).

168. van Zanten, J.H., S. Amin, and A.A. Abdala, *Brownian motion of colloidal spheres in aqueous PEO solutions.* Macromolecules, 2004. 37(10): p. 3874-3880.

169. Crocker, J.C., *et al*., *Two-point microrheology of inhomogeneous soft materials.* Physical Review Letters, 2000. 85(4): p. 888-891.

170. Rubinstein, M., Colby, R.H.,, *Polymer Physics*. 2003, New York: Oxford University Press.

171. Einstein, A., *The theory of the Brownian Motion.* Annalen Der Physik, 1906. 19(2): p. 371-381.

172. Starrs, L. and P. Bartlett, *Colloidal dynamics in polymer solutions: Optical two-point microrheology measurements.* Faraday Discussions, 2003. 123: p. 323-334.

173. Mason, T.G. *Estimating the viscoelastic moduli of complex fluids using the generalized Stokes-Einstein equation.* Rheologica Acta, 2000. 39: p 371

174. De Gennes, P-G. *Scaling concepts in polymer physics.* 1979. Cornell University Press.

175. Farge, E. and A.C. Maggs, *Dynamic scattering from semiflexible polymers.* Macromolecules, 1993. 26(19): p. 5041-5044.

176. Liverpool, T.B. and A.C. Maggs, *Dynamic scattering from semiflexible polymers.* Macromolecules, 2001. 34(17): p. 6064-6073.

177. Xu, J.Y., A. Palmer, and D. Wirtz, *Rheology and microrheology of semiflexible polymer solutions: Actin filament networks.* Macromolecules, 1998. 31(19): p. 6486-6492.

178. Schnurr, B., Gittes, F, MacKintosh, F. C, Schmidt, C. F., *Determining microscopic viscoelasticity in flexible and semiflexible polymer networks from thermal fluctuations.* Macromolecules, 1997. 30(25): p. 7781-7792.

179. Gisler, T. and D.A. Weitz, *Scaling of the microrheology of semidilute F-actin solutions.* Physical Review Letters, 1999. 82(7): p. 1606-1609.

180. Amblard, F., *et al*., *Subdiffusion and anomalous local viscoelasticity in actin networks.* Physical Review Letters, 1996. 77(21): p. 4470-4473.

181. Degennes, P.G., *Scaling concepts in polymer physics*. 1979: Cornell University Press.

182. Everaers, R., Julicher, F, Ajdari, A, Maggs, A. C., *Dynamic fluctuations of semiflexible filaments.* Physical Review Letters, 1999. 82(18): p. 3717-3720.

183. Liverpool, T.B., *Dynamics of inextensible semiflexible filaments.* Physical Review E, 2005. 72(2).

184. Xu, J., *et al*., *Mechanical Properties of Actin Filament Networks Depend on Preparation, Polymerization Conditions, and Storage of Actin Monomers.* Biophysical Journal, 1998. 74(5): p. 2731-2740.

185. Muller, O., Gaub, H. E, Barmann, M, Sackmann, E., *Viscoelastic moduli of sterically and chemically cross-linked actin networks in the dilute to semidilute regime – measurements by an oscillating disc rheometer.* Macromolecules, 1991. 24(11): p. 3111-3120.

186. Ruddies, R., Goldmann, W. H, Isenberg, G, Sackmann, E., *The viscoelasticity of entangled actin networks – the influence of defects and modulation by talin and viculin.* European Biophysics Journal with Biophysics Letters, 1993. 22(5): p. 309-321.

187. Atakhorrami, M., *et al*., *Short-time inertial response of viscoelastic fluids measured with Brownian motion and with active probes.* Physical Review E, 2008. 77(6).

188. Shin, J.H., Gardel, M. L, Mahadevan, L, Matsudaira, P, Weitz, D. A., *Relating microstructure to rheology of a bundled and cross-linked F-actin network in vitro.* Proceedings of the National Academy of Sciences of the United States of America, 2004. 101(26): p. 9636-9641.

189. Gardel, M.L., *et al*., *Prestressed F-actin networks cross-linked by hinged filamins replicate mechanical properties of cells.* Proceedings of the National Academy of Sciences of the United States of America, 2006. 103(6): p. 1762-1767.

190. Janmey, P.A., Hvidt, S, Lamb, J, Stossel, T. P., *Resemblance of actin-binding protein actin gels to covalently corss-linked networks.*. Nature, 1990. 345(6270): p. 89-92.

191. Shin, J.H., *et al*., *The mechanical properties and microstructure of bundled and cross-linked actin networks.* Biophysical Journal, 2003. 84(2): p. 437A-437A.

192. Lieleg, O., Kayser, J, Brambilla, G, Cipelletti, L, Bausch, A. R., *Slow dynamics and internal stress relaxation in bundled cytoskeletal networks.* Nature Materials. 10(3): p. 236-242.

193. Koenderink, G.H., *et al*., *An active biopolymer network controlled by molecular motors.* Proceedings of the National Academy of Sciences of the United States of America, 2009. 106(36): p. 15192-15197.

194. Lieleg, O., Claessens, M, Luan, Y, Bausch, A. R., *Transient binding and dissipation in cross-linked actin networks.* Physical Review Letters, 2008. 101(10).

195. Xu, J.Y., D. Wirtz, and T.D. Pollard, *Dynamic cross-linking by alpha-actinin determines the mechanical properties of actin filament networks.* Journal of Biological Chemistry, 1998. 273(16): p. 9570-9576.

196. Gardel, M.L., Valentine, M. T, Crocker, J. C, Bausch, A. R, Weitz, D. A., *Microrheology of bundled and cross-linked F-actin networks.* Biophysical Journal, 2002. 82(1): p. 1867.

197. Kasza, K.E., *et al*., *Actin Filament Length Tunes Elasticity of Flexibly Cross-Linked Actin Networks.* Biophysical Journal. 99(4): p. 1091-1100.

198. Geeves, M.A. and K.C. Holmes, *Structural mechanism of muscle contraction.* Annual Review of Biochemistry, 1999. 68: p. 687-728.

199. Lieleg, O., Schmoller, K. M, Claessens, M, Bausch, A. R., *Cytoskeletal Polymer Networks: Viscoelastic Properties are Determined by the Microscopic Interaction Potential of Cross-links.* Biophysical Journal, 2009. 96(11): p. 4725-4732.

200. Tharmann, R., M. Claessens, and A.R. Bausch, *Viscoelasticity of isotropically cross-linked actin networks.* Physical Review Letters, 2007. 98(8).

201. Luan, Y., Lieleg, O, Wagner, B, Bausch, A. R., *Micro- and macrorheological properties of isotropically cross-linked actin networks.* Biophysical Journal, 2008. 94(2): p. 688-693.

202. Marston, S.B., *The rates of formation and dissociation of actin-myosin complexes – effects of solvent, temperature, nucleotide binding head-head interactions.* Biochemical Journal, 1982. 203(2): p. 453-460.

203. Miyata, H., R. Yasuda, and K. Kinosita, *Strength and lifetime of the bond between actin and skeletal muscle alpha-actinin studied with an optical trapping technique.* Biochimica Et Biophysica Acta-General Subjects, 1996. 1290(1): p. 83-88.

204. Le Goff, L., F. Amblard, and E.M. Furst, *Motor-driven dynamics in actin-myosin networks.* Biophysical Journal, 2002. 82(1): p. 1812.

205. Mizuno, D., Tardin, C., Schmidt, C. F., MacKintosh, F. C., *Nonequilibrium mechanics of active cytoskeletal networks.* Science, 2007. 315(5810): p. 370-373.201.

206. Hale, C.M., S.X. Sun, and D. Wirtz, *Resolving the Role of Actoymyosin Contractility in Cell Microrheology.* PLoS ONE, 2009. 4(9).

207. Kollmannsberger, P. and B. Fabry, *Linear and Nonlinear Rheology of Living Cells*, in *Annual Review of Materials Research, Vol 41*, D.R.F.P. Clarke, Editor. p. 75-97.

208. Bursac, P., et al., *Cytoskeletal remodelling and slow dynamics in the living cell.* Nature Materials, 2005. 4(7): p. 557-561.

209. Nyquist, H., *Thermal Agitation of Electric Charge in Conductors*. Physical Review, 1928, 32: 110–113

210. Granek, R., *From semi-flexible polymers to membranes: Anomalous diffusion and reptation.* Journal De Physique Ii, 1997. 7(12): p. 1761-1788.

211. Humphrey, D., Duggan, C, Saha, D, Smith, D, Kas, J., *Active fluidization of polymer networks through molecular motors.* Nature, 2002. 416(6879): p. 413-416.

212. Chicurel, M.E., C.S. Chen, and D.E. Ingber, *Cellular control lies in the balance of forces.* Current Opinion in Cell Biology, 1998. 10(2): p. 232-239.

213. Parsons, J.T., A.R. Horwitz, and M.A. Schwartz, *Cell adhesion: integrating cytoskeletal dynamics and cellular tension.* Nat Rev Mol Cell Biol. 11(9): p. 633-643.

214. Nagy, T., *et al*., *O-GlcNAc modification of proteins affects volume regulation in Jurkat cells.* European Biophysics Journal, 2010. 39(8): p. 1207-1217.

215. Mountian, I., Waelkens, E, Missiaen, L, van Driessche, W., *Changes in actin cytoskeleton during volume regulation in C6 glial cells.* European Journal of Cell Biology, 1998. 77(3): p. 196-204.

216. Ebner, H.L., *et al*., *Importance of cytoskeletal elements in volume regulatory responses of trout hepatocytes.* American Journal of Physiology-Regulatory Integrative and Comparative Physiology, 2005. 289(3): p. R877-R890.

217. Bibby, K.J. and C.A.G. McCulloch, *Regulation of cell-volume and Ca^{2+} in attached human fibroblasts responding to anisosmotic buffers.* American Journal of Physiology, 1994. 266(6): p. C1639-C1649.

218. Moran, J., Sabanero, M, Meza, I, PasantesMorales, H., *Changes of actin cytoskeleton during swelling and regulatory volume decrease in cultured astrocytes.* American Journal of Physiology-Cell Physiology, 1996. 271(6): p. C1901-C1907.

219. Papakonstanti, E.A. and C. Stournaras, *Actin cytoskeleton architecture and signaling in osmosensing.* Osmosensing and Osmosignaling, 2007. 428: p. 227-240.

220. Lepple-Wienhues, A., *et al*., *The tyrosine kinase p56(lck) mediates activation of swelling-induced chloride channels in lymphocytes.* Journal of Cell Biology, 1998. 141(1): p. 281-286.

221. Levitan, I., Almonte, C, Mollard, P, Garber, S. S., *Modulation of a volume-regulated chloride current by F-actin*. Journal of Membrane Biology, 1995. 147(3): p. 283-294.

222. Bausch, A.R., Ziemann, F, Boulbitch, A. A, Jacobson, K, Sackmann, E., *Local measurements of viscoelastic parameters of adherent cell surfaces by magnetic bead microrheometry.* Biophysical Journal, 1998. 75(4): p. 2038-2049.

223. Bausch, A.R., Hellerer, U, Essler, M, Aepfelbacher, M, Sackmann, E., *Rapid stiffening of integrin receptor-actin linkages in endothelial cells stimulated with thrombin: A magnetic bead microrheology study.* Biophysical Journal, 2001. 80(6): p. 2649-2657.

224. Uhde, J., Feneberg, W, Ter-Oganessian, N, Sackmann, E, Boulbitch, A., *Osmotic force-controlled microrheometry of entangled actin networks.* Physical Review Letters, 2005. 94(19).

225. Rogers, S.S., T.A. Waigh, and J.R. Lu, *Intracellular microrheology of motile Amoeba proteus.* Biophysical Journal, 2008. 94(8): p. 3313-3322.

226. Massiera, G., Van Citters, K. M., Biancaniello, P. L., Crocker, J. C. *Mechanics of single cells: Rheology, time depndence, and fluctuations.* Biophysical Journal, 2007. 93: p. 3703-3713.

227. Cantiello, H.F., *Role of actin filament organization in cell volume and ion channel regulation.* Journal of Experimental Zoology, 1997. 279(5): p. 425-435.

228. Squires, T.M. and T.G. Mason, *Fluid Mechanics of Microrheology*, in *Annual Review of Fluid Mechanics*. p. 413-438.

229. Koyama, T., M. Oike, and Y. Ito, *Involvement of Rho-kinase and tyrosine kinase in hypotonic stress-induced ATP release in bovine aortic endothelial cells.* Journal of Physiology-London, 2001. 532(3): p. 759-769.

Appendix

Buffers

A. Guba-Straub

Purpose: To separate out the actin and myosin components of fresh muscle

0.3M KCl
0.1M KH_2PO_4
0.05M K_2HPO_4
1mM ATP
5mM $MgCl_2$
1mM DTT
pH 6.5

B. Actin extraction buffer

Purpose: To dissolve actin from actin precipitate.

0.4% $NaHCO_3$

C. ACEX

Purpose: To extract actin from acetone powder

2mM Tris pH 8.0
0.2mM Na_2ATP
0.2mM $CaCl_2$
1mM DTT
0.4mM Azide
pH 8.0

DTT and ATP added fresh, buffer left on ice in cold room

D. Myosin prep

Purpose: To resuspend the myosin pellet.

50mM	Potassium phosphate buffer [61.5vol K_2HPO_4 to 38.5vol KH_2PO_4]
5mM	DTT
5mM	EDTA
3M	KCl
pH t7.0	

E. Low salt myosin MIT

Purpose: To dissolve myosin.

50mM	KCl
0.7mM	$MgCl_2$
25mM	Imidazole
5mM	ATP
0.2nM	$CaCl_2$
pH 7.4	

F. High salt myosin MIT

Purpose: To dissolve myosin for the chymotrypsin digestion that creates the HMM fragment.

300mM	KCl
4mM	$MgCl_2$
1mM	DTT
25mM	Imidazole
pH 7.4	

G. 1xAB^+_{ICP}

Purpose: To polymerise G-actin to F-actin.

25mM	IMadizole-HCl
25mM	KCl
2mM	$MgCl_2$
1mM	EGTA

1mM	DTT
10mM	Creatine Phosphate
200μM	ATP
1mg/ml	Creatine Phosphokinase (added just before use)

Techniques

Optical density measurements

The optical density (or absorbance) is defined as $A_\lambda = \log(I_0 / I)$ where I_0 is the intensity of light of wavelength λ, and I is the intensity of light has passed through the sample. The absorbance of a sample is proportional to the thickness of the sample and the concentration of the absorbing species within the sample.

To calculate the concentration of Actin, the optical density was measured at a light wavelength of 290-310nm, and this was compared to a background measurement of ACEX buffer. The extinction coefficient of actin (*i.e.* the measure of how strongly the substance absorbs light at a given wavelength per mass density) is:

$$A_{290} - A_{310} \text{ extinction coefficient} = 0.62/cm^2/mg$$

The concentration of the myosin solutions were also measured, at a wavelength of 280-340nm, using buffer solutions as background measurements. The extinction coefficients of myosin, S1, and HMM are:

$$\text{Myosin: } A_{280} - A_{340} = 0.53/cm^2/mg$$

$$\text{S1: } A_{280} - A_{340} \text{ extinction coefficient} = 0.83/cm^2/mg$$

$$\text{HMM: } A_{280} - A_{340} \text{ extinction coefficient} = 0.53/cm^2/mg$$